Distinguishing primary versus secondary geochemical and silicon isotope characteristics of Precambrian chert and iron formation

A Dissertation Presented for the
Doctor of Philosophy
Degree
The University of Tennessee, Knoxville

Latisha Ashley Brengman
May 2015

Copyright © 2015 by Latisha Ashley Brengman.
All rights reserved.

ACKNOWLEDGEMENTS

This work would not have been possible without the support, insight, and guidance of my advisor Dr. Chris Fedo. His investment and interest in helping me pursue this research and foster a better understanding of the scientific endeavor was indispensable. I also need to thank the members of my committee both past (Dr. Michael Hren) and present (Dr. Linda Kah, Dr. Theodore Labotka, Dr. Steven Wilhelm) for their continued help, encouragement and assistance during this PhD. I am grateful to the rest of the faculty and staff of the Department of Earth and Planetary Science and the University of Tennessee for all of their support, as well as countless friends both inside and outside of the department. I am also thankful to have had the wonderful opportunity to work with several collaborators around the world. I would specifically like to thank Dr. Martin Whitehouse for his guidance in using the NORMSIMS facility at the Naturhistoriska riksmuseet in Stockholm Sweden, and Dr. Neil Banerjee and his lab manager Dr. Iffat Jabeen for their help in processing samples using the IRMS at the University of Western Ontario. In addition, I would like to thank all of those who helped me in the field including Brian Atkinson of the Ontario Ministry of Northern Development and Mines, Pierre Doucet of the Ministère de l'Énergie et des Ressources naturelles in Quebec, Dave Guindon of the Ontario Geological Survey, as well as my field assistants, Lindsey and Erika. Lastly, I would like to thank my parents for their endless support. This work would not have been possible without the help of all involved, and funding from NASA, ExxonMobil, Geological Society of America, Sedimentary Division of the Geological Society of America, and the UTK Department of Earth and Planetary Sciences.

ABSTRACT

Precambrian chert and banded iron formation (BIF) are defined as chemical sediments precipitated directly from seawater. As such, their geochemistry, including trace elements, rare earth elements (REE), and isotopes (O, Si) may preserve Precambrian seawater conditions. However, the chemical signature of these rocks may not simply reflect seawater, because hydrothermal interactions and metasomatism may produce rocks that petrographically and chemically resemble chert and BIF, including seawater-like compositional characteristics acquired during mineral replacement. Interpreting the major-, trace-, and rare-earth element signatures of these rocks requires the identification of geochemical and isotopic fingerprints that differentiate rocks formed from chemical sedimentation from rocks formed through replacement.

Previously, REE proxies have been used to identify chemically precipitated sedimentary rocks such as chert. However, these established proxies have proven to be non-diagnostic in depositional settings where alteration has resulted in element mobility. Silicon isotopes, by contrast, have the potential to discriminate rocks formed by chemical sedimentation from those formed through replacement, because they record process-specific information concerning the mechanism of quartz precipitation. Of equal importance, silicon isotopes can provide key information that may identify marine silicon sources.

Using information concerning what isotopic signatures can be preserved in quartz precipitates from different depositional settings, a compilation of the silicon isotope composition of chert can be deciphered to understand lithology-dependent trends. Archean-aged silicified rocks formed through replacement of primary minerals by quartz have a silicon-isotope composition similar to the original rock. Chemical sedimentary chert formed through quartz precipitation proximal to hydrothermal systems has a wide range of silicon-isotope compositions, and shows no apparent trend with respect to time. Only chemical sedimentary cherts associated with iron formation formed in continentally influenced depositional settings record a systematic trend with respect to time. These rocks record a unidirectional positive shift in silicon-isotope compositions. We interpret this trend to reflect chemical precipitation from a changing ocean reservoir, where, as a result of steady growth and emergence of continental masses, the ocean reservoir evolved from one dominated by a hydrothermal silicon isotope signature to a continental one.

TABLE OF CONTENTS

CHAPTER I Introduction....1
Purpose Statement....2
Introduction to chert....2
The problem of defining chert....2
Chert terminology....3
Chert outliers....3
Chert terminology used in this dissertation....4
General geochemical characteristics of chert and iron formation....4
Introduction to silicon isotope geochemistry and the Precambrian silica cycle....5
Introduction to dissertation....5
Dissertation Chapters....5
Chapter I: Introduction....5
Chapter II: Geochemical evolution and textural preservation in a suite of altered volcanic rocks and jaspilite from the ~2.72 Ga Hunter Mine Group in the Abitibi Greenstone Belt....6
Chapter III: Micro-scale silicon isotope heterogeneity observed in >3.7 Ga hydrothermal quartz precipitates: implications for interpreting the δ^{30}Si record of chert....6
Chapter IV: Silicon isotope evidence for continental emergence at ~3 Ga....7
Glossary of terms....9
List of references....10
Appendix A-1....14
CHAPTER II Geochemical evolution and textural preservation in a suite of altered volcanic rocks and jaspilite from the ~2.72 Ga Hunter Mine Group in the Abitibi Greenstone Belt....19
Abstract....20
Introduction....20
Geologic Setting....21
Analytical Techniques....22
Definition of Lithologic Groups....23
Petrography....23
Group 1....23
Description....23
Interpretation....23
Group 2....23
Description....23
Interpretation....25
Group 3....25
Description....25
Interpretation....25
Geochemistry....25
Whole-rock major-element, and individual mineral geochemistry....26
Group 1 volcanic rocks....26
Group 2 altered volcanic rocks....27
Group 3 jaspilite rocks....27
Trace- and rare-earth elements....27

Group 1 volcanic rocks 28
Group 2 altered volcanic rocks 28
Group 3 jaspilite rocks 28
Synthesis and interpretation of geochemical data for Groups 1, 2, 3 28
Major-elements 28
Trace- and rare-earth elements by group 29
Compositional evolution of Group 1 rocks to produce Group 3 rocks 30
Group 1 volcanic rock textures and geochemistry 30
Group 2 altered volcanic rock textures and geochemistry 31
Group 3 jaspilite rock textures and geochemistry 31
Implications for geochemical fingerprints of chert 32
Conclusions 33
List of references 34
Appendix A-2 38
CHAPTER III Extreme micro-scale silicon isotope heterogeneity observed in >3.7 Ga hydrothermal quartz precipitates: implications for interpreting the δ^{30}Si record of chert 53
Abstract 54
Introduction 54
Methods 55
Geologic context of samples and quartz petrography 55
Results 56
Silicon isotope composition 56
Oxygen isotope composition 56
Interpreting silicon isotopes in the rock record 56
Preservation potential of silicon isotope signatures 56
Kinetic isotope effects in quartz precipitates 57
Application of a kinetic model to understand δ^{30}Si micro-scale heterogeneity 57
Significance 58
Acknowledgements 58
List of references 59
Appendix A-3 63
CHAPTER IV Silicon isotope evidence for continental emergence at ~ 3 Ga 67
Abstract 68
Introduction 68
Silicon isotope sources and sinks 68
Methods 69
Buhwa Greenstone Belt, Zimbabwe Case study 70
Geologic setting of studied samples 70
Bedrock and detrital quartzite 70
Silicon isotope compositions of quartz from siliceous marine precipitates 71
Decoding the silicon isotope archive of chert 71
Geologic setting of studied samples 71
Isua Greenstone Belt, Greenland 71
Abitibi Greenstone Belt, Canada 72
Isotopic composition by rock type and depositional setting 72

Silicified volcanic rocks....72
Bedded chert....73
Algoma-type banded iron formation....73
Superior-type banded iron formation....74
Provisional flux model for the Precambrian silica cycle....74
Interpreting the decoded silicon isotope archive of chert....75
Significance....75
Acknowledgements....76
List of references....77
Appendix A-4....81
CHAPTER V Conclusions....91
Appendix A-5....94
Additional figures....94
Chapter III: Comparison of data from this study to experimental silicon isotope data....94
Chapter IV....99
Methods....106
Standard information....106
Sample information....111
Full mount maps, post-gold coat analyses....111
Individual sample maps....117
VITA....238

LIST OF TABLES

Appendix A-1 14
Table 1-1. Chert terminology used in this dissertation 14
Appendix A-5 94
Chapter II tables 153
Table 2-1. Criteria for defining lithologic groups 1, 2, 3 153
Table 2-2. Major element data for Groups 1, 2, 3 154
Table 2-3. Electron microprobe data for Group 1 feldspars inside silicification 155
Table 2-4. Electron microprobe data for Group 1 feldspars outside silicification 156
Table 2-5. Electron microprobe data for Group 1 quartz 157
Table 2-6. Electron microprobe data for Group 2 feldspars outside silicification 158
Table 2-7. Trace element data for Groups 1, 2, 3 159
Table 2-8. Rare earth element data for Groups 1, 2, 3 163
Chapter III tables 164
Table 3-1. $\delta^{18}O$ and $\delta^{30}Si$ isotope compositions of pillow basalt sample 164
Table 3-2. $\delta^{30}Si$ isotope compositions of chert and chert clast samples 167
Chapter IV tables 171
Table 4-1. Comparison of NBS-28 (international stnd.) with UTQ (internal stnd.) 171
Table 4-2. Measured $\delta^{30}Si$ values for standard runs 173
Table 4-3. Whole-rock $\delta^{30}Si$ and $\delta^{18}O$ data 191
Table 4-4. $\delta^{30}Si$ isotope data for all chert and iron formation samples in Chapter IV. 194
Table 4-5. Calculated $\delta^{30}Si$ peak values for each sample 223
Table 4-6. Compiled sources and sample locations for others $\delta^{30}Si$ data 224
Table 4-7. Preliminary run $\delta^{30}Si$ data including measured crystal sizes 227

LIST OF FIGURES

Appendix A-1 15
Figure 1-1. Hierarchy chart outlining chert terminology used in this dissertation 16
Figure 1-2. Plot showing shale-normalized REY pattern of chemical sedimentary chert/BIF (blue), and silicified komatiite (green), modified from Hofmann and Harris (2008) 17
Figure 1-3. δ^{30}Si composition of common abiotic silicon reservoirs. Igneous rocks include average values for both mafic and felsic rocks. Riverine input includes the range of values measured for silicic acid within different modern river systems. Soil clays include analyses from kaolinite separates. Ocean value represents homogenized ocean signature. Oceanic hydrothermal fluids represents values measured for vent fluids. Sea-floor Si deposits refers to (non-siliceous ooze). Ferruginous cherty Fe-oxide deposits measured from modern hydrothermal vent sites. Information from Andre et al. (2006). 18
Figure 1-4. Plot showing difference in silicon isotope composition between solid quartz precipitate and solution ($\Delta_{solid\text{-}solution}$), versus precipitation rate of quartz. Note kinetic isotope fractionation dominates earlier stages in the experiment where net reaction rate was greater. By contrast, equilibrium (steady-state) isotope fractionation dominated later stages of the experiment, where net reaction rate was slower. Figure from Oelze et al. (2015) experiment. 19
Appendix A-2 38
Figure 2-1. Geologic map of Hunter Mine Group region, of the Abitibi Greenstone Belt, with an inset showing the location of the greenstone belt in Canada. Samples in this study come from outcrops labeled 2.1, 2.3, and 2.4. Modified from Dostal and Mueller, (2012). 38
Figure 2-2. Representative stratigraphic column of the Hunter Mine Group. All samples from this study were collected near the contact between the middle and upper formational stages. Modified from Mueller and Mortensen (2002). Star (*) denotes units of interest to this study. 39
Figure 2-3. Incident light photographs, and plane and cross-polarized light photomicrographs of representative samples from Group 1, 2, and 3 rocks. (A) Incident light photograph documenting diffuse boundary between silicified and un-silicified volcanic material in Group 1 sample AB-11-11. (B) Cross-polarized light photomicrograph showing igneous quartz and feldspar phenocrysts surrounded by un-silicified volcanic matrix material in Group 1 sample AB-11-11. (C) Cross-polarized light photomicrograph showing preservation of primary igneous phenocrysts despite incipient silicification of matrix material in Group 1 sample AB-11-11. (D) Incident light photograph documenting diffuse nature of silicification in progressively altered Group 2 rocks (Sample AB-11-12). (E) Plane-polarized light photomicrograph of Group 2 sample AB-11-12 showing silicified material, and clear volcaniclastic material that passes through the edge of silicification from un-silicified volcanic matrix material indicating a replacement origin for the silicification, rather than a chemical sedimentation origin. (F) Cross-polarized light photomicrograph of (E). (G) Incident light photomicrograph showing only faint textural heterogeneity in some

jaspilite Group 3 samples. (H) Plane-polarized light image showing textural evidence of silicified volcaniclastic material that is now compositionally hematite (hm) and quartz in representative Group 3 sample AB-11-23. (I) Plane-polarized light image showing preservation of pronged glass shards enveloped in a quartz and hematite matrix in representative Group 3 sample AB-11-19. 40
Figure 2-4. Plane-polarized light and cross-polarized light images of representative Group 2 altered volcanic rock samples. (A) Plane-polarized light image showing an example of discontinuous silicification and preservation of un-silicified volcanic matrix material and quartz phenocryst. (B) Cross-polarized light image of (A). (C) Plane-polarized light image showing an example of discontinuous silicification and preservation of quartz phenocryst and original volcanic matrix material, as well as preservation of a clast of similar silicified material. (D) Cross-polarized light image of (C). Plane-polarized light image showing un-silicified volcaniclastic matrix material, and a silicified armored lapilli. (F) Cross-polarized light image of (E). 41
Figure 2-5. Plane-polarized light and cross-polarized light images of representative Group 3 jaspilite samples. (A) Plane-polarized light image showing preservation of glass shards. (B) Cross-polarized light image showing preservation of lapilli, now completely compositionally replaced by micro-crystalline quartz. (C) Plane-polarized light image showing volcaniclastic material now compositionally replaced by quartz and surrounded by hematite. (D) Same as (C). (E) Cross-polarized light image showing clastic textures preserved in the jaspilite, now compositionally entirely made of quartz. (F) Evidence of quartz and calcite veining. 42
Figure 2-6. (A) Major element oxide plot of Group 1 samples normalized to least altered volcanic rock sample from Group 1, AB-11-11. (B) Major element oxide plot of Group 2 samples normalized to least altered volcanic rock sample from Group 1, AB-11-11. (C) Major element oxide plot of Group 3 samples normalized to least altered volcanic rock sample from Group 1, AB-11-11. 43
Figure 2-7. Elemental X-ray maps for representative Group 1 felsic volcanic rock sample AB-11-11. (A) Backscatter electron image of volcanic rock sample showing preservation of quartz and feldspar phenocrysts, both inside (Q_{in}) and outside (Q_{out}, and fsp_{out}) of the silicified areas which are surrounded by a chloritic matrix. (B) Aluminum Kα x-ray map showing the non-uniform nature of incipient silicification is representative group 1 sample. (C) Silica Kα x-ray map showing preservation of phenocrysts inside the silicification patch, as well as documenting the compositional heterogeneities inside the silicification patch. (D) Iron Kα x-ray map showing Fe-rich composition of chloritic matrix material. 44
Figure 2-8. EMP Elemental X-ray maps for representative Group 2 altered volcanic rock sample AB-11-12. (A) Backscatter electron image of volcanic rock sample showing silicified areas surrounded by a chloritic matrix. (B) Aluminum Kα x-ray map showing silicified areas surrounded by a chloritic matrix. (C) Silica Kα x-ray map showing silicified areas surrounded by a chloritic matrix, and documenting minor compositional heterogeneities inside the silicification patch. (D) Iron Kα x-ray map highlighting compositional heterogeneities and potential preservation of remnant original volcanic textures inside of the silicification patch. 45

Figure 2-9. Elemental X-ray maps for representative Group 3 jaspilite rock sample AB-11-23. (A) Backscatter electron image of jaspilite rock sample showing silicified and iron-mineralized areas. (B) Aluminum Kα x-ray map showing silicified and iron-mineralized areas. (C) Silica Kα x-ray map showing silicified and iron-mineralized areas, potential preservation of remnant clastic textures. (D) Iron Kα x-ray map highlighting compositional heterogeneities in silicified and iron-mineralized areas, and potential preservation of remnant clastic textures. 46
Figure 2-10. (A) Spider plot of Group 1 samples normalized to average late Archean felsic volcanic rocks (Condie, 1993). (B) Rare earth element plot of Group 1 samples normalized to post Archean average shale composite. (C) Spider plot of Group 2 samples normalized to average late Archean felsic volcanic rocks (Condie, 1993). (D) Rare earth element plot of Group 2 samples normalized to post Archean average shale composite. Denotations mark important geochemical features of seawater as defined in the text. (E) Spider plot of Group 3 samples normalized to average late Archean felsic volcanic rocks (Condie, 1993). (F) Rare earth element plot of Group 3 samples normalized to Post Archean Average Shale composite. La_{SN}/La_{SN}* and Eu_{SN}/Eu_{SN}* mark important geochemical features of seawater as defined in the text, equations can be found in Lawrence and Kamber, 2006. Shaded area denotes typical pattern for Precambrian seawater. 48
Figure 2-11. Total alkali silica (TAS) plot of Group 1, 2, and 3 samples. 49
Figure 2-12. Traditional AFM volcanic discrimination diagram of group 1, 2, and 3 samples. Note the trend from groups 1 – 3 documenting Fe addition, and loss of other elements during the silicification process. Calc-alkaline volcanic trend marked for reference. 50
Figure 2-13. REE comparison plots for Group 1 (filled triangles), Group 2 (open squares), and Group 3 (open circles) samples. Grey shaded area indicates "seawater" signature. Note separation of Group 1 from Group 3 samples in plots A-E. (A) Plot showing slope (Pr_{SN}/Yb_{SN}) verses Europium anomaly (Eu_{SN}/Eu_{SN}*). (B) Plot showing Y/Ho verses Europium anomaly (Eu_{SN}/Eu_{SN}*). (C) Plot showing Y/Ho verses slope (Pr_{SN}/Yb_{SN}). (D) Plot showing Lanthanum anomaly (La_{SN}/La_{SN}*) verses Europium anomaly (Eu_{SN}/Eu_{SN}*). (E) Plot showing Y/Ho verses Lanthanum anomaly (La_{SN}/La_{SN}*). (F) Plot showing Y/Ho verses Zr/Hf. All samples fall within range expected for igneous rocks ($24 < Y/Ho < 34$, and $26 < Zr/Hf < 46$). 51
Figure 2-14. Schematic diagram showing stages of alteration for Group 1, 2 and 3 samples. (A) Represents stage 0 where no alteration has occurred, and primary volcanic mineralogy is preserved. (B) Represents stage 1 of alteration, where albitization, chloritization, and epidotization of primary volcanic material occur. Incident light photograph is of representative Group 1 sample (AB-11-11), showing preservation of volcanic material and incipient stages of silicification marked by the presence of quartz patches (white areas) (C) Represents stage 2 of alteration, which is characterized by silicification of both volcanic matrix, and phenocrystic material. Incident light photograph is of representative Group 2 sample (AB-11-12), showing silicification lenses (white areas), and preservation of volcanic material in between (green areas). (D) Represents stage 3 of alteration, which is characterized by further silicification and Fe-alteration, resulting in the formation of Fe-oxides, and pyrite

during VMS-style mineralization. Incident light photograph is of representative Group 3 sample (AB-11-23), showing silicified and Fe-altered areas. 52
Appendix A-3 63
Figure 3-1. (A) Compiled $\delta^{30}Si$ data (in ‰, n = 288; Van den Boorn et al., 2007, Abraham et al., 2011, André et al., 2006, Van den Boorn et al., 2010, Heck et al., 2011, Steinhoefel et al., 2010, Chakrabarti et al., 2012, Delvigne et al., 2012, Marin-Carbonne et al., 2012, Fan et al., 2013) from inorganic (non-biological) chert, and banded iron formation (BIF). Data were compiled from bulk (MC-ICP-MS, IRMS) and high-spatial resolution (SIMS, femtosecond laser ablation) techniques. To be comparable, spot data for individual samples were converted to a single value via the method outlined in Marin-Carbonne et al., (2012). Note the slight increasing trend through time. A single anomalously heavy data point ($\delta^{30}Si$ = +5.2 at 1.7 Ga) was omitted. (B) Plot showing SIMS $\delta^{30}Si$ (‰) data of quartz amygdules and quartz cement from a brecciated pillow basalt, bedded chert and a chert clast. Note the overlap between cement and chert/chert clast, potentially suggestive of similar precipitation mechanisms. (C) Plot showing SIMS $\delta^{30}Si$ (‰) vs. $\delta^{18}O$ (‰) data of quartz cement and quartz amygdules within a single sample of basaltic breccia from the >3.7 Ga Isua Greenstone Belt. Oxygen isotope values range from $\delta^{18}O_{VSMOW}$ = 16.81 to 18.09 ± 0.5 ‰. However, $\delta^{30}Si$ from the same crystals show a large range of values from $\delta^{30}Si_{NBS-28}$ = -5.09 to 0.83 ± 0.3 ‰. The heterogeneity indicates that the silicon isotopes have not been completely reset, even though the oxygen isotopes have. Shaded area highlights the maximum and minimum of data from this study, and a dashed line through $\delta^{30}Si$ = 0 ‰ is shown for reference. Both scales extend through geologically relevant ranges of $\delta^{30}Si$ and $\delta^{18}O$. 63
Figure 3-2. (A) Field photograph of quartz amygdaloidal, quartz-cemented pillow breccia from the >3.7 Ga Isua Greenstone Belt. Scale bar in cm. Dashed box shows the contact between cement and pillow fragment and outlines sample area used in this study. (B) Field photograph of bedded chert interlayered with amphibolite, adjacent to pillow breccia. Scale = 1.5 m. (C) Field photograph of the conglomerate unit showing chert clasts. Scale bar in cm. (D) Cross-polarized light image of quartz amygdules (a) and encasing quartz cement (c). Scale bar is 400 μm. (E) Cross-polarized light image of quartz crystals from bedded chert unit. Scale bar is 400 μm. (F) Cross-polarized light image of quartz crystals of chert clast. Scale bar is 500 μm. 64
Figure 3-3. Geologic map of the Northeastern section of the Isua Greenstone Belt, with an inset showing the location of the greenstone belt in SW Greenland. Modified from Fedo, 2001. Sample localities marked by numbers. 3 = chert clasts from conglomeritic unit (sample ISB 5b), 6 = bedded chert (samples ISB 26, ISB 28) 7 = brecciated pillow basalt (sample ISB 31b). Samples for locations 1, 2, 4, and 5 are from the study discussed in Chapter IV. 65
Figure 3-4 Cartoon showing different quartz lithologies used in this study. (A) Schematic of a typical hydrothermal system. Conditions of formation include vesicular standard pressures of 30-35 MPa, and hydrothermal fluid temperatures ($T_{HYD.\ FLUID}$) ranging from 5 – 407 °C, high dissolved silica (D_{Si}) concentrations, and silicon isotope signatures of basalt ($\delta^{30}Si_{Basalt}$ = -0.3 ‰; Fitoussi et al., 2012), and hydrothermal fluid ($\delta^{30}Si_{HYD.\ FLUID}$ = -0.3 ‰; De la Rocha et al., 2000). (B) Diagram of different types of

quartz samples from this study including: pillow basalt breccia, with quartz-filled amygdules (a), encased in quartz cement (c), adjacent bedded chert, and chert clasts from a conglomerate. Under conditions of disequilibrium, rapid precipitation from high temperature fluids likely led to preferential incorporation of ^{28}Si into the precipitating quartz filling vesicles during initial eruption of pillow basalt. As conditions approached equilibrium, quartz precipitated as encasing cement at slower rates, and lower temperatures, resulting in cement $\delta^{30}Si$ values similar to source fluid/rock composition. Geochemical and isotopic conditions for formation of quartz in the bedded chert unit, and chert clasts, were likely similar to those that formed the cement. 66
Appendix A-4 81
Figure 4-1. Silicon isotope record of chert and banded iron formation (BIF) through time, compared to the range of silicon isotope values of different chert and BIF types from this study from the 3 Ga Buhwa Greenstone Belt, Zimbabwe. (a) Plot showing all compiled $\delta^{30}Si$ data (2-12; in ‰, n = 288) versus time. Data were compiled from bulk (MC-ICP-MS, IRMS) and high-spatial resolution (SIMS, femtosecond laser ablation) techniques. Note what appears to be a slight increasing trend through time. A single anomalous data point ($\delta^{30}Si$ = +5.2 at 1.7 Ga) was omitted. (b) Plot showing our SIMS data from the ~3 Ga Buhwa Greenstone Belt, Zimbabwe. BR = bedrock, SS = quartz arenite sandstone, Chert = greenstone-associated chert, Sup IF = Superior-type banded iron formation, Alg IF = Algoma-type banded iron formation. X indicates the number of samples analyzed; n indicates the total number of spot analyses on x samples. (c) Probability density distribution plot (after Marin-Carbonne et al., 2012) for each sample in (b). 81
Figure 4-2. (a-f) Incident light images of representative rock types used in this study. Scale bar is 2.5 mm. (g-i) Reflected light images showing analytical spots from representative samples used in this study, scale bar 60 μm. (a) Tokwe segment gneissic bedrock (sample ZB_182) from the ~3Ga Buhwa Greenstone Belt (BGB), Zimbabwe, showing coarse-grained, bands of quartz, feldspar, and biotite, with typical gneissic texture. (b) Well-rounded, detrital quartz arenite sandstone (sample ZB_240) from the ~3 Ga BGB. (c) Greenstone-associated chert (sample ZB_105) from the ~3 Ga BGB showing alternating bands of quartz and organic carbon. (d) Superior-type BIF (sample ZB_23) from the ~ 3 Ga BGB, showing fine-grained bands of quartz (qtz) and hematite (hm). (e) Algoma-type BIF (sample IS_02_06) from the > 3.7 Ga Isua Greenstone Belt, SW Greenland, showing coarse-grained bands of quartz (qtz) and magnetite (mgt), with minor amounts of amphibole. (f) Silicified felsic volcanic rock (sample AB-11-12) from the ~ 2.72 Ga Hunter Mine Group, AGB. Note replacement patches of quartz (qtz), and preserved volcanic textures. (g) Superior-type BIF sample from the Buhwa Greenstone Belt showing SIMS analysis points on a single crystal. (h) Algoma-type BIF sample from the Isua Greenstone Belt showing SIMS analysis points on single crystals. (i) Algoma-type BIF sample from the Abitibi Greenstone Belt showing SIMS analysis points. 82
Figure 4-3. Geologic map of Buhwa Greenstone Belt, Zimbabwe, with an inset showing the location of the greenstone belt in Zimbabwe. Samples from this study are labeled with their respective sample numbers. Modified from Fedo et al. (1995). 83

Figure 4-4. Geologic map of the Northeastern section of the Isua Greenstone Belt, with an inset showing the location of the greenstone belt in SW Greenland. Modified from Fedo (2001). Sample localities marked by numbers. 1 = banded iron formation (sample IS-02-05), 2 = banded iron formation (sample IS-02-06), 3 = chert clasts from conglomeritic unit (sample ISB 5b), 4 = banded iron formation (sample IS-02-08), 5 = banded iron formation (sample ISB 55) 6 = bedded chert (samples ISB 26, ISB 28) 7 = brecciated pillow basalt (sample ISB 31b). 84
Figure 4-5. Geologic map of Hunter Mine Group region, of the Abitibi Greenstone Belt, with an inset showing the location of the greenstone belt in Canada. Samples in this study come from outcrops labeled 2.1, 2.3, and 2.4. Modified from Dostal and Mueller (2012). 85
Figure 4-6. All measured silicon isotope values separated into different rocks types. All points represent measured bulk values, or spot data that has been converted to bulk values utilizing a probability density distribution value as outlined in Marin-Carbonne et al. (2012). Open symbols for each plot represent data from previous studies; closed symbols represent data from this study. Where indicated, x = the number of samples analyzed, and n = the number of analyses on x samples. Dashed line represents $\delta^{30}Si$ = 0 ‰ for reference. (a) Plot containing all compiled $\delta^{30}Si$ data for silicified volcanic rocks. (b) Plot containing all compiled $\delta^{30}Si$ data for non-silicified volcanic chert against time. Greenst. = Greenstone-associated chert, CO_3-assoc. = chert hosted within carbonate rocks, and Bio = indicates chert formed after geologic evidence for silica-secreting organisms. (c) Plot showing spot $\delta^{30}Si$ data for greenstone chert. (d) Plot showing bulk $\delta^{30}Si$ data for diagenetic chert hosted within carbonate rocks. (e) Plot showing spot $\delta^{30}Si$ data for Algoma-type banded iron formation. (f) Plot showing bulk $\delta^{30}Si$ data for Algoma-type banded iron formation. 87
Figure 4-7. All measured silicon isotope values of Superior-type banded iron formation. All points represent measured bulk values, or spot data that has been converted to bulk values utilizing a probability density distribution value as outlined in Marine-Carbonne et al. (2012). Open symbols for each plot represent data from previous studies, while closed symbols represent data from this study. Where indicated x = the number of samples analyzed, and n = the number of analyses on x samples. Dashed line represents $\delta^{30}Si$ = 0 ‰. (a) Plot showing bulk $\delta^{30}Si$ data for Superior-type banded iron formation. (b) Plot showing spot $\delta^{30}Si$ data for Superior-type iron formation. Note the increasing trend from ~3 – 1.8 Ga. 88
Figure 4-8. Box model for estimating changing flux estimates during the time interval of sample deposition in this study (3.7 - 1.8 Ga). Flux estimates were made by adjusting modern values for continental and hydrothermal inputs (Treguer and de la Rocha, 2013) for changing Precambrian conditions (Isley, 1995) such as increased hydrothermal input, and the growth history of continental material. See text for details. 89
Figure 4-9. Schematic diagram showing growth and emergence of continental crust, and distribution of different rock types represented in the compiled $\delta^{30}Si$ archive through time. (a) Diagram representing the Paleo- through Meso-Archean, where oceans were dominated by hydrothermal sources ($\delta^{30}Si_{hyd.\ fl.} \approx 0$ ‰) three times greater than modern values and little riverine input (< 10%; Fig. 4-8; Isley, 1995) from small continents

($\delta^{30}Si_{BSE} \approx 0$ ‰ (Savage et al., 2012). Hyd. fl. = hydrothermal fluids, BSE = bulk silicate Earth. (b) Diagram representing the increased riverine delivery (30 – 70 % of modern; Fig. 4-8) of continentally sourced silicon ($\delta^{30}Si_{rivers} > 0$ ‰) to the oceans from chemical weathering of newly emergent continental crust. (c) Diagram representing the Phanerozoic silicon cycle dominantly by continental: hydrothermal sources of 10:1, with silicon isotope composition of the ocean overprinted by biology ($\delta^{30}Si_{biology} > 0$ ‰). Presence of silica-secreting organisms represented by siliceous sponge spicules. (d) Plot showing the distribution of rock types represented in the compiled silicon isotope record with respect to time. Note the temporal restrictions of certain rock types. 90
Appendix A-5 94
Figure 5-1. Geilert et al. (2014) experimental data (black circles), for $\Delta^{30}Si_{solid\text{-}fluid}$ at temperatures ranging from 10 to 60 °C. At temperature ranges expected for hydrothermal systems (200 – 400 °C), the predicted $\Delta^{30}Si_{solid\text{-}fluid}$ value would be > +6 ‰. Such positive $\Delta^{30}Si_{solid\text{-}fluid}$ values have never been measured for silicon isotopes. Furthermore, no known geochemical process predicts such positive values. At the y-intercept (0°C), the $\Delta^{30}Si_{solid\text{-}fluid}$ value is -2.3, which suggests that the lowest silicon isotope value for a quartz precipitate from a hydrothermal solution ($\delta^{30}Si_{HYD.\ FLUID}$ = -0.3‰) would be -2.6 (solving for the equation $\Delta^{30}Si_{solid\text{-}fluid} = \delta^{30}Si_{QTZ\ PPT} - \delta^{30}Si_{HYD.\ FLUID}$). As shown in in chapter III, many previous studies, and data presented in our study, have measured $\delta^{30}Si$ values lower than $\delta^{30}Si = -2.6$ ‰ in quartz from chert and banded iron formation. We therefore conclude that a linear fit to the Geilert et al. (2014) data does not help to explain the values we measure in this study, or values measured in previous studies. 95
Figure 5-2. Plot showing logarithmic fit to the Geilert et al. (2014) data. As in Figure 5-1, experimental data is plotted as black circles. This data was fit with a logarithmic function to extrapolate the experimental data to higher temperatures (the values of which are plotted as grey circles) relevant to hydrothermal systems. On this plot, as temperatures approach 0 °C, the fit predicts a large range of $\delta^{30}Si$ values should occur along the asymptote. At higher temperatures, positive $\Delta^{30}Si_{solid\text{-}fluid}$ values are predicted. 96
Figure 5-3. To understand how our data, which show extreme $\delta^{30}Si$ heterogeneity, fit in with the extrapolated experimental data in Figure 5-2, we used the logarithmic function to predict the temperature of precipitation for the quartz crystals in the amygdules, and cement from the pillow breccia sample, using the known $\delta^{30}Si$ value for hydrothermal fluid (-0.3 ‰) to plot $\Delta^{30}Si_{solid\text{-}fluid}$ verses temperature in Figure 5-3. Figure 5-3 shows that $\delta^{30}Si$ values measured for amygdules (gray squares), would correspond to temperatures mostly between 0-10°C, with some values extending to higher temperatures. This contradicts geologic information about the sample, which suggests quartz amygdules were formed under hydrothermal conditions (Appel et al., 2001). Additionally, $\delta^{30}Si$ values measured for cement (white squares) would correspond to temperatures roughly between 70-130°C, despite precipitating in between brecciated pillow basalt fragments, which indicate the basalt had cooled enough to exhibit brittle fracture. We argue that these temperatures are likely

geologically implausible for the encasing quartz cement of the pillow breccia unit which likely precipitated from cooler fluids than the amygdules. Adjacent bedded chert has similar $\delta^{30}Si$ values as the quartz cement, and likely precipitated from ambient, cold, seawater, or mixed seawater and hydrothermal fluids. Based on this figure however, one would interpret our chert, and pillow breccia cement to have formed at temperatures reaching >120°C, which again is not geologically reasonable. 97
Figure 5-4. Probability density distribution plot calculated sample TEM-cf. Peak height was calculated following the methods outlined in Marin-Carbonne et al., 2012. Calculated peak value for 31 analyses on the TEM-cf sample was $\delta^{30}Si = -0.4 \pm 0.7$ ‰, which overlaps with the measured whole-rock value of the same sample ($\delta^{30}Si = -0.66 \pm 0.03$ ‰)……..99
Figure 5-5. Plot of silicon isotope data separated by rock type for all samples from the ~3 Ga Buhwa Greenstone Belt, Zimbabwe. X = number of samples analyzed, n = number of points analyzed. 100
Figure 5-6. Plot of silicon isotope data separated by sample for all samples from the shelf association of the ~3 Ga Buhwa Greenstone Belt, Zimbabwe. 101
Figure 5-7. Cartoon representation of major sources and sinks in system for the shelf association of the ~3 Ga Buhwa Greenstone Belt, Zimbabwe. 102
Figure 5-8. Plot of silicon isotope data separated by sample for all samples from the basinal association of the ~3 Ga Buhwa Greenstone Belt, Zimbabwe. 103
Figure 5-9. Cartoon representation of major sources and sinks in system for the basinal association of the ~3 Ga Buhwa Greenstone Belt, Zimbabwe. 104
Figure 5-10. Plot showing raw measured $\delta^{30}Si$ verses crystal size (microns). Note no trend with increasing crystal size. Data are uncorrected for standard comparison for use in this plot, data are tabulated in Appendix A-5, Table 4-7. 105
Figure 5-11. Plot showing $\delta^{30}Si$ isotope values of international standard (NBS-28; red filled circles) and internal house standard (UTQ; black filled squares) vs. Run #. Different pieces of the internal house standard UTQ include UTQ_C, UTQ_D, and UTQ_Isua_3, are labeled at the top of the plot. The "peak" value of each UTQ standard piece used was determined via the methods outlined in Marin-Carbonne et. al (2012). 106
Figure 5-12. Plot showing $\delta^{30}Si$ isotope values of international standard (NBS-28; red filled circles) vs. run #. 107
Figure 5-13. Plot showing $\delta^{30}Si$ isotope values of internal standard (UTQ-D red filled circles) vs. run #. 108
Figure 5-14. Plot showing $\delta^{30}Si$ isotope values of internal standard (UTQ-A red filled circles) vs. run #. 109
Figure 5-15. Plot showing $\delta^{30}Si$ isotope values of internal standard (UTQ-C red filled circles) vs. run #. 110
Figure 5-16. Full gold coat, post-analysis map of samples ZB-169a, b, ZB-07, ZB-27, ZB-05 (in clock-wise order starting at North). Sample ZB 05 is ~ 1 cm in length for scale. 111

Figure 5-17. Full gold coat, post-analysis map of samples ISB 26, ISB 28, UTQ, ISB-31b (in clock-wise order starting from Northwest). UTQ standard chip is ~5 mm in length for scale. 112
Figure 5-18. Full gold coat, post-analysis map of sample AB-11-11. Length of sample is roughly ~ 1 cm for scale. 113
Figure 5-19. Full gold coat, post-analysis map of samples AB-11-12, TEM-cf, and AB-11-26 (in clock-wise order starting from Northwest). Length of TEM-cf sample is roughly ~7 mm for scale. 114
Figure 5-20. Full gold coat, post-analysis map of samples UTQ, sm-9796, IS-02-05, IS-02-06, IS-02-08 (in clock-wise order starting at Northwest with the clear standard). Length of UTQ standard is roughly ~5 mm for scale. 115
Figure 5-21. Full gold coat, post-analysis map of samples ZB 23, ZB 117, UTQ, ZB 105 (in clock-wise order starting at Northwest). Length of UTQ standard is roughly ~ 6 mm for scale. 116
Figure 5-22. Reflected light image of sample ZB-05 (left). Cross-polarized light image of sample ZB-05 (right). Length of ZB 05 sample is roughly ~1cm for scale. 117
Figure 5-23. Reflected light image of sample ZB-169. Length of ZB 169 sample is roughly ~0.5 cm for scale. 118
Figure 5-24. Plane polarized light image of sample ZB-169. Length of ZB 169 sample is roughly ~0.5 cm for scale. 119
Figure 5-25. Cross-polarized light image of sample ZB-169. Length of ZB 169 sample is roughly ~0.5 cm for scale. 120
Figure 5-26. Reflected light image of sample ZB-07. Length of ZB 07 sample is roughly ~0.6 cm for scale. 121
Figure 5-27. Plane-polarized light image of sample ZB-07. Length of ZB 07 sample is roughly ~0.6 cm for scale. 122
Figure 5-28. Cross-polarized light image of sample ZB-07. Length of ZB 07 sample is roughly ~0.6 cm for scale. 123
Figure 5-29. Plane-polarized light image of sample ZB-23. Length of ZB 23 sample is roughly ~0.6 cm for scale. 124
Figure 5-30. Cross-polarized light image of sample ZB-23. Length of ZB 23 sample is roughly ~0.6 cm for scale. 125
Figure 5-31. Plane-polarized light image of sample ZB-117. Length of ZB 117 sample is roughly ~0.5 cm for scale. 126
Figure 5-32. Cross-polarized light image of sample ZB-117. Length of ZB 117 sample is roughly ~0.5 cm for scale. 127
Figure 5-33. Plane-polarized light image of sample ZB-105. Length of ZB 105 sample is roughly ~0.6 cm for scale. 128
Figure 5-34. Cross-polarized light image of sample ZB-105. Length of ZB 105 sample is roughly ~0.6 cm for scale. 129
Figure 5-35. Plane -polarized light image of sample ZB-105. Length of ZB 105 sample is roughly ~0.8 cm for scale. 130
Figure 5-36. Cross-polarized light image of sample ZB-105. Length of ZB 105 sample is roughly ~0.8 cm for scale. 131

Figure 5-37. Plane-polarized light image of sample ZB-20. Length of ZB 20 sample is roughly ~0.5 cm for scale. 132
Figure 5-38. Cross-polarized light image of sample ZB-20. Length of ZB 20 sample is roughly ~0.5 cm for scale. 133
Figure 5-39. Plane-polarized light image (left) and cross-polarized image (right) of sample ZB-18. Length of ZB 18 sample is roughly ~1 cm for scale. 134
Figure 5-40. Plane-polarized light image of sample ZB-17. Length of ZB 17 sample is roughly ~0.8 cm for scale. 135
Figure 5-41. Cross-polarized light image of sample ZB-17. Length of ZB 17 sample is roughly ~0.8 cm for scale. 136
Figure 5-42. Reflected–light image of sample ZB-143. Length of ZB 143 sample is roughly ~0.6 cm for scale. 137
Figure 5-43. Cross-polarized light image of sample ZB-143. Length of ZB 143 sample is roughly ~0.6 cm for scale. 138
Figure 5-44. Reflected-light image of sample ZB-32. Length of ZB 32 sample is roughly ~0.7 cm for scale. 139
Figure 5-45. Cross-polarized light image of sample ZB-32. Length of ZB 32 sample is roughly ~0.7 cm for scale. 140
Figure 5-46. Reflected-light image of sample ZB-03. Length of ZB 03 sample is roughly ~0.6 cm for scale. 141
Figure 5-47. Cross-polarized light image of sample ZB-03. Length of ZB 03 sample is roughly ~0.6 cm for scale. 142
Figure 5-48. Reflected-light light image of sample ZB-272. Length of ZB 272 sample is roughly ~0.5 cm for scale. 143
Figure 5-49. Cross-polarized light image of sample ZB-272. Length of ZB 272 sample is roughly ~0.5 cm for scale. 144
Figure 5-50. Reflected-light image of sample ZB-182. Length of ZB 182 sample is roughly ~0.5 cm for scale. 145
Figure 5-51. Reflected-light image of sample ZB-240. Length of ZB 240 sample is roughly ~0.6 cm for scale. 146
Figure 5-52. Reflected-light image of sample ISB-55. Length of ISB 55 sample is roughly ~0.6 cm for scale. 147
Figure 5-53. Reflected-light image of sample ISB-26. Length of ISB 26 sample is roughly ~0.6 cm for scale. 148
Figure 5-54. Reflected-light image of sample TEM-13-V2. Length of TEM-13-V2 sample is roughly ~0.5 cm for scale. 149
Figure 5-55. Reflected-light image of sample TEM-13-V2. Length of TEM-13-V2 sample is roughly ~0.5 cm for scale. 150
Figure 5-56. Reflected-light image of sample TEM-cf. Length of TEM-cf sample is roughly ~0.6 cm for scale. 151
Figure 5-57. Reflected-light image of sample TEM-cf. Length of TEM-cf sample is roughly ~0.6 cm for scale. 152

CHAPTER I

INTRODUCTION

PURPOSE STATEMENT

The purpose of this dissertation is to identify criteria that differentiate primary from secondary geochemical and isotopic signatures preserved in quartz from Precambrian chert. The work presented here focuses on major-, trace-, and rare-earth element geochemical and silicon isotope characteristics of chert, chert bands in iron formation, and silicified rocks. To accomplish this, I studied samples of these types of rocks from three localities: (1) >3.7 Ga Isua Greenstone Belt, Greenland, (2) ~3 Ga Buhwa Greenstone Belt, Zimbabwe, and (3) ~2.7 Ga Abitibi Greenstone Belt, Canada.

The dissertation is divided into five chapters. Chapter I (this chapter) provides an introduction to the dissertation contents, and serves as a brief introduction to siliceous chemical sedimentary rocks and silicified rocks, their elemental geochemistry, and silicon isotope geochemistry. Chapter II tracks changes in major-, trace-, and rare-earth element geochemistry from a suite of volcanic rocks from the ~2.7 Ga Abitibi Greenstone Belt, Canada, which represent different stages of silicification, from incipient stages, to the point of complete replacement such that they resemble iron formation. Chapter III tests whether primary silicon isotope compositions can be preserved in the geologic record of quartz precipitates such as chert and iron formation. Chapter IV uses the information gained in Chapter III to further investigate silicon isotope signatures of different rock types, and to understand the compiled silicon isotope archive of chert and iron formation through time. The final chapter, Chapter V, serves as a conclusion to the dissertation.

INTRODUCTION TO CHERT

The problem of defining chert

The word chert has multiple connotations. Chert is recognized as a specific rock formed via chemical precipitation of SiO_2 phases, as a general term for a fine-grained, quartz-rich rock formed via multiple pathways, and as a petrographic term. The purpose of this section is to briefly discuss how the word chert is used in literature, and clarify how it will be used in this dissertation. Chert is commonly defined as "a chemically-precipitated sedimentary rock, essentially mono-mineralic and composed chiefly of microcrystalline and/or chalcedonic quartz, with subordinate mega-quartz and minor amounts of impurities" (Folk, 1980). Similar definitions can be found in Boggs (2001), Tucker (1991), and Blatt and Tracy (1996). However, such a definition of chert does not encompass all rocks that are consistently termed "chert" in literature. Rocks that resemble chert mineralogically, compositionally, and texturally (and are referred to as chert in literature) form by replacement of primary mineral phases by quartz rather than chemical sedimentation (Lowe, 1994; Hofmann and Harris, 2008; van den Boorn, 2007; van den Boorn et al., 2010; Abraham et al., 2011). Such rocks do not fall under a strict definition of chert, but may be identified as such based on mineralogy/texture. Because the formal definition of chert encompasses a genetic definition of how the rock formed (via the sedimentary process of chemical precipitation) terminology problems exist when discussing chert and associated rocks that lack the information necessary to determine their genesis. To resolve terminology complications in this dissertation, in the following sections of the introduction we outline how chert is currently defined/classified, identify rocks that are outliers to this classification scheme, and subsequently provide a table (Table 1-1), chart (Figure 1-1), and glossary of terms to explain the usage of the word chert within this dissertation.

Chert terminology

As chemically precipitated sedimentary rocks, cherts originate due to precipitation of ordered or amorphous hydrated phases from a fluid either through chemical or biological processes (Folk, 1980; Boggs, 2001). As a group of rocks, cherts have been subdivided based on mineralogy, biogenic componentry, and macro-texture into flint, novaculite, porcellanite, siliceous sinter, diatomaceous, radiolarian, and spicular cherts, nodular chert, bedded chert, jasper and jaspilite (Boggs, 2001). The types of chert directly relevant to this dissertation are bedded chert, jasper, and jaspilite, all of which are defined in the glossary of terms (see below). In addition, chert is divided based on petrographic micro-textures (Folk, 1980), namely: (1) micro-quartz (crystals 1-5 μm), (2) chalcedonic quartz (fibrous crystals), and (3) mega-quartz (crystals >20 μm) (Folk, 1980). In the rock record, recrystallization and metamorphism affect most rocks, which commonly results in changes to crystal size, and renders a petrographic definition insufficient to handle coarsely recrystallized quartz common to rocks of the Precambrian, and certainly to rocks in this study.

Because recrystallization and metamorphism may obscure original textures and mineralogy, certain assumptions are often made for how primary minerals in chert form. Today, low-temperature deposits that consist predominantly of siliceous organisms are composed of amorphous opal-A, which is a meta-stable SiO_2 phase that easily recrystallizes to more stable SiO_2 phases such as micro- and mega-quartz (Calvert, 1977). Based on this observed pathway, it is assumed that inorganic, abiotic cherts found in the rock record likely formed through progressive recrystallization of low-temperature amorphous opal-A, to opal-CT, to micro-quartz (1-5 μm), to mega-quartz (>20 μm) (e.g., Marin-Carbonne et al., 2014), a process termed 'maturation theory' (e.g., Calvert, 1977). This assumption may not apply to all Precambrian cherts because direct precipitation of quartz from solution is possible (Calvert 1977; Knauth 1994, Mackenzie and Gees, 1971), and can occur in systems where quartz precipitates from high-temperature (hydrothermal) fluids (Hopkinson, 1999; Oehler, 1976). Because SiO_2 is precipitated under different temperature regimes as potentially different phases (e.g., opal versus quartz), it is important to understand the genesis of different chert deposits, though this is not always possible.

Chert outliers

To complicate matters, rocks that are not formed by chemical sedimentation can resemble chert, making the two different rock types hard to differentiate. Silicified rocks result from the replacement of primary mineral phases by quartz to produce a rock that resembles chert both macroscopically and petrographically, but does not fall under the definition of a chemically precipitated sedimentary rock. The process of silicification proceeds through fluid-rock interaction, regardless of the original rock composition (Lowe, 1994; Duchac and Hanor, 1990; Hofmann and Harris, 2008; van den Boorn, 2007). In platform and continental shelf depositional settings, silicification results in the formation of nodular cherts, which are formed via diagenetic replacement of carbonate minerals by silica phases with the potential to preserve original fossils and sedimentary structures (Boggs, 2001). Replacement can also occur along bedding planes to form rocks that superficially resemble bedded cherts. In hydrothermal depositional settings, silicification often proceeds through the replacement of primary volcanic rocks by silica phases (Duchac and Hanor, 1990; van den Boorn, 2007; van den Boorn et al., 2010; Abraham et al., 2011) to form a rock that may resemble chert macroscopically and petrographically. This type of replacement can affect all rock types, and can occur at any time during diagenesis and

metamorphism. As a result, such silicified rocks do not always record the primary geochemical and isotopic information of the original rock, but instead record information regarding the fluid associated with replacement. A tool for discriminating quartz/chert formed through silicification from quartz/chert formed through chemical sedimentation is therefore required in order to better interpret primary geochemical signatures from secondary ones.

Chert terminology used in this dissertation

As described above, rocks collectively considered chert form under conditions of low- and high-temperature, under varying geochemical conditions, by both chemical sedimentation from an open water column, and replacement. This presents a problem for interpreting genetic processes, as well as primary geochemical information. The chert nomenclature problem is central to discussion in this dissertation, where I have analyzed samples that fall under the textbook definition of chert, as well as samples colloquially referred to as chert, but that are actually silicified volcanic rocks. To effectively clean up chert nomenclature, in this dissertation I use the word chert in its broadest sense to mean a rock that predominantly consists of authigenic quartz, which is commonly, but not necessarily, microcrystalline. In doing so, two options arise for grouping samples to interpret geochemical and isotopic information. The first is to pool all siliceous rocks together that consist of non-detrital quartz regardless of depositional environment or mechanism of formation, and interpret the compiled record (geochemical or isotopic) of such rocks as a whole. However, such an approach does not allow for the discrimination between chemical sedimentary cherts, which have the potential to record primary geochemical information relating to seawater, from silicified rocks, which only provide geochemical information about the silicifying fluid. The second possible solution is to divide the chert record based on formative mechanism and depositional affinity. In this dissertation, I have chosen the second solution to presenting the data. I have divided the samples used in this dissertation based on whether or not they formed via chemical sedimentation or silicification, as well by their respective depositional affinity. The terminology used in the dissertation to describe these different groups of chert is listed in Table 1-1, and Figure 1-1.

General geochemical characteristics of chert and iron formation

Previous studies have utilized the REE patterns of chemical sedimentary chert to identify a primary mixed seawater and hydrothermal fluid signature indicative of chemical precipitation (Bau and Moller, 1993; Bau, 1996; Kamber and Webb, 2001; Bolhar et al., 2004; Lawrence and Kamber, 2006). REEs in the water column are primarily sourced from land. In estuaries, REEs fractionate under low-temperature conditions due to complexation with organic compounds and the oxidizing potential of the water column (Lawrence and Kamber, 2006). As a result, the ocean possesses a diagnostic REE signature, and chemical precipitates (such as chert) are thought to record this signature (Bau and Moller, 1993; Bau, 1996; Kamber and Webb, 2001; Bohlar et al., 2004; Lawrence and Kamber 2006). Shale-normalized seawater REE-patterns preserved in chemically precipitated rocks include a positive overall slope seen as HREE enrichment ($Pr_{SN}/Yb_{SN}<1$; Bohlar et al., 2004), a positive Eu anomaly (Danielson et al., 1992), that reflects hydrothermal input, and a positive Ce anomaly reflecting Ce^{3+} oxidation and subsequent Ce^{4+} precipitation (Fryer et al., 1977). A positive lanthanum anomaly, where La behaves like the heavy rare earth elements possibly due to enhanced stability in solution, is also considered a signature of chemical precipitation from seawater (Bolhar et al., 2004; Zhang and Nozaki, 1996; Fig. 1-2).

Although a REE signature may be diagnostic of primary precipitation from seawater and/or mixed hydrothermal fluids under ideal conditions of preservation, other studies (Paris et al., 1985; Lowe et al., 1999; Hofmann and Harris 2008) have shown that during high fluid-rock ratio alteration, trace elements mobilize, causing silicified komatiites and associated mafic volcanic rocks to inherit seawater-like REE signatures (Fig. 1-2). In hydrothermal systems then, the process of silicification may involve extensive seawater and hydrothermal water alteration, which could severely overprint the original igneous REE chemistry with increasing SiO_2 content. Such results question the use of a REE-based proxy to define chemical sedimentation versus replacement origin of cherts. To address this issue, I investigated the use of the silicon isotope composition of quartz to determine whether chemical sedimentary cherts and silicified rocks could be differentiated, and thus provide critical information necessary to interpret the geochemical and isotopic evolution of both seawater and alteration.

Introduction to silicon isotope geochemistry and the Precambrian silica cycle

To interpret the silicon isotope composition of abiotic, inorganic Precambrian chert it is necessary to identify the major silicon sources to the ocean and understand the abiotic processes that affect silicon isotope fractionation. Today, hydrothermal fluids at vent systems are buffered by the composition of mantle-derived sea-floor volcanic rocks that possess a $\delta^{30}Si$ value of about -0.3 ‰ (Fitoussi and Bourdon, 2012 and references therein). Hydrothermal fluids that derive silica from the alteration sea-floor volcanic rocks possess a similar $\delta^{30}Si$ value of roughly -0.3 ‰ (De la Rocha et al., 2000; Fig. 1-3). By contrast, on land, chemical weathering products, such as clays, are ^{30}Si-depleted (Ziegler et al., 2005) resulting from fractionation during clay formation and adsorption of mono-silicic acid onto Al- and/or Fe-oxides (Delstanche et al., 2009; Orpfergelt et al., 2009; Oelze et al., 2014). Fractionation during chemical weathering yields ^{30}Si-enriched riverine waters (Ding et al., 2004), which ultimately deliver ^{30}Si-enriched to the oceans (homogenized $\delta^{30}Si$ = +1.1 ‰; De la Rocha, 2000; Ding et al., 2004; Fig. 1-3). Although continentally derived silica overwhelmingly buffers the modern ocean reservoir (Treguer and De la Rocha, 2013), the balance between continental and hydrothermal silica sources to the ocean is not likely to have been constant over Earth history, given the growth history of the continents (Taylor and McClennan, 1985; Allegre et al., 1984; Collerson and Kamber, 1999; Hawkesworth and Kemp, 2006; Herzberg et al., 2010), which provides the possibility that chert could preserve trends in the silicon isotope record through time.

Silicon isotopes are also fractionated during precipitation from solution from adsorption to Al. In quartz precipitation experiments (Oelze et al., 2015), silicon isotopes of the precipitate (quartz) are enriched in the light isotope (^{28}Si) relative to the fluid (Fig. 1-4). The measurement of silicon isotopes of quartz within chert makes it possible to determine changes in the isotopic composition of the ocean throughout the Precambrian, under the condition that primary $\delta^{30}Si$ signatures can be preserved in the geologic record.

INTRODUCTION TO DISSERTATION

Dissertation Chapters

Chapter I: Introduction

Chapter I provides a guide to the organization and scope of this dissertation. Additionally, it serves to describe what rock types are investigated in this work, and provide an introduction to the Precambrian silica cycle. Finally, it provides a brief introduction to the geochemistry of silicon isotopes, and their application to studying the Precambrian silica cycle.

Chapter II: Geochemical evolution and textural preservation in a suite of altered volcanic rocks and jaspilite from the ~2.72 Ga Hunter Mine Group in the Abitibi Greenstone Belt

Chapter II investigates a group of progressively silicified volcanic rocks from the 2.72 Ga Hunter Mine Group, Abitibi Greenstone Belt, Canada to document geochemical changes to original volcanic rocks during silicification, and determine what these changes may mean for developing a unique geochemical fingerprint. The degree of silicification ranges from incipient, where only a minor amount of original material has been replaced by quartz, to intense, where all original material has been completely replaced by quartz to form a rock that superficially resembles banded iron formation and chert. The least altered volcanic rocks preserve primary igneous rock textures at both the outcrop and thin section scale, and are characterized geochemical signatures expected for felsic igneous rocks in the region. The most altered rocks mineralogically and geochemically resemble siliceous chemical sediments. However, remnant volcanic textures can be found across the suite of samples documenting the progressive compositional replacement from rhyolite, to rhyolite with patchworks of microcrystalline quartz ± iron minerals.

Textural evidence supports an origin via progressive silicification for the rocks in this study, but geochemical evidence is harder to interpret. I suggest that during the process of silicification, geochemical exchange occurs, causing incipient altered volcanic rocks to have different geochemical signatures than intensely silicified volcanic rocks. Rocks that have only been affected by incipient alteration maintain original volcanic geochemical signatures, whereas intensely silicified rocks have geochemical signatures that resemble seawater mixed with hydrothermal fluids. An important finding of this study is the decoupling of textural information from geochemical information, leading to a conclusion that textural replacement and geochemical alteration are not simplistically linked. As a result, the REE geochemical signatures of chert are not uniquely linked to a single geologic process, and therefore cannot be used as a geochemical "fingerprint" to distinguish rocks formed through silicification, from those formed from chemical sedimentation.

Chapter III: Micro-scale silicon isotope heterogeneity observed in >3.7 Ga hydrothermal quartz precipitates: implications for interpreting the δ^{30}Si record of chert

Chapter III seeks to identify primary silicon isotope heterogeneity in the geologic record, by measuring the silicon isotope composition of several different types of quartz formed in an inferred hydrothermal environment where a large range of silicon isotope values is expected. I present silicon isotope compositions of quartz crystals measured by secondary ion mass spectrometry (SIMS) from three rock types from the >3.7 Ga Isua Greenstone Belt, SW Greenland: (1) quartz-cemented, amygdaloidal, basaltic, pillow breccia, (2) chert, and (3) chert clasts, thought to represent quartz precipitation under hydrothermal conditions. Chert, chert clasts, and quartz cement have overlapping δ^{30}Si values, and δ^{30}Si values of quartz amygdules span nearly the entire known range of values previously measured for quartz precipitates. Based on comparison with experimental work on silicon isotope fractionation and theoretical work for isotopic fractionation during the precipitation of minerals from solution, I interpret the extreme heterogeneity of amygdules to derive from a kinetic isotope effect during quartz precipitation under disequilibrium conditions in a hydrothermal setting. I conclude that silicon isotope heterogeneity can be preserved in the rock record, and as a result, can be used to understand

processes of quartz formation. Additionally, I infer that heterogeneity in the compiled $\delta^{30}Si$ record of chert can be explained if samples are separated based on geologic context.

Chapter IV: Silicon isotope evidence for continental emergence at ~3 Ga

Since the original use of Si-isotopes in chert as a paleo-ocean thermometer (Robert and Chaussidon, 2006) a number of studies have attempted to explain what appears to be a secular enrichment in the silicon isotope record of marine sedimentary rocks as either a mixing of hydrothermal and continental silicon sources to the ocean, or, more prominently, as a gradual cooling of ocean temperatures since the Archean. Either interpretation gives rise to two significant concerns. First, pooling all data together regardless of rock type (i.e., chert, Algoma-type [hydrothermal] BIF, Superior-type [continental] BIF) is unwarranted because cherts are known to precipitate in highly varied depositional settings (hydrothermal vs. open-ocean; Kimberley, 1979; Klein, 2005; Bekker et al., 2010) from different formational processes (replacement vs. precipitation from a water column), under both equilibrium, and disequilibrium conditions. Second, simple source mixing requires an assumption that the delivery of continental and hydrothermal silicon to the ocean remained has remained constant throughout geologic time despite ample evidence to the contrary.

In this chapter, I present newly acquired, high-spatial resolution silicon isotope data from quartz within chert and iron formation that range in age from ~3.7 to 2.7 billion years ago, which I compare and contrast to previously published data. The data set presented here was collected *in situ* from rock chips and thin sections using SIMS, and nearly doubles the number of silicon isotope data published for Archean banded iron formation collected by SIMS, in addition to filling in a critical gap in the geologic record of chert and iron formation from different depositional environments at 3 Ga.

This study takes a different approach compared to previous silicon isotope studies of chert. Instead of interpreting a compiled record of chert, I first separated chert formed from primary chemical sedimentation from chert formed by replacement, and then further separated chemical sedimentary chert based on depositional affinity. In doing so, I identified that silicified volcanic rocks uniformly possess $\delta^{30}Si$ values near 0 ‰. Chemical sedimentary chert/iron formation deposited in hydrothermal depositional settings possess $\delta^{30}Si$ isotope values that span similar ranges to modern Fe-Si deposits at modern hydrothermal vents, and do not show any trend with respect to time. I interpret the consistent range of values of these rocks through time to indicate similar depositional mechanisms wherein precipitation occurs along a temperature gradient between hydrothermal fluids and cooler seawater, which results in saturation differences that drive precipitation.

By contrast, the silicon isotope signatures ($\delta^{30}Si$) of iron formation formed in continentally influenced depositional settings from 3 Ga to 1.88 Ga, record a gradual, unidirectional shift from ^{30}Si-depleted ($\delta^{30}Si \leq 0$ ‰) to ^{30}Si-enriched ($\delta^{30}Si \geq 0$ ‰). I interpret this shift to reflect a change in silicon sources to the ocean reservoir from dominantly hydrothermal to continental, due to the initiation of chemical weathering of emergent continental material beginning at ~3 Ga. Over the period of deposition of iron formation formed in continentally-influenced depositional environments (termed Superior-type iron formation), the production of ^{30}Si-enriched silicic acid during chemical weathering of newly exposed silicic continental crust, and it's subsequent delivery to the oceans, changed the isotopic composition of the marine reservoir from a dominantly hydrothermal signature ($\delta^{30}Si \sim 0$ ‰), to a continental one ($\delta^{30}Si > 1$ ‰). Based on these findings, I suggest increased and widespread delivery of bio-

essential nutrients to surface oceans over the time interval from ~ 3 Ga – 2.5 Ga, due to chemical weathering of newly emergent continents. I conclude that contrary to the conclusion of previous studies (Robert and Chaussidon, 2006; Heck et al., 2011) no single secular silicon-isotope trend actually exists in the compiled chert record. Instead, the silicon isotope archive can best be deciphered by grouping rocks that have similar formational mechanisms, leading to a three-step evolution of the Precambrian silica cycle from a hydrothermal-dominated ocean to a continentally-dominated one, followed by one obscured by silica-utilizing biology.

Glossary of terms

Amygdule – a gas cavity or vesivle in an igneous rock which is filled with such secondary minerals as zeolites, cacltie, quartz, or chalcedony (Bates and Jackson, 1984).

Bedded chert – layers of nearly pure chert ranging up to several cm in thickness and commonly interbedded with mm-thick partings, or laminae, of siliceous shale … and can be divided into those that contain siliceous or organic biogenic remains, and those that do not (Boggs, 2001).

Chalcedonic quartz – forming sheaf-like bundles of radiating, extremely thin crystals about 0.1 mm long (Folk, 1980).

Chemical precipitate – primary or secondary mineral precipitation from solution in either an open system or closed system, with different water: rock ratios

Jasper – variety of chert colored red by impurities of disseminated hematite (Boggs, 2001).

Jaspilite – jasper interbedded with hematite in Precambrian iron formations (Boggs, 2001).

Greenstone – altered basaltic material

Microquartz – nearly equidimenstional grains of quartz 1-5 μm in size (Folk, 1980).

Megaquartz –equant to elongated grains [of quartz] greater than 20 μm (Folk, 1980).

Opal-A – a mineral or mineral gel, SiO_2-nH_2O. It has been shown by electron diffraction to consist of packed spheres of silica, water content is usually 3-9 % (Bates and Jackson, 1984).

Silicification –the introduction of, or replacement by, silica, esp. in the form of fine-grained quartz, chalcedony, or opal, which may fill pores and replace existing minerals (Bates and Jackson, 1984).

LIST OF REFERENCES

Abraham, K., Hofmann, A., Foley, S.F., Cardinal, D., Harris, C., Barth, M.G., André, L., 2011. Coupled silicon–oxygen isotope fractionation traces Archaean silicification. Earth and Planetary Science Letters, 301: 222-230.

Allegre, C. J., and Rousseau, D., 1984. The growth of continents through geological time studied by Nd isotope analysis of shales. Earth Planetary Science Letters. 67: 19–34.

Bates, R.L., Jackson, J.A., 1984. Dictionary of Geological Terms, 3rd edition, Anchor Press, NY.

Bau, M. and Möller, P., 1993. Rare earth element systematics of the chemically precipitated component in Early Precambrian iron formations and the evolution of the terrestrial atmosphere-hydrosphere-lithosphere system. Geochimica et Cosmochimica Acta, 57: 2239-2249.

Bau, M., 1996. Controls on the fractionation of isovalent trace elements in magmatic and aqueous systems: evidence from Y/Ho, Zr/Hf, and lanthanide tetrad effect. Contributions to Mineralogy and Petrology, 123: 323-333.

Bekker, A., Slack, J.F., Planavsky, N., Krapež, B., Hofmann, A., Konhauser, K.O., Rouxel, O.J., 2010. Iron Formation: The Sedimentary Product of a Complex Interplay among Mantle, Tectonic, Oceanic, and Biospheric Processes. Economic Geology, 105: 467-508.

Blatt, H., Tracy, R.J., 1996. Petrology: igneous, sedimentary, and metamorphic, W.H. Freeman and Company, NY.

Boggs, S, 2001. Principles of Sedimentology and Stratigraphy, 3rd edition, Prentice Hall, 726 p.

Bolhar, R., Kamber, B., Moorbath, S., Fedo, C., and Whitehouse, M., 2004. Characterization of early Archean chemical sediments by trace element signatures: Earth and Planetary Science Letters, 222: 43-60.

Calvert, S.E., 1977. Mineralogy of silica phases in deep-sea cherts and porcelanites. Phil. Trans. R. Soc. Lond A. 286: 239-252.

Collerson, K. D. and Kamber, B. S., 1999. Evolution of the continents and the atmosphere. Science, 283: 1519-1522.

Danielson, A., Moller, P., Dulski, P., 1992. The europium anomalies in banded iron formations and the thermal history of the oceanic crust. Chemical Geology, 97: 89-100.

Delstanche, S., Opfergelt, S., Cardinal D., Elsass, F., Andre´ L., Delvaux, B., 2009. Silicon isotopic fractionation during adsorption of aqueous monosilicic acid onto iron oxide. Geochimica et Cosmochimica Acta 73: 923–934.

De La Rocha C. L., Brzezinski M. A. and De Niro M. J., 1997. Fractionation of silicon isotopes

by marine diatoms during biogenic silica formation. Geochimica et Cosmochimica Acta 61: 5051–5056.

De la Rocha, C.L., Brzezinski, M.A., DeNiro, M.J., 2000. A first look at the distribution of the stable isotopes of silicon in natural waters, Geochimica et Cosmochimica Acta, 64: 2467-2477.

Ding T., Wan D., Wang C., and Zhang F., 2004. Silicon isotope compositions of dissolved silicon and suspended matter in the Yangtze River, China. Geochimica et Cosmochimica Acta 68: 205–216.

Duchac, K.C., and Hanor, J.S., 1990. Origin and timing of the metasomatic silicification of an Early Archean komatiite sequence, Barberton Mountain Land, South Africa. Precambrian Research, 37: 125-146.

Fitoussi, C., Bourdon, B., 2012. Silicon isotope evidence against an enstatite chondrite Earth. Science, 335: 1477-1480.

Folk R. L., 1980. Petrology of Sedimentary Rocks p. 79.

Fryer, B.J., 1977. Rare earth evidence in iron formations for changing Precambrian oxidation states. Geochimica et Cosmochimica Acta, 41: 361-367.

Hawkesworth, C. J., Kemp, A. I. S., 2006. Evolution of the continental crust. Nature, 443: 811 – 817.

Herzberg, C., Condie, K., Korenaga, J., 2010. Thermal history of the Earth and its petrological expression. Earth and Planetary Science Letters, 292: 79-88.

Hofmann, A., Harris, C., 2008. Silica alteration zones in the Barberton greenstone belt: A window into subseafloor processes 3.5–3.3 Ga ago. Chemical Geology, 257: 221-239.

Hopkinson, L., Roberts, S., Herrington, R., Wilkinson, J., 1999, Self-organization of submarine hydrothermal siliceous deposits: Evidence from the TAG hydrothermal mound, 26°N Mid-Atlantic Ridge, Geology, 26: 347-350.

Kamber, B.S., Webb, G.E., 2001. The geochemistry of late Archaean microbial carbonate: implications for ocean chemistry and continental erosion history. Geochimica et Cosmochimica Acta, 65: 2509-2525.

Kimberley, M.M., 1979. Geochemical distinctions among environmental types of iron formations. Chemical Geology, 25: 185-212.

Klein, C., 2005. Some Precambrian banded iron-formations (BIFs) from around the world: Their age, geologic setting, mineralogy, metamorphism, geochemistry, and origins. American Mineralogist, 90: 1473-1499.

Knauth, L.P., 1994, Petrogenesis of chert: In Reviews in Mineralogy, 29: 233-256.

Lawrence, M.G., Kamber, B.S., 2006. The behaviour of the rare earth elements during estuarine mixing – revisited. Marine Chemistry, 100: 147-161.

Lowe, D.R., 1994. Chapter 4, Archean Greenstone-Related Sedimentary Rocks, in: Condie, K.C. (Ed.), Developments in Precambrian Geology, Elsevier: 121-169.

Lowe, D.R., 1999. Petrology and sedimentology of cherts and related silicified sedimentary rocks in the Swaziland Supergroup. Geological Society of America Bulletin, 329: 83–114.

Mackenzie, F.T., Gees, R., 1971. Quartz: synthesis at Earth-surface conditions, Science, 173: 533–534.

Marin-Carbonne, J., Robert, F., Chaussidon, M., 2014. The silicon and oxygen isotope compositions of Precambrian cherts: a record of oceanic paleo-temperatures? Precambrian Research, 247: 223-234.

Oehler, J.H., 1976, Hydrothermal crystallization of silica gel, Geological Society of America Bulletin, 87: 1143-1152.

Oelze, M., von Blanckenburg, F., Hoellen, D., Dietzel, M., Bouchez, J., 2014, Si stable isotope fractionation during adsorption and the competition between kinetic and equilibrium isotope fractionation: Implications for weathering systems, Chemical Geology, 380: 161-171.

Oelze, M., von Blanckenburg, F., Bouchez, J., F., Hoellen, D., Dietzel, 2015. The effect of Al on Si isotope fractionation investigated by silica precipitation experiments, Chemical Geology, 397, 95-105.

Orpfergelt , S., de Bournonville, G., Cardinal, D., Andre, L., Delstanche, S., Delvaux, B., 2009. Impact of soil weathering degree on silicon isotope fractionation during adsorption onto iron oxides in basaltic ash soils, Cameroon. Geochimica et Cosmochimica Acta 73: 7226-7240.

Paris, I., Stanistreet, I.G., Hughes, M.J., 1985. Cherts of the Barberton greenstone belt interpreted as products of submarine exhalative activity. Journal of Geology, 93: 11-129.

Robert, F., Chaussidon, M., 2006. A paleotemperature curve for the Precambrian oceans based on silicon isotopes in chert. Nature, 443: 969-972.

Taylor, S. R., and McLennan, S. M., 1985. The Continental Crust: Its Composition and Evolution (Blackwell, Malden, MA).

Treguer, P. J., De La Rocha, C. L., 2013. The World Ocean Silica Cycle. Annual Review of Marine Science, 5: 477-501.

Tucker, M. E., 1991. Sedimentary Petrology: an introduction to the origin of sedimentary rocks. 2nd edition, Blackwell Science.

Van den Boorn, S.H.J.M., van Bergen, M.J., Nijman, W., Vroon, P.Z., 2007. Dual role of seawater and hydrothermal fluids in Early Archean chert formation: Evidence from silicon isotopes. Geology, 35: 939-942.

Van den Boorn, S.H.J.M., van Bergen, M.J., Vroon, P.Z., de Vries, S.T., Nijman, W., 2010. Silicon isotope and trace element constraints on the origin of ~3.5 Ga cherts: Implications for Early Archean marine environments. Geochimica et Cosmochimica Acta, 74: 1077-1103.

Zhang, J., Nozaki, Y., 1996. Rare earth elements and yttrium in seawater: ICP-MS determinations in the East Caroline, Coral Sea, and South Fiji basins of the western South Pacific Ocean. Geochimica et Cosmochimica Acta, 60: 4631-4644.

Ziegler, K., Chadwick, O. A., White, A. F., Brzezinski, M. A., 2005. δ^{30}Si systematics in a granitic saprolite, Puerto Rico. Geology 33: 817-820.

APPENDIX A-1

Table 1-1. Chert terminology used in this dissertation

Term in Dissertation	Rock genesis (± depositional affinity)	Metamorphic terminology	Protolith terminology
Chert	chemical precipitation	quartzite	chert
Silicified (rock)	high-/low-T replacement of primary phases	original rock (texture preserved) quartzite (texture not preserved)	original rock
Greenstone chert	chemical precipitation (in hydrothermal systems)	quartzite	chert
Algoma-type banded iron formation	chemical precipitation (in hydrothermal systems)	quartzite, meta- iron formation	chert, iron formation
Bedded chert (generic) 1) hydrothermal 2) continental	chemical precipitation (in hydrothermal systems) (in continental systems)	quartzite	chert
Superior-type banded iron formation	chemical precipitation (in continental systems)	quartzite, meta-iron formation	chert, iron formation
Quartz arenite	clastic sedimentation (in continental systems)	quartzite	quartz arenite
Bedrock	igneous processes	orthogneiss	granite, granodiorite

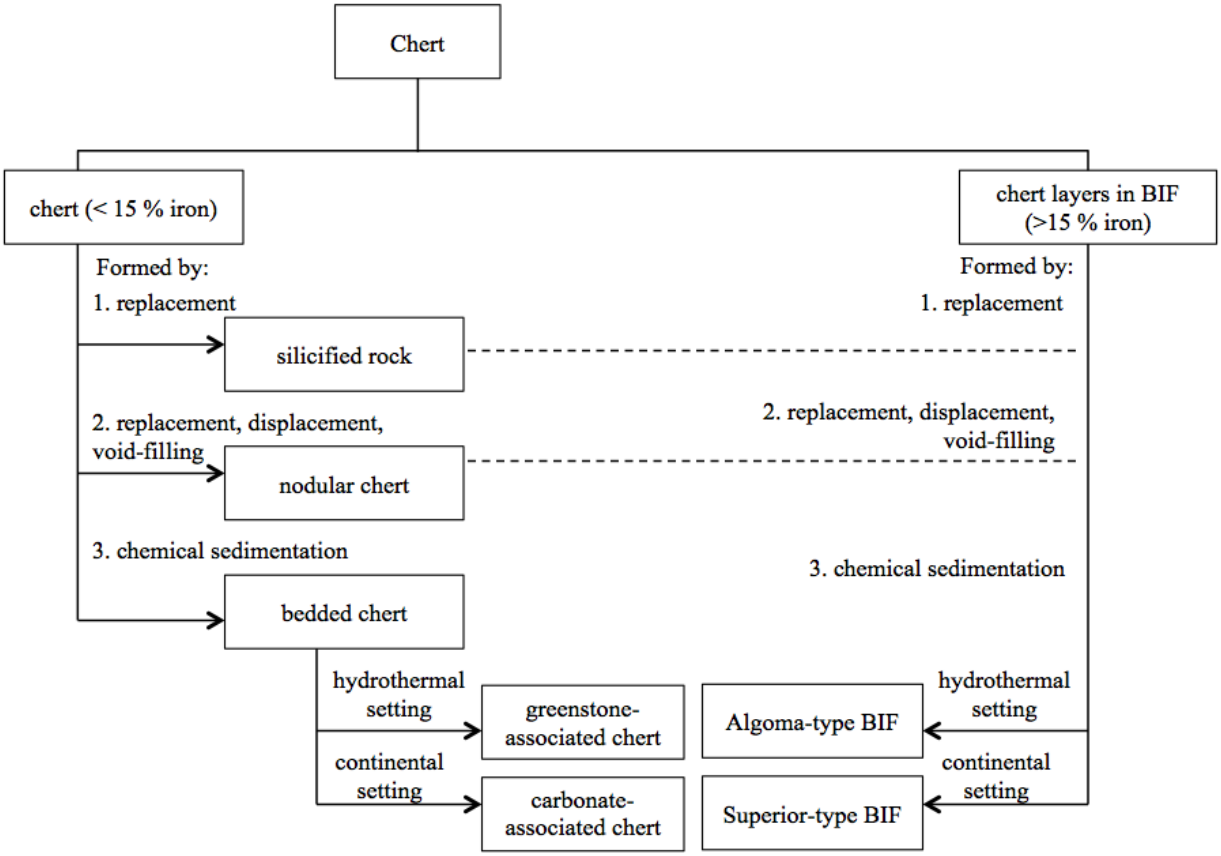


Figure 1-1. Hierarchy chart outlining chert terminology used in this dissertation.

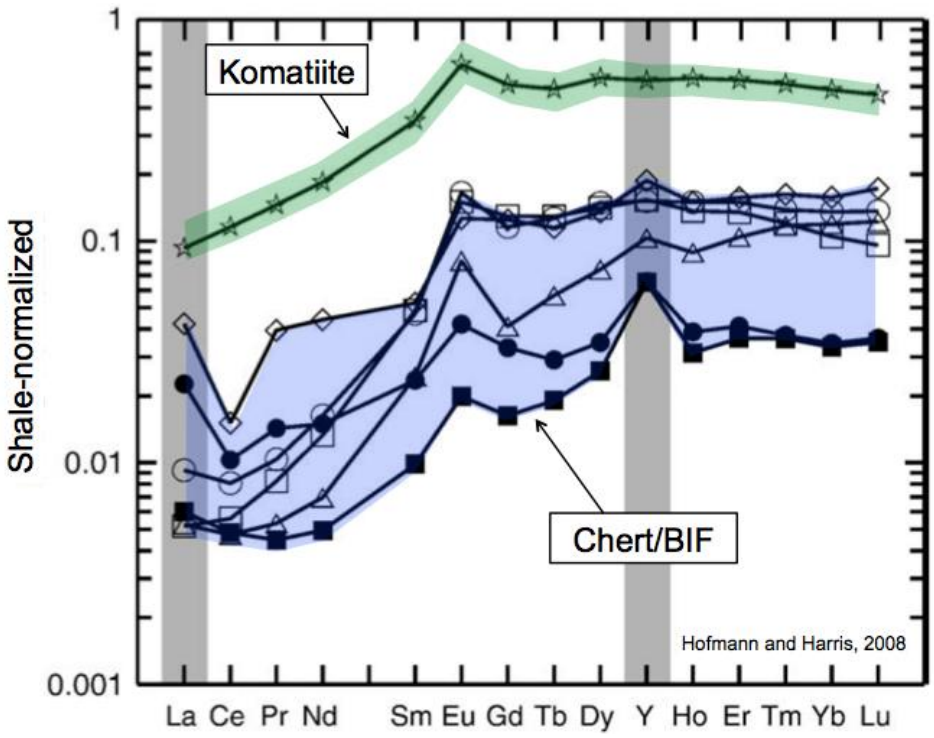


Figure 1-2. Plot showing shale-normalized REY pattern of chemical sedimentary chert/BIF (blue), and silicified komatiite (green), modified from Hofmann and Harris (2008).

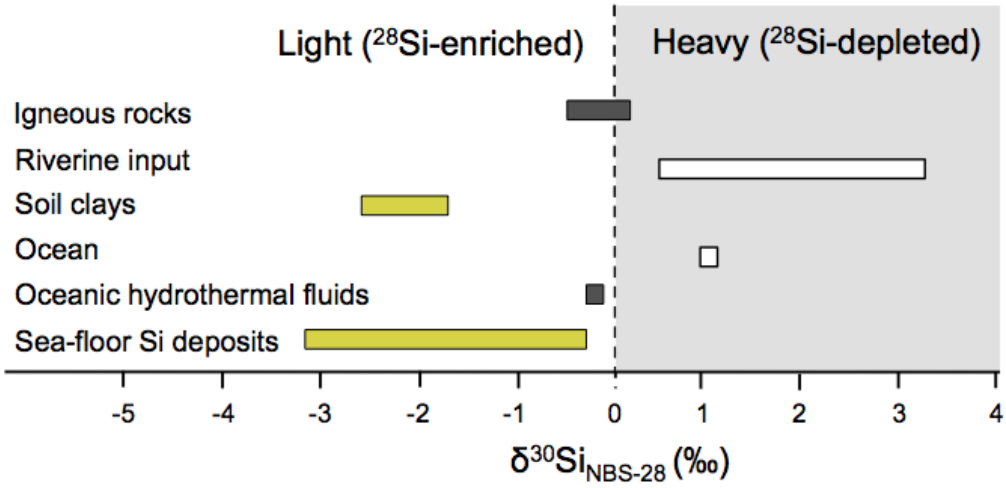


Figure 1-3. δ^{30}Si composition of common abiotic silicon reservoirs. Igneous rocks include average values for both mafic and felsic rocks. Riverine input includes the range of values measured for silicic acid within different modern river systems. Soil clays include analyses from kaolinite separates. Ocean value represents homogenized ocean signature. Oceanic hydrothermal fluids represent values measured for vent fluids. Seafloor Si deposits refers to (non-siliceous ooze) Ferruginous cherty Fe-oxide deposits measured from modern hydrothermal vent sites. Information from Andre et al. (2006).

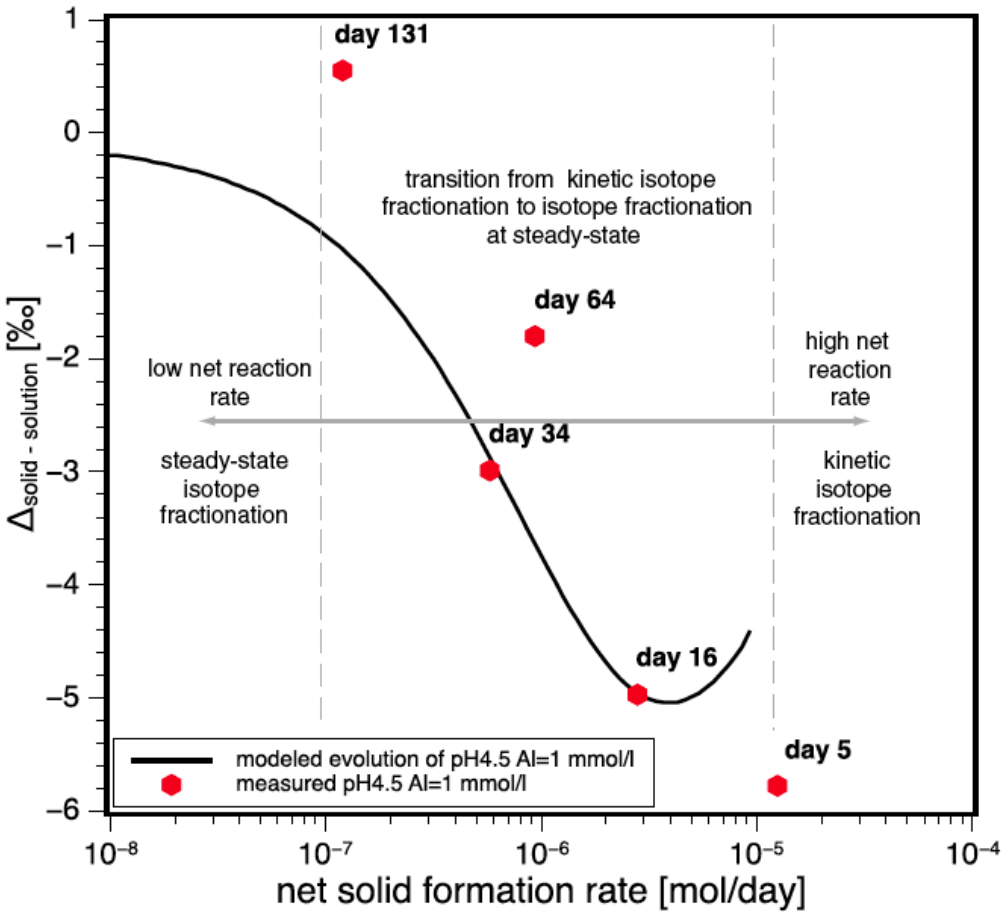


Figure 1-4. Plot showing difference in silicon isotope composition between solid quartz precipitate and solution ($\Delta_{solid\text{-}solution}$), versus precipitation rate of quartz. Note kinetic isotope fractionation dominates earlier stages in the experiment where net reaction rate was greater. By contrast, equilibrium (steady-state) isotope fractionation dominated later stages of the experiment, where net reaction rate was slower. Figure from Oelze et al. (2015) experiment.

CHAPTER II

GEOCHEMICAL EVOLUTION AND TEXTURAL PRESERVATION IN A SUITE OF ALTERED VOLCANIC ROCKS AND JASPILITE FROM THE ~2.72 GA HUNTER MINE GROUP IN THE ABITIBI GREENSTONE BELT, CANADA

This chapter was taken from a manuscript in preparation:

Brengman, L.A., Fedo, C. M., 2015, **Geochemical evolution and textural preservation in a suite of altered volcanic rocks and jaspilite from the ~2.72 Ga Hunter Mine Group in the Abitibi Greenstone Belt, Canada**

ABSTRACT

We investigated a group of rocks from the 2.72 Ga Hunter Mine Group (HMG), Abitibi Greenstone Belt, Canada (Mueller and Mortensen, 2002) which represents a collapsed subaqueous caldera associated with volcanogenic massive sulfide deposits (Mueller and Mortensen, 2002). Pervasive hydrothermal alteration resulted in extensive silicification of volcanic edifice rocks (Mueller and Mortensen, 2002). The least altered volcanic rocks (Group 1) have primary igneous rock textures, and are characterized by volcanic major element (ME), trace element (TE), and rare earth element (REE) compositions expected for felsic igneous rocks in the region. Group 2 rocks (altered volcanic rocks) preserve volcanic phenocrysts and matrix material, but have been partly silicified. Group 2 samples possess transitional ME, TE, and REE geochemistry, different from host volcanic rocks, but similar to seawater. The most altered samples (Group 3) consist of chert ± iron-rich rocks (jaspilite), with remnant clasts, glass shards, lapilli, pseudo-fiamme, and micro-breccia. Mineralogically and compositionally, Group 3 jaspilite rocks resemble primary chemical sediments. However, remnant volcanic textures can be traced through Groups 2 and 3 and show a progressive compositional replacement from rhyolite, to rhyolite with patchworks of chert, to chert ± iron minerals. Based on textural evidence, we propose that in the HMG, primary igneous phenocrysts, volcaniclastic textures and glass shards have been replaced by quartz, and original glassy matrix has been replaced by a combination of Fe-rich chlorite, quartz, iron-oxide, and iron-sulfide to form the jaspilite. Based on geochemical evidence, we suggest that the chert ± iron-rich jaspilite rocks of the HMG likely formed through silicification via interactions of mixed hydrothermal fluid and seawater with glass-rich, felsic igneous rock, and volcaniclastic material. Such a process is consistent with alteration seen within associated Abitibi VMS deposits in the area (Galley et al., 1995). We conclude that the REE signatures of chert are not uniquely linked to a single geologic process, and therefore cannot be used as a geochemical fingerprint.

INTRODUCTION

A geochemical fingerprint represents a combination of elemental or isotopic signatures that connect a rock sample to a singular geologic process (Kamber, 2009). Previous studies have identified what is thought to be a geochemical fingerprint diagnostic of rocks formed through chemical precipitation from seawater (Bau, 1993; Lawrence and Kamber, 2006). This fingerprint consists of diagnostic patterns on shale-normalized rare earth elements (REE), or rare-earth plus yttrium (REY) plots that are considered to be preserved through most geologic processes (Bau and Moller, 1993).

The REE geochemical signature of modern seawater consists of the following characteristics: (1) a positive slope seen as HREE enrichment ($Pr_{SN}/Yb_{SN}<1$, where $_{SN}$ = shale normalized; Bohlar et al., 2004; Lawrence and Kamber, 2006), (2) a positive Ce anomaly ($Ce_{SN}/Ce_{SN}^* >1$) due to Ce^{3+} oxidation and subsequent Ce^{4+} precipitation under oxidizing conditions (Fryer et al., 1977), (3) a positive lanthanum anomaly ($La_{SN}/La_{SN}^* >1$; Bohlar et al.,

2004; Lawrence and Kamber, 2006), (4) Y/Ho > 34 (Bohlar et al., 2004; Lawrence and Kamber, 2006), and (5) Zr/Hf < 26 (Bohlar et al., 2004; Lawrence and Kamber, 2006). In addition to these key features, a positive Eu anomaly ($Eu_{SN}/Eu_{SN}^* > 1$; Danielson et al., 1992) is considered to be a part of the geochemical fingerprint of seawater during times of predominant hydrothermal input to the ocean (see Lawrence and Kamber, 2006 for anomaly equations). In the modern ocean, REEs are primarily sourced from land through continental weathering. In estuaries, REEs fractionate under low-temperature conditions due to complexation with organic compounds and the oxidizing potential of the water column (Lawrence and Kamber, 2006), resulting in the delivery of a distinct signature to the open ocean (Bau and Moller 1993; Bau, 1996; Kamber and Webb, 2001; Lawrence and Kamber 2006). Chemical sediments that precipitate from the ocean capture the REE geochemical signature of seawater. In the Precambrian, seawater could have retained many of these geochemical features. As a result, the REE geochemical fingerprint of chemical sedimentary rocks has been used to document changes in ocean chemistry throughout geologic time.

Two common chemical sedimentary rocks that occur in the Precambrian are chert, and banded iron formation (BIF). Chert is defined as a chemically-precipitated sedimentary rock (Fold, 1980), generally thought to be formed by the chemical precipitation of an SiO_2 phase from seawater (Siever, 1992), or mixed hydrothermal fluids (Klein, 2005; see Chapter I for details on chert terminology). During part of the Precambrian (>3.7 Ga – 1.8 Ga), chert also commonly forms as layers in BIF, which frequently consists of alternating layers of chert and Fe-oxide minerals (Klein, 2005 and references therein). Because chert and chert within BIF form via chemical sedimentation, these rocks have the potential to record the geochemical signature of seawater (Klein, 2005 and references therein).

During the Archean (>3.7 Ga – 2.5 Ga) chert and BIF comprise essential lithologic components in greenstone belt terrains which often host volcanogenic massive sulfide (VMS) deposits thought to represent ancient hydrothermal systems (Huston and Logan, 2004). In this depositional setting, chert and BIF occur interstratified with volcanic rocks of ultramafic to felsic composition (Bekker et al., 2010). Such sequences are generally characterized by extensive hydrothermal alteration, and are commonly affected by secondary silicification (van den Boorn, 2007; van den Boorn, 2010). The process of silicification involves the replacement of a precursor rock by microcrystalline quartz (which resembles chert petrographically) via fluid-rock interaction (e.g. Lowe, 1994; Duchac and Hanor, 1990; Hofmann and Harris, 2008; van den Boorn, 2007). In settings with intense hydrothermal alteration, silicification often proceeds through the replacement of primary volcanic rocks by silica phases (van den Boorn, 2007; Duchac and Hanor, 1990) to form a rock that resembles chert. However, such rocks are by definition not chemical sedimentary rocks, because they are formed via replacement. Replacement can affect all rock types at any time during hydrothermal alteration, diagenesis or metamorphism. As a result, silicified rocks do not always record seawater chemistry at the time of deposition or formation. Because the processes of silicification and chemical sedimentation may occur in the same depositional setting, both silicified rocks, and chert/BIF produced via exhalative chemical sedimentation commonly occur together within the same succession (Kimberley, 1979; 1989; see Chapter I for clarifications on terminology).

Despite the recognition that chert can form by two distinct geological processes, (chemical sedimentation and replacement), their REE and REY geochemical fingerprints have been used to suggest a singular process of formation, chemical sedimentation. Data presented here demonstrate that the REE signatures of chert are not uniquely linked to a single geologic

process, and therefore cannot be used as a true geochemical fingerprint. We suggest that without geologic context and textural information to support a specific process of formation, the REE geochemical fingerprints of chert, and even chert in BIF, are non-diagnostic, and cannot be used alone to differentiate between rocks formed via primary chemical sedimentation from those rocks formed via replacement during silicification of precursor material.

GEOLOGIC SETTING

To investigate how to better understand the geochemical evolution of chert, we specifically targeted a group of well preserved, progressively silicified volcanic rocks, and a jaspilite body of uncertain depositional origin from the ~2.7 Ga Abitibi Greenstone Belt (AGB), in Canada (Fig. 2-1). The AGB represents a composite arc terrane, proposed to have formed through several stages of arc formation, collision, fragmentation, and exhumation (Mueller et al., 1996) during a 65 million year period, from 2735-2670 Ma. The tectonic evolution is represented by both plume, and arc-related volcanism, and long depositional gaps, when exhalative chemical sedimentation, silicification of volcanic rocks, and concurrent mineralization occurred. During these periods of volcanic quiescence, chert and BIF deposits are hypothesized to have formed from chemical sedimentation, and/or silicification. Chemical sedimentation is the result of precipitation proximal to VMS deposits due to hydrothermal circulation through existing volcanic stratigraphy. Silicification is the result of low sedimentation rates leading to chert formation through water-rock interaction, and replacement of volcanic edifice rocks by quartz (Thurston et al., 2008).

The AGB is characterized by multiple volcano-sedimentary sequences, divided into the northern and southern volcanic zone (Mueller et al., 2009; Muller and Mortensen, 2002). Typical volcano-sedimentary sequences of the northern volcanic zone include felsic and mafic volcanic suites, Algoma-type (greenstone-associated) BIF and chert, pervasively altered hydrothermal rocks, and localized VMS mineralization (Thurston et al., 2008). The 2.72 Ga Hunter Mine Group (HMG) of the northern volcanic zone (Mueller and Mortensen, 2002) represents a collapsed subaqueous caldera, associated with VMS, in which pervasive hydrothermal alteration resulted in extensive silicification of volcanic edifice rocks (Mueller and Mortensen, 2002). The HMG crops out on the southern limb of an overturned, east-plunging anticline, (Fig. 1-1; Chown et al., 2000; Mueller and Mortensen, 2002), and is overlain by two komatiite units and the volcano-sedimentary Stroughton Roquemaure Group. Samples collected for this study come from locations 2.1, 2.3, and 2.4 (Fig. 2-1) from the detailed outcrop maps of Mueller and Mortenson (2002) and Chown et al. (2000). The entire area has experienced greenschist facies metamorphism, but local preservation has allowed detailed identification of delicate primary volcanic and sedimentary features (Mueller and Mortensen, 2002).

The HMG is divided into the lower, middle, and upper formational stages which are characterized primarily by voluminous felsic and mafic volcanic rocks (Mueller and Mortensen, 2002), and a small (meter-scale) jaspilite body. The units of interest to this study lie at the contact between the middle and upper formational stages, where primary volcanic rocks are intimately associated with VMS-mineralization, jaspilite as well as rocks replaced by quartz, hematite, magnetite, and carbonate (Fig. 2-2). Mueller and Mortensen (2002) interpreted the HMG as a subaqueous caldera system, where continuous eruptions formed a zone between inner and outer caldera depressions that provided hydrothermal fluids that facilitated both VMS mineralization and silicification of host volcanic rocks (Mueller et al., 2009). Faults, fractures, and fissures associated with caldera collapse and volcanic edifice development provided conduits

for hydrothermal fluid, resulting in the precipitation of hydrothermal minerals during volcanic arc evolution. The presence of a massive felsic dyke provides evidence for an extensive fluid transport network, where abundant seawater circulated through the system, possibly driven by the emplacement of the Fe-rich Roquemaure sill (Fig. 2-1; Mueller and Mortensen, 2002). Fluid circulation involved extensive fluid-rock interactions and drove hydrothermal alteration and silicification of the volcanic edifice rocks, followed by later carbonitization and VMS mineralization (Mueller et al., 2009).

The purpose of our study is to investigate the origin of the jaspilite body and its potential genetic link to surrounding silicified rocks in the HMG. We collected samples from three distinct lithologic groups based on mineralogic and textural criteria (Table 2-1). Group 1 rocks include felsic volcanic rocks that locally preserve identifiable volcanic textures. Group 2 rocks include a range of hydrothermally altered rhyolite, andesite, and pyroclastic rocks. These rocks preserve volcanic textures, but have been variably silicified. Group 3 rocks include banded chert ± hematite and magnetite-rich rocks (jaspilite), that strongly resemble classical BIF, but whose origin may be more closely linked to silicification of host volcanic rocks. To determine the origin of the jaspilite rocks in the HMG, we use well-established major-, trace-, and rare-earth element geochemical proxies in addition to critical textural analysis.

ANALYTICAL TECHNIQUES

Samples were cut into <1 cm cubes and trimmed to remove modern weathering rinds, then crushed using a ceramic dish and puck. Samples were carefully prepped to avoid cross-contamination between samples where prior to and after each sample a blank quartz sample was crushed to ensure maximum cleaning of the instruments used. Powdered whole-rock samples were sent to Activation Laboratories (Actlabs) for major- and trace-element geochemical analyses (4Lithores, Option: 4B-INAA). Samples were analyzed for a suite of 46 trace and rare earth elements (Li, Be, Sc, Ti, V, Cr, Co, Ni, Cu, Zn, Ga, As, Rb, Sr, Y, Zr, Nb, Mo, Ag, Cd, In, Sn, Sb, Cs, Ba, La, Ce, Pr, Nd, Sm, Eu, Gd, Tb, Dy, Ho, Er, Tm, Yb, Lu, Gf, Ta, W, Tl, Pb, Th, U) by inductively coupled plasma mass spectrometry (ICP-MS) using standard procedures. Blind duplicate samples were analyzed to test precision of digestion methods, in addition to duplicates processed for analytical accuracy. For elements analyzed in this study, detection limits were as follows: >0.01 % for major elements, >0.001 % for MnO_2 and TiO_2, >30 ‰ for Zn, >20 ‰ for Cr, Ni, >10 ‰ for Cu, >5 V, As, Pb, >0.1 ‰ for In, Cs, Hf Bi, U, >3 ‰ for Ba, >2 ‰ for Sr, Mo, >1 ‰ for Sc, Be, Co, Ga, Rb, Sn, >0.05 ‰ for Ge, Y, Ag, La, Ce, Nd, W, Th, >0.01 ‰ Pr, Sm, Gd, Tb, Dy, Ho, Er, Yb, Ta, >0.0005 ‰ for Eu, Tm, >0.0002 ‰ for Lu.

Polished thin sections were made for mineralogic examination using a Nikon petrographic microscope with reflected and transmitted light capabilities. Detailed digital maps were made using reflected light images of the thin section. Individual mineral analyses were performed using the fully automated CAMECA SX-50 electron microprobe analyzer (EMPA) at the University of Tennessee. Analytical conditions were as follows: 15keV excitation potential, 20-30 second peak and background counting times, 20nA beam current for quartz, pyrite, and titanite, 10nA beam current for feldspars, with a 1-3 μm beam size for quartz, pyrite, and titanite, and a larger 5-7 μm beam size for feldspars. Synthetic standards were used and standard ZAF (PAP) corrections were applied.

DEFINITION OF LITHOLOGIC GROUPS

Group 1 samples represent volcanic edifice rocks (Fig. 2-3a-c). These rocks are primarily felsic in composition, with primary volcanic textures including phenocrysts (Fig. 2-3b, c) and spherules. Group 1 rocks have the following characteristics: (1) contain <15% of precipitated mineral phases with Si or Fe; (2) lack sedimentary layering; and (3) do not compositionally resemble iron formation (Table 2-1). Group 2 samples possess phenocrysts and volcaniclastic textures (Fig. 2-3d, e) similar to group 1, but also contain large (centimeter-scale) irregular lensoidal areas of microcrystalline quartz (Fig. 2-3b-e). Some of these altered volcanic rocks contain >15% Si (Fig. 2-3d, e) and/or Fe minerals. Additionally, microcrystalline quartz occurs along boundaries of volcaniclastic layering (Table 2-1). Group 3 samples primarily consist of layers of microcrystalline quartz ± hematite, magnetite (Fig. 2-3f) and local carbonate minerals. Macroscopic volcanic textures are not prevalent (Fig. 2-3f), but rare preservation of lapilli, remnant clasts (Fig. 2-3g), glass shards (Fig. 2-3h), pseudo-fiamme and micro-brecciated textures are observed in thin section suggesting a volcanic precursor.

PETROGRAPHY

Group 1

Description

Group 1 rocks (Fig. 2-3a, b) consist of fine-grained chloritic matrix (65 %), phenocrysts of feldspar and quartz (30 %), and minor phases pyrite, epidote, and titanite (< 5 %). Locally, mm-scale, irregular patches of micro-crystalline quartz occur (Fig. 2-3a-c) interspersed with fine-grained chlorite matrix (Fig. 2-3a, b). Quartz and feldspar phenocrysts remain even in areas where microcrystalline quartz occurs (Fig. 2-3c). In sample AB-11-11, which is an example of a typical Group 1 rock, overall, the phenocryst mineral assemblage represents 35 % of the thin-section, and includes feldspar (20 %) and quartz (15 %). Other minerals include secondary fracture-filling pyrite (4 %) and interstitial epidote (<1 %). The groundmass represents 65 % of the thin section, and consists of a mixture of chlorite, and Fe-Mg-rich clay minerals (60 %), quartz (35 %), and minor minerals: sphene, magnetite, pyrite, epidote and apatite (<5 %) (Fig. 2-3a, b). Fracture-filling pyrite grains are associated with interstitial epidote and magnetite. Most quartz phenocrysts occur as mm-scale, broken, anhedral grains, although euhedral quartz phenocrysts are still present in thin-section. Feldspar phenocrysts are anhedral to euhedral crystals (1-3 mm scale) that show Carlsbad-twinning and are heavily sericitized (Fig. 2-3c). In addition, quartz spherules are present in some samples. In addition to primary volcanic features, group 1 volcanic rocks contain minor irregular-shaped diffuse patchworks of micro-crystalline quartz that partly surround feldspar phenocrysts (Fig. 2-3a, c).

Interpretation

We interpret Group 1 samples as primary volcanic rocks, as evidenced by the preservation of volcanic phenocrysts and spherules (Simonson, 2003). We interpret the minor micro-crystalline quartz to reflect incipient stages of silicification that replaced chloritic matrix material, while preserving volcanic textures.

Group 2

Description

Group 2 rocks consist of fine-grained chloritic matrix (up to 30 %) surrounding lenses and/or layers of micro- to mega-quartz (~10 to 90 %) with varying percentage of feldspar and

quartz phenocrysts (60 to <5 %), and pyrite, magnetite, epidote, calcite, and titanite (<5 %) present in the groundmass (Fig. 2-3d-f). Preserved phenocrysts of quartz and feldspar are commonly broken, and form mm-scale, anhedral to euhedral crystals. Feldspar phenocrysts are heavily sericitized similar to Group 1 samples. Quartz lenses have diffuse edges (Fig. 2-3d –f), and consist of micro- to mega-crystalline quartz that exhibits irregular grain boundaries, similar to Group 1 samples.

Interpretation

We interpret Group 2 samples as altered volcanic rocks, compositionally similar to group 1 samples, but that have been affected to varying degrees by silicification. We interpret micro- to mega-crystalline quartz patches and lenses to reflect silicification of both chloritic matrix material and phenocrystic material. This interpretation is supported by the rare presence of quartz phenocrysts and volcanic clasts preserved both inside and outside of the microcrystalline quartz silicification lenses (Fig. 2-3e, f). Additionally, chloritic matrix material exists both outside of quartz patches and lenses, and interstitial to quartz crystals within the quartz patches/lenses (Fig. 2-4a, b), consistent with replacement origin (Doyle and Huston, 1999), rather than a clastic origin. Volcanic clasts of the silicified material from the same unit can be found in a single thin section of one of the volcaniclastic rocks (Fig. 2-4c, d), supporting syn-formational alteration for volcanic rocks. In addition, quartz ± magnetite replaced armored lapilli can be identified (Fig. 2-4e, f), indicating rare preservation of primary volcanic features through this step in the silicification process. We suggest that silicification of volcanic rocks has led to non-uniform preservation of volcanic textures, and overprinting of original textures by quartz.

Group 3

Description

Group 3 rocks consist of microcrystalline quartz (15-90 %) with varying amounts of hematite, magnetite (10-80 %) and minor phases that include apatite, chlorite, calcite, epidote, amphibole, and pyrite (5-10 %). Overall, samples possess uniform, banded textures at both outcrop and hand sample scale, forming alternating mm-scale layers of magnetite, and cm-scale layers of quartz + hematite. Despite the absence of volcanic textures at the macro-scale, micro-textures preserved in thin section include glass shards (Fig. 2-5a) lapilli (Fig. 2-5b), and potential clasts (Fig. 2-5c, d, e). As in Group 2 samples, veins of both silica and carbonate minerals exist and are pervasive in some samples (Fig. 2-5f). Quartz is predominantly microcrystalline and exhibits irregular crystal boundaries, expect in veins and micro-brecciated areas, where mega-quartz exists (Fig. 2-5f). Hematite is fine-grained and dispersed throughout samples, though where clast-like objects occur, hematite occurs primarily along clast edges (Fig. 2-5c, d, e). Magnetite exists principally as euhedral, micron-scale crystals contained within millimeter-scale bands. Carbonate minerals only exist within secondary veins.

Interpretation

Group 3 rocks are considered jaspilite in hand sample reflecting a primary mineralogy of quartz, hematite, and magnetite. However, based on textural information, we interpret Group 3 rocks as silicified and Fe-mineralized volcanic rocks, rather than chemical sedimentary rocks. Group 3 rocks do not commonly record macroscopic volcanic textures, but rare preservation of volcanic glass shards, volcanic clasts, and lapilli in thin section (Fig. 2-5a-f), are consistent with

a primary volcanic precursor. All of these volcanic and volcaniclastic features have been compositionally replaced by microcrystalline quartz ± hematite and/or magnetite.

The apparent decoupling between texture and mineralogy observed in Group 3 samples led us to investigate the major, trace, and rare earth element geochemistry of these samples to better understand their genetic relationship to the other two lithologies (Groups 1 and 2), determine the preservation potential of original volcanic geochemical signatures in silicified rocks that superficially resemble chemical sediments.

GEOCHEMISTRY

Whole-rock major-element, and individual mineral composition

Group 1 volcanic rocks

Whole-rock major-element and individual mineral geochemical data are presented in Appendix A-5, Tables 2-2 through 2-5. Group 1 volcanic rocks contain primary volcanic phenocryst and matrix assemblages, retain primary volcaniclastic textures, and display petrographic evidence for incipient silicification. Overall, group 1 rocks possess whole-rock major-element geochemistry generally comparable to Late Archean felsic volcanic rocks (Condie, 1993; Appendix A-5, Table 2-2). Based on petrography, the least altered Group 1 sample is AB-11-11. In order to evaluate geochemical changes to group 1 rocks, group 1 samples were normalized to AB-11-11 (Fig. 2-6a). Overall, samples from Group 1 maintain major element values near 1, which indicates they are similar in composition to AB-11-11. Observable deviations include K_2O enrichment in one sample, and CaO enrichment in two samples (Fig. 2-6a).

To better understand chemical exchange involved in incipient alteration of the felsic volcanic rocks of group 1, we measured the composition of phenocrysts, and generated backscatter electron images and compositional X-Ray maps (Si Kα, Al Kα, and Fe Kα). The purpose behind mineral analyses was to estimate major-element mobility proximal to, and within, silicified areas, and better determine the preservation state of phenocrysts (Fig. 2-7a-d). In the backscatter electron image (BSE; Fig. 2-7a), a patch of microcrystalline quartz, interpreted to be of replacement origin is outlined with a dashed line, and appears as uniformly dark when compared to the chloritic matrix. We specifically targeted feldspar and quartz phenocrysts both inside and outside of silicified areas for analysis. Feldspars in almost all samples have albite (Ab_{95-100}) compositions. Homogeneous end-member albite compositions (>95%) suggest albitization, i.e. the loss of CaO, and Al_2O_3, and gain of Na_2O and SiO_2 (Putnis, 2002; Van Lente, 2009) in the feldspars. Feldspar phenocrysts both inside and outside of the silicification patches possess end-member albite compositions (Appendix A-5, Table 2-3, 3-4).

Although phenocrysts are not affected compositionally or texturally by silicification, surrounding matrix material shows partial replacement by microcrystalline quartz. The aluminum k-α X-ray map (Fig. 2-7b) shows that, despite the presence of uniform microcrystalline quartz in thin section, patchy aluminum-rich areas exist within the zone of silicification. Aluminum is possibly residual from primary matrix material, potentially representing the only element left from replacement of original volcanic glass, chlorite and quartz and feldspar microlites (Fig. 2-7b). The patchy nature of silicification is highlighted in the silicon k-alpha x-ray map (Fig. 2-7c). The iron k-α X-ray map indicates that despite retaining aluminum (Fig. 2-7b), iron has been mobilized from the silicified areas, and is only present in the residual matrix material.

Group 2 altered volcanic rocks

Altered volcanic rocks of group 2 contain primary volcanic phenocryst and matrix assemblages similar to group 1 samples, and retain primary volcaniclastic textures, but are heavily silicified, with silica enrichment up to 92 wt. %. As with Group 1 samples, Group 2 rocks were normalized to sample AB-11-11 from group 1 to identify compositional changes that occurred (Fig. 2-6b). Group 2 samples show Depletion of Al_2O3, Na_2O, MgO, and TiO_2 depletion, and enrichment of SiO_2, Fe_2O_3, CaO, and P_2O_5 are consistent with replacement of chlorite and feldspar by quartz, magnetite, calcite, and apatite (Fig. 2-6b).

Within Group 2 samples, patchy silicification results in the near complete replacement original phenocrysts and matrix, leaving few traces of original volcanic material. Rare feldspar phenocrysts were identified outside of silicified lenses, and electron microprobe analyses revealed albite compositions comparable to samples from Group 1 (Appendix A-5, Table 2-6). Backscatter electron images show areas of intense silicification (Fig. 2-8a), surrounded by regions where chloritic matrix is still partially preserved (Fig. 2-8a). Aluminum k-α X-ray maps indicate areas where aluminum has been retained, despite silicification (Fig. 2-8b). Silicon k-alpha x-ray maps again highlights the non-uniform nature of silicification (Fig. 2-8c). Additional textural variance is observed in the iron k-α X-ray map, where silicified patches internally consist of apparent clast-like objects (Fig. 2-8d) that are outlined by minor amounts of Fe-enrichment and an absence of silica along potential clast boundaries (Fig. 2-8c, d), consistent with petrographic observations. In addition, boundaries of the silicification lenses are diffuse, where an outer layer of the boundary is depleted in iron relative to the inner portion of the silicified lenses (Fig. 2-8d).

Group 3 jaspilite rocks

Group 3 jaspilite samples consist of $SiO_2 \pm$ Fe-oxides, and/or carbonate minerals. In thin section, some primary volcanic textures are preserved, but all remnant clasts, lapilli, and glass shards have been replaced by microcrystalline quartz ± hematite and/or magnetite. As with Group 1 and 2 samples, Group 3 rocks were normalized to AB-11-11 to determine element mobility (Fig. 2-6c). Group 3 samples show enrichment of SiO_2, Fe_2O_3T, and CaO, and depletion of Al_2O_3 Na_2O and MgO (Fig. 2-6c). Two samples exhibit extreme CaO and K_2O enrichment, likely reflecting the presence of calcite veins, and a K-rich mineral phase not represented in other samples (Fig. 2-6c). Changes in major elements are likely consistent with the addition of quartz (SiO_2), hematite, magnetite, pyrite (Fe_2O_3T), and calcite (CaO) at the expense of primary constituents during progressive silicification.

Backscattered electron images document dark areas of silicification (Fig. 2-9a), with spotty areas of Fe-mineralization (Fig. 2-9a). Aluminum k-alpha x-ray maps do not show detectable amounts of aluminum compared to previous group 1 and 2 samples. We interpret this as evidence for near complete compositional replacement of original volcanic material to silica, and iron phases (Fig. 2-9b). Remnant clast-like objects are visible in the backscatter image (Fig. 2-9a) silicon k-alpha map (Fig. 2-9c), and the iron k-α X-ray map (Fig. 2-9d). Both silicon and iron k-alpha x-ray maps highlight the textural heterogeneity associated with silicified areas (Fig. 2-9c, d).

Trace- and Rare-earth elements

Trace-element and rare-earth element (REE) concentrations for Group 1, 2, and 3 samples are presented in Appendix A-5, Tables 2-7, 2-8.

Group 1 volcanic rocks

Group 1 felsic volcanic samples from the HMG possess TE geochemistry patterns consistent with average Late Archean felsic volcanic rocks (Fig. 2-9a; normalization values Condie, 1993). Minor differences include slight enrichment in Th, U, V, Co, and Ni, and depletion in Ba, Y, Eu, and Sc relative to Late Archean felsic volcanic rocks. Group 1 volcanic rock samples are characterized by REE signatures similar to reference volcanic rocks (Fig. 2-9b; Condie, 1993), and clastic sediment derived from weathering of such rocks. These samples uniformly possess flat REE slopes (Fig. 2-9b), Y/Ho values 24 – 34, $Eu/Eu^*_{SN} < 1$, $Pr_{SN}/Yb_{SN} \leq 1$, and $La/La^*_{SN} < 1$ (equations in Lawrence and Kamber, 2006), all of which are characteristic of volcanic rocks.

Group 2 altered volcanic rocks

Group 2 altered volcanic rock samples, which preserve phenocrysts and/or matrix material, but have been partly silicified, possess TE and REE geochemistry patterns that deviate slightly from average Late Archean felsic volcanic rocks (Fig. 2-10a; normalization values Condie, 1993). Overall, these samples are slightly depleted in Th, U, Nb, Zr, Hf, and Sr, and enriched in Sr, Eu, Sc, V, Cr, Co, and Ni relative to Group 1, felsic volcanic rocks (Fig. 2-10a; Appendix A-5; Tables 2-7, 2-8). These rocks have a positive overall slope (Fig. 2-10b), Y/Ho values 23.9 – 34, $Eu/Eu^*_{SN} > 1$, $Pr_{SN}/Yb_{SN} < 1$, and $La/La^*_{SN} > 1$, which is atypical of the host volcanic rocks, but similar in a number of respects to expected patterns for chemical precipitates from seawater (e.g., Bohlar et al., 2004).

Group 3 jaspilite rocks

Group 3 jaspilite samples consist of chert ± iron-rich rocks, which mineralogically and compositionally resemble chemically-precipitated sedimentary rocks but preserve remnant volcanic textures. These samples are depleted in all TE, especially Th, U, Nb, Zr, Hf, and Sr, relative to Group 1, and 2 rocks (Fig. 2-11a), although still enriched in Rb, Ba, V, Ni, and Co compared to seawater precipitates in the region (Appendix A-5, Table 2-7, sample TEM-cf). Group 3 jaspilite samples are characterized by REE signatures that most closely resemble those of chemically-precipitated sedimentary rocks (Fig. 2-11b; Appendix A-5, Table 2-8). These rocks possesses a positive slope (Fig. 2-11b), Y/Ho values from 25-55, $Eu/Eu^*_{SN} > 1$, $Pr_{SN}/Yb_{SN} < 1$, and $La/La^*_{SN} > 1$ (Appendix A-5, Table 2-8), all of which are characteristic of seawater precipitates.

Synthesis and interpretation of geochemical data for Groups 1, 2, 3

Major-Elements

To understand the evolution of major elements within of the volcanic rocks in this study, we plotted Group 1, 2, and 3 samples on a conventional total alkali silica (TAS) classification diagram (Fig. 2-11). This plot compares total alkali elements ($Na_2O + K_2O$ %) to silica content (SiO_2). On this plot, volcanic rock samples from group 1 are generally silica-rich, and dominantly plot in the rhyolite and dacite fields (Fig. 2-11). Group 2 altered volcanic rock samples mostly plot in the rhyolite field, likely reflecting the addition of SiO_2 during progressive silicification (Fig. 2-11). Group 3 jaspilite samples plot in the andesite and dacite fields (Fig. 2-11), likely reflecting the loss of alkali elements during silicification and the addition of iron during Fe-mineralization.

To determine the relationship of major elements among the three different lithologic groups, we plotted each group in conventional AFM ternary space for volcanic rocks (Fig. 2-12). The AFM plot uses the alkali ($Na_2O + K_2O$), FeO, and MgO content to distinguish rocks with a calc-alkaline trend, which indicates crystallization from an oxidized melt, from those with a tholeiitic trend, which crystallize from a reduced melt. Following the alteration series from Group 1 to Group 2 to Group 3 samples, a distinct trend of FeO enrichment is identified (Fig. 2-12). Group 1 volcanic rocks follow a calc-alkaline trend consistent with other rocks in the region (Dostal and Mueller, 1996). Group 2 samples plot away from the alkali pole (A), following a trend of FeO enrichment, possibly reflecting Fe-mineralization of the groundmass, and depletion of alkali elements due to replacement by silica (Fig. 2-12). Group 3 samples are centered primarily at the F pole, due to further enrichment of FeO and depletion of all other elements during SiO_2-replacement (Fig. 2-12). We interpret that major-element changes from Group 1 to Group 2 document progressive SiO_2 enrichment of volcanic rocks resulting from hydrothermal alteration and silicification, which resulted in the dilution of other elements. Group 2 to Group 3 major-element changes indicate Fe-mineralization of silicified, Group 2-type samples, and further dilution of all other major elements due to complete replacement by $SiO_2 \pm$ FeO/CaO.

Trace- and rare-earth elements by group

To determine the relationship between TE and REE for samples in this study, we compared several Post Archean Australian Shale (PAAS) normalized plots utilizing elements that are a part of the geochemical fingerprint for chemical precipitates. Samples with a seawater signature should possess a positive REE slope ($Pr_{SN}/Yb_{SN}<1$), a positive lanthanum anomaly ($La_{SN}/La_{SN}^* >1$), Y/Ho > 34, Zr/Hf < 26, in addition to a positive Eu anomaly ($Eu_{SN}/Eu_{SN}^* > 1$) (calculations and values published in Lawrence and Kamber (2006) and references therein). Igneous rocks, by contrast should possess a flat REE slope, no positive Lanthanum anomaly, and should have Y/Ho ratios between 24 and 34, and Zr/Hf ratios between 26 and 46. To compare samples from this study, we will use the geochemical fingerprint of seawater, and compare our data to established data for seawater precipitates and igneous rocks defined within these geochemical fields. The only excluded parameter is the positive cerium anomaly, due to different redox conditions at the time of formation for rocks in this study, and complications associated with the weathering and alteration history of the samples, which can effect the Ce anomaly.

Group 1 volcanic rocks possess the geochemical signature of average felsic volcanic rocks (Fig. 2-13a-f). Group 1 rocks consistently fall in the volcanic field on plots comparing Pr_{SN}/Yb_{SN}, Eu_{SN}/Eu_{SN}, Y/Ho, La_{SN}/La_{SN}, and Zr/Hf, and do not possess features characteristic of seawater (Fig. 2-13a-e). Group 2 rocks possess mixed signatures between that of a pure igneous rock signature, and a pure seawater signature. Transitional geochemistry is observed when comparing Pr_{SN}/Yb_{SN}, Eu_{SN}/Eu_{SN}, Y/Ho, La_{SN}/La_{SN}, and Zr/Hf values. Overall trends also show features indicative of seawater, including a positive slope ($Pr_{SN}/Yb_{SN}<1$), $Eu_{SN}/Eu_{SN}^*>1$, $La_{SN}/La_{SN}^* >1$ (Fig. 2-13a-f). The only parameters where Group 2 samples plot in the expected field for igneous rocks are Y/Ho and Zr/Hf (Fig. 2-13f). Group 3 jaspilite samples, which still possess relict volcanic textures, possess a geochemical signature similar to that of seawater (Fig. 2-13a, d). These samples plot consistently within the field for seawater precipitates, and have positive REE slopes ($Pr_{SN}/Yb_{SN}<1$; Fig. 2-13a, c; Bohlar et al., 2004), a positive lanthanum anomaly ($La_{SN}/La_{SN}^*>1$; Fig. 2-13d, e), and a positive Eu anomaly ($Eu_{SN}/Eu_{SN}^*>1$) (Fig. 2-13a, b, d). Despite possessing a REE geochemical signature diagnostic of seawater, all but one Group 3 samples plot within the igneous rock field for Y/Ho, Zr/Hf (Fig. 2-13f).

Based on textural observations, we interpret the geochemistry of Group 1 samples to represent original volcanic origin. We interpret the mixed geochemical signatures of transitional Group 2 samples to be the result of overprinting of original volcanic geochemical signatures in preserved volcanic material, during silicification. Group 3 samples likely originated near-complete silicification and Fe-mineralization of Group 2-type samples.

Compositional evolution of Group 1 volcanic rocks to produce Group 3 jaspilite rocks

Silicification is a well documented process in Precambrian greenstone belts around the world (Orberger et al., 2006; Lowe, 1999; Duchac and Hanor, 1990; Hofmann and Harris, 2008). For example, in the North Pole chert-barite unit of the Dresser Formation in Australia, microcrystalline quartz has replaced euhedral and subhedral crystals interpreted as precursor volcanic phenocrysts (Orberger et al., 2006). Similarly, in volcaniclastic sediments of the Swaziland Supergroup of the Barberton Greenstone Belt, primary volcanic grains are texturally preserved, and retain original twinning patterns, but only quartz grains retain their original mineralogical composition (Lowe, 1999). All other grains have been silicified (Lowe, 1999). Examples of silicified komatiite also exist in the Barberton Greenstone Belt. In the komatiites, original spinifex crystals of olivine and pyroxene have been compositionally replaced by quartz (Duchac and Hanor, 1990; Hofmann and Harris, 2008). Similar to these literature examples, we propose we propose that the Group 3 jaspilite rocks studied here were formed by silicification, rather than chemical sedimentation. Below we present the textural and geochemical evidence to justify this interpretation.

Group 1 volcanic rock textures and geochemistry

Group 1 felsic volcanic rocks contain a preserved primary phenocryst assemblage of quartz and feldspar, with a matrix predominantly consisting of rutile, feldspar and quartz microlites, and some amount of chlorite. Textural evidence in thin sections for initial stages of hydrothermal alteration include albitization, early chloritization of matrix material, and some silicification and epidotization (Fig. 2-14a, b). Electron microprobe analyses of feldspar phenocrysts in group 1 samples demonstrate that all measured feldspar phenocrysts possess compositions of Ab_{95} or greater, indicating albitization, and chemical exchange of Na^{+} and Ca^{2+}, likely upon contact of volcanic rocks with seawater. Evidence for chloritization of matrix is documented in thin section and confirmed by electron microprobe analyses where nearly all matrix material is compositionally replaced to both Fe- and Mg-rich chlorite. Epidotization of samples is confirmed by the presence of anhedral, non-magmatic epidote throughout Group 1 samples.

Feldspar albitization is well documented in many different geologic settings and is not restricted to a particular rock-type (Putnis, 2002). Several experimental studies have confirmed that the albitization reaction proceeds via a pseudomorphic replacement process termed 'interface-coupled dissolution re-precipitation' (e.g., Putnis, 2002). This mechanism is responsible for the coupled cation exchange of Ca^{2+} and Al^{3+} by Na^{+} and Si^{4+}. The key to moving this pseudomorphic reaction forward is the development of a sharp chemical gradient between the parent and product phase, due to solubility differences, as well as the development of porosity in the product phase (Hovelmann et al., 2010). During this process, parent phase dissolution produces a thin supersaturated fluid film. The product phase is then precipitated onto the surface of the parent phase. This pseudomorphic replacement preserves the original crystallographic orientation of the grains, as well as preserving the original external grain

boundaries. This is possible because the reaction front utilizes pre-existing grain fractures, moving from the surface and outer grain edges inward, with porosity generated during the process, allowing further replacement (Hovelmann et al., 2010). This type of hydrothermal alteration is common among felsic volcanic rocks and basalts in back-arc basin settings, where total replacement of primary calcic plagioclase releases Ca causing the re-precipitation of calcite, epidote and sphene (Van Lente et al., 2009), consistent with the mineralogy of Group 1 samples in our study.

Chloritization and epidotization of Group 1 samples likely occurred either prior to or at the same time as incipient silicification, as evidenced by samples that contain un-silicified, but chloritized and epidotized matrix (ex: sample AB-11-11). During chloritization, original feldspar and quartz microlite matrix material was replaced by Fe- and Mg-chlorite, which likely facilitated the incorporation of heavy rare earth elements, Cr, Zn, Sb, Ta, Th, U, and the removal of Ti, Y, and other REE from the system (Maslennikov et al., 2012). Epidotization likely involved the replacement of original feldspar microlites by epidote and quartz, as well as growth of void-filling epidote, which nucleated and replaced some ground mass material (Maslennikov et al., 2012). Both chloritization and epidotization are common alteration processes associated with volcanic rocks proximal to VMS deposits, the known environment of formation for Group 1 samples.

Incipient silicification is evidenced by the presence of patchy areas of micro-crystalline quartz with diffuse boundaries in both hand sample and thin section, the composition of which was confirmed through electron microprobe analyses. Group 1 rocks possess major and trace element compositions similar to average late Archean felsic volcanic rocks. On PAAS normalized REE plots, Group 1 volcanic rocks show primary volcanic REE chemistry, $Pr_{SN}/Yb_{SN} > 1$, $Eu_{SN}/Eu_{SN}^* < 1$, Y/Ho = 24 – 34, $La_{SN}/La_{SN}^* \geq 1$, $Ce_{SN}/Ce_{SN}^* \sim 1$, and Zr/Hf = 26 - 46. Overall, Group 1 felsic volcanic rocks have primary igneous rock textures, and are characterized by volcanic and/or volcaniclastic major element ME, TE, and REE chemistries expected for felsic igneous rocks in the region.

Group 2 altered volcanic rock textures and geochemistry

Group 2 rocks show more extensive silicification, evidenced by the presence of large lensoidal areas of micro-crystalline quartz with diffuse boundaries in both hand sample and thin section. Additionally, Group 2 rocks possess major and trace element compositions with much higher SiO_2 contents (up to 92 wt. %) compared to late Archean felsic volcanic rocks. On PAAS normalized REE plots, Group 2 samples possess transitional ME, TE, and REE geochemistry, atypical of the host volcanic rocks, but similar to seawater. Group 2 altered volcanic rocks show transitional REE chemistry, with $Pr_{SN}/Yb_{SN} > 1$, $Eu_{SN}/Eu_{SN}^* > 1$, Y/Ho = 24 – 34, $La_{SN}/La_{SN}^* \geq 1$, $Ce_{SN}/Ce_{SN}^* \sim 1$, and Zr/Hf = 26 - 46. Transitional geochemistries reflect a combination of preserved igneous phenocryst and matrix, along with precipitated phases of silica ± hematite and magnetite, which contribute the geochemical signatures of the fluids from which these minerals precipitated.

Group 3 jaspilite rock textures and geochemistry

By contrast, group 3 rocks superficially resemble iron formation in the macroscopic banding of chert ± iron minerals. Micro-textural evidence however, reveals relict clasts, glass shards, lapilli, pseudo-fiamme, and micro-brecciated textures (Fig. 2-14d). Group 3 rocks possess ME, TE, and REE compositions that generally resemble seawater. Given the textural

evidence for volcanic/volcaniclastic components in Group 3 rocks, the seawater signature preserved in these samples likely reflects the presence of several mineral phases precipitated from mixed seawater and hydrothermal fluids, which overprinted the original igneous geochemical signatures of the rocks during silicification. On PAAS normalized REE plots (Fig. 2-14a-h), Group 3 samples possess ME, TE, and REE geochemistry that mostly resemble seawater mixed with hydrothermal fluids, with $Pr_{SN}/Yb_{SN} < 1$, $Eu_{SN}/Eu_{SN}^* > 1$, $La_{SN}/La_{SN}^* \geq 1$, though Y/Ho = 24 – 34, and Zr/Hf = 26 – 46, are values expected for igneous rocks. Overall, Group 3, jaspilite rocks do have primary igneous rock textures, but are dominantly characterized by ME, TE, and REE signatures of seawater.

Previous studies (Paris et al., 1985; Lowe et al., 1999; Hofmann and Harris 2008) have shown that during high fluid-rock interaction, elements mobilize, causing silicified rocks to have a seawater-like REE signature (Maslennikov et al., 2012). In the Archean Barberton Greenstone Belt, for example silicified mafic and ultramafic rocks (Lowe et al., 1999; Paris et al., 1985; Duchac and Hanor, 1990) possess seawater-like REE patterns (Hofmann and Harris, 2008; Hofmann and Bolhar, 2007). We suggest a similar origin for Group 3 jaspilite samples in this study. Based on the textural evidence for the volcanic origin of Group 3 jaspilite rocks, we propose group 1-3 rocks reflect differences in the extent of silicification of volcanic edifice. Group 1 felsic volcanic rocks represent the least silicified end members, which still possess original volcanic geochemical signatures. With increasing degree of silicification, volcanic phenocrysts and matrix material of Group 1 rocks were replaced to yield Group 2 rocks with transitional geochemical signatures, and some preserved volcanic textures, but where >50 % of the sample has been significantly replaced by silica-phases. In the most silicified rocks (Group 3), all volcanic material is completely replaced by silica-phases and samples possess a seawater-like REE pattern. In Group 3 rocks, high-field strength and other immobile elements such as Al_2O_3, TiO_2, and Zr have also been removed from the system. In this setting, felsic volcanic rocks similar to those of Groups 1 and 2 were completely replaced by microcrystalline quartz ± hematite, and magnetite. This type of alteration is similar to that seen at other with VMS deposits (Leistel et al., 1998).

IMPLICATIONS FOR GEOCHEMICAL FINGERPRINTS OF CHERT

Previous studies (e.g., Bau, 1993; Lawrence and Kamber, 2006) have used REE signatures as a tool by which to identify rocks formed by chemical precipitation from seawater and/or mixed hydrothermal fluids. Such geochemical fingerprints have also been used to identify chemical sedimentary protoliths in high-grade metamorphic rocks (Mojzsis et al., 1996; Mojzsis et al., 2002; Lepland et al., 2002; Cates and Mojzsis, 2007; Dauphas et al., 2007a, 2007b; O'Neil et al., 2007; Craddock and Dauphas, 2011; Mloszewska et al., 2012) where textural evidence for the origin of the rocks has been obliterated. Here we infer that Group 3 jaspilite samples preserved in the HMG formed via silicification of primary volcanic phases in volcanic edifice rocks in a collapsing caldera system. As a result of silicification, these rocks possess the geochemical "fingerprints" of seawater and mixed hydrothermal fluids that drove the replacement process. If, in the absence of textural evidence, a seawater-like REE pattern alone is considered diagnostic of a chemical sedimentary origin, the Group 3 jaspilite rocks would be misclassified as chemical sediments. Because both silicified rocks, like Group 3 jaspilite samples in this study, and chemical sediments are preserved in greenstone belts around the world, a simple bulk rock geochemical REE fingerprint cannot be diagnostic of origin. Instead, without textural evidence to support origin via chemical sedimentation, versus replacement silicification,

the bulk rock REE signature can only provide direct evidence for seawater/hydrothermal fluid involvement at some point during the evolution of the rock.

We have demonstrated that rocks other than those formed from chemical precipitation possess seawater-like REE signatures, and, therefore, the use of a diagnostic fingerprint for the genesis of a particular rock where textural evidence is lacking should be approached with caution. Overall, the results of our study illustrate the complication of using REE proxies alone for establishing a chemical sedimentary origin for any particular lithology, particularly in the case of identifying a sedimentary protolith in highly deformed, metamorphosed, and metasomatized terranes.

CONCLUSIONS

- We divided rocks of the ~2.72 Ga Hunter Mine Group into three groups based on mineralogy and texture that include volcanic rocks (Group 1), altered volcanic rocks (Group 2) and jaspilite rocks (Group 3).

- Petrographic evidence suggests silicification of volcanic rocks (Group 1) produced transitional altered volcanic rocks (Group 2), and jaspilite rocks (Group 3).

- Major, trace- and rare-earth element mobility occurred during the process of silicification, where volcanic rocks with less alteration (Group 1) had different geochemical signatures than those that were moderately silicified (Group 2), or intensely silicified (Group 3).

- During the process of silicification, jaspilite rocks (Group 3) acquired the rare-earth element geochemical signatures of seawater precipitates.

- Because intensely silicified rocks possess seawater-like rare-earth element characteristics, caution must be exercised when interpreting the geochemical information preserved in altered rocks where original genesis is unknown.

LIST OF REFERENCES

Bau, M. and Möller, P., 1993. Rare earth element systematics of the chemically precipitated component in Early Precambrian iron formations and the evolution of the terrestrial atmosphere-hydrosphere-lithosphere system. Geochimica et Cosmochimica Acta, 57: 2239-2249.

Bau, M., 1996. Controls on the fractionation of isovalent trace elements in magmatic and aqueous systems: evidence from Y/Ho, Zr/Hf, and lanthanide tetrad effect. Contributions to Mineralogy and Petrology, 123: 323-333.

Bekker, A., Slack, J.F., Planavsky, N., Krapež, B., Hofmann, A., Konhauser, K.O., Rouxel, O.J., 2010. Iron Formation: The Sedimentary Product of a Complex Interplay among Mantle, Tectonic, Oceanic, and Biospheric Processes. Economic Geology, 105: 467-508.

Bolhar, R., Kamber, B., Moorbath, S., Fedo, C., and Whitehouse, M., 2004. Characterization of early Archean chemical sediments by trace element signatures: Earth and Planetary Science Letters, 222: 43-60.

Cates, N.L., Mojzsis, S.J., 2007. Pre-3750 Ma supracrustal rocks from the Nuvvuagittuq supracrustal belt, northern Québec. Earth and Planetary Science Letters, 255: 9–21.

Chown, E.H., N'dah, E., Mueller, W.U., 2000. The relation between iron-formation and low temperature hydrothermal alteration in an Archean volcanic environment. Precambrian Research, 101: 263-275.

Condie, K.C., 1993. Chemical composition and evolution of the upper continental crust: Contrasting results from surface samples and shales. Chemical Geology, 104: 1-37.

Craddock, P.R., Dauphas, N., 2011. Iron and carbon isotope evidence for microbial iron respiration throughout the Archean. Earth and Planetary Science Letters, 303: 121-132.

Danielson, A., Moller, P., Dulski, P., 1992. The europium anomalies in banded iron formations and the thermal history of the oceanic crust. Chemical Geology, 97: 89-100.

Dauphas, N., van Zuilen, M., Busigny, V., Lepland, A., Wadhwa, M., Janney, P.E., 2007a. Iron isotope, major and trace element characterization of early Archean supracrustal rocks from SW Greenland: protolith identification and metamorphic overprint. Geochimica et Cosmochimica Acta 71, 4745–4770.

Dauphas, N., Cates, N.L., Mojzsis, S.J., Busigny, V., 2007b. Identification of chemical sedimentary protoliths using iron isotopes in the >3750 Ma Nuvvuagittuq supracrustal belt, Canada. Earth and Planetary Science Letters, 254, 358–376.

Doyle, M.G., Huston, D.L., 1999. The Subsea-Floor Replacement Origin of the Ordovician Highway-Reward Volcanic-Associated Massive Sulfide Deposit, Mount Windsor Subprovince, Australia. Economic Geology, 94: 825-844.

Duchac, K.C., and Hanor, J.S., 1990. Origin and timing of the metasomatic silicification of an Early Archean komatiite sequence, Barberton Mountain Land, South Africa. Precambrian Research, 37: 125-146.

Fryer, B.J., 1977. Rare earth evidence in iron formations for changing Precambrian oxidation states. Geochimica et Cosmochimica Acta, 41: 361-367.

Galley, A.G., Watkinson, D.H., Jonasson, I.R., Riverin, G., 1995. The Subsea-Floor Formation of Volcnai-Hostred Massive Sulfide: Evidence from the Ansil Deposit, Rouyn-Noranda, Canada. Economic Geology, 90: 2006-2017.

Hofmann, A., 2005. The geochemistry of sedimetnary rocks from the Fig Tree Group, Barberton greenstone belt: Implications for tectonic, hydrothermal, and surface processes during mid-Archean times. Precambrian Research, 143: 23-49.

Hofmann, A., and Bolhar, R., 2007. Carbonaceous cherts in the Barberton greenstone belt and their significance for the study of early life in the Archean record. Astrobiology, 7: 355-388.

Hofmann, A., Harris, C., 2008. Silica alteration zones in the Barberton greenstone belt: A window into subseafloor processes 3.5–3.3 Ga ago. Chemical Geology, 257: 221-239.

Hovellmann, J., Putnis, A., Giesler, T., Schmidt, B.C., Golla-Schindler, U., 2010. The replacement of plagioclase feldspars by albite: observations from hydrothermal experiments. Contributions to Mineral Petrology. 159: 43-49.

Huston, D.L., Logan, G.A., 2004. Barite, BIFs and bugs: evidence for the evolution of the Earth's early hydrosphere. Earth and Planetary Science Letters, 220: 41-55.

Kamber, B.S., Webb, G.E., 2001. The geochemistry of late Archaean microbial carbonate: implications for ocean chemistry and continental erosion history. Geochimica et Cosmochimica Acta, 65: 2509-2525.

Kamber, B.S., 2009. Geochecmial fingerprinting: 40 years of analytical development and real world applications. Applied Geochemistry. 24: 1074-1086.

Kimberley, M.M., 1979. Geochemical distinctions among environmental types of iron formations. Chemcial Geology, 25: 185-212.

Kimberley, M.M., 1989. Exhalative Origins of Iron formations. Ore Geology Reviews, 5: 13-145.

Klein, C., 2005. Some Precambrian banded iron-formations (BIFs) from around the world: Their age, geologic setting, mineralogy, metamorphism, geochemistry, and origins. American Mineralogist, 90: 1473-1499.

Lawrence, M.G., Kamber, B.S., 2006. The behaviour of the rare earth elements during estuarine mixing – revisited. Marine Chemistry, 100: 147-161.

Lepland, A., Arrhenius, G., Cornell, D., 2002. Apatite in early Archean Isua supracrustal rocks, southern West Greenland: its origin, association with graphite and potential as a biomarker. Precambrian Research, 118: 221-241.

Leistel, J.M., Marcoux, E., Deschamps, Y., 1998. Chert in the Iberian Pyrite Belt. Mineralium Deposita. 33: 59-81.

Lowe, D.R., 1994. Chapter 4, Archean Greenstone-Related Sedimentary Rocks, in: Condie, K.C. (Ed.), Developments in Precambrian Geology, Elsevier, 121-169.

Lowe, D.R., 1999. Petrology and sedimentology of cherts and related silicified sedimentary rocks in the Swaziland Supergroup. Geological Society of America Bulletin, 329: 83–114.

Maslennikov, V.V., Ayupova, N.R., Herrington, R.J., Danyushevsky, L.V., Large, R.R., Ferruginous and manganiferous haloes around massive sulphide deposits of the Urals. Ore Geology Reviews. 47: 5-41.

Mloszewska, A.M., Pecoits, E., Cates, N.L., Mojzsis, S.J., O'Neil, J., Robbins, L.J., Konhauser, K.O., 2012. The composition of Earth's oldest iron formations: The Nuvvuagittuq Supracrustal Belt (Quebec, Canada). Earth and Planetary Science Letters, 317: 331-342.

Mojzsis, S., Arrhenius, G., McKeegan, K., Harrison, T., Nutman, A., and Friend, C., 1996. Evidence for life on Earth before 3,800 million years ago, Nature, 384: 55-59.

Mojzsis, S.J., Harrison, T.M., 2002. Origin and Significance of Archean Quartzose Rocks at Akilia, Greenland. Science, 298: 917a.

Mueller, W.U., Mortensen, J.K., 2002. Age constraints and characteristics of subaqueous volcanic construction, the Archean Hunter Mine Group, Abitibi greenstone belt. Precambrian Research, 115: 119-152.

Mueller, W.U., Stix, J., Corcoran, P.L., Daigneault, R., 2009. Subaqueous calderas in the Archean Abitibi greenstone belt: An overview and new ideas. Ore Geology Reviews, 35: 4-46.

O'Neil, J., Maurice, C., Stevenson, R.K., Larocque, J., Cloquet, C., David, J., Francis, D., 2007. The Geology of the 3.8 Ga Nuvvuagittuq (Porpoise Cove) Greenstone Belt, Northeastern Superior Province, Canada. Developments in Precambrian Geology, 15: 219–250.

Orberger, B., Rouchon, V., Westall, F., de Vries, S.T., Pinti, D.L., Wagner, C., Wirth, R., Hashizume, K., 2006. Microfacies and origin of some Archean cherts (Pilbara, Australia). Geological Society of America Special Papers, 405: 133-156.

Paris, I., Stanistreet, I.G., Hughes, M.J., 1985. Cherts of the Barberton greenstone belt interpreted as products of submarine exhalative activity. Journal of Geology, 93: 11-129.

Putnis, A., 2002. Mineral replcaement reactions: from macroscopci observations to microscopic mechansims. Mnieralogical Magazine, 66: 689-708.

Siever, R., 1992. The silica cycle in the Precambrian. Geochimica et Cosmochimica Acta, 56: 3265-3272.

Thurston, P.C., Ayer, J.A., Goutier, J., Hamilton, M.A., 2008. Depositional Gaps in Abitibi Greenstone Belt Stratigraphy: A Key to Exploration for Syngenetic Mineralization. Economic Geology, 103: 1097-1134.

Van den Boorn, S.H.J.M., van Bergen, M.J., Nijman, W., Vroon, P.Z., 2007. Dual role of seawater and hydrothermal fluids in Early Archean chert formation: Evidence from silicon isotopes. Geology, 35: 939-942.

Van den Boorn, S.H.J.M., van Bergen, M.J., Vroon, P.Z., de Vries, S.T., Nijman, W., 2010. Silicon isotope and trace element constraints on the origin of ~3.5 Ga cherts: Implications for Early Archean marine environments. Geochimica et Cosmochimica Acta, 74: 1077-1103.

Van Lente, B., Ashwal, L.D., Pandit, M.K., Bowring, S.A., Torsvik, T.H., 2009. Neoproterozoic hydrotheramlly altered basaltic rocks from Rajasthan, nrothwest India: Implications for late Precabmrain tectonic evolution of the Aravalli Craton. Precambrian Research, 170: 202-222.

APPENDIX A-2

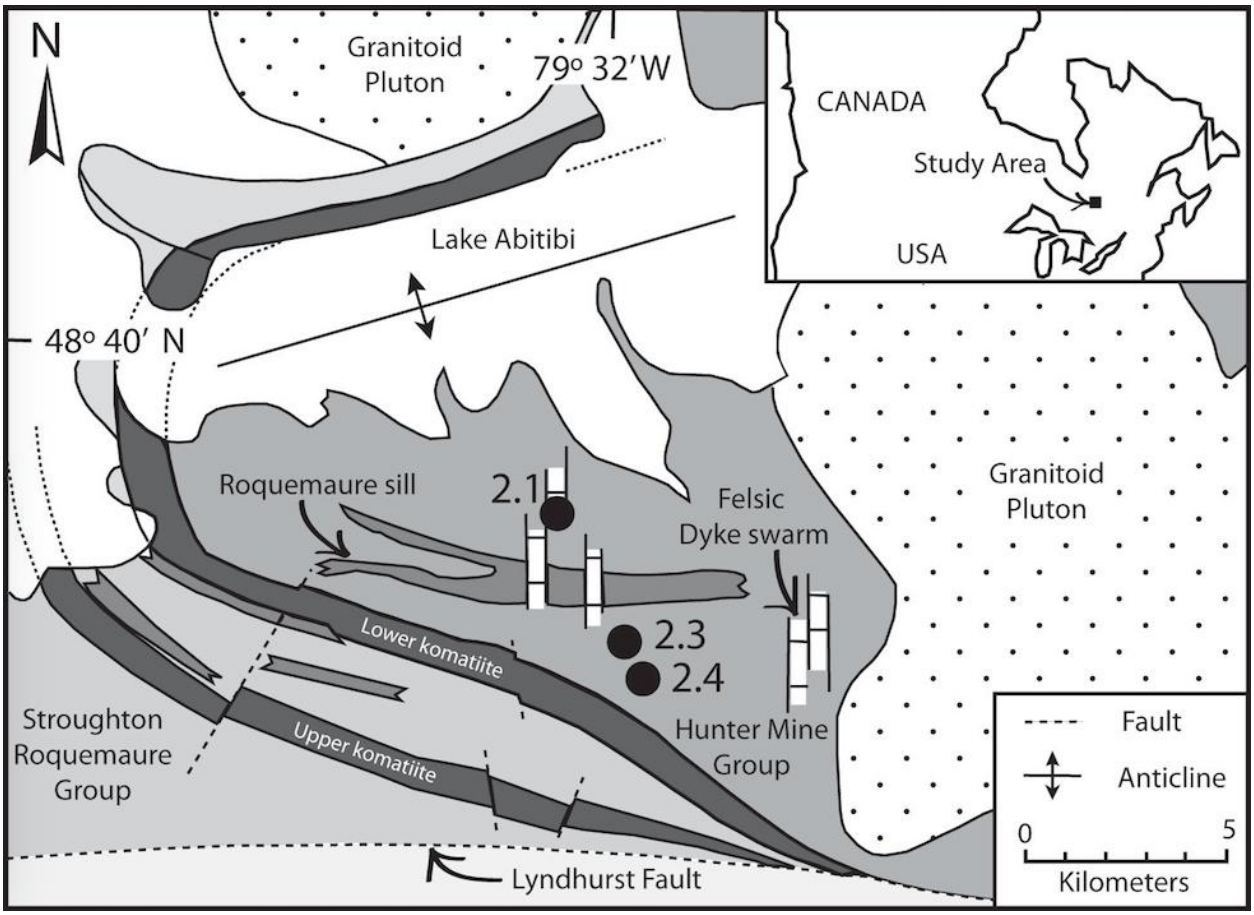


Figure 2-1. Geologic map of Hunter Mine Group region, of the Abitibi Greenstone Belt, with an inset showing the location of the greenstone belt in Canada. Samples in this study come from outcrops labeled 2.1, 2.3, and 2.4. Modified from Dostal and Mueller, (2012).

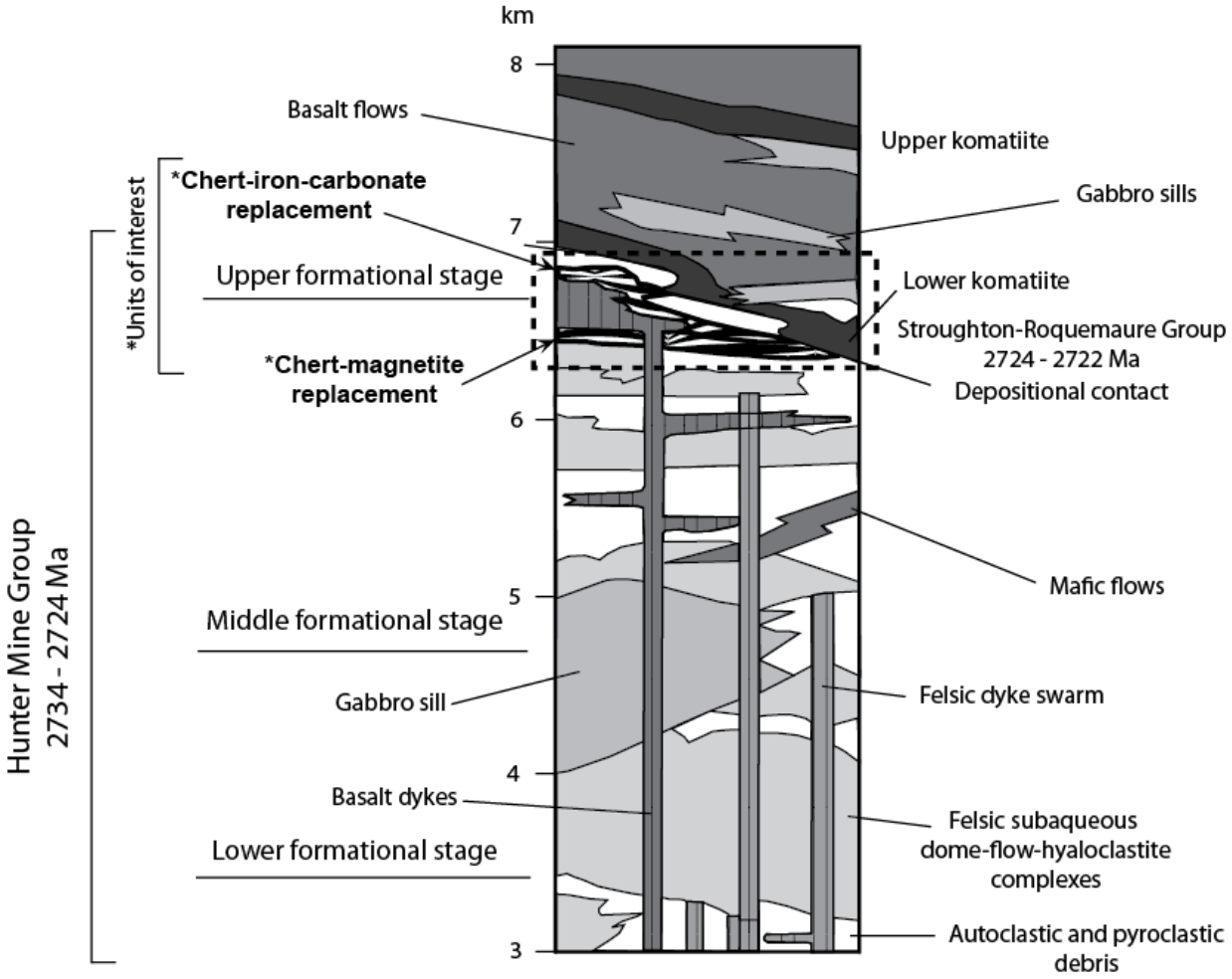


Figure 2-2. Representative stratigraphic column of the Hunter Mine Group. All samples from this study were collected near the contact between the middle and upper formational stages. Modified from Mueller and Mortensen (2002). Star (*) denotes units of interest to this study.

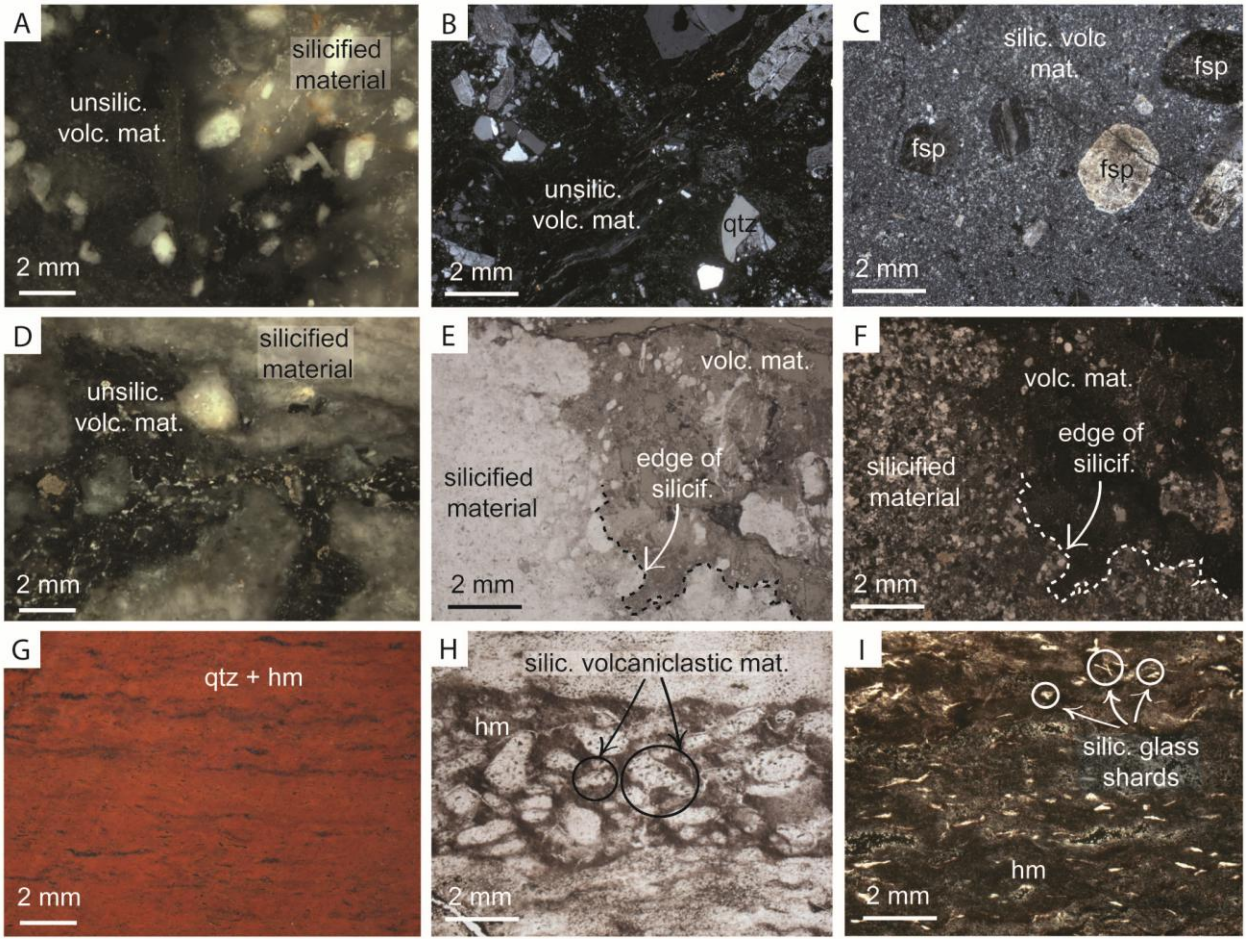


Figure 2-3. Incident light photographs, and plane and cross-polarized light photomicrographs of representative samples from Group 1, 2, and 3 rocks. (A) Incident light photograph documenting diffuse boundary between silicified and un-silicified volcanic material in Group 1 sample AB-11-11. (B) Cross-polarized light photomicrograph showing igneous quartz and feldspar phenocrysts surrounded by un-silicified volcanic matrix material in Group 1 sample AB-11-11. (C) Cross-polarized light photomicrograph showing preservation of primary igneous phenocrysts despite incipient silicification of matrix material in Group 1 sample AB-11-11. (D) Incident light photograph documenting diffuse nature of silicification in progressively altered Group 2 rocks (Sample AB-11-12). (E) Plane-polarized light photomicrograph of Group 2 sample AB-11-12 showing silicified material, and clear volcaniclastic material that passes through the edge of silicification from un-silicified volcanic matrix material indicating a replacement origin for the silicification, rather than a chemical sedimentation origin. (F) Cross-polarized light photomicrograph of (E). (G) Incident light photomicrograph showing only faint textural heterogeneity in some jaspilite Group 3 samples. (H) Plane-polarized light image showing textural evidence of silicified volcaniclastic material that is now compositionally hematite (hm) and quartz in representative Group 3 sample AB-11-23. (I) Plane-polarized light image showing preservation of pronged glass shards enveloped in a quartz and hematite matrix in representative Group 3 sample AB-11-19.

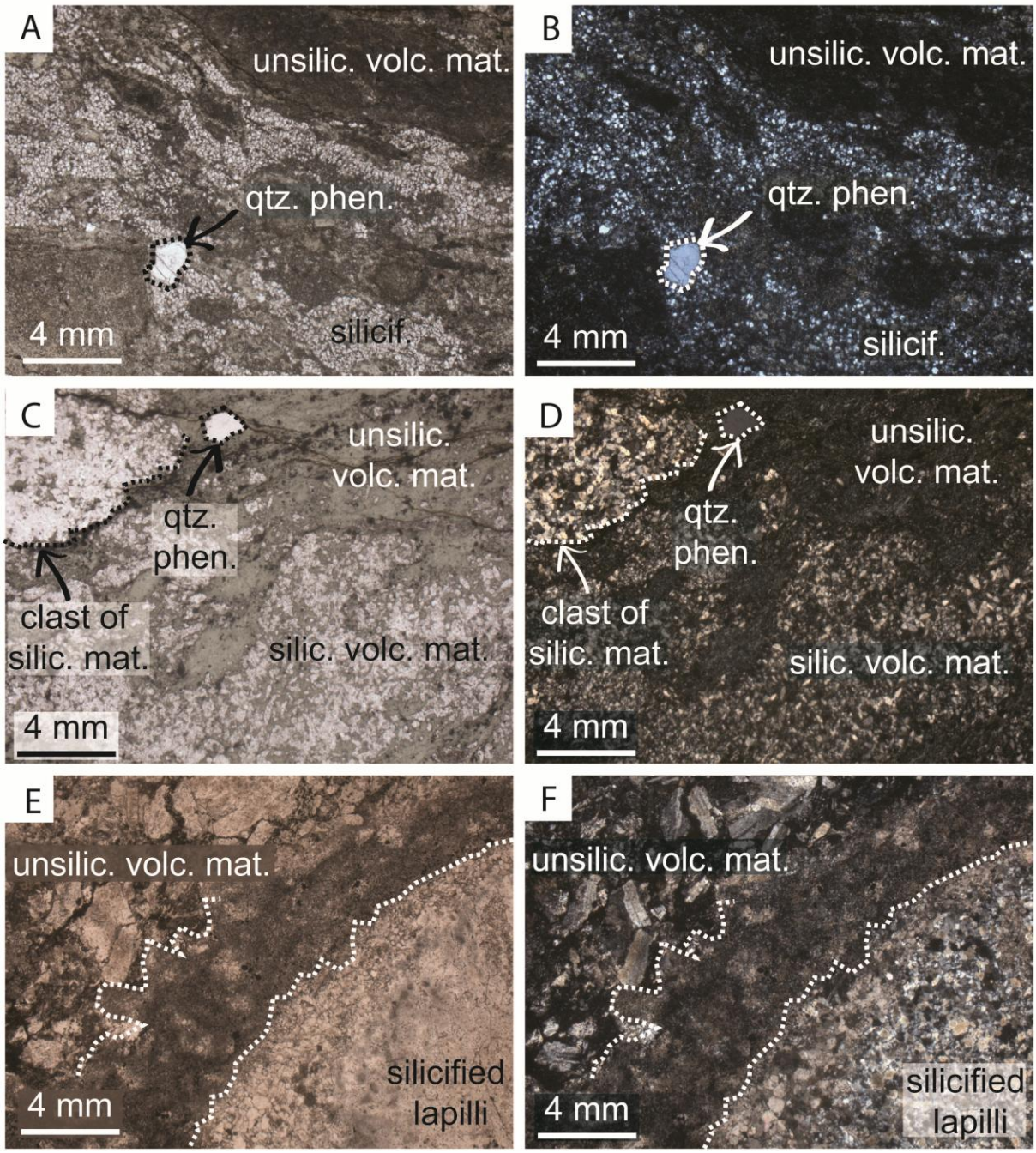


Figure 2-4. Plane-polarized light and cross-polarized light images of representative Group 2 altered volcanic rock samples. (A) Plane-polarized light image showing an example of discontinuous silicification and preservation of un-silicified volcanic matrix material and quartz phenocryst. (B) Cross-polarized light image of (A). (C) Plane-polarized light image showing an example of discontinuous silicification and preservation of quartz phenocryst and original volcanic matrix material, as well as preservation of a clast of similar silicified material. (D) Cross-polarized light image of (C). Plane-polarized light image showing un-silicified volcaniclastic matrix material, and a silicified armored lapilli. (F) Cross-polarized light image of (E).

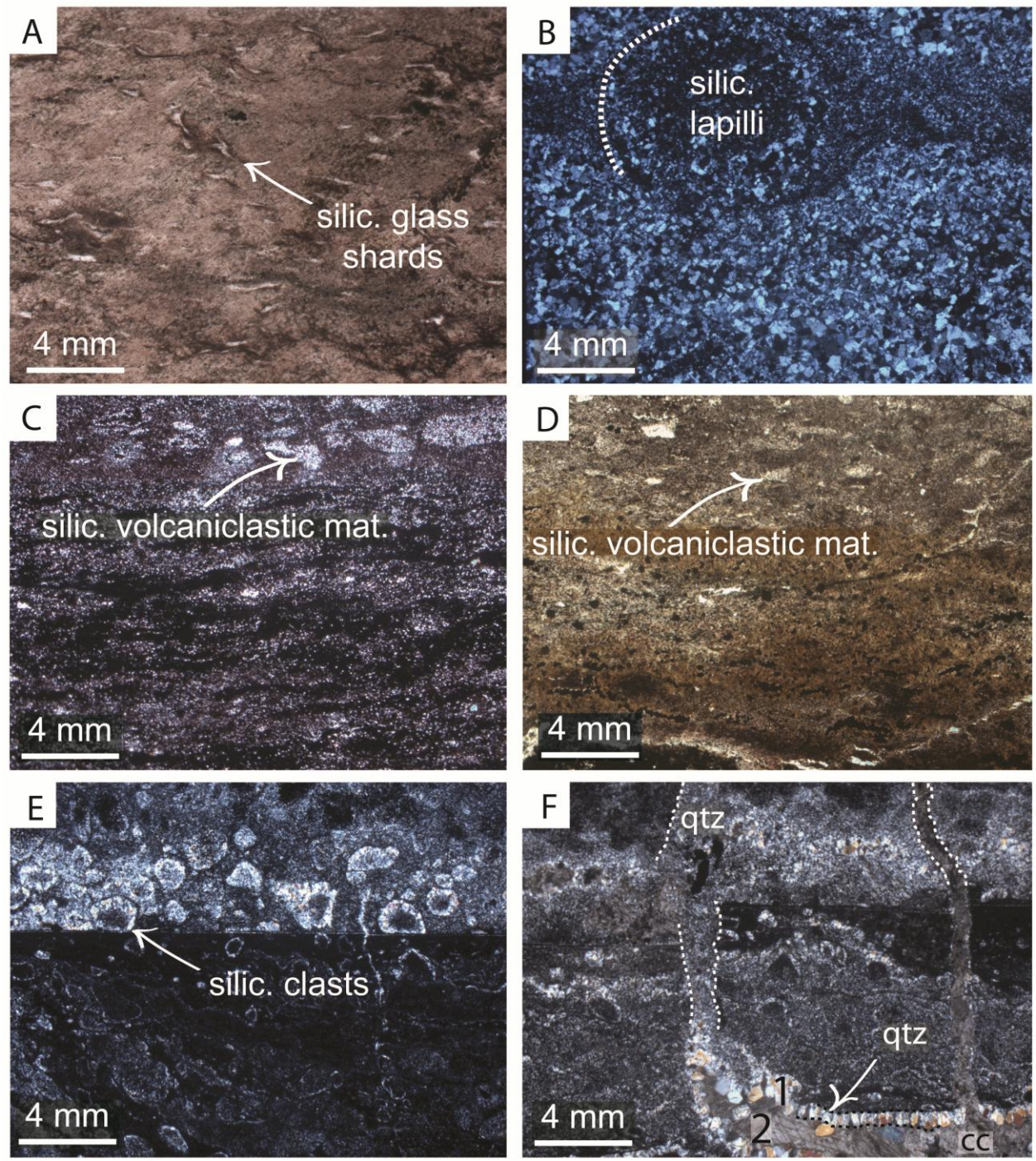


Figure 2-5. Plane-polarized light and cross-polarized light images of representative Group 3 jaspilite samples. (A) Plane-polarized light image showing preservation of glass shards. (B) Cross-polarized light image showing preservation of lapilli, now completely compositionally replaced by micro-crystalline quartz. (C) Plane-polarized light image showing volcaniclastic material now compositionally replaced by quartz and surrounded by hematite. (D) Same as (C). (E) Cross-polarized light image showing clastic textures preserved in the jaspilite, now compositionally entirely made of quartz. (F) Evidence of quartz and calcite veining.

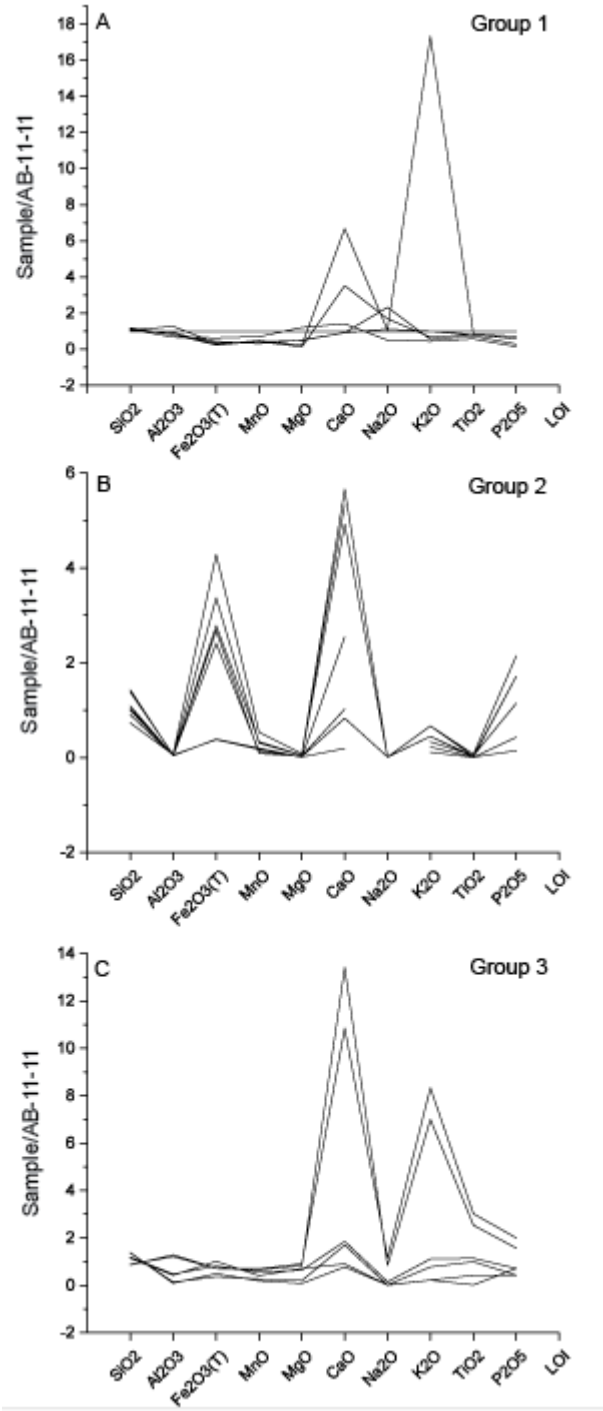


Figure 2-6. (A) Major element oxide plot of Group 1 samples normalized to least altered volcanic rock sample from Group 1, AB-11-11. (B) Major element oxide plot of Group 2 samples normalized to least altered volcanic rock sample from Group 1, AB-11-11. (C) Major element oxide plot of Group 3 samples normalized to least altered volcanic rock sample from Group 1, AB-11-11.

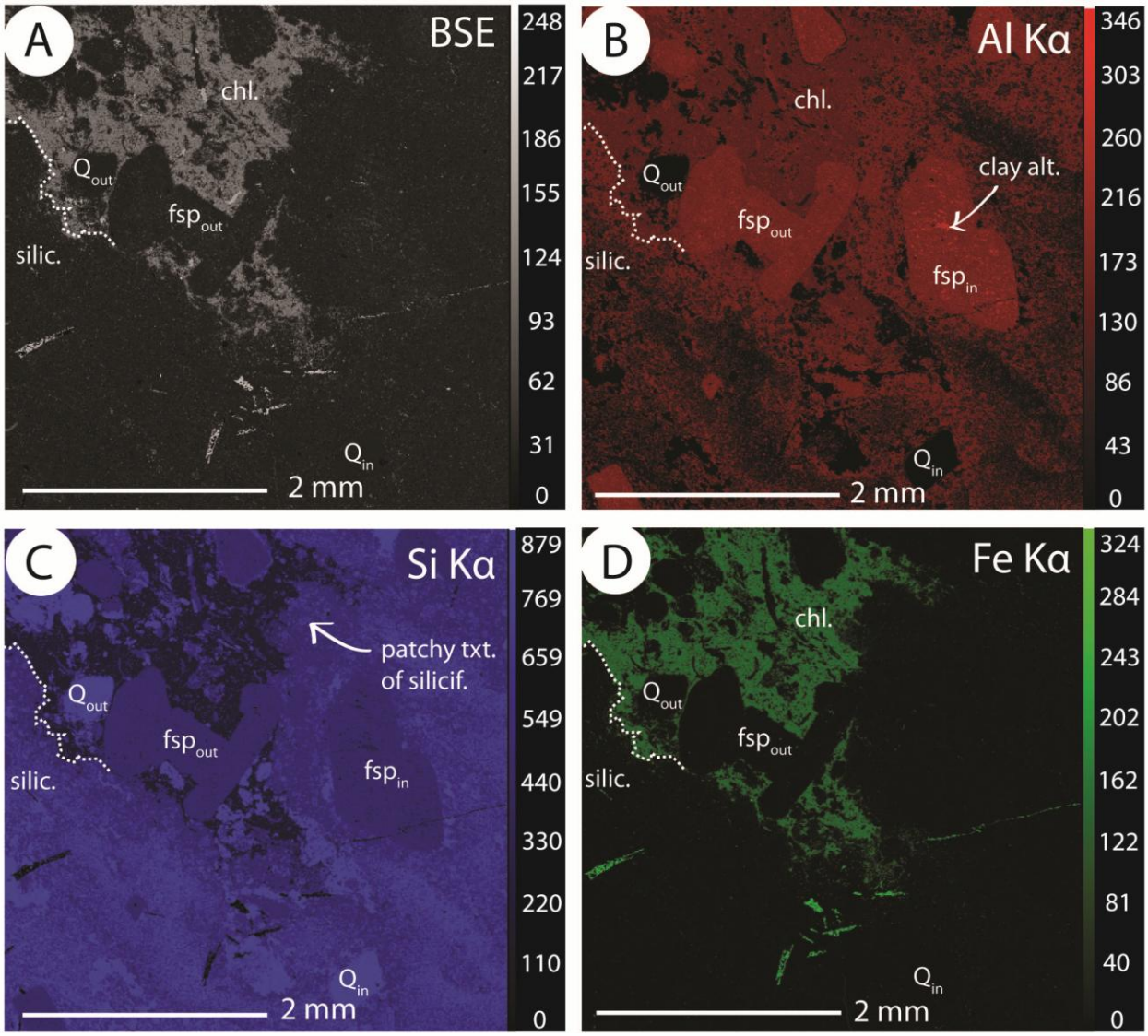


Figure 2-7. Elemental X-ray maps for representative Group 1 felsic volcanic rock sample AB-11-11. (A) Backscatter electron image of volcanic rock sample showing preservation of quartz and feldspar phenocrysts, both inside (Q_{in}) and outside (Q_{out}, and fsp_{out}) of the silicified areas which are surrounded by a chloritic matrix. (B) Aluminum Kα x-ray map showing the non-uniform nature of incipient silicification is representative group 1 sample. (C) Silica Kα x-ray map showing preservation of phenocrysts inside the silicification patch, as well as documenting the compositional heterogeneities inside the silicification patch. (D) Iron Kα x-ray map showing Fe-rich composition of chloritic matrix material.

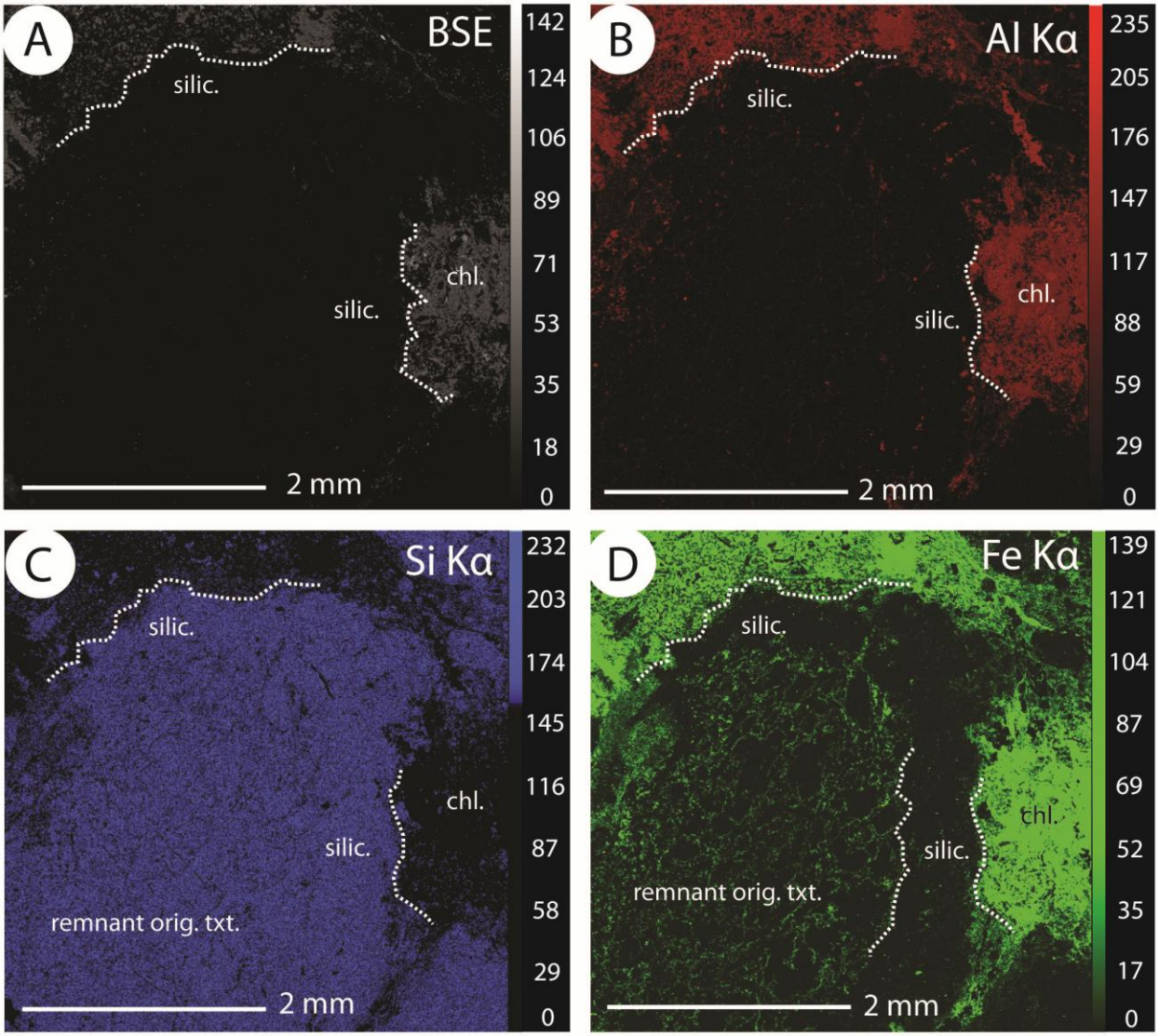


Figure 2-8. Elemental X-ray maps for representative Group 2 altered volcanic rock sample AB-11-12. (A) Backscatter electron image of volcanic rock sample showing silicified areas surrounded by a chloritic matrix. (B) Aluminum Kα x-ray map showing silicified areas surrounded by a chloritic matrix. (C) Silica Kα x-ray map showing silicified areas surrounded by a chloritic matrix, and documenting minor compositional heterogeneities inside the silicification patch. (D) Iron Kα x-ray map highlighting compositional heterogeneities and potential preservation of remnant original volcanic textures inside of the silicification patch.

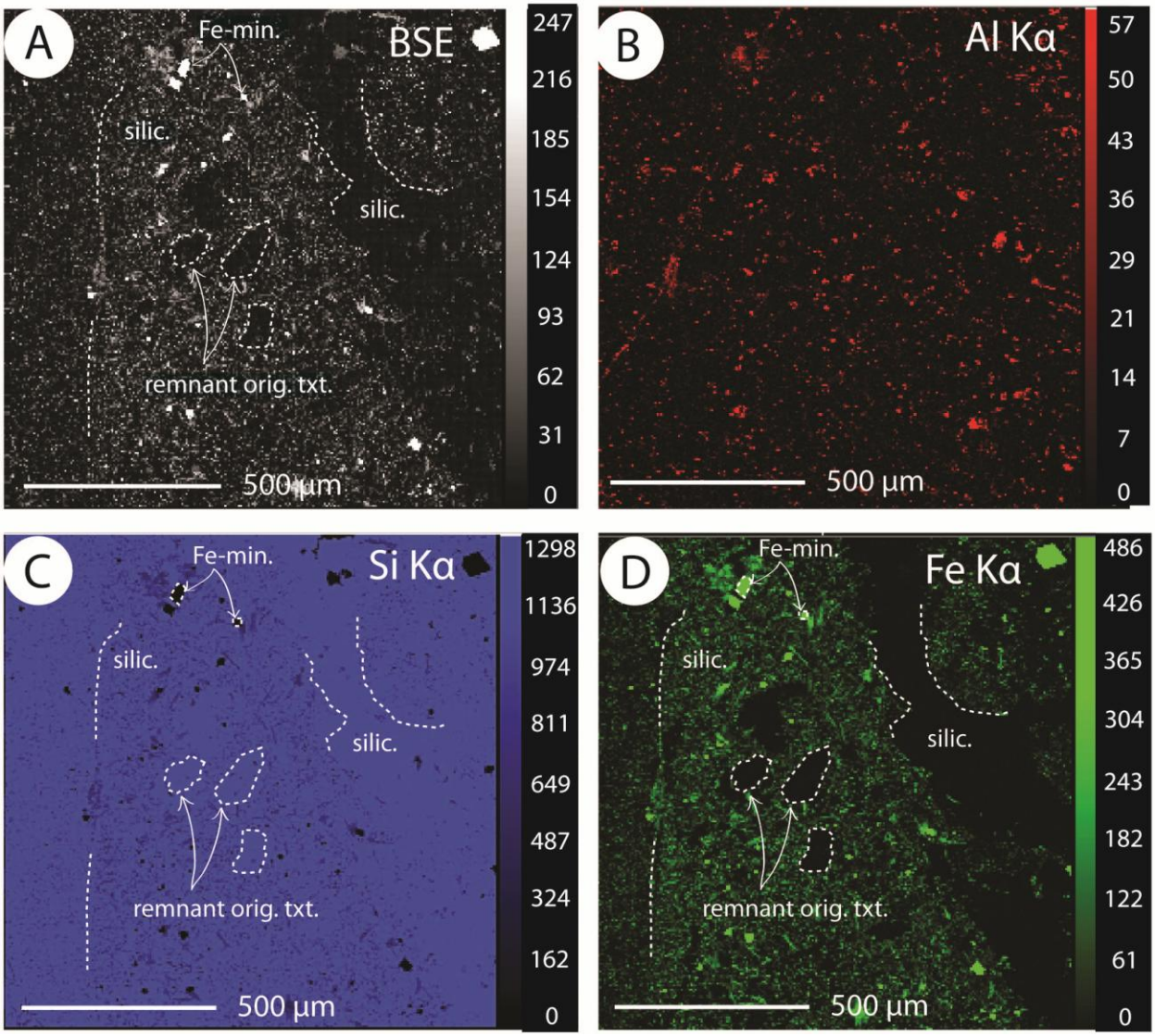
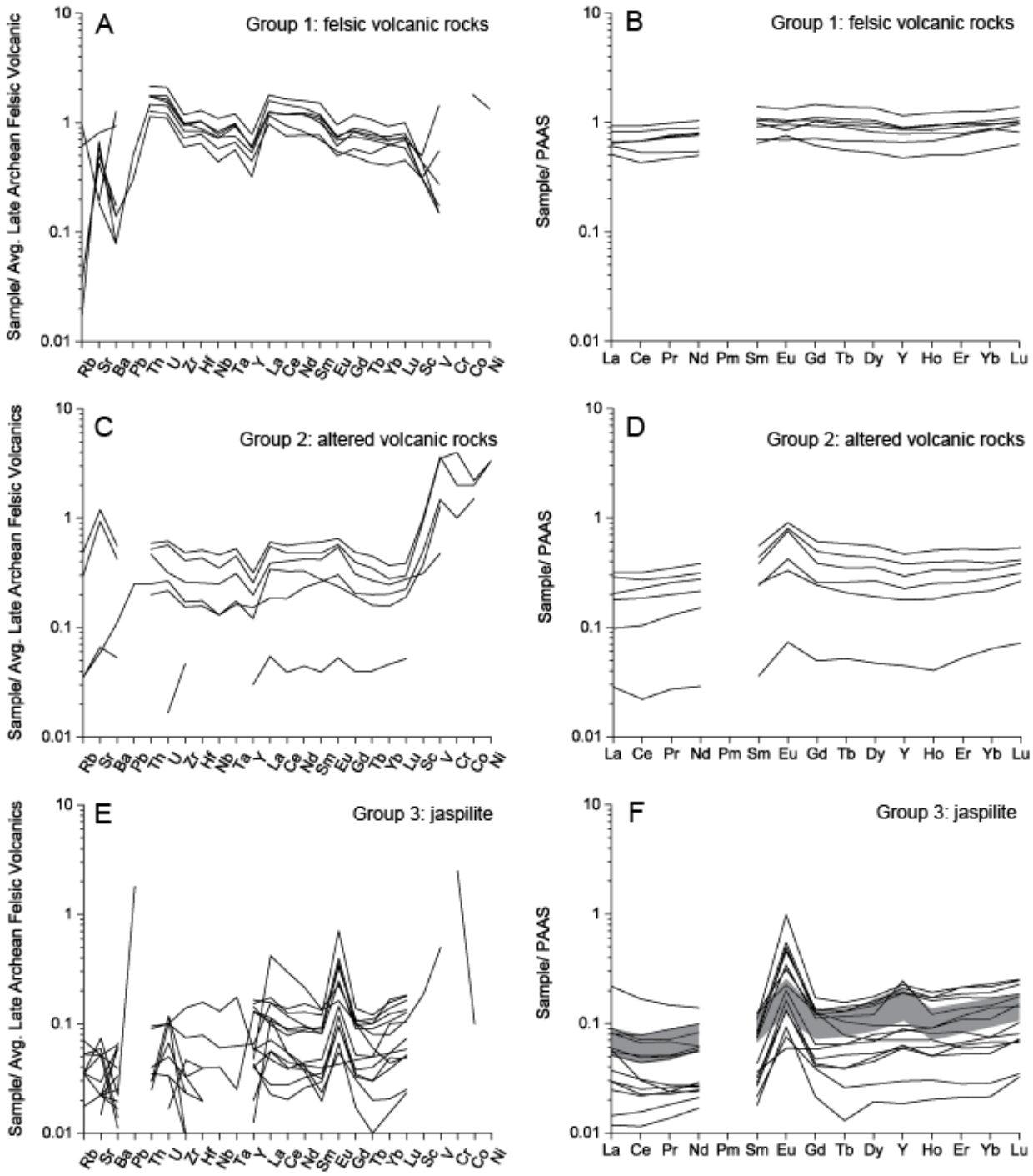


Figure 2-9. Elemental X-ray maps for representative Group 3 jaspilite rock sample AB-11-23. (A) Backscatter electron image of jaspilite rock sample showing silicified and iron-mineralized areas. (B) Aluminum Kα x-ray map showing silicified and iron-mineralized areas. (C) Silica Kα x-ray map showing silicified and iron-mineralized areas, potential preservation of remnant clastic textures. (D) Iron Kα x-ray map highlighting compositional heterogeneities in silicified and iron-mineralized areas, and potential preservation of remnant clastic textures.

Figure 2-10. (A) Spider plot of Group 1 samples normalized to average late Archean felsic volcanic rocks (Condie, 1993). (B) Rare earth element plot of Group 1 samples normalized to post Archean average shale composite. (C) Spider plot of Group 2 samples normalized to average late Archean felsic volcanic rocks (Condie, 1993). (D) Rare earth element plot of Group 2 samples normalized to post Archean average shale composite. Denotations mark important geochemical features of seawater as defined in the text. (E) Spider plot of Group 3 samples normalized to average late Archean felsic volcanic rocks (Condie, 1993). (F) Rare earth element plot of Group 3 samples normalized to Post Archean Average Shale composite. La_{SN}/La_{SN}^* and Eu_{SN}/Eu_{SN}^* mark important geochemical features of seawater as defined in the text, equations can be found in Lawrence and Kamber, 2006. Shaded area denotes typical pattern for Precambrian seawater.


A
Group 1: felsic volcanic rocks
Sample/ Avg. Late Archean Felsic Volcanic
B
Group 1: felsic volcanic rocks
Sample/ PAAS
C
Group 2: altered volcanic rocks
Sample/ Avg. Late Archean Felsic Volcanics
D
Group 2: altered volcanic rocks
Sample/ PAAS
E
Group 3: jaspilite
Sample/ Avg. Late Archean Felsic Volcanics
F
Group 3: jaspilite
Sample/ PAAS
10
1
0.1
0.01
Rb Sr Ba Pb Th U Zr Hf Nb Ta Y La Ce Nd Sm Eu Gd Tb Dy Ho Er Yb Lu V Cr Co Ni
La Ce Pr Nd Pm Sm Eu Gd Tb Dy Y Ho Er Yb Lu

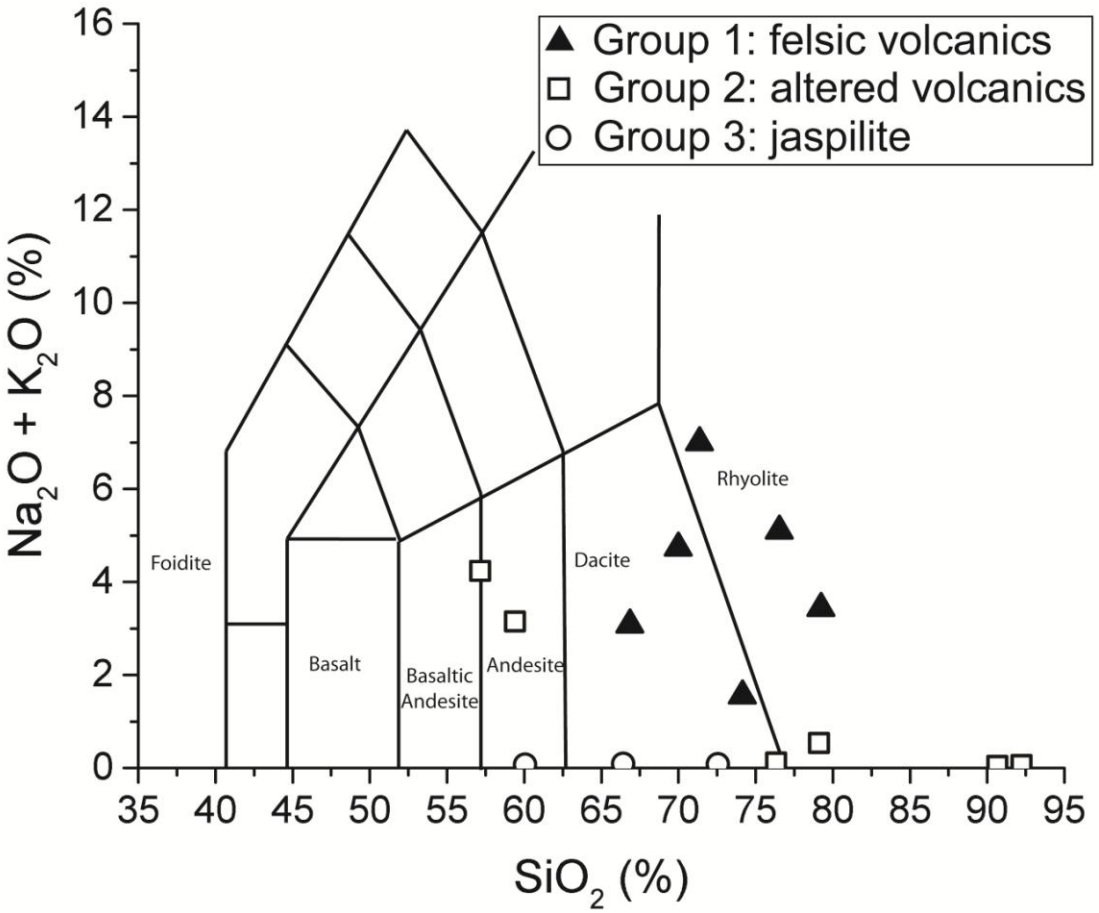


Figure 2-11. Total alkali silica (TAS) plot of Group 1, 2, and 3 samples.

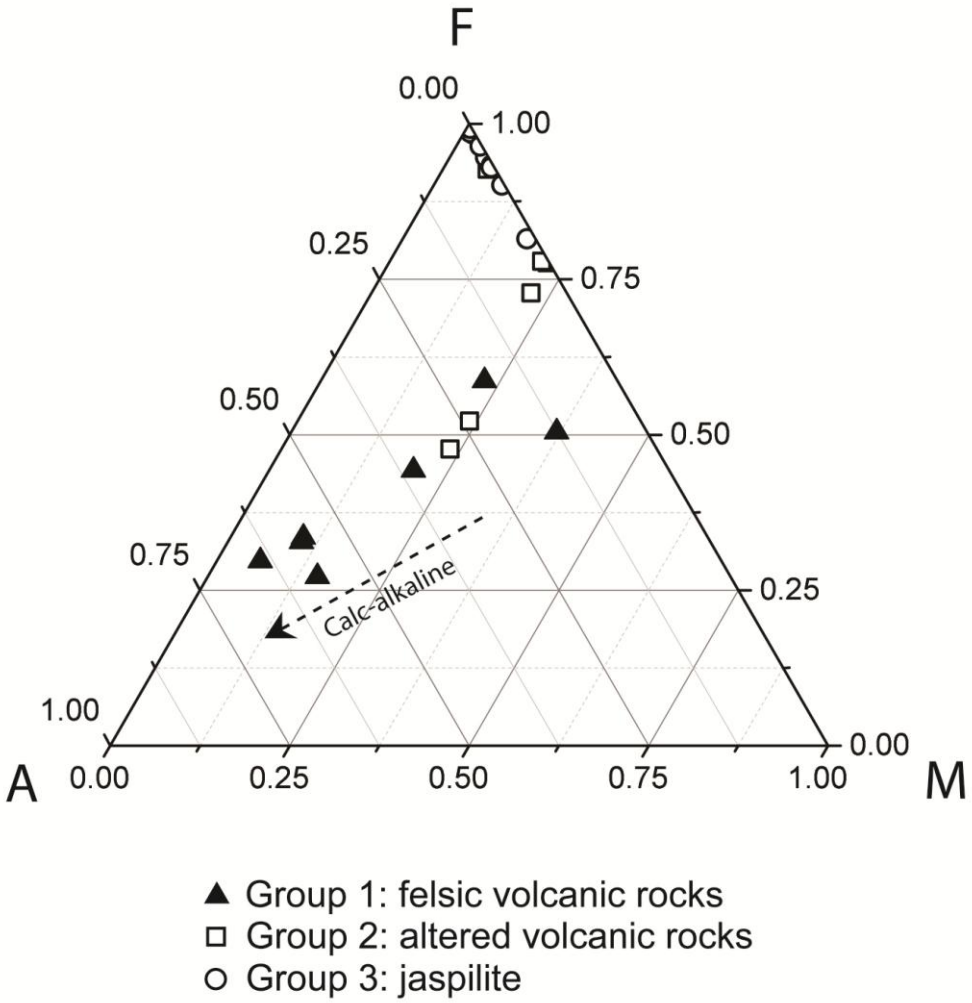


Figure 2-12. Traditional AFM volcanic discrimination diagram of group 1, 2, and 3 samples. Note the trend from groups 1 – 3 documenting Fe addition, and loss of other elements during the silicification process. Calc-alkaline volcanic trend marked for reference.

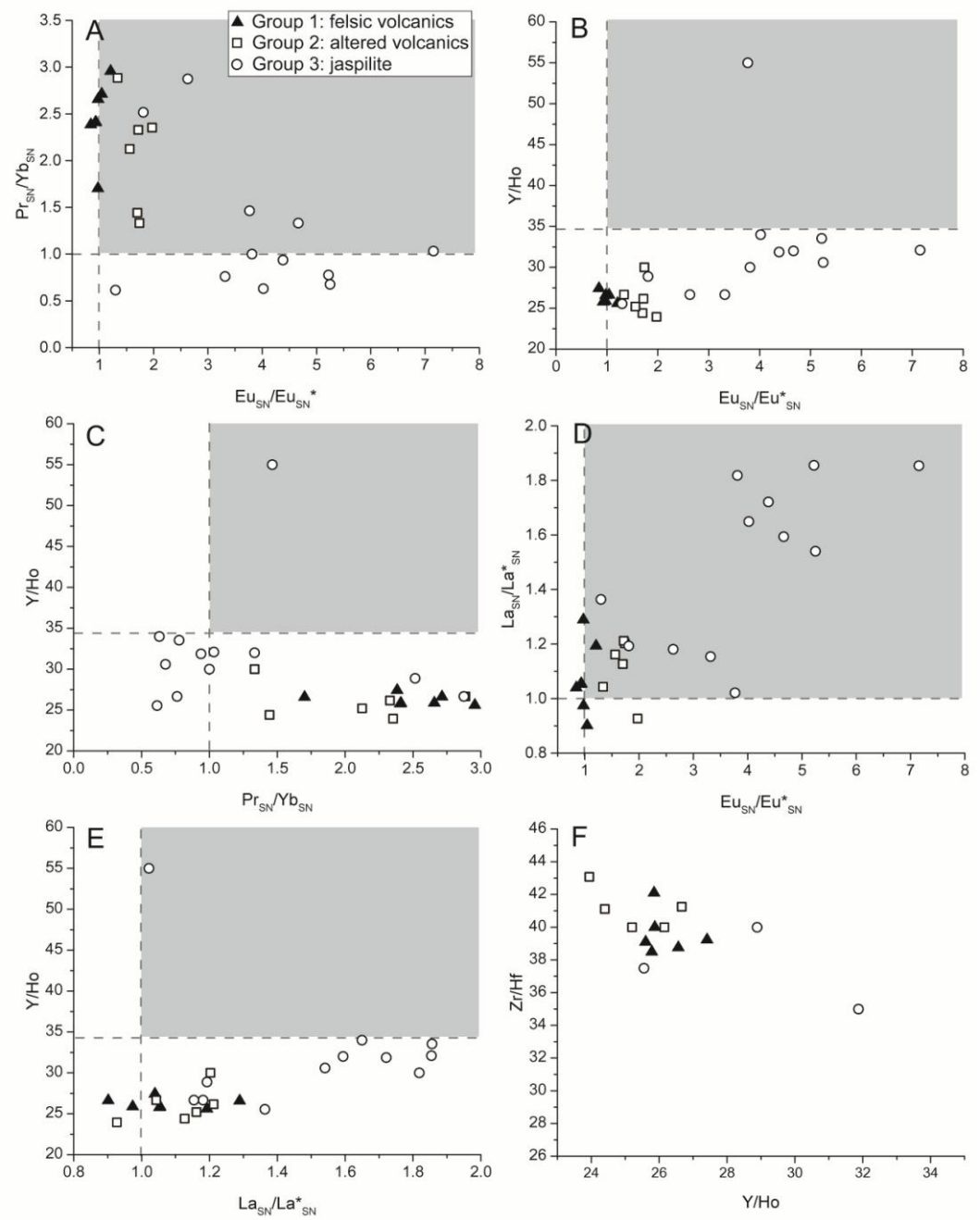


Figure 2-13. REE comparison plots for Group 1 (filled triangles), Group 2 (open squares), and Group 3 (open circles) samples. Grey shaded area indicates "seawater" signature. Note separation of Group 1 from Group 3 samples in plots A-E. (A) Plot showing slope (Pr_{SN}/Yb_{SN}) verses Europium anomaly (Eu_{SN}/Eu_{SN}*). (B) Plot showing Y/Ho verses Europium anomaly (Eu_{SN}/Eu_{SN}*). (C) Plot showing Y/Ho verses slope (Pr_{SN}/Yb_{SN}). (D) Plot showing Lanthanum anomaly (La_{SN}/La_{SN}*) verses Europium anomaly (Eu_{SN}/Eu_{SN}*). (E) Plot showing Y/Ho verses Lanthanum anomaly (La_{SN}/La_{SN}*). (F) Plot showing Y/Ho verses Zr/Hf. All samples fall within range expected for igneous rocks (24 < Y/Ho < 34, and 26 < Zr/Hf <46).

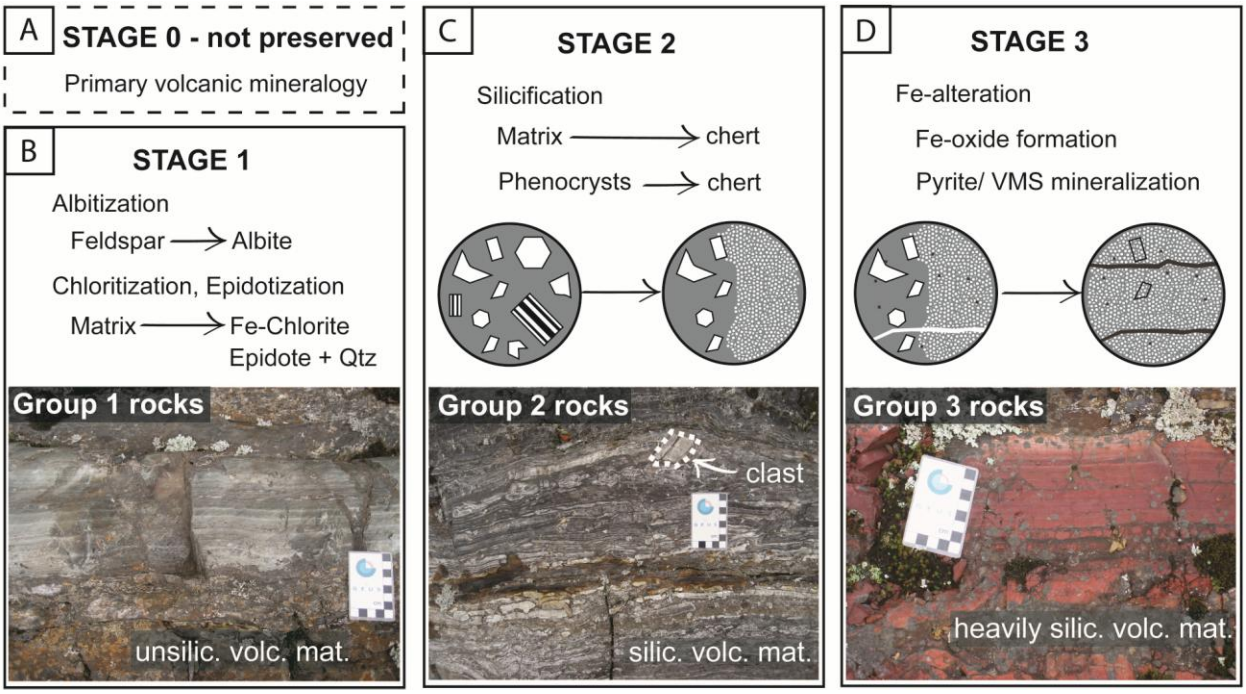


Figure 2-14. Schematic diagram showing stages of alteration for Group 1 , 2 and 3 samples. (A) Represents stage 0 where no alteration has occurred, and primary volcanic mineralogy is preserved. (B) Represents stage 1 of alteration, where albitization, chloritization, and epidotization of primary volcanic material occur. Incident light photograph is of representative Group 1 sample (AB-11-11), showing preservation of volcanic material and incipient stages of silicification marked by the presence of quartz patches (white areas) (C) Represents stage 2 of alteration, which is characterized by silicification of both volcanic matrix, and phenocrystic material. Incident light photograph is of representative Group 2 sample (AB-11-12), showing silicification lenses (white areas), and preservation of volcanic material in between (green areas). (D) Represents stage 3 of alteration, which is characterized by further silicification and Fe-alteration, resulting in the formation of Fe-oxides, and pyrite during VMS-style mineralization. Incident light photograph is of representative Group 3 sample (AB-11-23), showing silicified and Fe-altered areas.

CHAPTER III

MICRO-SCALE SILICON ISOTOPE HETEROGENEITY OBSERVED IN >3.7 Ga HYDROTHERMAL QUARTZ PRECIPITATES: IMPLICATIONS FOR INTERPRETING THE δ^{30}Si RECORD OF CHERT

This chapter was taken from a manuscript currently in review in the journal *Terra Nova*:

Brengman, L.A., Fedo, C.M., Whitehouse, M. J., 2015, **Extreme micro-scale silicon isotope heterogeneity observed in >3.7 Ga hydrothermal quartz precipitates: implications for interpreting the δ^{30}Si record of chert.**

ABSTRACT

We present silicon isotope compositions of quartz crystals measured by secondary ion mass spectrometry (SIMS) from three rock types, (quartz-cement, and amygdules within brecciated pillow basalt, chert, and chert clasts), thought to represent quartz precipitation under hydrothermal conditions from the >3.7 Ga Isua Greenstone Belt, SW Greenland. Although chert, chert clasts, and quartz cement have overlapping δ^{30}Si values, δ^{30}Si values of quartz amygdules span nearly the entire known range previously measured for quartz precipitates. This extreme heterogeneity does not result from metamorphism. Instead we suggest the heterogeneity derives from primary kinetic isotope fractionation during quartz precipitation under disequilibrium conditions in a hydrothermal setting. We infer that heterogeneity in the compiled δ^{30}Si record of chert can be explained if samples were to be separated on the basis of geologic context.

INTRODUCTION

Previous studies (e.g., Robert and Chaussidon, 2006) of Precambrian chert and banded iron formation (BIF) have identified a trend toward heavier silicon isotope values through time (Fig. 3-1A). This trend has been attributed to either gradual cooling of the oceans (Robert and Chaussidon, 2006) or mixing between hydrothermal and continental silica input (Chakrabarti et al., 2012; Heck et al., 2011). For either interpretation to be valid, each must overcome significant concerns. First, interpreting silicon isotope values obtained from chert, regardless of chert type, fundamentally assumes that all siliceous marine rocks originated under the same geochemical conditions, even though deposition occurs in a variety of settings (Kimberley, 1979). Second, simple source mixing between hydrothermal and continental silicon pools (Marin-Carbonne et al., 2014) assumes that the values and contributions of each are known, and unchanging over geologic time. These two problems preclude the possibility of developing a simple, unified interpretation a temporal trend in the silicon isotope archive of chert and BIF.

Most silicon isotope investigations (e.g., Marin-Carbonne et al., 2012, 2014; Chakrabarti et al., 2012; Delvigne et al., 2012; Steinhoefel et al., 2010) and experiments (Geilert et al., 2014; Appendix A-5, Fig. 5-1, 5-2, 5-3) have focused on chert hypothesized to form through progressive recrystallization and maturation of low-temperature amorphous opal-A, to opal-CT, to micro-quartz (<20 μm), to mega-quartz (>20 μm) (e.g. Calvert, 1977 and references therein; Marin-Carbonne 2014). Fewer studies have focused on chert formed in hydrothermal systems (van den Boorn 2007, 2010; André et al., 2006), where direct precipitation of quartz from hydrothermal fluids has been proposed (Calvert 1977; Knauth 1994), observed (Hopkinson, 1999), and experimentally demonstrated (Mackenzie and Gees, 1971; Oehler, 1976). In high-temperature seafloor hydrothermal systems, quartz precipitation occurs under disequilibrium conditions (Wells and Ghiorso, 1991), and silica-water reactions are governed by kinetics (Martin and Lowell, 2000). To date, no high-resolution silicon isotope studies of high-temperature hydrothermal quartz precipitates exist; consequently the sign and magnitude of any kinetic isotope effect (KIE) remains unknown. The purpose of this paper is to investigate the silicon isotope composition of hydrothermal quartz precipitates and to consider the effects of

kinetics on the silicon isotope system, as well as assess the potential impact these results have on interpreting the compiled silicon isotope record of Precambrian chert and BIF. To do this, we use secondary ion mass spectrometry (SIMS) to measure the $\delta^{30}Si$ composition of quartz amygdules and encasing quartz cement of a brecciated pillow basalt, and adjacent chert and chert clasts from the >3.7 Ga Isua Greenstone Belt (IGB), in SW Greenland (Fig. 3-2, 3-3).

METHODS

Centimeter-scale sample rock chips were embedded in epoxy along with quartz reference material (NBS-28 or an internal standard), polished to 1 μm, mapped using a petrographic microscope, and gold-coated (30 nm) prior to analysis. In-situ Si- and O-isotope measurements were made using a CAMECA-IMS 1280 SIMS instrument at the Swedish Museum of Natural History, Stockholm (NordSIMS facility). Silicon and oxygen isotope ratios were measured in separate analytical sessions. A $^{133}Cs^{+}$ primary beam (ca. 5nA for Si, 2.5 nA for O) with an incident energy of 20keV was used to sputter secondary ions from specifically targeted >20μm crystals. Sample charging was minimized by use of a low-energy normal-incidence electron gun. Secondary ions were measured at a mass resolution of 2,500 (M/ΔM) by multicollection on Faraday detectors attached to low-noise amplifiers housed in a thermally stabilized, evacuated chamber. The magnetic field was locked at high precision using an NMR field sensor. Fully automated analytical sessions regularly bracketed unknowns between reference analyses, and individual analyses comprised a pre-sputter to remove the Au coat, beam centering and 48 seconds (Si) and 64 seconds (O) of data acquisition. We report isotope values expressed in standard delta notation ($\delta^{H}X=[(^{H}X/^{L}X_{sample})/ (^{H}X/^{L}X_{standard})-1]x1000$, where H=heavy isotope, L=light isotope, and X=element measured). Corrections for instrumental mass fractionation were made using international standard NBS-28, with an accepted value of $\delta^{30}Si = 0$ ‰. External reproducibility (1σ) for $\delta^{30}Si$ of ± 0.16 ‰, and $\delta^{18}O$ of ± 0.46 ‰, was derived from bracketing NBS-28 analyses propagated onto within-run uncertainties.

GEOLOGIC CONTEXT OF SAMPLES AND QUARTZ PETROGRAPHY

Samples in this study include: (1) quartz-cement and quartz-amygdales within a basaltic pillow breccia, (2) bedded chert, and (3) chert clasts from a conglomerate. Detailed field relationships of samples in this study can be found in Fedo (2000), Appel et al. (2001), and Fedo et al. (2001). The pillow basalt unit occurs as centimeter-scale, quartz-amygdaloidal, brecciated basaltic pillow fragments encased by quartz "cement" (Fig. 3-2A). Fluid inclusions from quartz amygdules in this pillow breccia unit suggest that quartz could have formed during degassing in the initial eruption stages of the pillow basalt (Appel et al., 2001; Touret, 2003), precipitating from hydrothermal fluids, similar to other localities (Gibson et al., 1983). By contrast, encasing quartz cement (Fig. 3-2A) likely precipitated from mixed hydrothermal fluids and ambient seawater, after the pillow basalt had cooled sufficiently to fracture brittly. Recrystallized bedded chert occurs adjacent to the pillow breccia unit as centimeter-thick layers associated with banded amphibolite (Fig. 3-2C; Appel et al., 1998; Fedo, 2000; Fedo et al., 2001). A polymictic conglomerate unit (Fig. 3-2D) crops out nearby, and consists of gravel-sized clasts of recrystallized chert, amygdaloidal mafic volcanic rocks and dark schistose mafic volcanic rocks, set in a fine-grained biotite, garnet matrix (Fedo, 2000). Recrystallized chert clasts in the conglomerate likely represent pieces of bedded chert that have been eroded and re-deposited (Fedo, 2000). The chert clasts are mineralogically and texturally similar to pillow breccia cement and chert (Fedo, 2000).

Quartz crystals analyzed from all rocks in this study share similar textural characteristics. Crystals range from ~100 to 1000 μm, and generally show evidence for annealing, such as perfect 120° triple junctions (Fig. 3-2D-F). These features would be expected from the amphibolite-facies metamorphism that has affected the area (Rollinson, 2003). Amygdules commonly consist of polycrystalline quartz (Fig. 3-2D), though few amygdules are filled with single quartz crystals. Quartz crystals in the cement are texturally similar to those in amygdules (Fig. 3-2D), although smaller crystals form at the contact with the basalt. We analyzed individual quartz crystals in single and polycrystalline amygdules, and quartz cement across a distance of 2 millimeters from the brecciated basalt contact. For chert and chert clasts, we analyzed inclusion-free areas of single quartz crystals (Fig. 3-2E, F). Detailed petrographic descriptions of the pillow breccia sample can be found in Appel et al. (2001) and Touret (2003).

RESULTS

Silicon isotope composition

All silicon isotope values are reported in Tables 3-1, and 3-2 in Appendix A-5. Quartz crystals that comprise amygdules possess values depleted in ^{30}Si, ranging from $\delta^{30}Si_{amyg}$ = -5.09 to +0.2 ± 0.3 ‰ (Fig. 3-1B). Such values span nearly the entire known dynamic range for silicon isotopes (roughly -5 to +3 ‰). By contrast, encasing quartz cement, separated only by millimeters, has $\delta^{30}Si_{NBS-28}$ values that range from $\delta^{30}Si_{cem}$ = +0.01 to +0.83 ± 0.3 ‰ (Fig. 3-1B). Silicon isotope compositions do not systematically vary with amygdule or crystal size, morphology, or distance from the brecciated cement contact. Quartz crystals from the bedded chert, and the chert clast possess a much smaller range of values ($\delta^{30}Si_{chert}$ = -1.61 to +1.24 ± 0.3 ‰; $\delta^{30}Si_{clast}$ = -0.78 to -0.23 ± 0.3 ‰; Fig. 3-1B).

Oxygen isotope composition

Because of the heterogeneity of silicon isotope values in the pillow breccia sample, we measured the oxygen isotope composition of cement and amygdules to test if oxygen isotopes preserve similar-scale heterogeneity. Oxygen isotope compositions of quartz crystals in both amygdules and cement display relatively similar and uniform values, ranging from 16.81 to 18.02 ± 0.5 ‰ and 16.89 to 18.09 ± 0.5 ‰, respectively (Fig. 3-1C; Appendix A-5, Tables 3-1, 3-2). Such isotopic compositions lie within the expected range for metamorphosed quartz precipitates in the region ($\delta^{18}O_{chert}$ = 12.9-20.4 ‰; Perry et al., 1978; Gregory et al., 1989).

INTERPRETING SILICON ISOTOPES IN THE ROCK RECORD

Preservation potential of silicon isotope signatures

Previous studies (Marin-Carbonne et al., 2012; Marin-Carbonne et al., 2014) have used oxygen isotope compositions to determine the preservation state of chert and to infer the veracity of $\delta^{30}Si$ isotopes. Based on this screening method, a closed system, dissolution-precipitation model for equilibrium fractionation of oxygen and silicon isotopes has been developed to explain micro-scale heterogeneity in diagenetic chert formed from an original amorphous silica precursor (Marin-Carbonne and Chaussidon, 2012). If the $\delta^{30}Si$ heterogeneity measured in this study were the result of the above model, we would expect micro-scale $\delta^{18}O$ isotope heterogeneity to be preserved in the same sample.

In the pillow breccia studied here, oxygen isotopes of quartz from amygdules and cement display relatively similar, uniform values (Fig. 3-1C), yet silicon isotopes of the same crystals display substantial heterogeneity (nearly 6 ‰ range; Fig. 3-1C). Because oxygen isotope data are

homogeneous, the range of silicon isotope values measured in the pillow breccia cannot easily be explained by equilibrium fractionation of both isotopic systems during differential diagenetic transformations at the micrometer scale. Consistent with other $\delta^{18}O$ isotope studies of quartz (Perry et al., 1978; Gregory et al., 1989) we interpret the $\delta^{18}O$ values were homogenized during metamorphism. Such an interpretation is consistent with studies that suggest that oxygen diffuses faster than silicon in quartz (Cherniak, 2003).

Kinetic isotope effects in quartz precipitates

Because an equilibrium fractionation model does not fully explain decoupling of the oxygen and silicon isotope systems, here we consider a kinetic isotope fractionation model to explain the $\delta^{30}Si$ heterogeneity measured in this study. Kinetic processes often govern the precipitation of minerals from aqueous solutions (DePaolo, 2011). Consequently, kinetic isotope effects should be recorded in the precipitated phase. For comparison, experimental evidence and molecular dynamics simulations for calcium isotopes of calcite precipitated from solution (DePaolo, 2011; Hofmann et al., 2012) demonstrate that changes in precipitation rate result in differences in the observed magnitude of the fractionation factor (α), generating a large isotopic difference between the solution and the precipitate ($\Delta_{ppt\text{-}solution} = \delta_{ppt} - \delta_{soln}$). Under experimental conditions of rapid calcite precipitation, the system is in disequilibrium, and the light isotope preferentially incorporates into the precipitated phase (Tang et al., 2008; $\Delta^{44/40}Ca_{ppt\text{-}solution} < 0$; $\alpha < 1$). As the system approaches equilibrium, crystal growth rate slows, and the fractionation factor decreases (Tang et al., 2008; $\Delta^{44/40}Ca_{ppt\text{-}solution} \sim 0$; $\alpha \sim 1$). In the SiO_2 system, temperature and precipitation rate are directly linked (Rimstidt and Barnes, 1980) and, under hydrothermal conditions, disequilibrium conditions control quartz precipitation (Wells and Ghiorso, 1991). In this light, we propose that the $\delta^{30}Si$ values of the quartz amygdules within the pillow breccia result from kinetic fractionation during precipitation from hydrothermal fluids at different rates, rather than heterogeneous diagenetic recrystallization, which is consistent with experimental evidence for the Si system (Oelze et al., 2015).

Application of a kinetic model to understand $\delta^{30}Si$ micro-scale heterogeneity

In hydrothermal systems, experimental and field evidence suggests that a maximum rate of quartz precipitation occurs at temperatures near 230 ºC (Rimstidt and Barnes, 1980) in solutions with dissolved silicon concentrations ranging from 15-20 mM (Von Damm et al., 1985), similar to concentrations proposed for Archean seawater (Siever, 1992). Below 230 ºC, net quartz precipitation (reaction rate) decreases, and below 100 ºC, precipitation rates are extremely low, even under supersaturated conditions (Rimstidt and Barnes, 1980). In the temperature range allowing for rapid precipitation rates, (T > 230 ºC), we predict quartz precipitates would record a KIE ($\Delta^{30/28}Si_{ppt\text{-}solution} < 0$), where the magnitude of fractionation ($\alpha < 1$) should vary extensively under conditions of disequilibrium. By contrast, if the silica in solution precipitates at a slower rate (as is expected at lower temperatures) the system is more likely to be near equilibrium (Oelze et al., 2015), and the silicon isotope value of the precipitate is likely to more closely reflect source fluid or source rock.

Samples studied here represent different quartz types formed in an Eoarchean hydrothermal system (Fig. 3-4A; Appel et al., 2001). Vesicular pillow basalts likely formed on the Precambrian seafloor (Polat et al., 2003) where, during initial stages of cooling, quartz precipitated from silica-saturated hydrothermal fluids to fill vesicles and form quartz amygdules ("a" in Fig. 3-4B). Because this process likely occurred at high-temperatures, where rapid quartz

precipitation is possible, we interpret the ~6 ‰ range of negative isotope values measured in the quartz amygdules to result from KIEs. After the basalt cooled enough to brecciate (Fig. 3-4B), quartz precipitated around basalt fragments to form the cement ("c" in Fig. 3-4B). Because this process involved cooler seawater mixed with hydrothermal fluids, we interpret the much smaller, ~1 ‰ range of values measured in the quartz cement to be the result of slower quartz precipitation under lower-temperature conditions. As a result, δ^{30}Si values of cement could approximate those of the source fluid from which the quartz precipitated. This situation is also likely true for chert (and chert clasts; Fig. 3-4B), and provides an explanation for the difference in values observed between these types of quartz and the quartz amygdules. Future experimental studies focused on understanding the maximum fractionation factors achieved under these high-temperature conditions would help to clarify interpretations of the range of silicon isotope values observed in hydrothermal precipitates.

SIGNIFICANCE

In this paper, we demonstrate the potential importance of kinetic isotope effects in the precipitation of quartz under disequilibrium conditions in an Archean hydrothermal system. The kinetic model proposed here predicts and explains the occurrence of micro-scale δ^{30}Si heterogeneity in quartz precipitated from hydrothermal fluids. Because hydrothermal quartz precipitates in a system far from equilibrium, it forms under different geochemical conditions than quartz in shallow water cherts or diagenetic cherts hosted within carbonate successions. Therefore, we conclude that the geologic context of each chert sample should be evaluated in order to understand what information silicon isotopes record, and cherts formed under hydrothermal conditions, should be separated from those formed in other depositional settings. We finally suggest that the compiled silicon isotope archive should be separated by chert type in order to interpret any perceived temporal trends recorded in the δ^{30}Si record of chert.

ACKNOWLEDGMENTS

This work was funded by NASA grant EXOB08-0063 awarded to C. M. F., and student research grants awarded to L. A. B. from ExxonMobil, the Geological Society of America, the Sedimentary Division of GSA, and the Department of Earth and Planetary Sciences at the University of Tennessee. The NordSIMS facility is a joint Nordic infrastructure funded by the research funding agencies of Denmark, Norway and Sweden, the University of Iceland and the Geological Survey of Finland. We thank Ted Labotka for comments on a previous version of the manuscript.

LIST OF REFERENCES

Abraham, K., Hofmann, A., Foley, S.F., Cardinal, D., Harris, C., Barth, M.G., André, L., 2011, Coupled silicon-oxygen isotope fractionation traces Archean silicification, Earth and Planetary Science Letters, 301: 222-230.

André, L., Cardinal, D., Alleman, L.Y., Moorbath, S., 2006, Silicon isotopes in ~3.8 Ga West Greenland rocks as clues to the Eoarchaean supracrustal Si cycle, Earth and Planetary Science Letters, 245: 162-173.

Appel, P.W.U., Fedo, C.M., Moorbath, S., Myers, J.S., 1998, Recognizable primary volcanic and sedimetnary features in a low-strain domain of the highly deformed, oldest known (≈ 3.7 – 3.8 Gyr) Greenstone Belt, Isua, West Greenland, Terra Nova, 10: 57-62.

Appel, P.W.U., Rollinson, H.R., Touret, J.L.R., 2001, Remnants of an Early Archaean (>3.75 Ga) sea-floor, hydrothermal system in the Isua Greenstone Belt, Precambrian Research, 112: 27-49.

Calvert, S.E., 1977. Mineralogy of silica phases in deep-sea cherts and porcelanites. Phil. Trans. R. Soc. Lond A. 286: 239-252.

Chakrabarti, R., Knoll, A.H., Jacobsen, S. B., Fischer, W.W., 2012, Si isotope variability in Proterozoic cherts. Geochimica et Cosmochimica Acta, 91: 187-201.

Cherniak, D.J., 2003. Silicon self-diffusion in single-crystal natural quartz and feldspar, Earth and Planetary Science Letters, 214: 655-668.

De la Rocha, C.L., Brzezinski, M.A., DeNiro, M.J., 2000, A first look at the distribution of the stable isotopes of silicon in natural waters, Geochimica et Cosmochimica Acta, 64: 2467-2477.

Delstanche, S., Opfergelt, S., Cardinal D., Elsass, F., André L., Delvaux, B., 2009, Silicon isotopic fractionation during adsorption of aqueous monosilicic acid onto iron oxide, Geochimica et Cosmochimica Acta, 73: 923–934.

Delvigne, C., Cardinal, D., Hofmann, A., L. André, 2012, Stratigraphic changes of Ge/Si, REE + Y and silicon isotopes as insights into the deposition of a Mesoarchean banded iron formation, Earth and Planetary Science Letters, 355-356: 109-118.

DePaolo, D.J., 2011, Surface kinetic model for isotopic and trace element fractionation during precipitation of calcite from aqueous solutions, Geochimica et Cosmochimica Acta, 75: 1039-1056.

Ding, T., 1996, Silicon isotope geochemistry, Geological Publishing house, pp. 1-105.

Dove, P.M., Rimstidt, J.D., 1994, Silica-water interactions: In Reviews in Mineralogy, 29: 259-308.

Fan, H., Wen, H., Zhu, X., Hu, R., Tian, S., 2013, Hydrothermal activity during Ediacaran-Cambrian transition: Silicon isotopic evidence, Precambrian Research, 224: 23-35.

Fedo, C.M., 2000, Setting and origin for problematic rocks from the >3.7 Ga Isua Greenstone Belt, southern west Greenland: Earth's oldest coarse clastic sediments, Precambrian Research, 101: 69-78.

Fedo, C.M., Myers, J.S., Appel, P.W.U., 2001, Depositional setting and paleogeographic implications of earth's oldest supracrustal rocks, the >3.7 Ga Isua Greenstone belt, West Greenland, Sedimentary Geology, 141-142: 61-77.

Fitoussi, C., and Bourdon, B., 2012. Silicon Isotope Evidence Against an Enstatite Chondrite Earth, Science, 335: 1477-1480.

Gibson, H.L., Watkinson, D.H., Comba, C.D.A., 1983, Silicification: Hydrothermal Alteration in an Archean Geothermal System within the Amulet Rhyolite Formation, Noranda, Quebec, Economic Geology, 78: 954-971.

Gregory, R.T., Criss, R.E., Taylor, H.P., 1989, Oxygen isotope exchange kinetics of mineral pairs in closed and open systems: Applications to problems of hydrothermal alteration of igneous rocks and Precambrian iron formations, Chemical Geology, 75: 1-42.

Heck, P.R., Huberty, J.M., Kita, N.T., Ushikubo, T., Kozdon, R., Valley, J.W., 2011, SIMS analyses of silicon and oxygen isotope ratios for quartz from Archean and Paleoproterozoic banded iron formations, Geochimica et Cosmochimica Acta, 75: 5879-5891.

Hofmann, A.E., Bourg, I.C., DePaolo, D.J., 2012, Ion desolvation as a mechanism for kinetic isotope fractionation in aqueous systems, Proceedings of the National Academies, 109: 18689-18694.

Hopkinson, L., Roberts, S., Herrington, R., Wilkinson, J., 1999, Self-organization of submarine hydrothermal siliceous deposits: Evidence from the TAG hydrothermal mound, 26°N Mid-Atlantic Ridge, Geology, 26: 347-350.

Kamber, B.S., Webb, G.E., 2001, The geochemistry of late Archaean microbial carbonate: implications for ocean chemistry and continental erosion history, Geochimica et Cosmochimica Acta, 65: 2509-2525.

Kimberley, M.M., 1979, Geochemical distinctions among environmetal types of iron formations, Chemical Geology, 25: 185-212.

Knauth, L.P., Lowe, D.R., 2003, High Archean climatic temperature inferred from oxygen isotope geochemistry of cherts in the 3.5 Ga Swaziland Supergroup, South Africa, GSA Bulletin, 115: 566-580.

Knauth, L.P., 1994, Petrogenesis of chert: In Reviews in Mineralogy, 29: 233-256.

Mackenzie, F.T., Gees, R., 1971. Quartz: synthesis at Earth-surface conditions, Science, 173: 533–534.

Marin-Carbonne, J., Chaussidon, M., Robert, F., 2012, Micrometer-scale chemical and isotopic criteria (O and Si) on the origin and history of Precambrian cherts: Implications for paleo-temperature reconstructions, Geochimica et Cosmochimica Acta, 92: 129-147.

Marin-Carbonne, J., Robert, F., Chaussidon, M., 2014, The silicon and oxygen isotope compositions of Precambrian cherts: a record of oceanic paleo-temperatures? Precambrian Research, 247: 223-234.

Martin, J.T., and Lowell, R.P., 2000, Precipitation of quartz during high-temperature, fracture-controlled hydrothermal upflow at ocean ridges: Equilibrium verses linear kinetics, Journal of Geophysical Research, 105: 869-882.

Oehler, J.H., 1976, Hydrothermal crystallization of silica gel, Geological Society of America Bulletin, 87: 1143-1152.

Oelze, M., von Blanckenburg, F., Hoellen, D., Dietzel, M., Bouchez, J., 2014, Si stable isotope fractionation during adsorption and the competition between kinetic and equilibrium isotope fractionation: Implications for weathering systems, Chemical Geology, 380: 161-171.

Perry, E.,C, Ahmad, S.N., Swulius, T.M., 1978, The oxygen isotope composition of 3,800 m.y. Old Metamorphosed Chert and Iron Formation from Isukasia, West Greenland, The Journal of Geology, 86: 223-239.

Polat, A., Hofmann, A.W., Münker, C., Regelous, M, Appel, P.W.U., 2003, Contrasting geochemical patterns in the 3.7-3.8 Ga pillow basalt cores and rims, Isua Greenstone belt, Southwest Greenland: implications for postmagmatic alteration processes, Geochimica et Cosmochimica Acta, 67: 441-457.

Rimstidt, J.D., and Barnes, H.L., 1980, The kinetics of silica-water reactions, Geochimica et Cosmochimica Acta, 44: 1683-1699.

Robert, F., Chaussidon, M., 2006, A paleotemperature curve for the Precambrian oceans based on silicon isotopes in chert, Nature, 443: 969-972.

Rollinson, H., 2003, Metamorphic history suggested by garnet-growth chronologies in the Isua Greenstone Belt, West Greenland, Precambrian Research, 126: 181-196.

Siever, R., 1992, The silica cycle in the Precambrian, Geochimica et Cosmochimica Acta, 56: 3265-3272.

Steinhoefel, G., von Blanckenburg, F., Horn, I., Konhauser, K.O., Beukes, N.J., Gutzmer, J., 2010, Deciphering formation processes of banded iron formations from the Transvaal and the Hamersley successions by combined Si and Fe isotope analysis using UV femtosecond laser ablation, Geochimica et Cosmochimica Acta, 74: 2677-2696.

Tang, J., Dietzel, M., Bohm, F., Kohler, S.J., Eisonhauer, A., 2008, Sr2+/Ca2+ and 44Ca/4-Ca fractionation during inorganic calcite formation: II. Ca isotopes, Geochimica et Cosmochimica Acta, 72: 3733-3745.

Touret, J.J., 2003, Remnants of early Archaean hydrothermal methane and brines in pillow-breccia from the Isua Greenstone Belt, West Greenland, Precambrian Research, 126: 219-233.

Van den Boorn, S. H. J. M., van Bergen, M. J., Nijman, W., Vroon, P. Z., 2007, Dual Role of seawater and hydrothermal fluids in Early Archean chert formation: Evidence from silicon isotopes, Geology, 35: 939-942.

Van den Boorn, S.H.J.M., van Bergen, M.J., Vroon, P., de Vries, S.T., Nijman, W., 2010, Silicon isotope and trace element constraints on the origin of ~3.5 Ga cherts: Implications for Early Archaean marine environments, Geochimica et Cosmochimica Acta, 74: 1077-1103.

Von Damm, K.L., Bischoff, J.L., Rosenbauer, R.J., 1985, Quartz solubility in hydrothermal seawater: an experimental study and equation desecribing quartz solubility for up to 0.5M NaCl solutions, American Journal of Science, 291: 977-1007.

Wells, J.T., Ghiorso, M.S., 1991. Coupled fluid flow and reaction in mid-ocean ridge hydrothermal systems: The behavior of silica, Geochimica et Cosmochimica Acta, 55: 2467-2481.

APPENDIX A-3

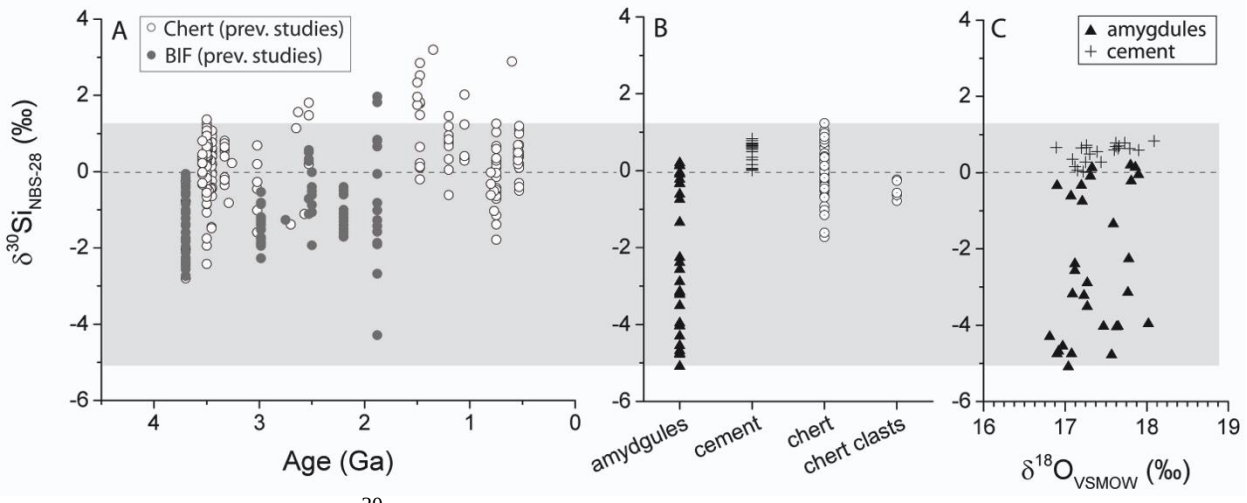


Figure 3-1. (A) Compiled $\delta^{30}Si$ data (in ‰, n = 288; Van den Boorn et al., 2007, Abraham et al., 2011, André et al., 2006, Van den Boorn et al., 2010, Heck et al., 2011, Steinhoefel et al., 2010, Chakrabarti et al., 2012, Delvigne et al., 2012, Marin-Carbonne et al., 2012, Fan et al., 2013) from inorganic (non-biological) chert, and banded iron formation (BIF). Data were compiled from bulk (MC-ICP-MS, IRMS) and high-spatial resolution (SIMS, femtosecond laser ablation) techniques. To be comparable, spot data for individual samples were converted to a single value via the method outlined in Marin-Carbonne et al., (2012). Note the slight increasing trend through time. A single anomalously heavy data point ($\delta^{30}Si$ = +5.2 at 1.7 Ga) was omitted. (B) Plot showing SIMS $\delta^{30}Si$ (‰) data of quartz amygdules and quartz cement from a brecciated pillow basalt, bedded chert and a chert clast. Note the overlap between cement and chert/chert clast, potentially suggestive of similar precipitation mechanisms. (C) Plot showing SIMS $\delta^{30}Si$ (‰) vs. $\delta^{18}O$ (‰) data of quartz cement and quartz amygdules within a single sample of basaltic breccia from the >3.7 Ga Isua Greenstone Belt. Oxygen isotope values range from $\delta^{18}O_{VSMOW}$ = 16.81 to 18.09 ± 0.5 ‰. However, $\delta^{30}Si$ from the same crystals show a large range of values from $\delta^{30}Si_{NBS-28}$ = -5.09 to 0.83 ± 0.3 ‰. The heterogeneity indicates that the silicon isotopes have not been completely reset, even though the oxygen isotopes have. Shaded area highlights the maximum and minimum of data from this study, and a dashed line through $\delta^{30}Si$ = 0 ‰ is shown for reference. Both scales extend through geologically relevant ranges of $\delta^{30}Si$ and $\delta^{18}O$.

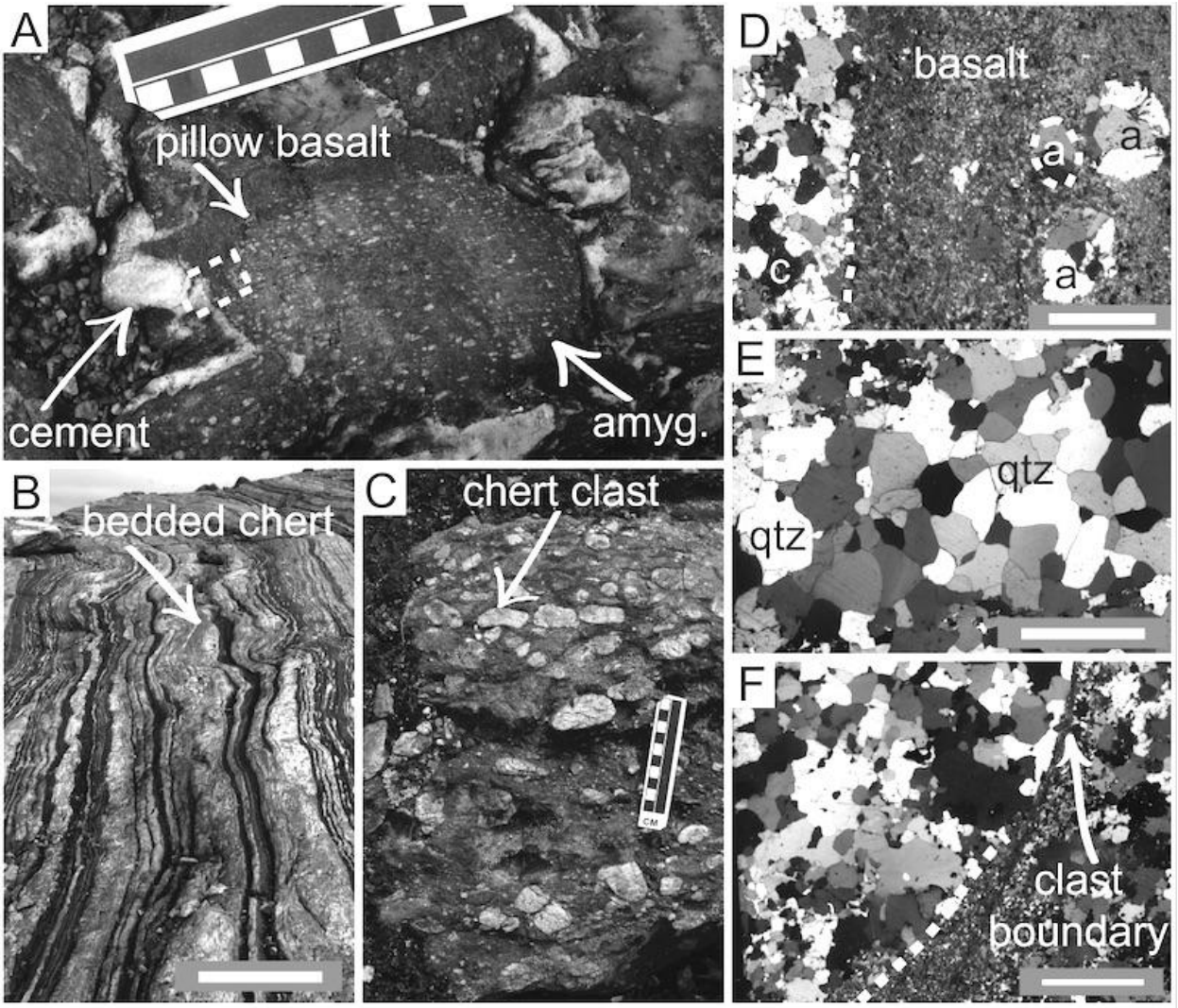


Figure 3-2. (A) Field photograph of quartz amygdaloidal, quartz-cemented pillow breccia from the >3.7 Ga Isua Greenstone Belt. Scale bar in cm. Dashed box shows the contact between cement and pillow fragment and outlines sample area used in this study. (B) Field photograph of bedded chert interlayered with amphibolite, adjacent to pillow breccia. Scale = 1.5 m. (C) Field photograph of the conglomerate unit showing chert clasts. Scale bar in cm. (D) Cross-polarized light image of quartz amygdules (a) and encasing quartz cement (c). Scale bar is 400 μm. (E) Cross-polarized light image of quartz crystals from bedded chert unit. Scale bar is 400 μm. (F) Cross-polarized light image of quartz crystals of chert clast. Scale bar is 500 μm.

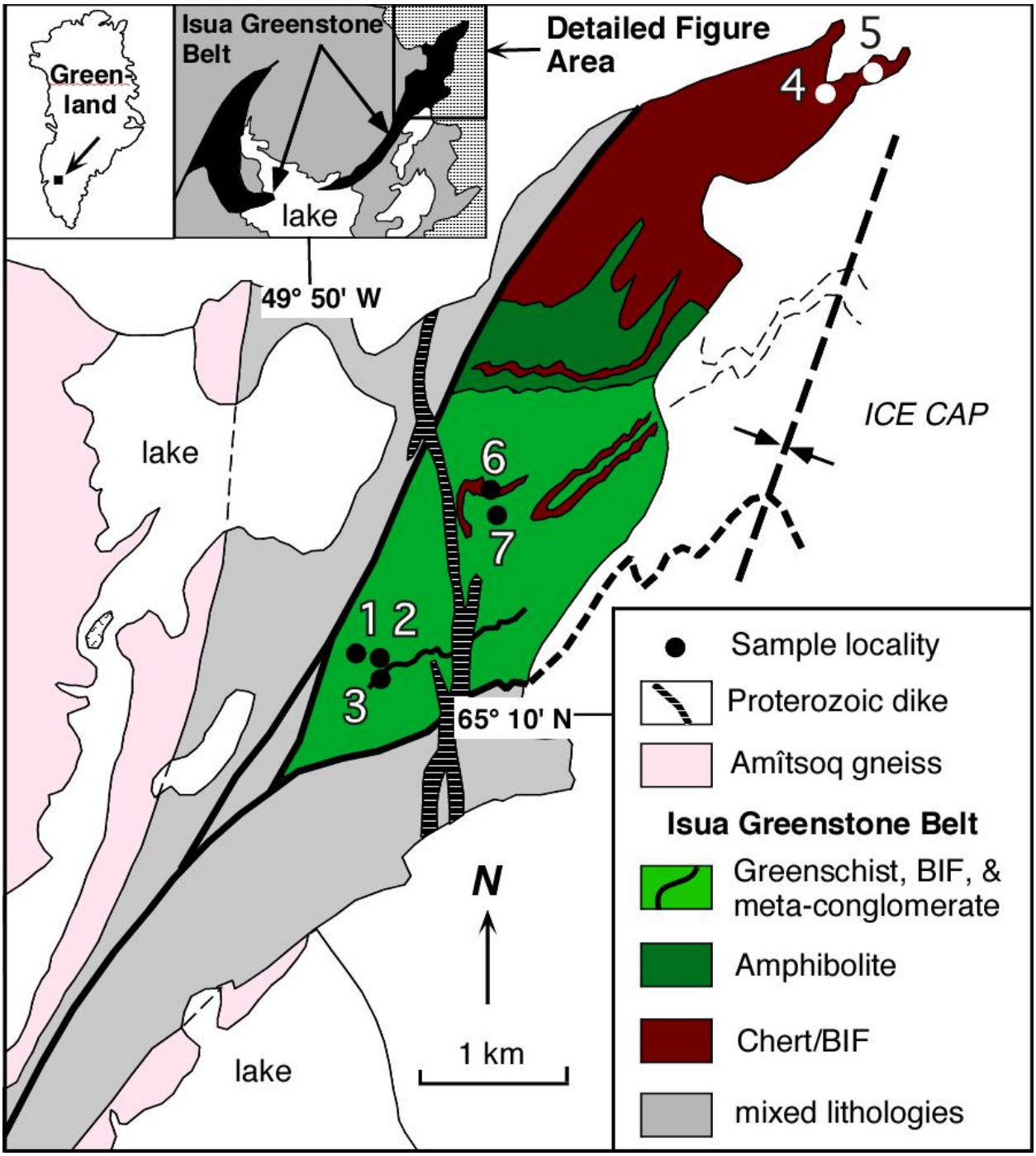


Figure 3-3. Geologic map of the Northeastern section of the Isua Greenstone Belt, with an inset showing the location of the greenstone belt in SW Greenland. Modified from Fedo, 2001. Sample localities marked by numbers. 3 = chert clasts from conglomeritic unit (sample ISB 5b), 6 = bedded chert (samples ISB 26, ISB 28) 7 = brecciated pillow basalt (sample ISB 31b). Samples for locations 1, 2, 4, and 5 are from the study discussed in Chapter IV.

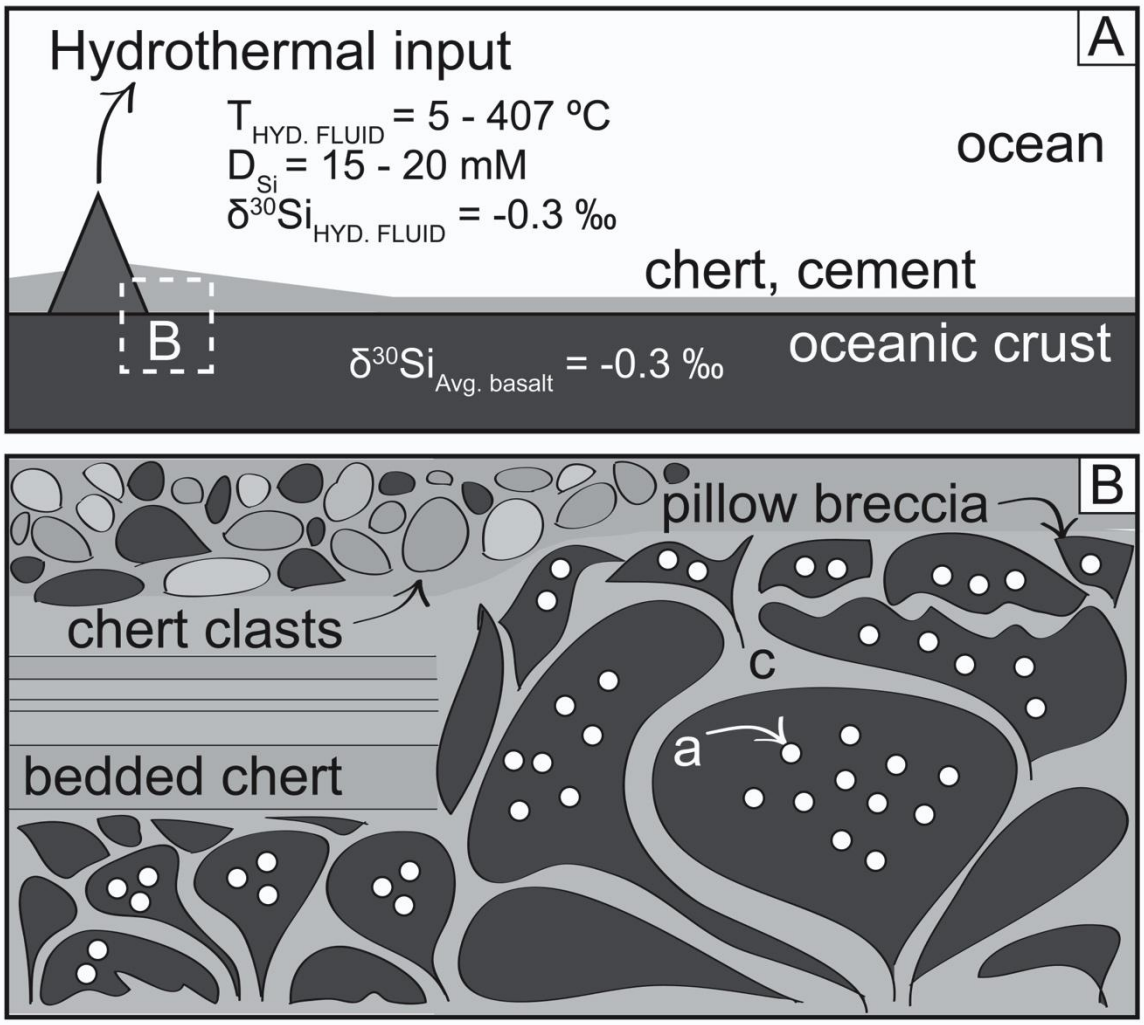


Figure 3-4. Cartoon showing different quartz lithologies used in this study. (A) Schematic of a typical hydrothermal system. Conditions of formation include vesicular standard pressures of 30-35 MPa, and hydrothermal fluid temperatures ($T_{HYD. FLUID}$) ranging from 5 – 407 °C, high dissolved silica (D_{Si}) concentrations, and silicon isotope signatures of basalt ($\delta^{30}Si_{Basalt}$ = -0.3 ‰; Fitoussi et al., 2012), and hydrothermal fluid ($\delta^{30}Si_{HYD. FLUID}$ = -0.3 ‰; De la Rocha et al., 2000). (B) Diagram of different types of quartz samples from this study including: pillow basalt breccia, with quartz-filled amygdules (a), encased in quartz cement (c), adjacent bedded chert, and chert clasts from a conglomerate. Under conditions of disequilibrium, rapid precipitation from high temperature fluids likely led to preferential incorporation of ^{28}Si into the precipitating quartz filling vesicles during initial eruption of pillow basalt. As conditions approached equilibrium, quartz precipitated as encasing cement at slower rates, and lower temperatures, resulting in cement $\delta^{30}Si$ values similar to source fluid/rock composition. Geochemical and isotopic conditions for formation of quartz in the bedded chert unit, and chert clasts, were likely similar to those that formed the cement.

CHAPTER IV

SILICON ISOTOPE EVIDENCE FOR CONTINENTAL EMERGENCE AT ~3 GA

This chapter was taken from a manuscript in preparation:

Brengman, L.A., Fedo, C.M., Whitehouse, M.J., 2015, **Silicon isotope evidence for continental emergence at ~3 Ga.**

ABSTRACT

The silicon isotope signatures ($\delta^{30}Si$) of Precambrian Superior-type banded iron formation (BIF) from 3 Ga to 1.88 Ga, record a unidirectional shift in silicon sources to the ocean reservoir from dominantly hydrothermal to continental. This shift is the result of continental emergence beginning at ~3 Ga. Over the period of deposition of Superior-type BIF, the production of ^{30}Si-enriched silicic acid during chemical weathering of newly exposed silicic continental crust, and subsequent delivery to the oceans, changed the isotopic composition of the marine reservoir from a dominantly hydrothermal signature ($\delta^{30}Si \sim 0$ ‰), to a continental one ($\delta^{30}Si > 1$ ‰). Based on our findings, the ~ 3 Ga – 2.5 Ga time interval should carry critical implications for increased and widespread delivery of bio-essential nutrients to surface oceans and the development of a terrestrial biosphere on newly emergent continents.

INTRODUCTION

Since the original use of silicon isotopes in chert (SiO_2) as a paleo-ocean thermometer (Robert and Chaussidon, 2006), a number of studies have attempted to explain a perceived secular rise in the silicon isotope composition (expressed as $\delta^{30}Si$) of marine siliceous precipitates (chert and BIF) through time (van den Boorn et al., 2007; Abraham et al., 2011; André et al., 2006; van den Boorn et al., 2010; Heck et al., 2011; Steinhoefel et al., 2010; Chakrabarti et al., 2012; Delvigne et al., 2012; Marin-Carbonne et al., 2012; Kejun et al., 2014; Fan et al., 2013; Fig. 4-1a) as either a mixing of hydrothermal and continental silicon sources to the ocean (Heck et al., 2011) or a gradual cooling of ocean temperatures since the Archean (Robert and Chaussidon, 2006; Marin-Carbonne et al., 2012; 2014). Either interpretation of this heterogeneous data set raises two significant concerns. First, the pooling of all data together regardless of rock/chert type (e.g., silicified precursor rocks, shallow-water chert, greenstone chert, Algoma-type [hydrothermal] BIF, and Superior-type [continental] BIF) requires that each distinct type of siliceous marine sediment records precipitation under identical geochemical conditions from a single, unchanging marine reservoir. Second, simple source mixing requires proportions of end-member hydrothermal and continental inputs to remain constant through time, despite ample evidence to the contrary (Isley, 1995). The purpose of this paper is to provide an explanation for the observed heterogeneity in the compiled $\delta^{30}Si$ record of chert and BIF, and provide a predictive model with which to decipher the evolving record of silicon sources to the Precambrian ocean. Using this approach, we document the first geologic evidence for continental emergence beginning at ~3 Ga.

Silicon isotope sources and sinks

To interpret the silicon isotope composition of Precambrian chert and BIF, it is necessary to establish the major Si sources to the ocean, and to understand the abiotic processes that affect silicon isotope fractionation. Today, silica-utilizing organisms profoundly overprint the modern silicon cycle (Treguer and De la Rocha 2013). Despite this, the main sources to the present ocean reservoir, hydrothermal emanations and riverine inputs, maintain distinct $\delta^{30}Si$ isotopic

signatures. In a Precambrian world devoid of silica-utilizing organisms, abiotic processes responsible for creating distinct isotopic signatures in hydrothermal and continental settings must have dominated the silicon cycle. The main sinks for silicon, Precambrian silica-rich chemical sedimentary rocks (chert, BIF), precipitate in diverse marine environments, in addition to forming from diagenetic and metasomatic replacement of precursor materials (e.g. silicified rocks, nodular cherts within carbonates). Greenstone-belt chert and Algoma-type BIF occur in association with mafic volcanic rocks (Klein, 2005). By contrast, large-scale Superior-type BIF form in continental-margin settings and are commonly interbedded with shale, sandstone, and carbonate (Klein, 2005). Because chert, Algoma-, and Superior-type BIF accumulate in different depositional settings, we hypothesize these rocks could record distinct isotopic source signatures related to the silicon reservoir from which each precipitated. We further consider that dividing the current silicon-isotope archive into rock/chert types based on depositional affinity (e.g., hydrothermal versus continental shelf) and mode of formation (chemical sedimentation versus replacement) will explain the observed heterogeneity and allow for mechanistic explanations of any perceived temporal trends.

METHODS

Samples (small rock chips) were embedded in epoxy along with a quartz reference material (UT-Q), polished to 1 μm, mapped using Nikon petrographic microscope, and gold-coated (30 nm) prior to analysis (sample mount photos can be found in Appendix A-5, Figs. 5-16 through 5-56; Tables 4-1, 4-2). In situ Si-isotope measurements were made using a CAMECA IMS 1280 SIMS instrument at the Swedish Museum of Natural History, Stockholm (NordSIMS facility). $^{30}Si/^{28}Si$ ratios were measured in separate analytical sessions. A $^{133}Cs^{+}$ primary beam (ca. 5nA) with an incident energy of 20 keV was used to sputter secondary ions from specifically targeted <20 μm individual grains; microcrystalline domains were avoided (cf. ref. Marin-Carbonne et al., 2012) except during methodological testing. Sample charging was minimized by use of a low-energy normal-incidence electron gun. Secondary ions were measured at a mass resolution of 2,500 (M/ΔM) by multicollection on Faraday detectors attached to low noise amplifiers housed in a thermally stabilized, evacuated chamber. The magnetic field was locked at high precision using an NMR field sensor.

Fully automated analytical sessions regularly bracketed unknowns between reference analyses and individual analyses comprised a pre-sputter to remove the Au coat, beam centering and 48 seconds (Si) of data acquisition. We report isotope values expressed in standard delta notation ($\delta^{H}X=[(^{H}X/^{L}X_{sample})/ (^{H}X/^{L}X_{standard})-1]x1000$, where H=heavy isotope, L=light isotope, and X=element measured). Corrections for instrumental mass fractionation were made using internal standard UTQ with a bulk $\delta^{30}Si$ value of 0.08 ± 0.01 ‰, determined at the University of Western Ontario. External reproducibility (1 std. dev.) for $\delta^{30}Si$ of ± 0.15 ‰ was derived from the bracketing UTQ analyses (Appendix A-5, Fig. 5-10-5-14; Tables 4-1, 4-2) and propagated onto within-run uncertainties. Following the approach of previous studies (Marin-Carbonne et al., 2012), probability density distributions were calculated with the R statistical package v2.14.1 to yield $\delta^{30}Si_{peak}$ values. The subscript 'peak' refers to a homogenized isotope composition determined using a probability density distribution calculated for each individual sample, and per locality based on the methods of Marin-Carbonne et al. (2012) (representative sample plot Appendix A-5, Fig. 5-4; comparable bulk data Appendix A-5, Table 4-3).

BUHWA GREENSTONE BELT, ZIMBABWE CASE STUDY

To test our hypothesis, we measured the silicon isotope composition of quartz by secondary isotope mass spectrometry (SIMS) from different rock types (bedrock, sandstone, chert, Superior-type BIF, Algoma-type BIF; Fig. 4-2; Appendix A-5, Table 4-4) from the weakly metamorphosed ~3 Ga Buhwa Greenstone Belt (BGB), Zimbabwe (Fedo and Eriksson, 1996), where the known silicon sources and sinks could be identified in a single basin. Before interpreting the δ^{30}Si record from deformed and metamorphosed Archean rocks, we first tested how several critical factors might influence interpreting Si isotope data collected by SIMS. We found no correlation between silicon isotope values and regional metamorphic grade (greenschist through upper amphibolite facies) or crystal size (15-220 μm), or in cases of contact metamorphism (Appendix A-5; Fig. 5-10; Table 4-4 contact metamorphism samples TEMj, TEM-13-Db, TEM-cf; Table 4-7 crystal size measurements). Consequently, we are confident that silicon isotope data presented here represent primary values.

Geologic setting of studied samples

The ~3.0 Ga Buhwa Greenstone belt (BGB) is located on the southern margin of the Zimbabwe Archean Craton. Supracrustal rocks comprising the belt were deposited as a kilometer-thick, upward-deepening, stable-shelf sedimentary cover sequence that laterally transitions from a presumed shelf edge into deeper water environments (Fedo et al., 1995; Fedo and Eriksson, 1996; Fig. 4-3). Facies include a western shelf association, transitional zone, and basinal eastern assemblage. The kilometer-thick western shelf facies consists of an upward-fining succession of interbedded quartz-arenite (ZB 240; Fig. 4-3; Appendix A-5, Tables 4-4, 4-5) and shale, overlain by shale, which is in turn overlain by Superior-type iron formation (ZB 17, ZB 18, ZB 20, ZB 23, ZB 143, ZB 169; Fig. 4-2 D, G, Appendix A-5, Tables 4-4, 4-5). The km-thick eastern basinal assemblage includes metamorphosed mafic-ultramafic volcanic rocks, recrystallized metachert (ZB 105, ZB 07; Fig. 4-2 C, G, Appendix A-5, Tables 4-4, 4-5) Algoma-type iron formation (ZB 05; Appendix A-5, Tables 4-4, 4-5) and shale. A zone of transitional deposits between the eastern and western assemblages that consists predominantly shale, Superior-type iron formation, and muddy sandstone (Fedo and Eriksson, 1996). Regional-scale, brittle and ductile folding and thrusting affected the entire BGB cover sequence during the uplift of the Northern Marginal Zone of the Limpopo Belt (Rollinson and Blenkinsop, 1995; Hawkesworth et al., 1979; Dodson et al., 1988). The minimum depositional age of BGB is constrained by the age of the ~2.9 Ga Chipinda Batholith (Hawkesworth et al., 1979; Fedo, unpublished data), which is interpreted to intrude the clastic facies (Fedo and Eriksson, 1996), with a maximum age (3.05 Ga) bracketed by the age of detrital zircons from quartz arenites (Dodson et al., 1988). The source rock for detrital quartz is the Tokwe Segment (ZB 182; Fig. 4-2A; Appendix A-5, Tables 4-4, 4-5; Fedo et al., 1996).

Bedrock and detrital quartzite

Quartz crystals from a gneissic bedrock sample (Tokwe segment; Wilson, 1990) possess an overall δ^{30}Si signature of ~1 ‰, with little internal heterogeneity (0.54 – 1.21 ‰; Fig. 4-1b; δ^{30}Si = 0.94 ± 41 ‰; Fig. 4-1c). Individual mono-crystalline quartz grains from a quartz arenite sample from the BGB with quartz sand, likely derived from the Tokwe segment (Wilson, 1990) possess a similar, relatively homogeneous δ^{30}Si signature near ~1 ‰, (δ^{30}Si = -0.24 – 1.02 ‰; Fig. 4-1b; $\delta^{30}Si_{peak}$ = 0.59 ± 0.44 ‰; Fig. 4.1c; Appendix A-5, Fig. 5-5; Tables 4-4, 4-5). The overlap in δ^{30}Si values between the bedrock and derived quartz sand do not show significant

fractionation consistent with the lack of evidence for fractionation during the mechanical breakdown of detrital grains and subsequent physical transport of quartz sand originated from crystalline bedrock sources.

Silicon isotope compositions of quartz from siliceous marine precipitates

Siliceous marine precipitates (chert and BIF) in the BGB occur in two separate associations, namely (1) interbedded with mafic volcanic rocks (greenstones), and (2) overlying quartz arenite and shale as part of a km-thick succession (Fedo and Eriksson, 1996). Overall, chert and BIF are ^{30}Si-depleted, and show additional inter- and intra-sample heterogeneity (Fig. 4-1b, c; Appendix A-5, Figs. 5-5 through 5-9) compared to bedrock and detrital quartzite.

Greenstone-associated chert samples range from $\delta^{30}Si$ = -1.5 to 1.6 ± 0.3 ‰ (Fig. 4-1b; $\delta^{30}Si_{peak}$ = 0.79 ± 1.37 ‰; Fig 4-1c). Algoma-type BIF samples associated with greenstones are ^{30}Si-depleted relative to bedrock, sandstone, and chert samples, possessing $\delta^{30}Si$ compositions that range from -3.6 to -1 ± 0.3 ‰ (Fig. 4-1b; $\delta^{30}Si_{peak}$ = -2.14 ± 0.57 ‰; Fig. 4-1c). Similarly, Superior-type BIF samples from association 2 are on average ^{30}Si-depleted (Fig. 4-1b; $\delta^{30}Si$ = -3.3 to -0.2 ± 0.3 ‰; $\delta^{30}Si_{peak}$ = -0.67 ± 1.41 ‰; Fig. 4-1c) compared to bedrock, sandstone, and pure chert, although they are ^{30}Si-enriched relative to Algoma-type BIF. The $\delta^{30}Si$ heterogeneity measured in rocks of approximately the same age, from a single ocean basin in this study spans nearly the entire range of silicon isotopes.

We interpret the intra-sample heterogeneity to reflect differences in the magnitude of kinetic isotope effect, similar to that which is observed in experimentally precipitated quartz (Oelze et al., 2015). Larger, inter-sample heterogeneity is interpreted to reflect variance in the $\delta^{30}Si$ source composition. Statistically significant $\delta^{30}Si$ differences between rock types (Fig. 4-1c; Appendix A-5, Table 4-5) in the BGB suggest that distinct silicon-isotope fractionation mechanisms operate in shelf versus basinal settings. Consequently, the sedimentary record of the BGB captured the transfer of distinct, process-specific, isotope compositions from the marine reservoir. Given this interpretation, it should be possible to apply this to a broader of understanding of the evolution of silicon isotope compositions through time.

DECODING THE SILICON ISOTOPE ARCHIVE OF CHERT

To better understand how chert/BIF acquire their Si-isotope composition, we combine all published silicon isotope data from quartz in chert/BIF from previous studies (Appendix A-5; Table 4-6) with additional new data of quartz from selected Archean BIF, chert, and silicified rock samples interpreted to represent precipitation across a spectrum of depositional environments and ages. In addition to the analyses used form the BGB described above, we also present new data from the >3.7 Ga Isua Greenstone Belt (IGB), SW Greenland, and the ~2.7 Ga Abitibi Greenstone Belt (AGB), Canada (Appendix A-5; Table 4-4, 4-5).

Geologic setting of studied samples

Isua Greenstone Belt, Greenland (3700-3800 Ma)

The Eoarchean, arcuate-shaped, Isua Greenstone Belt (IGB), SW Greenland, represents the largest of many supracrustal enclaves that occur within the Amîtsoq gneiss complex, and that have been termed the Akilia Association (McGregor and Mason, 1977; Fig. 4-4). Tonalite–trondjhemite–granodiorite-suite rocks representing the Amîtsoq gneisses intruded the terrane that includes the IGB at about 3700 Ma and 3800 Ma (Nutman et al., 2009), while supracrustal rocks belonging to IGB have yielded ages consistent with eruption and deposition between 3700 and

3800 Ma (Kamber et al., 2005). Samples studied here (Fig. 4-2; Appendix A-5, Table 4-4) come from the northeastern part of the IGB, which has been divided into three tectonic panels (northwest, central, and southeast domains) that are separated by ductile faults (Appel et al., 1998). Of the three domains, the central is comparatively less deformed, such that primary features (e.g., pillows) are locally preserved (Myers, 2001; Fedo et al., 2001), even though most rocks carry a prominent foliation, and a steeply plunging stretching lineation. Metamorphosed rocks of the central domain have protoliths that include basalt, pillow basalt, conglomerate, chert (ISB 26, ISB 28), and BIF (Myers, 2001; Fedo et al., 2001; Whitehouse and Fedo, 2007). Algoma-type BIF (IS-02-05, IS-02-06, IS-02-08, ISB 55; Fig. 4-2E, H) primarily consist of alternations of magnetite and recrystallized quartz ± amphibole. Field relations show that the IGB was deformed and regionally metamorphosed at amphibolite facies (Rollinson, 2003).

Abitibi Greenstone Belt, Canada (~2700 Ma)

The Abitibi greenstone belt (AGB) in Québec, Canada evolved over a 65 million year period, from 2735-2670 Ma, and represents the complex evolution of oceanic arc formation, collision, and fragmentation, characterized by multiple volcano-sedimentary sequences, divided into the northern volcanic zone (NVZ) and the southern volcanic zone (SVZ) (Mueller and Mortensen, 2002; Chown et al., 2000; Fig. 4-5). Typical volcano-sedimentary sequences of the NVZ include felsic and mafic volcanic suites, Algoma-type BIF, pervasively altered hydrothermal rocks, and localized volcanic massive sulfide mineralization. Samples in this study from the AGB include Algoma-type BIF (Fig. 4-2i; Appendix A-5, Table 4-4) and silicified rocks (Fig. 4-2f; Appendix A-5, Table 4-4). Algoma-type banded iron formation samples TEM-CF, TEMj, and TEM-13-Db come from a well-exposed road outcrop just north of Temagami, Ontario on the east side of Route 11. The samples consist of alternating, fine-grained bands of magnetite and chert with minor amounts of hematite. Silicified rock sample (AB-11-12) comes from the 2.72 Ga (Mueller and Mortensen, 2002; Chown et al., 2000) volcano-sedimentary Hunter Mine Group located on the southern limb of the overturned, northward dipping Lake Abitibi anticline and are a part of a collapsed subaqueous caldera complex (Mueller and Mortensen, 2002; Chown et al., 2000). The entire area has experienced greenschist facies metamorphism, but local preservation of volcanic and sedimentary features has allowed detailed identification of graded pyroclastic flows (Mueller and Mortensen, 2002; Chown et al., 2000). In this subaqueous caldera system, continuous eruptions formed a zone between inner and outer caldera depressions that provided ample hydrothermal fluid circulation and facilitating extensive alteration that resulted in volcanic massive sulfide (VMS) deposit and associated quartz replacement (Chown et al., 2000). Faults, fractures, and fissures associated with caldera collapse and volcanic edifice development provided fluid conduits for hydrothermal fluid, resulting in the precipitation of hydrothermal minerals during volcanic arc evolution. Felsic dyke complex, and the emplacement of the Fe-rich Roquemaure sill (Mueller and Mortensen, 2002) likely drove hydrothermal fluid circulation, which resulted in fluid-rock interactions and drove low-temperature hydrothermal alteration and silicification of the volcanic edifice rocks, followed by later carbonitization and VMS mineralization (Mueller and Mortensen, 2002).

Isotopic composition by rock type and depositional setting

Silicified volcanic rocks

Silicification of volcanic rocks in greenstone belt terranes involves the transformation of precursor lithologies into chert adjacent to hydrothermal systems (van den Boorn et al., 2007).

Figure 4-6a contains our data from silicified volcanic rocks in the AGB, which, together with data compiled from previous studies (André et al., 2006; van den Boorn, 2007; 2010; Abraham et al., 2011) demonstrates that silicified rocks uniformly possess δ^{30}Si values near 0 ‰ (van den Boorn, 2007; 2010; Abraham et al., 2011) during the Archean. During silicification, dissolution of igneous material precedes quartz precipitation and replacement of the original rock. In this system, quartz likely precipitated in equilibrium with hydrothermal fluids (δ^{30}Si = -0.3‰; De la Rocha et al., 2000) saturated with silicon derived from original igneous material (δ^{30}Si = -0.3‰; Ding et al., 1996). No significant fractionation during precipitation is observed. As a result, silicified volcanic rocks inherit the silicon-isotope signature of the precursor material. Consequently, these cherts cannot directly represent ocean chemistry, and should not appear as part of a plot designed to do so.

Bedded chert

When pooled together, all bedded cherts show an apparent increasing trend in δ^{30}Si values, followed by a decrease with respect to time after about 1.5 Ga (Fig. 4-6b). However, when separated based on depositional affinity, this trend disappears. Bedded chert hosted within greenstone terrains (greenstone chert; Fig. 4-6c), is dominantly of Archean age, and formed in environments with profuse hydrothermal input, where quartz precipitated locally via conductive cooling in rapidly evolving hydrothermal systems (Chapter III). Like associated Algoma-type BIF, greenstone chert displays a similar range of silicon isotope values, consistent with deposition associated with local hydrothermal conditions. Bedded chert hosted within carbonate successions (Fig. 4-6d) is generally Proterozoic in age, and can form from direct precipitation from seawater, or from dissolution and precipitation of locally or externally sourced siliceous material within carbonate beds (e.g., Siever, 1992). In this respect, these cherts can record either seawater composition, or can acquire the isotopic composition of the source for the silicon (e.g., siliceous shale). Additionally, silica-utilizing organisms with the potential to fractionate silicon evolved during the late Proterozoic (Perry and Lefticariu, 2007), and could have obscured abiotic silicon signatures of the ocean reservoir, or led to preservation of local effects in this depositional setting. At the very least, such effects would make it impossible to compare these data sets equally.

Algoma-type banded iron formation

Algoma-type BIF are thought to form from exhalative precipitation proximal to sub-aqueous hydrothermal systems, and commonly occur in greenstone-belt terranes interstratified with volcanic rocks and silicified equivalent (Kimberley, 1979; Klein, 2005). Figure 4-6 illustrates all published spot (Fig. 4-6e; SIMS, LA-ICP-MS; Appendix A-5, Tables 4-4, 4-5, 4-6) and bulk (Fig. 4-6f; Appendix A-5, Table 4-2) data for Algoma-type BIF, including our data from the AGB (~2.7 Ga) and IGB (~3.7 Ga). We propose that the range of silicon-isotope values observed in Algoma-type BIF samples of a given age result from kinetic isotope effects due to precipitation via conductive cooling (Chapter III). In this model, under disequilibrium conditions of rapid quartz precipitation in the presence of Al, ^{28}Si preferentially incorporates into the product phase, and $\Delta^{30/28}Si_{ppt\text{-}soln} < 0$ (Oelze et al., 2015). As the system nears equilibrium and quartz precipitates at a slower rate, the product possesses values closer to the source rock/fluid composition, and $\Delta^{30/28}Si_{ppt\text{-}soln} \sim 0$ (Oelze et al., 2015). The heterogeneous values measured for these Precambrian deposits overlap values measured for modern Fe-Si-rich deposits that flank modern mid-ocean-ridge hydrothermal systems (δ^{30}Si = -0.4 to -3.1 ‰; Ding et al., 1996). We

interpret the scattered but consistent range of $\delta^{30}Si$ values of Algoma-type BIF to indicate that the hydrothermal processes responsible for Algoma-type BIF deposition remained constant over this billion-year time frame, and most likely throughout Earth history.

Superior-type banded iron formation

In depositional settings distant from hydrothermal systems, silica precipitation occurs directly from the ambient water column because of adsorption to continentally sourced Al- and Fe-clays (Oelze et al., 2014; 2015), Fe-oxides (Delstance et al., 2009; Opfergelt et al., 2009), or organic carbon (Siever, 1992), and/or via precipitation under super-saturated conditions (Siever, 1992). Silicon isotopes fractionate during both adsorption to Al- and Fe-oxides (Delstance et al., 2009; Opfergelt et al., 2009) and clay minerals, and during precipitation directly from supersaturated fluids at ambient ocean temperatures (Geilert et al., 2014). As a result, a record of continentally sourced silicon therefore should be recorded in the quartz deposited in Superior-type BIF, which form in basins floored by continental crust and occur interbedded with open-marine deposits. Silicon-isotope data presented here includes one of the oldest known Superior-type BIF (~3 Ga; BGB) combined with all previously collected data (Heck et al., 2011; Steinhoefel et al., 2010; Chakrabarti et al., 2012; Delvinge et al., 2012; Marin-Carbonne et al., 2012) that span the entire time frame of Superior-type BIF deposition (Fig. 4-7a, b). Both the bulk (Fig. 4-7a) and spot data (Fig. 4-7b) show a systematic increasing trend from negative ($\delta^{30}Si_{peak}$ = -0.69 ± 1.5 ‰) to positive ($\delta^{30}Si_{peak}$ = 1.92 ± 0.76 ‰) across the 3 Ga to 1.9 Ga time frame, which indicates the incremental addition of isotopically heavy silicon (^{30}Si) to the Superior-type BIF record. The only documented ^{30}Si-enriched source for silicon during this time frame is mono-silicic acid (H_4SiO_4), a product of terrestrial chemical weathering, where hydrolysis reactions result in concurrent feldspar dissolution and in-situ authigenic clay precipitation. Such clays possess ^{30}Si-depleted signatures ($\delta^{30}Si \approx$ -3 to -1 ‰; Ziegler et al., 2005) complemented by resultant ^{30}Si-enriched silicic acid ($\delta^{30}Si \approx$ +1 to +3 ‰; Ziegler et al., 2005), which enters the ocean reservoir via riverine transport.

Despite heterogeneities within samples of any single age, which may reflect heterogeneous fractionation during adsorption or precipitation via super-saturation, the differences recorded in $\delta^{30}Si$ values of Superior-type BIF from 3 Ga to 1.9 Ga exceed what would be expected by fractionation from an isotopically unchanging ocean reservoir. I interpret this increase in silicon isotope values of Superior-type BIF to represent precipitation from an evolving ocean reservoir with respect to $\delta^{30}Si$, ultimately reflecting the addition of ^{30}Si-enriched silicon delivered by riverine waters draining newly emergent, chemically weathered continents.

Provisional flux model for the Precambrian silica cycle

By modifying previous modern flux estimates for Precambrian hydrothermal and continental sources to the ocean (Fig. 4-8), we can describe the evolving Precambrian marine reservoir using basic isotopic mass balance equations, and determine broader implications for how the emergence of the continents would have affected habitable environmental niches for early life. Using flux estimates from modern systems (Treguer and De la Rocha, 2013), and adjusting them for changing silicon fluxes to the Precambrian ocean (Isley, 1995; Siever, 1992), coupled with the Si-isotope record discussed above, we divided the rock record into stage 1 (>3.7 Ga – 3 Ga), stage 2 (3 Ga – 2.5 Ga), and stage 3 (2.5 Ga – 1.8 Ga). We used estimated Precambrian conditions of: $[Si]_{ocean}$ = >60 μmol/L (Siever, 1992), $[Si]_{hyd.\ fluid}$ = 11-25 mmol/L

(Von Damm et al., 1985), τ_{Si} = >? 20,000 years, Mixing (t) = ~10^3 yrs (Treguer and De la Rocha, 2013).

Stage 1 (>3.7 Ga – 3 Ga) is dominantly composed of granite-greenstone rock successions where hydrothermal flux is potentially 3x greater than modern values (Isley, 1995), and riverine delivery of material is only 10 % that of the modern (Isley, 1995), resulting in a ratio of continental to hydrothermal input near 1:3.83 (values adjusted for lack of biological input from Treguer and De la rocha, 2013). Stage 2 (3 Ga – 2.5 Ga) marks the first documented appearance of large continental shelf successions and thus the first known Superior-type BIF. Hydrothermal flux is still likely 3x greater than modern values (Isley, 1995) at the beginning of Stage 2, but with formed continental crust exposed to sub-aerial weathering, riverine delivery of material could increase to roughly 30 – 70% of the current value (Isley, 1995). This results in a ratio of continental to hydrothermal input near 1:1.28 (modified using proportional adjustments to modern flux values in Treguer and De la Rocha, 2013). Stage 3 (2.5 Ga – 1.8 Ga) is dominated by continental margin terrains, and while hydrothermal flux likely remained high, increased delivery (70-100% of the modern value, Isley, 1995) of material at from riverine input would result in continental:hydrothermal input ratios to the ocean of 2.6:1 (modified using proportional adjustments to modern flux values in Treguer and De la Rocha, 2013), which represents a wholesale turnover to a continental buffered ocean. During stage 3, Superior-type BIFs (and granular iron formation) dominate the record in continental platform environments, and shallow water cherts, and diagenetic cherts formed via replacement of carbonate layers become predominant.

Interpreting the decoded silicon isotope archive of chert

Based on our flux model and the silicon isotope archive chert separated by rock type, it becomes apparent that a hydrothermal silicon signature dominated the ocean early in Earth history (Fig. 4-9a), and silica deposition dominantly occurred in sub-aqueous hydrothermal settings (Klein, 2005). In this scenario, silicon isotopes of hydrothermally sourced quartz in Algoma-type BIF and associated greenstone chert (Fig. 4-9d) record silicon derived from igneous rocks and precipitated from hydrothermal fluids (Fig. 4-6c, e, f) in a mantle-buffered marine reservoir (Kamber and Webb, 2001). After the initial establishment of continental shelf environments (Fig. 4-9b), which served as platforms for Superior-type BIF deposition (Fig. 4.9d), the continents became a new, and eventually dominant, source of silicon to the ocean. With increasing continental growth (Hawkesworth and Kemp, 2006) and chemical weathering on emergent land surfaces (Fig. 4-9b), continentally derived Si was delivered in increasing quantity to the ocean resulting in a shift in reservoir composition. The silicon-isotope record of Superior-type BIF therefore provides the only known timeline of the unidirectional evolution from predominantly subaqueous, high-temperature hydrothermal weathering to low-temperature, sub-aerial chemical weathering of emergent continental crust. After the cessation of Superior-type BIF deposition at ~1.8 Ga, the silicon-isotope record becomes dominated by shallow-water bedded chert and chert formed via replacement of carbonate layers (Fig. 4-9d). Once silica-utilizing organisms evolved in the Neoproterozoic, abiotic isotopic signatures became obscured, due to biological utilization of silicon (Fig. 4-9c).

SIGNIFICANCE

Overall, our findings presented here predict the heterogeneity that occurs within the current compiled δ^{30}Si isotope record. Furthermore, our research indicates that the evolution of

BIF from Algoma- to Superior-type in the rock record could have occurred in response to the initiation of sub-aerial chemical weathering on newly exposed continental crust, recording the introduction of a continental source of silicon to the Precambrian ocean. In addition, weathering of emergent continental crust would initiate cycling of key, bio-essential nutrients, allowing enhanced delivery of these elements to the ocean. From an emerging biosphere perspective, this places new recognition of the 3 – 2.5 Ga time interval with implications for explaining the observed rapid increase in genetic innovation at 3 Ga (David and Alm, 2011) in concert with the development of a terrestrial biosphere (Battistuzzi et al., 2004).

ACKNOWLEDGEMENTS

This work was funded by NASA grant EXOB08-0063 awarded to CMF, and student research grants awarded to LAB from ExxonMobil, the Geological Society of America, the Sedimentary Division of GSA, and the Department of Earth and Planetary Sciences at the University of Tennessee. The data reported in this paper are tabulated in Appendix A-5, Tables 4-1 through 4-6. The NordSIMS facility is a joint Nordic infrastructure funded by the research funding agencies of Denmark, Norway and Sweden, the University of Iceland and the Geological Survey of Finland. We thank Balz Kamber, Grant Young, and Tom McCollom for comments on a previous version of the manuscript.

LIST OF REFERENCES

Abraham, K., Hofmann, A., Foley, S.F., Cardinal, D., Harris, C., Barth, M.G., André, L., 2011. Coupled silicon-oxygen isotope fractionation traces Archean silicification. Earth and Planetary Science Letters 301: 222-230.

André, L., Cardinal, D., Alleman, L.Y., Moorbath, S., 2006. Silicon isotopes in ~3.8 Ga West Greenland rocks as clues to the Eoarchaean supracrustal Si cycle. Earth and Planetary Science Letters 245: 162-173.

Appel, P. W. U., Fedo, C. M., Moorbath, S., Myers, J. S. 1998. Recognizable primary volcanic and sedimentary features in a low-strain domain of the highly deformed, oldest known (3.7–3.8 Gyr) greenstone belt, Isua, West Greenland. Terra Nova 10. 57–62.

Battistuzzi, F., Andreia, F., Blair, H.S., 2004. A genomic timescale of prokaryote evolution: insights into the origin of methanogenesis, phototrophy, and the colonization of land. BMC Evolutionary Biology 4(44): 1-14.

Chakrabarti, R., Knoll, A. H., Jacobsen, S. B., Fischer, W. W., 2012. Si isotope variability in Proterozoic cherts. Geochimica et Cosmochimica Acta 91: 187-201.

Chown, E. H., N'dah, E., Mueller, W. U., 2000. The relation between iron-formation and low temperature hydrothermal alteration in an Archean volcanic environment. Precambrian Research 101, 263-275.

David, L. A., Alm, E.J., 2011. Rapid evolutionary innovation during an Archean genetic expansion. Nature 469: 93-96.

De la Rocha, C.L., Brzezinkski, M.A., DeNiro, M.J., 2000. A first look at the distribution of the stable isotopes of silicon in natural waters. Geochimica et Cosmochimica Acta 64: 2467-2477.

Delstanche, S., Opfergelt, S., Cardinal D., Elsass, F., André L., Delvaux, B., 2009. Silicon isotopic fractionation during adsorption of aqueous monosilicic acid onto iron oxide. Geochimica et Cosmochimica Acta 73: 923–934.

Delvigne, C., Cardinal, D., Hofmann, André L., 2012. Stratigraphic changes of Ge/Si, REE + Y and silicon isotopes as insights into the deposition of a Mesoarchean banded iron formation. Earth and Planetary Science Letters 355-356: 109-118.

Ding, T., 1996, Silicon isotope geochemistry, Geological Publishing house, pp. 1-105.

Dodson, M.H., Compston, W., Williams, I.S., Wilson, J.F., 1988. A search for ancient zircons in Zimbabwean sediments. Journal of the Geological Society London 145, 977 983.

Fan, H., Wen, H., Zhu, X., Hu, R., Tian, S., 2013. Hydrothermal activity during Ediacaran-Cambrian transition: Silicon isotopic evidence. Precambrian Research 224: 23-35.

Fedo, C. M., Eriksson, K. A., 1996. Stratigraphic framework of the ~3.0 Ga Buhwa Greenstone Belt: a unique stable-shelf succession in the Zimbabwe Archean Craton. Precambrian Research 77: 161-178.

Fedo, C. M., Myers, J. S., Appel, P. W. U., 2001. Depositional setting and paleogeographic implications of earth's oldest supracrustal rocks, the >3.7 Ga Isua Greenstone belt, West Greenland. Sedimentary Geology 141-142: 61-77.

Fedo C. M., Eriksson K. A., 1996. Stratigraphic framework of the ~ 3.0 Ga Buhwa Greenstone Belt: a unique stable-shelf succession in the Zimbabwe Archean Craton. Precambrian Research 77, 161-178.

Fedo, C. M., Eriksson, K. A., and Blenkinsop, T.G., 1995. Geologic history of the Archean Buhwa Greenstone Belt and surrounding granite-gneiss terrane, Zimbabwe, with implications for the evolution of the Limpopo Belt. Canadian Journal of Earth Sciences 32, 1977-1990 .

Fedo, C., Myers, J., Appel, P., 2001. Depositional setting and paleogeographic implications of Earth's oldest supracrustal rocks, the >3.7 Ga Isua Greenstone Belt, West Greenland. Sedimentary Geology 141-142, 61-77.

Geilert, S., Vroon, P.Z., Roerdink, D.L., Van Cappellen, P., van Bergen, M.J., 2014. Silicon isotope fractionation during abiotic silica precipitation at low temperatures: Inferences from flow-through experiments. Geochimica et Cosmochimica Acta 142: 95-114.

Hawkesworth, C. J., Bickle, M. J., Gledhill, A. R., Wilson, J. F., and Orpen, J. L., 1979. A 2.9 b.y. event in the Rhodesian Archaean. Earth and Planetary Science Letters 43, 285 -297 (1979).

Hawkesworth, C. J., Kemp, A. I. S., 2006. Evolution of the continental crust. Nature 443: 811 – 817.

Heck, P.R., Huberty, J.M., Kita, N.T., Ushikubo, T., Kozdon, R., Valley, J.W., 2011. SIMS analyses of silicon and oxygen isotope ratios for quartz from Archean and Paleoproterozoic banded iron formations. Geochimica et Cosmochimica Acta 75: 5879-5891.

Isley, A.E., 1995. Hydrothermal plumes and the Delivery of Iron to Banded Iron Formation. The Journal of Geology 103: 169-185.

Kamber, B. S., Whitehouse, M. J., Bolhar, R., Moorbath, S., 2005. Volcanic resurfacing and the early terrestrial crust: Zircon U-Pb and REE constraints from the Isua Greenstone Belt, southern West Greenland. Earth and Planetary Science Letters 240, 276-290.

Kamber, B.S., Webb, G.E., 2001. The geochemistry of late Archaean microbial carbonate: implications for ocean chemistry and continental erosion history: Geochimica et Cosmochimica Acta 65: 2509-2525.

Kejun, H., Yanhe, L., Jiangeng, G., Feng, L., Yan, Q., 2014. Ore Geology Reviews. 57: 288-298.

Klein, C., 2005. Some Precambrian banded iron-formations (BIFs) from around the world: Their age, geologic setting, mineralogy, metamorphism, geochemistry, and origin. American Mineralogist 90: 1473-1499.

Marin-Carbonne, J., Chaussidon, M., Robert, F., 2012. Micrometer-scale chemical and isotopic criteria (O and Si) on the origin and history of Precambrian cherts: Implications for paleo-temperature reconstructions. Geochimica et Cosmochimica Acta 92: 129-147.

McGregor, V. R., and Mason, B., 1977. Petrogenesis and geochemistry of metabasaltic and metasedimentary enclaves in the Amîtsoq gneisses, West Greenland. American Mineralogist 62, 887-904.

Mueller, W. U., Mortensen, J. K., 2002. Age constraints and characteristics of subaqueous volcanic constructions, the Archean Hunter Mine Group, Abitibi greenstone belt. Precambrian Research 115: 119-152.

Mueller, W. U., Stix, J., Corcoran, P. L., Daigneault, R., 2009. Subaqueous calderas in the Archean Abitibi greenstone belt: An overview and new ideas. Ore Geology Reviews 35, 4-46.

Myers, J. S., 2001. Protoliths of the 3.8-3.7 Ga Isua greenstone belt, West Greenland. Precambrian Research 105, 129-141.

Nutman, A. P., Friend, C. R. L., Paxton, S., 2009. Detrital zircon sedimentary provenance ages for the Eoarchean Isua supracrustal belt southern West Greenland: Juxtaposition of an imbricated ca. 3700 Ma juvenile arc against an older complex with 3920-3760 Ma components. Precambrian Research 172, 212-233.

Oelze, M., von Blanckenburg, F., Hoellen, D., Dietzel, M., Bouchez, J., 2014. Si stable isotope fractionation during adsorption and the competition between kinetic and equilibrium isotope fractionation: Implications for weathering systems. Chemical Geology 380: 161-171.

Perry, E.C., Lefticariu, L., 2007. Treatise on Geochemistry. Volume 7 Sediments, Diagenesis, and Sedimentary Rocks, pp. 1-27. Ch. 7.05 – Formation and Geochemistry of Precambrian Cherts.

Robert, F., Chaussidon, M., 2006. A paleotemperature curve for the Precambrian oceans based on silicon isotopes in chert. Nature 443: 969-972.

Rollinson, H., 2003. Metamorphic history suggested by garnet-growth chronologies in the Isua Greenstone Belt, West Greenland. Precambrian Research 126, 181-196 (2003).

Rollinson, H. R., and Blenkinsop, T. G., 1995. The magmatic, metamorphic and tectonic evolution of the Northern Marginal Zone of the Limpopo Belt in Zimbabwe. Journal of the Geological Society (London) 152, 65 – 75.

Siever, R., 1992. The silica cycle in the Precambrian. Geochimica et Cosmochimica Acta 56: 3265-3272.

Steinhoefel, G., von Blanckenburg, F., Horn, I., Konhauser, K.O., Beukes, N.J., Gutzmer, J., 2010. Deciphering formation processes of banded iron formations from the Transvaal and the Hamersley successions by combined Si and Fe isotope analysis using UV femtosecond laser ablation. Geochimica et Cosmochimica Acta 74: 2677-2696.

Treguer, P.J., De La Rocha, C.L., 2013. The World Ocean Silica Cycle, Annu. Rev. Mar. Sci. 5, 477-501.

Van den Boorn, S.H.J.M., van Bergen, M.J., Vroon, P., de Vries, S.T., Nijman, W., 2010. Silicon isotope and trace element constraints on the origin of ~3.5 Ga cherts: Implications for Early Archaean marine environments. Geochimica et Cosmochimica Acta 74: 1077-1103.

Van den Boorn, S. H. J. M., van Bergen, M. J., Nijman, W., Vroon, P. Z., 2007. Dual Role of seawater and hydrothermal fluids in Early Archean chert formation: Evidence from silicon isotopes. Geology 35: 939-942.

Whitehouse, M. J., Fedo, C. M., 2007. Microscale heterogeneity of Fe isotopes in >3.71 Ga banded iron formation from the Isua Greenstone Belt, southwest Greenland. Geology 35, 719-722.

Wilson, J.F., 1990. A craton and its cracks: some of the behavior of the Zimbabwe block from the Late Archean to the Mesozoic in response to horizontal movements, and the significance of some of its mafic dyke fracture patterns. Journal of African Earth Sciences (and the Middle East) 10: 483-501.

Ziegler, K., Chadwick, O. A., White, A. F., Brzezinski, M. A., 2005. δ^{30}Si systematics in a granitic saprolite, Puerto Rico. Geology 33: 817-820.

APPENDIX A-4

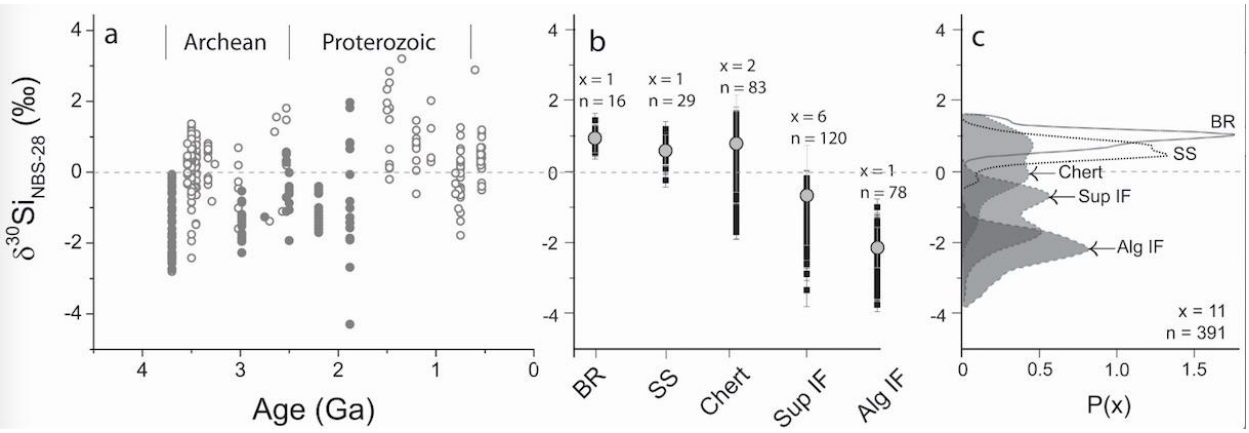


Figure 4-1. Silicon isotope record of chert and banded iron formation (BIF) through time, compared to the range of silicon isotope values of different chert and BIF types from this study from the 3 Ga Buhwa Greenstone Belt, Zimbabwe. (a) Plot showing all compiled $\delta^{30}Si$ data (2-12; in ‰, n = 288) versus time. Data were compiled from bulk (MC-ICP-MS, IRMS) and high-spatial resolution (SIMS, femtosecond laser ablation) techniques. Note what appears to be a slight increasing trend through time. A single anomalous data point ($\delta^{30}Si$ = +5.2 at 1.7 Ga) was omitted. (b) Plot showing our SIMS data from the ~3 Ga Buhwa Greenstone Belt, Zimbabwe. BR = bedrock, SS = quartz arenite sandstone, Chert = greenstone-associated chert, Sup IF = Superior-type banded iron formation, Alg IF = Algoma-type banded iron formation. X indicates the number of samples analyzed; n indicates the total number of spot analyses on x samples. (c) Probability density distribution plot (after Marin-Carbonne et al., 2012) for each sample in (b).

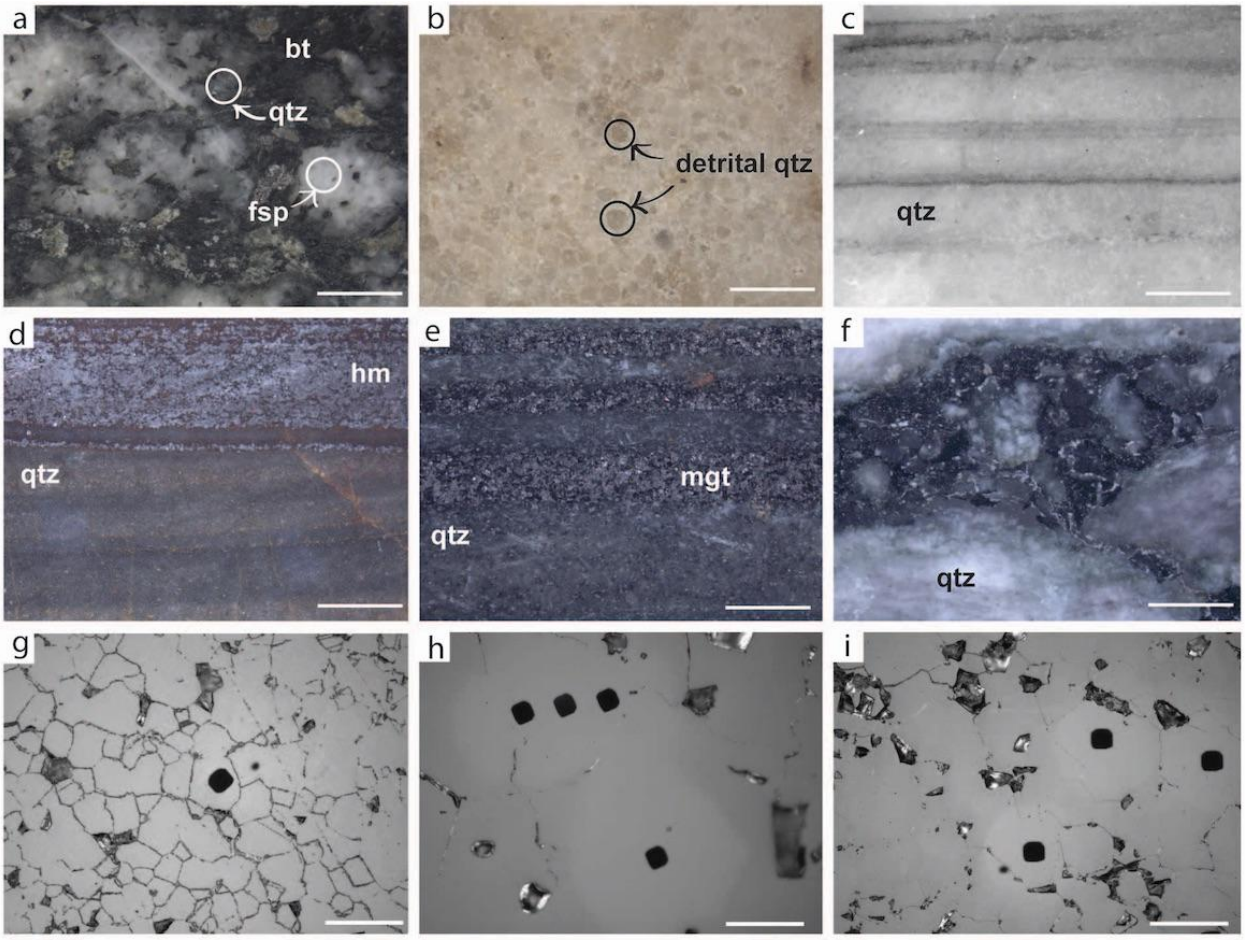


Figure 4-2. (a-f) Incident light images of representative rock types used in this study. Scale bar is 2.5 mm. (g-i) Reflected light images showing analytical spots from representative samples used in this study, scale bar 60 μm. (a) Tokwe segment gneissic bedrock (sample ZB_182) from the ~3Ga Buhwa Greenstone Belt (BGB), Zimbabwe, showing coarse-grained, bands of quartz, feldspar, and biotite, with typical gneissic texture. (b) Well-rounded, detrital quartz arenite sandstone (sample ZB_240) from the ~3 Ga BGB. (c) Greenstone-associated chert (sample ZB_105) from the ~3 Ga BGB showing alternating bands of quartz and organic carbon. (d) Superior-type BIF (sample ZB_23) from the ~ 3 Ga BGB, showing fine-grained bands of quartz (qtz) and hematite (hm). (e) Algoma-type BIF (sample IS_02_06) from the > 3.7 Ga Isua Greenstone Belt, SW Greenland, showing coarse-grained bands of quartz (qtz) and magnetite (mgt), with minor amounts of amphibole. (f) Silicified felsic volcanic rock (sample AB-11-12) from the ~ 2.72 Ga Hunter Mine Group, AGB. Note replacement patches of quartz (qtz), and preserved volcanic textures. (g) Superior-type BIF sample from the Buhwa Greenstone Belt showing SIMS analysis points on a single crystal. (h) Algoma-type BIF sample from the Isua Greenstone Belt showing SIMS analysis points on single crystals. (i) Algoma-type BIF sample from the Abitibi Greenstone Belt showing SIMS analysis points.

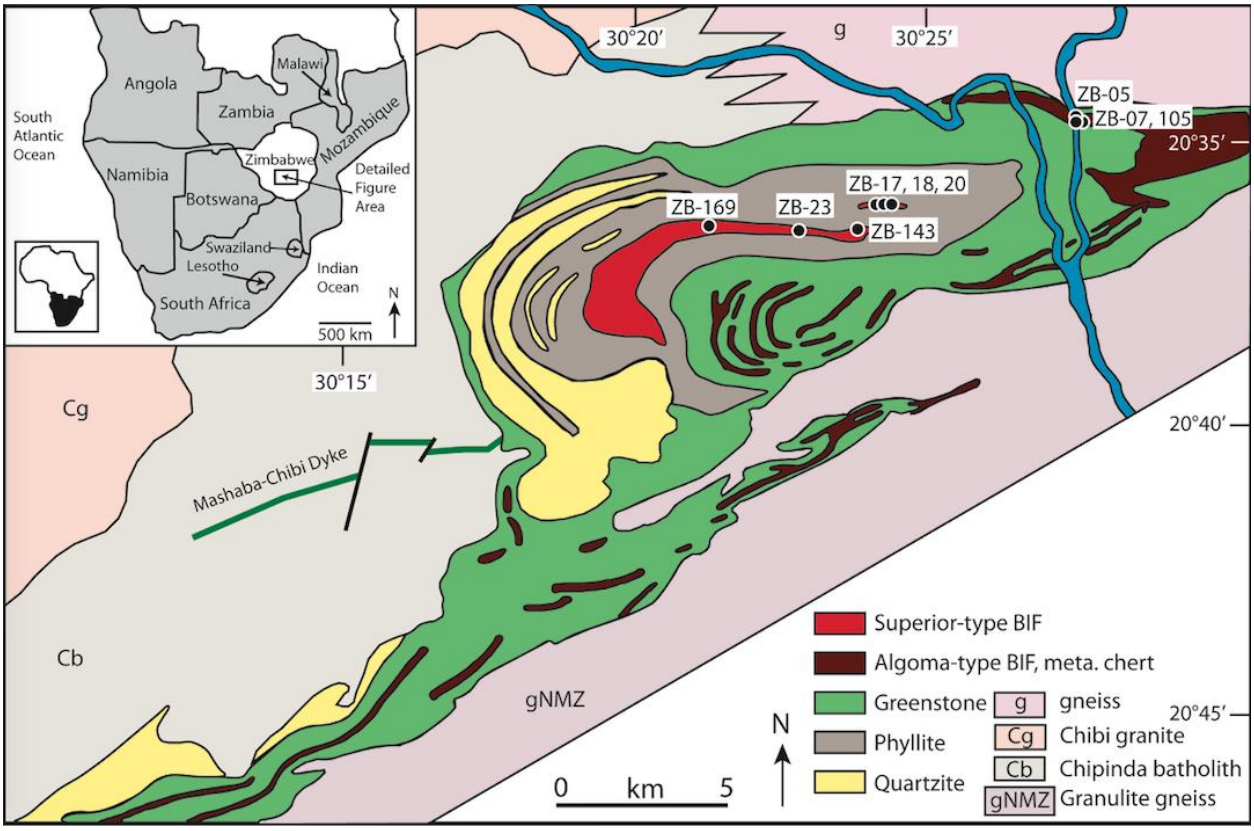


Figure 4-3. Geologic map of Buhwa Greenstone Belt, Zimbabwe, with an inset showing the location of the greenstone belt in Zimbabwe. Samples from this study are labeled with their respective sample numbers. Modified from Fedo et al. (1995).

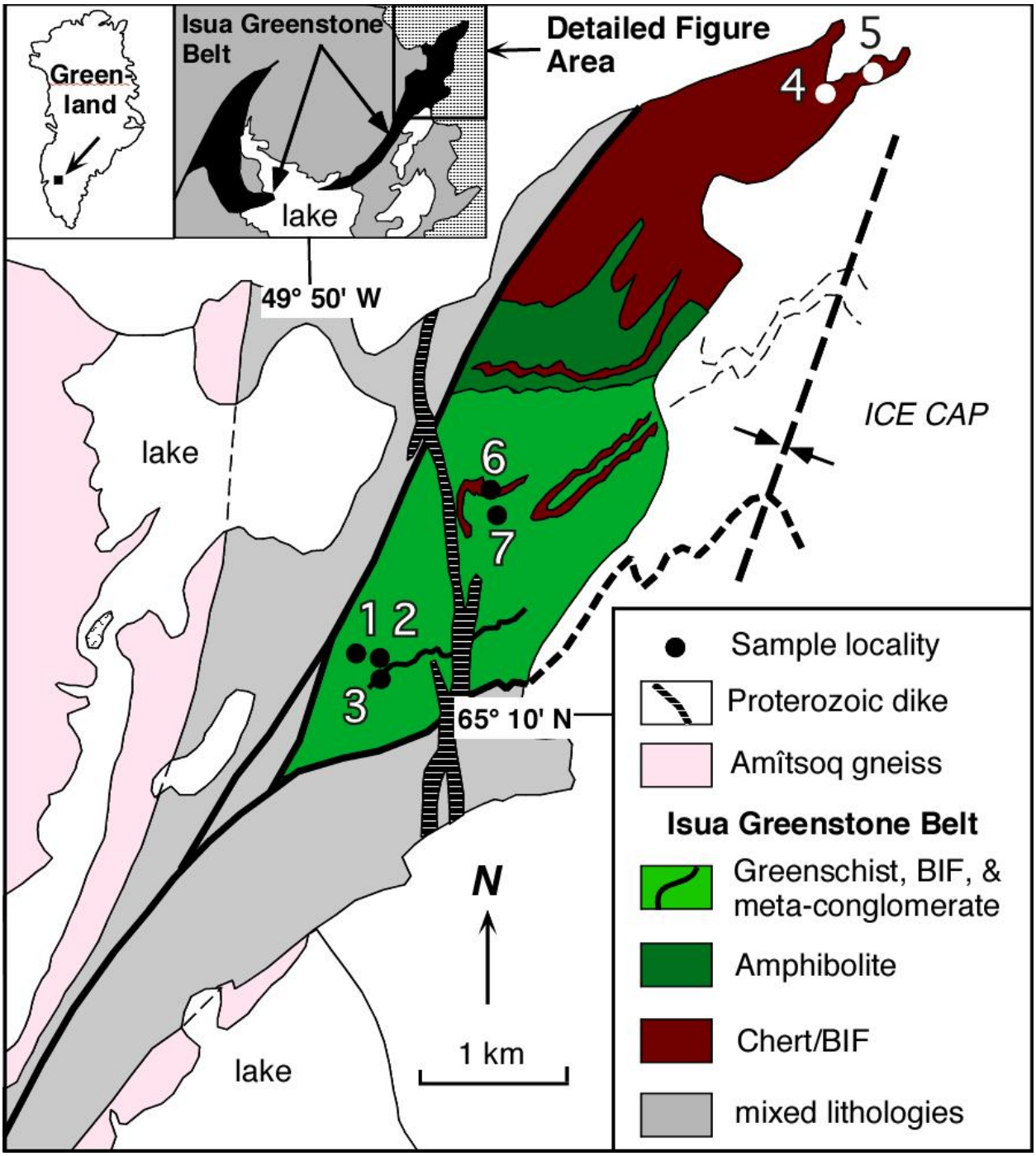


Figure 4-4. Geologic map of the Northeastern section of the Isua Greenstone Belt, with an inset showing the location of the greenstone belt in SW Greenland. Modified from Fedo (2001). Sample localities marked by numbers. 1 = banded iron formation (sample IS-02-05), 2 = banded iron formation (sample IS-02-06), 3 = chert clasts from conglomeritic unit (sample ISB 5b), 4 = banded iron formation (sample IS-02-08), 5 = banded iron formation (sample ISB 55) 6 = bedded chert (samples ISB 26, ISB 28) 7 = brecciated pillow basalt (sample ISB 31b).

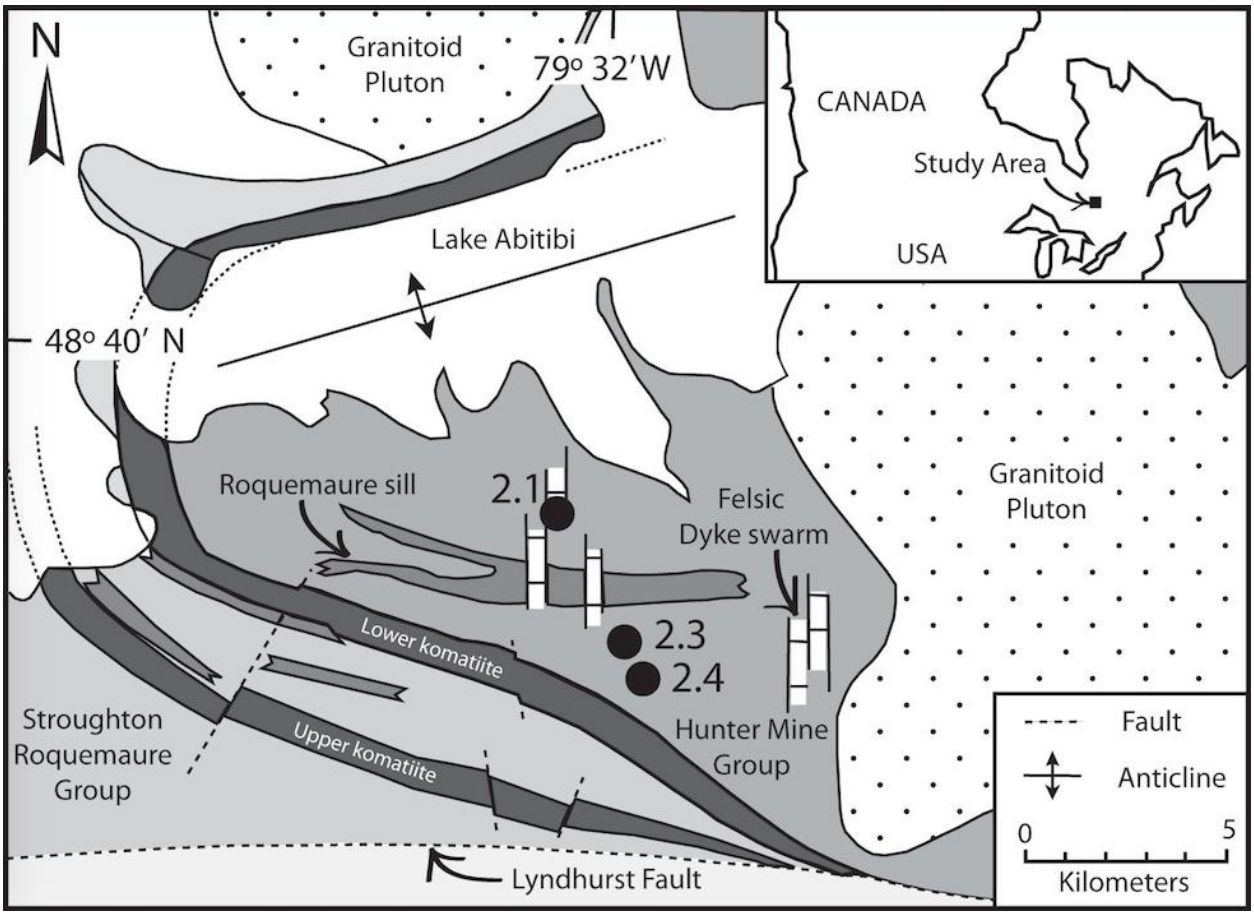
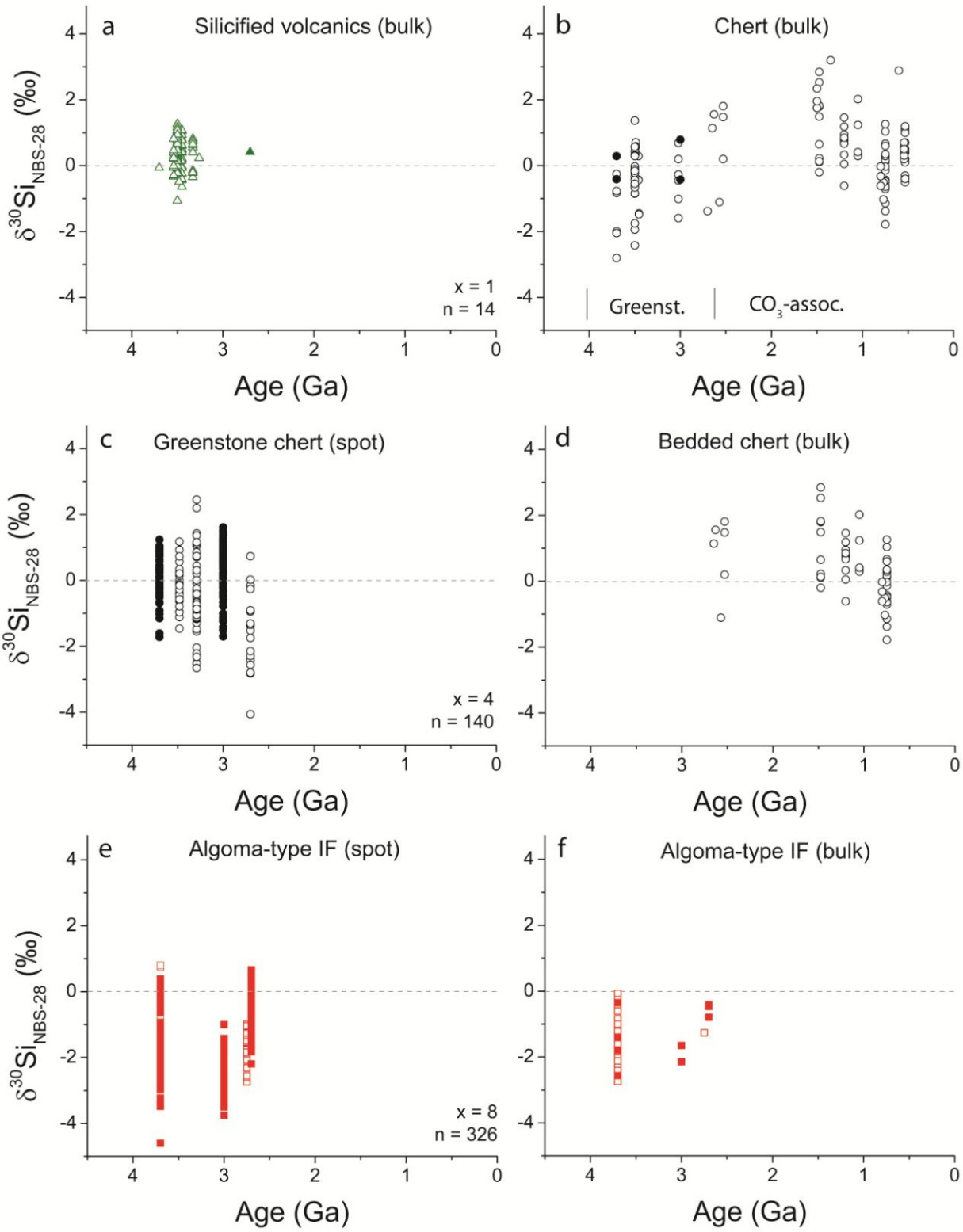


Figure 4-5. Geologic map of Hunter Mine Group region, of the Abitibi Greenstone Belt, with an inset showing the location of the greenstone belt in Canada. Samples in this study come from outcrops labeled 2.1, 2.3, and 2.4. Modified from Dostal and Mueller (2012).

Figure 4-6. All measured silicon isotope values separated into different rocks types. All points represent measured bulk values, or spot data that has been converted to bulk values utilizing a probability density distribution value as outlined in Marin-Carbonne et al. (2012). Open symbols for each plot represent data from previous studies; closed symbols represent data from this study. Where indicated, x = the number of samples analyzed, and n = the number of analyses on x samples. Dashed line represents $\delta^{30}Si = 0$ ‰ for reference. (a) Plot containing all compiled $\delta^{30}Si$ data for silicified volcanic rocks. (b) Plot containing all compiled $\delta^{30}Si$ data for non-silicified volcanic chert against time. Greenst. = Greenstone-associated chert, CO_3-assoc. = chert hosted within carbonate rocks, and Bio = indicates chert formed after geologic evidence for silica-secreting organisms. (c) Plot showing spot $\delta^{30}Si$ data for greenstone chert. (d) Plot showing bulk $\delta^{30}Si$ data for diagenetic chert hosted within carbonate rocks. (e) Plot showing spot $\delta^{30}Si$ data for Algoma-type banded iron formation. (f) Plot showing bulk $\delta^{30}Si$ data for Algoma-type banded iron formation.


a
Silicified volcanics (bulk)
x = 1
n = 14
b
Chert (bulk)
Greenst.
CO3-assoc.
c
Greenstone chert (spot)
x = 4
n = 140
d
Bedded chert (bulk)
e
Algoma-type IF (spot)
x = 8
n = 326
f
Algoma-type IF (bulk)
δ30SiNBS-28 (‰)
Age (Ga)

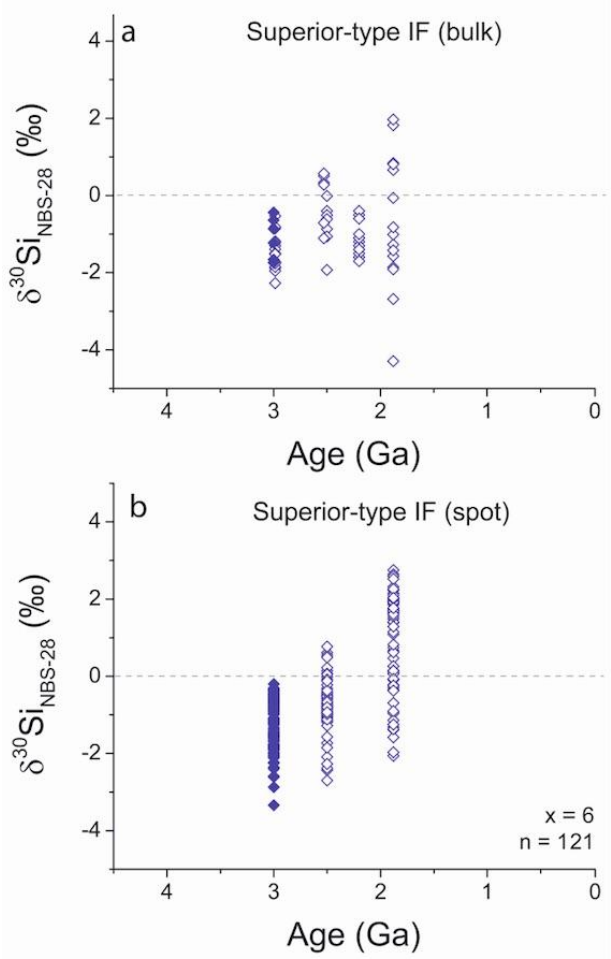


Figure 4.7. All measured silicon isotope values of Superior-type banded iron formation. All points represent measured bulk values, or spot data that has been converted to bulk values utilizing a probability density distribution value as outlined in Marine-Carbonne et al. (2012). Open symbols for each plot represent data from previous studies, while closed symbols represent data from this study. Where indicated x = the number of samples analyzed, and n = the number of analyses on x samples. Dashed line represents $\delta^{30}Si = 0$ ‰. (a) Plot showing bulk $\delta^{30}Si$ data for Superior-type banded iron formation. (b) Plot showing spot $\delta^{30}Si$ data for Superior-type iron formation. Note the increasing trend from ~3 – 1.8 Ga.

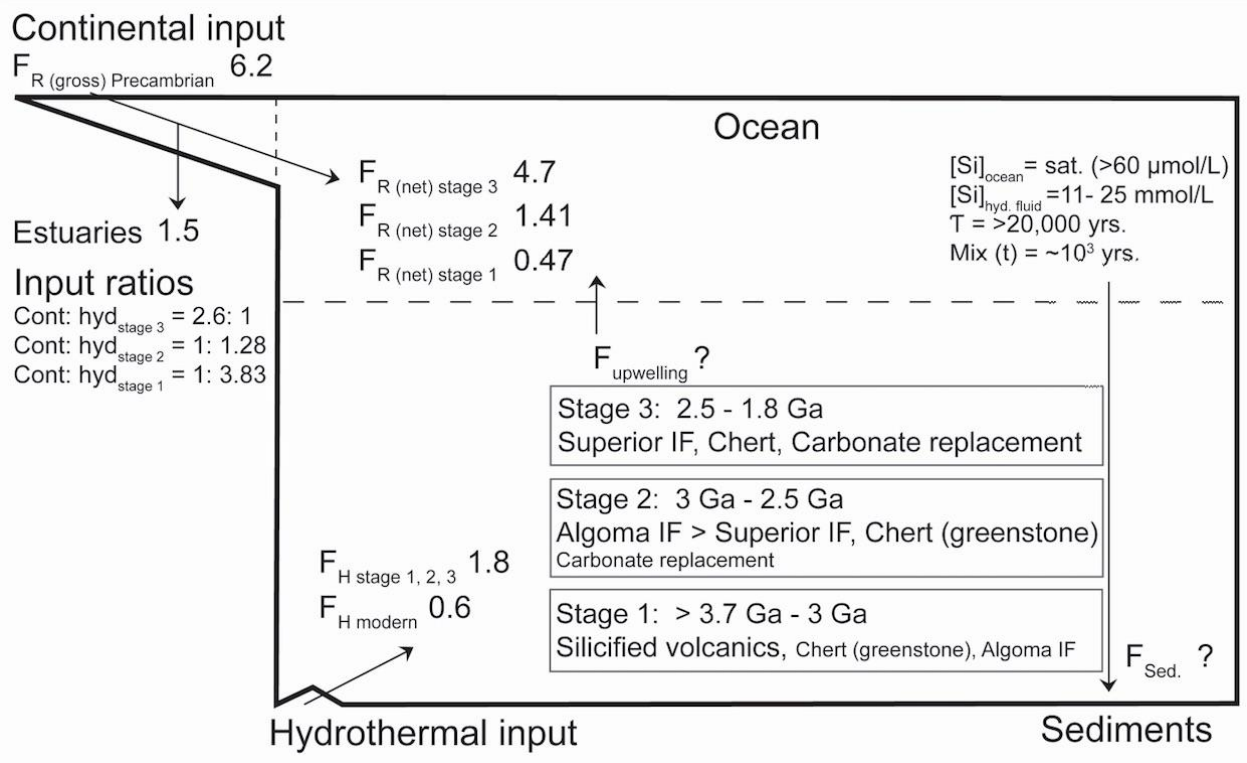


Figure 4-8. Box model for estimating changing flux estimates during the time interval of sample deposition in this study (3.7 - 1.8 Ga). Flux estimates were made by adjusting modern values for continental and hydrothermal inputs (Treguer and de la Rocha, 2013) for changing Precambrian conditions (Isley, 1995) such as increased hydrothermal input, and the growth history of continental material. See text for details.

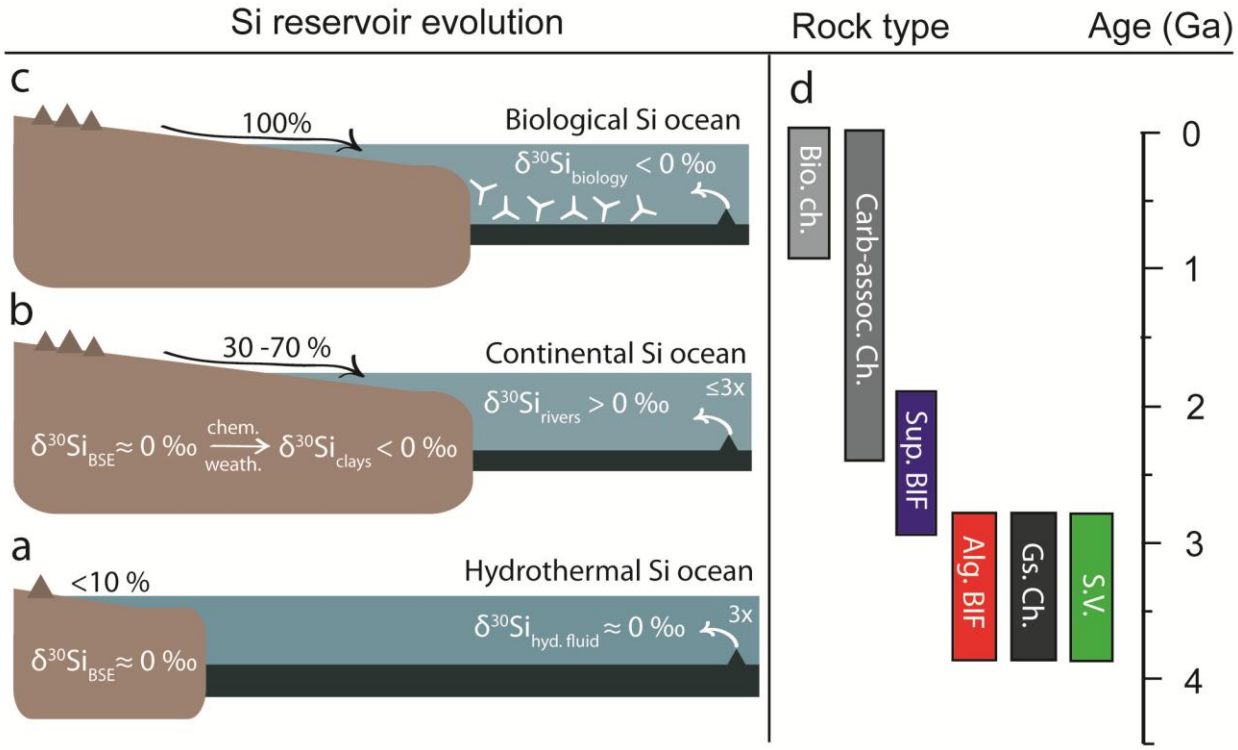


Figure 4-9. Schematic diagram showing growth and emergence of continental crust, and distribution of different rock types represented in the compiled $\delta^{30}Si$ archive through time. (a) Diagram representing the Paleo- through Meso-Archean, where oceans were dominated by hydrothermal sources ($\delta^{30}Si_{hyd.\ fl.} \approx 0$ ‰) three times greater than modern values and little riverine input (< 10%; Fig. 4-8; Isley, 1995) from small continents ($\delta^{30}Si_{BSE} \approx 0$ ‰ (Savage et al., 2012). Hyd. fl. = hydrothermal fluids, BSE = bulk silicate Earth. (b) Diagram representing the increased riverine delivery (30 – 70 % of modern; Fig. 4-8) of continentally sourced silicon ($\delta^{30}Si_{rivers} > 0$ ‰) to the oceans from chemical weathering of newly emergent continental crust. (c) Diagram representing the Phanerozoic silicon cycle dominantly by continental: hydrothermal sources of 10:1, with silicon isotope composition of the ocean overprinted by biology ($\delta^{30}Si_{biology} > 0$ ‰). Presence of silica-secreting organisms represented by siliceous sponge spicules. (d) Plot showing the distribution of rock types represented in the compiled silicon isotope record with respect to time. Note the temporal restrictions of certain rock types.

CHAPTER V

CONCLUSION

Research in this dissertation has investigated the use of geochemical and isotopic tools to differentiate silicified volcanic rocks from chemical sedimentary cherts, established that primary silicon isotope heterogeneity can be preserved in Precambrian rocks, and determined that silicon isotope compositions process-specific silicon isotope compositions are transferred to the geologic record.

In the second chapter, the compositional evolution of volcanic rocks through progressive silicification is documented petrographically and geochemically. During the process of silicification, volcanic rocks lost their primary original REE signatures, and gained the signature of seawater. Because of this, REE patterns of silicified rocks cannot be used to determine process of formation, even though this is commonplace, and used regularly to interpret the protoliths of highly deformed and metamorphosed quartz-rich rocks. The lack of being able to successfully "fingerprint" a protolith through geochemistry led to the idea of measuring silicon isotopes in quartz as a potential tool to differentiate between these silicified rocks and chemical sedimentary precipitates.

The third chapter investigates the application of silicon isotopes to understanding how silicified rocks and chemical sedimentary cherts are formed by testing whether or not primary silicon-isotope heterogeneity can be preserved in the geologic record. To do this, silicon isotopes from quartz were measured using the SIMS from a quartz-amygdaloidal, quartz-cemented, basaltic pillow breccia and chert samples from the ~3.7 Ga Isua Greenstone Belt. In the pillow breccia, oxygen and silicon isotope measurements were measured in quartz from both the amygdules, which have been interpreted to have formed contemporaneous with pillow formation, and the later cement that binds pillow fragments. Both occurrences of quartz have the same oxygen isotope composition, which is consistent with resetting during amphibolite-facies metamorphism. By contrast, amygdules are isotopically light and show extreme micro-scale heterogeneity (nearly the entire dynamic range of silicon isotope compositions) consistent with rapid disequilibrium precipitation from hydrothermal solutions and experimental studies; the cement is isotopically heavier and preserves much less silicon isotope heterogeneity more suggestive of lower temperature slow precipitation of quartz. The data indicate that primary silicon isotope heterogeneity can be preserved. Adjacent chert samples have silicon isotope compositions that overlap the cement, suggesting they precipitated under the same cooler, but overall similar hydrothermal conditions. This research indicates that oxygen isotopes do not need to be used as a screen to determine whether silicon isotopes in the same sample can preserve primary signatures.

With the knowledge that primary silicon isotope values can be preserved even in metamorphosed rocks, Chapter four investigates whether process-specific isotope compositions of different rock types could be transferred to the geologic record by measuring the silicon isotope composition in quartz of multiple rock types across a basin that preserves (1) shallow shelf clastic sediments and Superior-type BIF and (2) basinal rocks dominated by mafic and ultramafic volcanic rocks that are interlayered with Algoma-type chert and BIF. Quartz from the inferred gneissic bedrock, as well as detrital quartz likely derived from that source, have the expected isotope compositions associated with igneous rocks. Because there is no compositional change attached with the mechanical breakdown of bedrock, detrital quartz should have approximately the same value as the source. Different chert and BIF types (Algoma versus Superior), however, have statistically distinct silicon "whole-rock" isotope compositions (determined from pooling individual spot analyses), despite each having a considerable amount of inter- and intra-sample heterogeneity. Any interpretation of the compiled silicon isotope

archive must be divided into different chert types based on depositional affinity and process of formation. To test whether or not some of the heterogeneity in the current compiled silicon isotope archive of chert is the result of pooling all samples together regardless of depositional environment or mechanism of formation, additional chert samples from different environments and ages were analyzed, then combined with all previously published silicon isotope data, and tagged by chert type. Regardless of age (although all analyzed samples are Archean), silicified rocks have a silicon-isotope composition of essentially zero, which is similar to both the host rock composition and that of hydrothermal solutions. Greenstone chert, dominantly of Archean age, likely formed in environments with profuse hydrothermal input, where quartz precipitates locally via conductive cooling in rapidly evolving hydrothermal systems. Archean Algoma-type BIFs have a wide range of silicon-isotope compositions, but typically are isotopically light, and interpreted to result from kinetic isotope effects due to disequilibrium precipitation via conductive cooling. Unlike all other divisions of samples studied, Superior-type BIFs (3 Ga to 1.88 Ga) record a systematic unidirectional shift in silicon-isotope compositions that goes from negative to positive through time. Because river water is the only known source of isotopically heavy silicon due to fractionation during silicate weathering, the pattern is interpreted to be the result of incremental continental emergence beginning at ~3 Ga. As a result, the marine reservoir evolved from a dominantly hydrothermal signature until about 3 Ga and then a continental one until about 1 Ga. After this time, the advent of silica-fixing organisms modified the marine reservoir to one greatly influenced by biology.

APPENDIX A-5

Additional figures

Chapter III - Comparison of data from this study to experimental silicon isotope data

The focus of chapter III is explaining the extreme silicon isotope heterogeneity we have identified in the quartz amygdules of the pillow breccia sample. Because quartz amygdules likely precipitated from hydrothermal fluid, we extrapolated the very limited experimental data from low-temperature (T < 60ºC) quartz precipitation experiments (Geilert et al., 2014) to determine $\Delta^{30}Si_{solid\text{-}fluid}$ values relevant for high temperature precipitation of quartz using both linear (Fig. 5-1) and logarithmic (Fig. 5-2) functions.

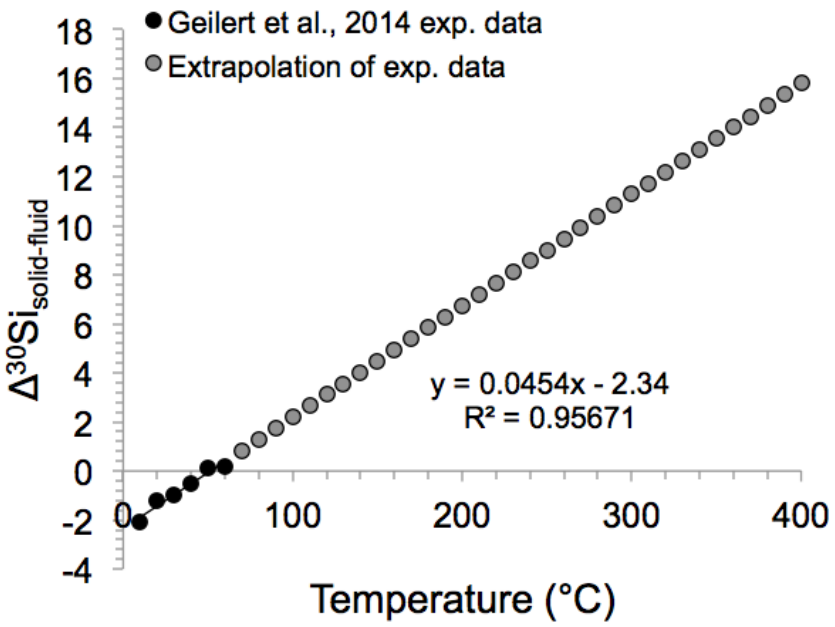


Figure 5-1. Geilert et al. (2014) experimental data (black circles), for $\Delta^{30}Si_{solid\text{-}fluid}$ at temperatures ranging from 10 to 60 °C. At temperature ranges expected for hydrothermal systems (200 – 400 °C), the predicted $\Delta^{30}Si_{solid\text{-}fluid}$ value would be > +6 ‰. Such positive $\Delta^{30}Si_{solid\text{-}fluid}$ values have never been measured for silicon isotopes. Furthermore, no known geochemical process predicts such positive values. At the y-intercept (0°C), the $\Delta^{30}Si_{solid\text{-}fluid}$ value is -2.3, which suggests that the lowest silicon isotope value for a quartz precipitate from a hydrothermal solution ($\delta^{30}Si_{HYD.\ FLUID}$ = -0.3‰) would be -2.6 (solving for the equation $\Delta^{30}Si_{solid\text{-}fluid} = \delta^{30}Si_{QTZ\ PPT} - \delta^{30}Si_{HYD.\ FLUID}$). As shown in in chapter III, many previous studies, and data presented in our study, have measured $\delta^{30}Si$ values lower than $\delta^{30}Si$ = -2.6 ‰ in quartz from chert and banded iron formation. We therefore conclude that a linear fit to the Geilert et al. (2014) data does not help to explain the values we measure in this study, or values measured in previous studies.

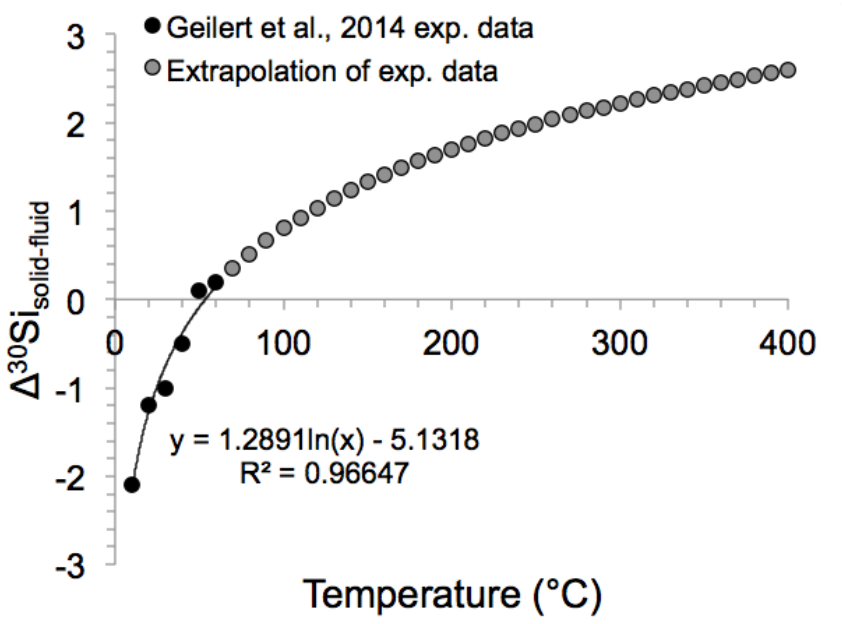


Figure 5-2. Plot showing logarithmic fit to the Geilert et al. (2014) data. As in Figure 5-1, experimental data is plotted as black circles. This data was fit with a logarithmic function to extrapolate the experimental data to higher temperatures (the values of which are plotted as grey circles) relevant to hydrothermal systems. On this plot, as temperatures approach 0 °C, the fit predicts a large range of $\delta^{30}Si$ values should occur along the asymptote. At higher temperatures, positive $\Delta^{30}Si_{solid\text{-}fluid}$ values are predicted.

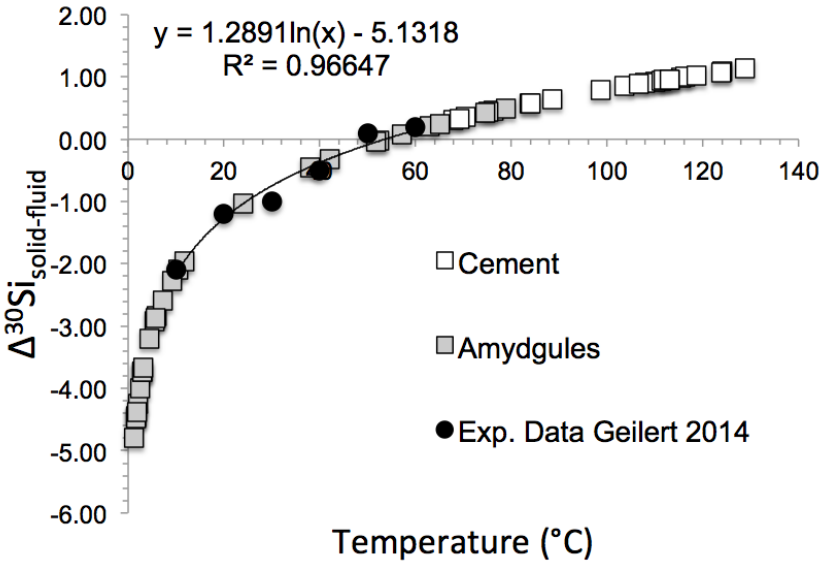


Figure 5-3. To understand how our data, which show extreme $\delta^{30}Si$ heterogeneity, fit in with the extrapolated experimental data in Figure 5-2, we used the logarithmic function to predict the temperature of precipitation for the quartz crystals in the amygdules, and cement from the pillow breccia sample, using the known $\delta^{30}Si$ value for hydrothermal fluid (-0.3 ‰) to plot $\Delta^{30}Si_{solid\text{-}fluid}$ verses temperature in Figure 5-3. Figure 5-3 shows that $\delta^{30}Si$ values measured for amygdules (gray squares), would correspond to temperatures mostly between 0-10°C, with some values extending to higher temperatures. This contradicts geologic information about the sample, which suggests quartz amygdules were formed under hydrothermal conditions (Appel et al., 2001). Additionally, $\delta^{30}Si$ values measured for cement (white squares) would correspond to temperatures roughly between 70-130°C, despite precipitating in between brecciated pillow basalt fragments, which indicate the basalt had cooled enough to exhibit brittle fracture. We argue that these temperatures are likely geologically implausible for the encasing quartz cement of the pillow breccia unit which likely precipitated from cooler fluids than the amygdules. Adjacent bedded chert has similar $\delta^{30}Si$ values as the quartz cement, and likely precipitated from ambient, cold, seawater, or mixed seawater and hydrothermal fluids. Based on this figure however, one would interpret our chert, and pillow breccia cement to have formed at temperatures reaching >120°C, which again is not geologically reasonable.

Based on Figures 5-1-5-3, we suggest that the experimental data of Geilert et al. (2014) cannot explain the large range of $\delta^{30}Si$ values that we measured in quartz amygdules, which span from approximately -5 to +1 ‰. Additionally, the experimental data contradicts geologic evidence for probable temperatures of precipitation for cherts and cement in our study. No experiments have measured silicon isotope fractionations as large as 6 ‰, and no $\delta^{30}Si$ values from experimental precipitates have been measured as low as -5 ‰. We feel justified in using a theoretical kinetic isotope fractionation model to explain the isotopically light values that we measure, because no equilibrium fractionation model for silicon isotopes can explain the extreme heterogeneity we have measured in crystals that come from a single sample and separated by just a few millimeters. More recent experimental work by Oelze et a. (2014) and (2015) confirms this approach. Moreover, we point out that all published experiments to date have measured the silicon isotope composition of quartz precipitated as amorphous opal-A, despite observations and experiments that suggest direct quartz precipitation from solution can occur, particularly at high-temperatures (e.g., Rimstidt and Barnes, 1980; Oehler, 1971; Mackenzie and Gees, 1971). Because we are studying samples that come from a hydrothermal system, where quartz precipitation was likely due to conductive cooling of hydrothermal fluids upon contact with cooler seawater (e.g., Van den Boorn, 2007), we further suggest our data cannot easily be explained by $\Delta^{30}Si_{solid\text{-}fluid}$ values determined for amorphous silica precipitated in low-temperature experiments.

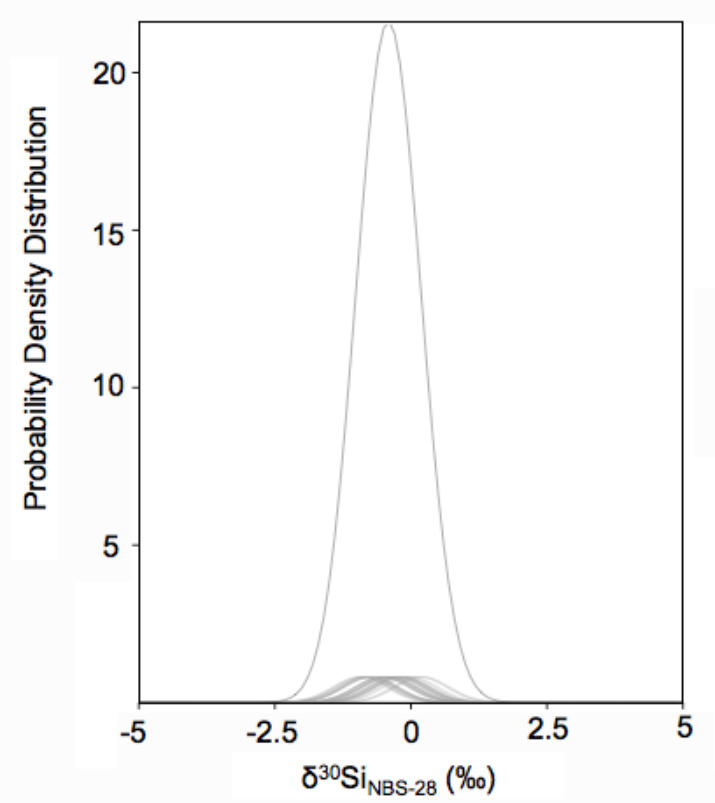


Figure 5-4. Probability density distribution plot calculated sample TEM-cf. Peak height was calculated following the methods outlined in Marin-Carbonne et al., 2012. Calculated peak value for 31 analyses on the TEM-cf sample was $\delta^{30}Si$ = -0.4 ± 0.7 ‰, which overlaps with the measured whole-rock value of the same sample ($\delta^{30}Si$ = -0.66 ± 0.03 ‰).

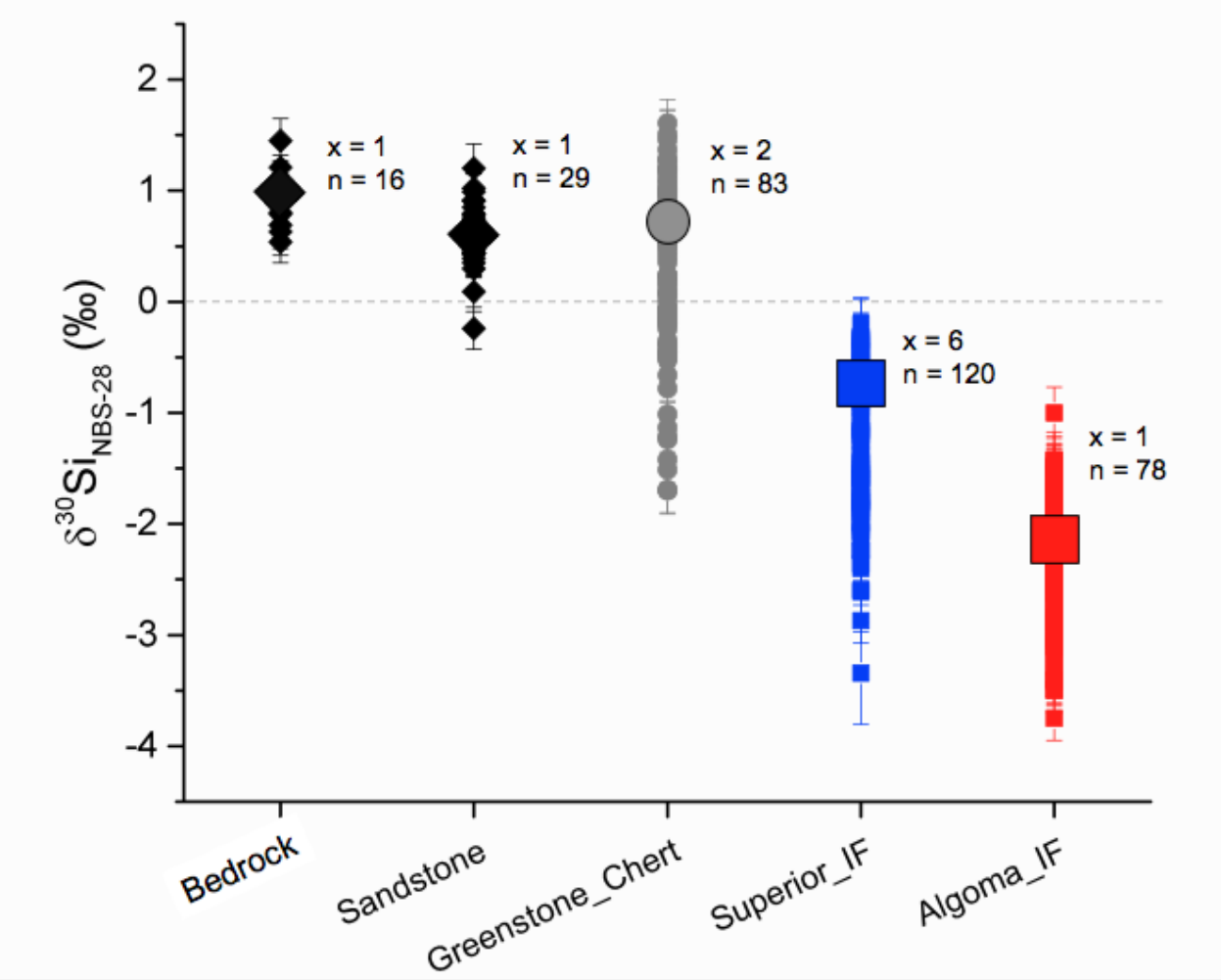


Figure 5-5. Plot of silicon isotope data separated by rock type for all samples from the ~3 Ga Buhwa Greenstone Belt, Zimbabwe. X = number of samples analyzed, n = number of points analyzed.

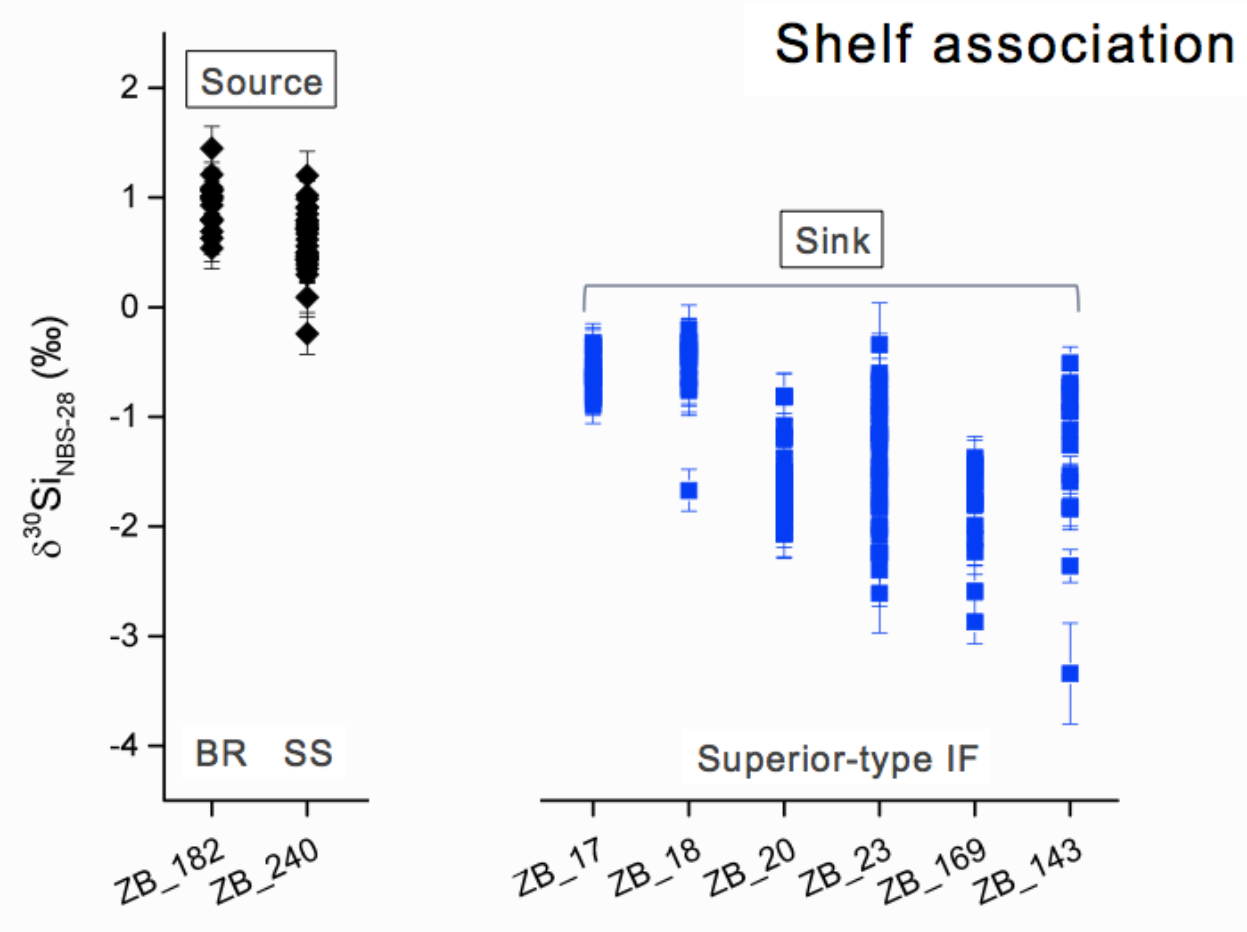


Figure 5-6. Plot of silicon isotope data separated by sample for all samples from the shelf association of the ~3 Ga Buhwa Greenstone Belt, Zimbabwe.

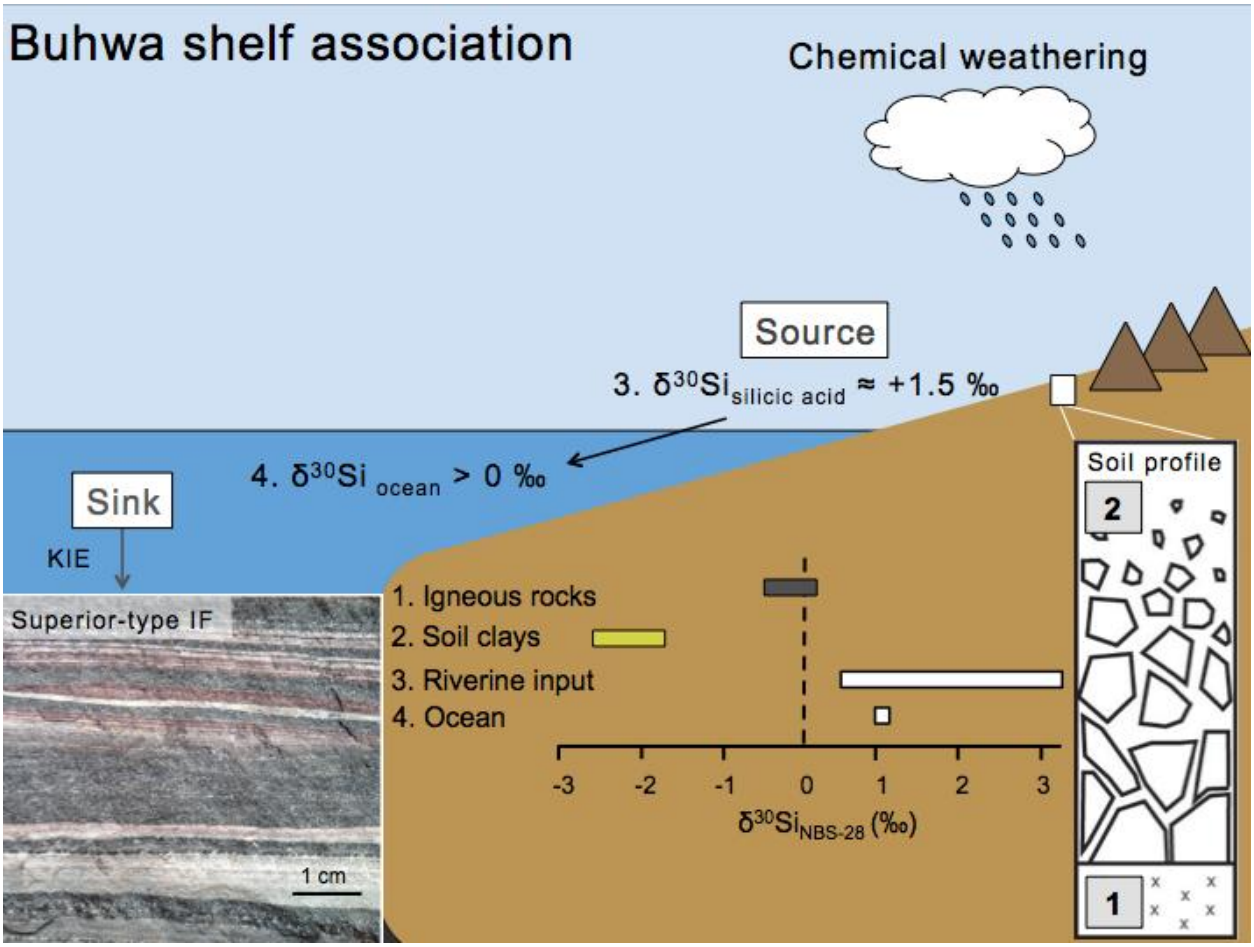


Figure 5-7. Cartoon representation of major sources and sinks in system for the shelf association of the ~3 Ga Buhwa Greenstone Belt, Zimbabwe.

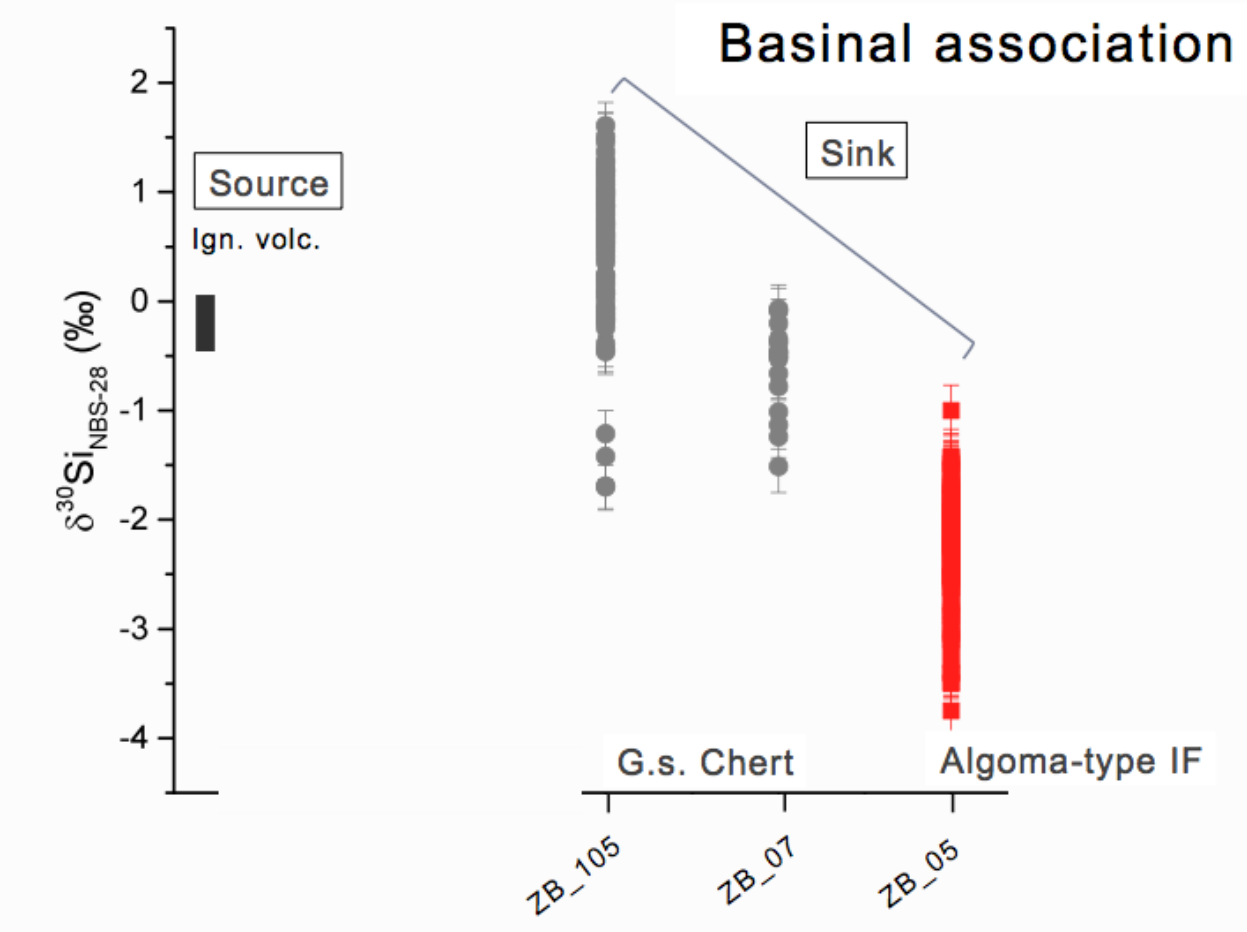


Figure 5-8. Plot of silicon isotope data separated by sample for all samples from the basinal association of the ~3 Ga Buhwa Greenstone Belt, Zimbabwe.

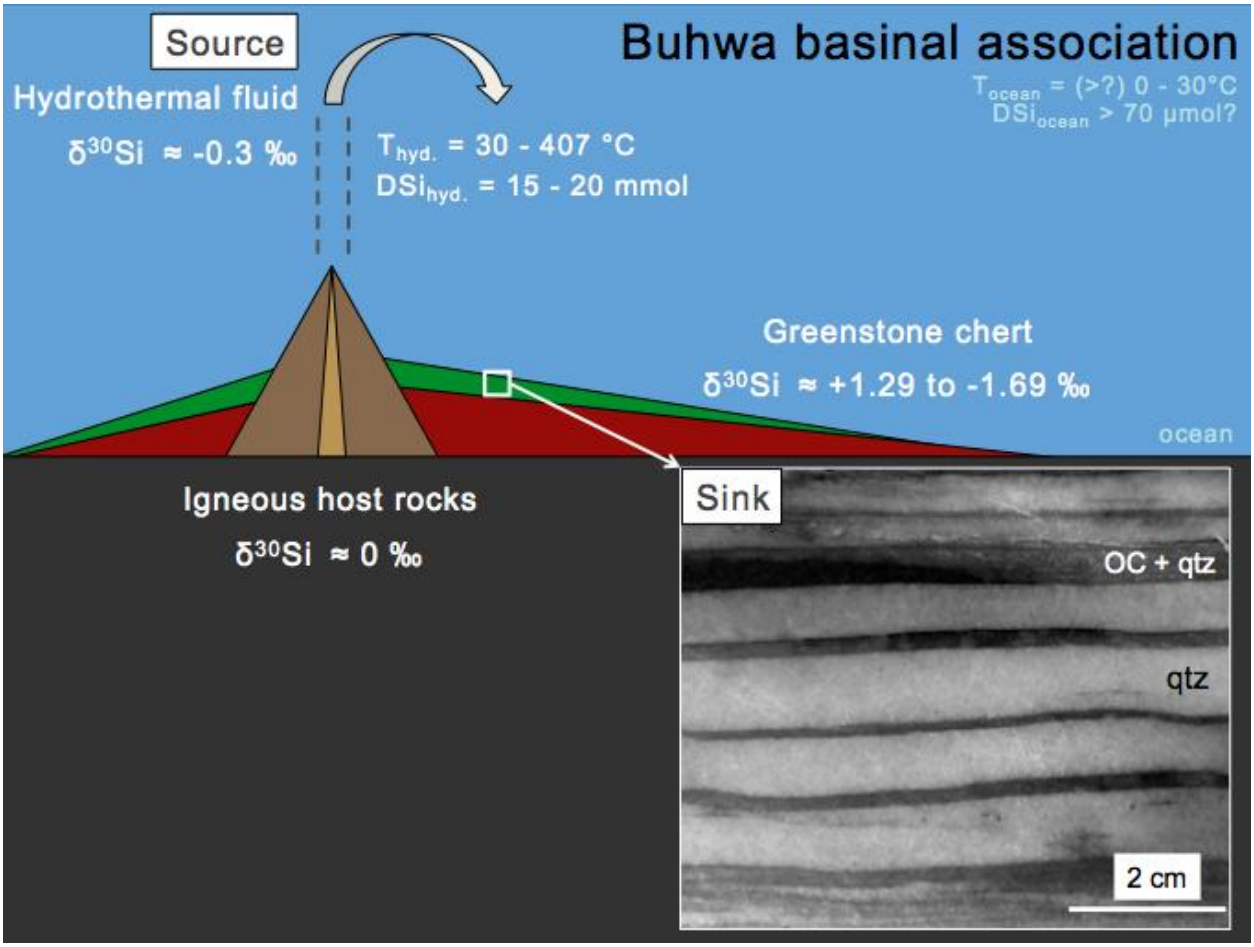


Figure 5-9. Cartoon representation of major sources and sinks in system for the basinal association of the ~3 Ga Buhwa Greenstone Belt, Zimbabwe.

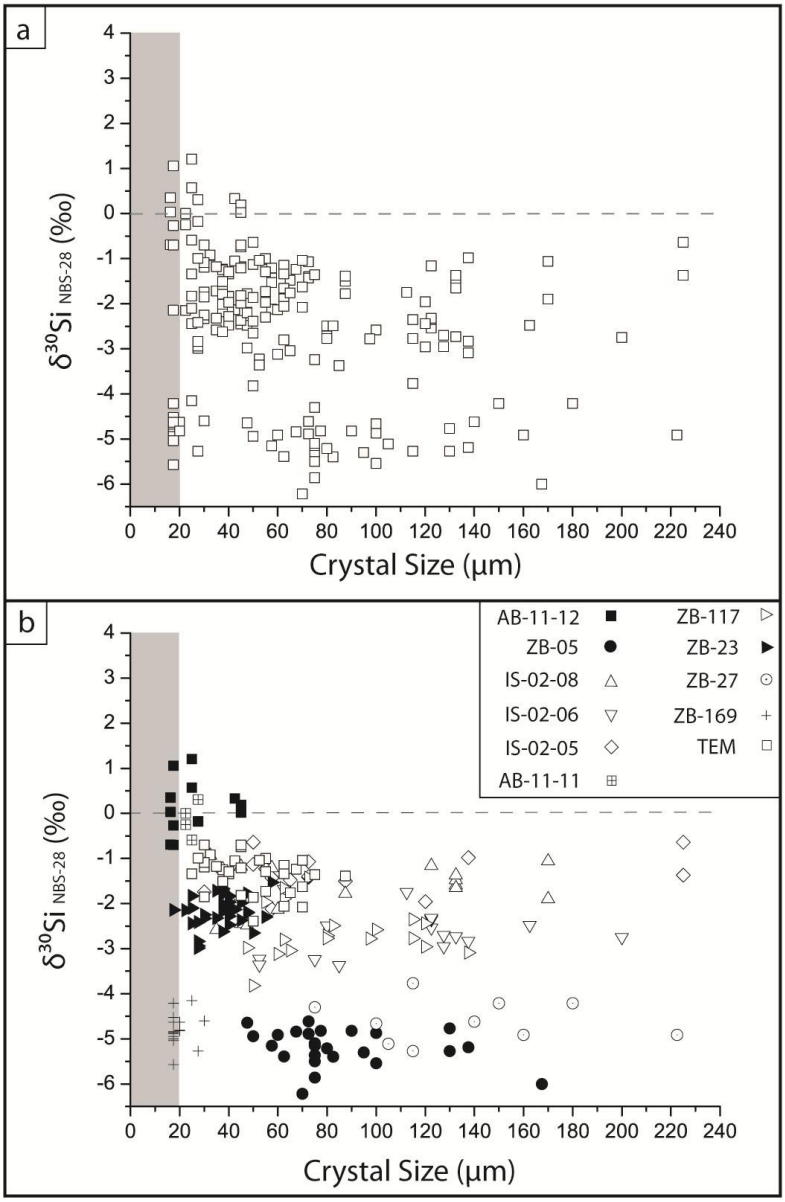


Figure 5-10. Plot showing raw measured $\delta^{30}Si$ verses crystal size (microns). Note no trend with increasing crystal size. Data are uncorrected for standard comparison for use in this plot, data are tabulated in Appendix A-5, Table 4-7.

Methods

Standard information

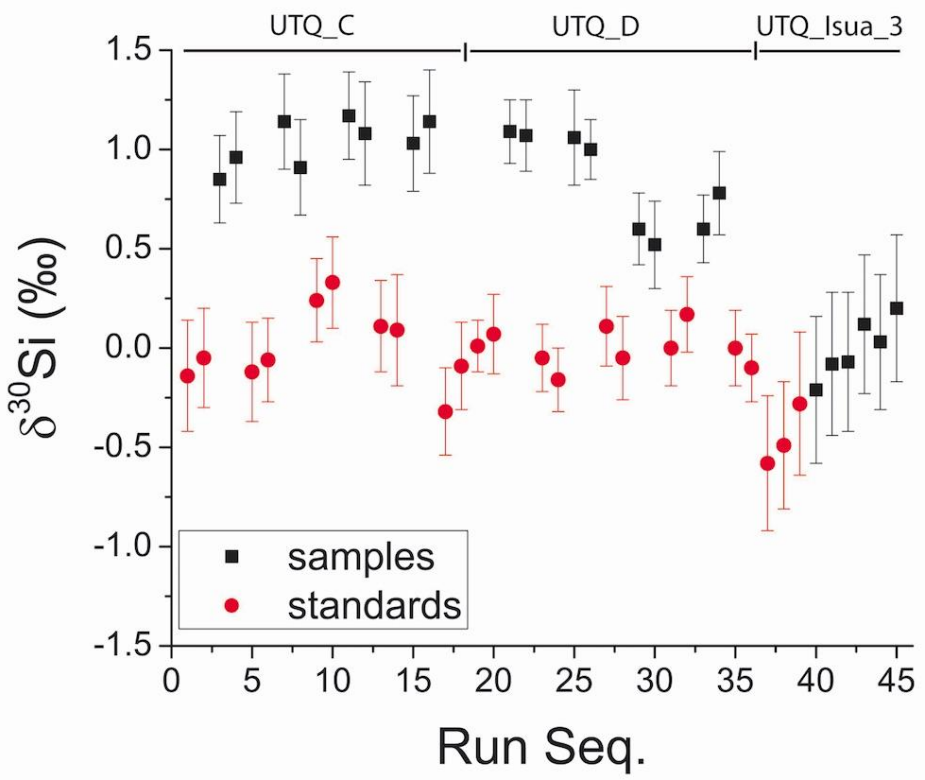


Figure 5-11. Plot showing δ^{30}Si isotope values of international standard (NBS-28; red filled circles) and internal house standard (UTQ; black filled squares) vs. Run #. Different pieces of the internal house standard UTQ include UTQ_C, UTQ_D, and UTQ_Isua_3, are labeled at the top of the plot. The "peak" value of each UTQ standard piece used was determined via the methods outlined in Marin-Carbonne et. al (2012).

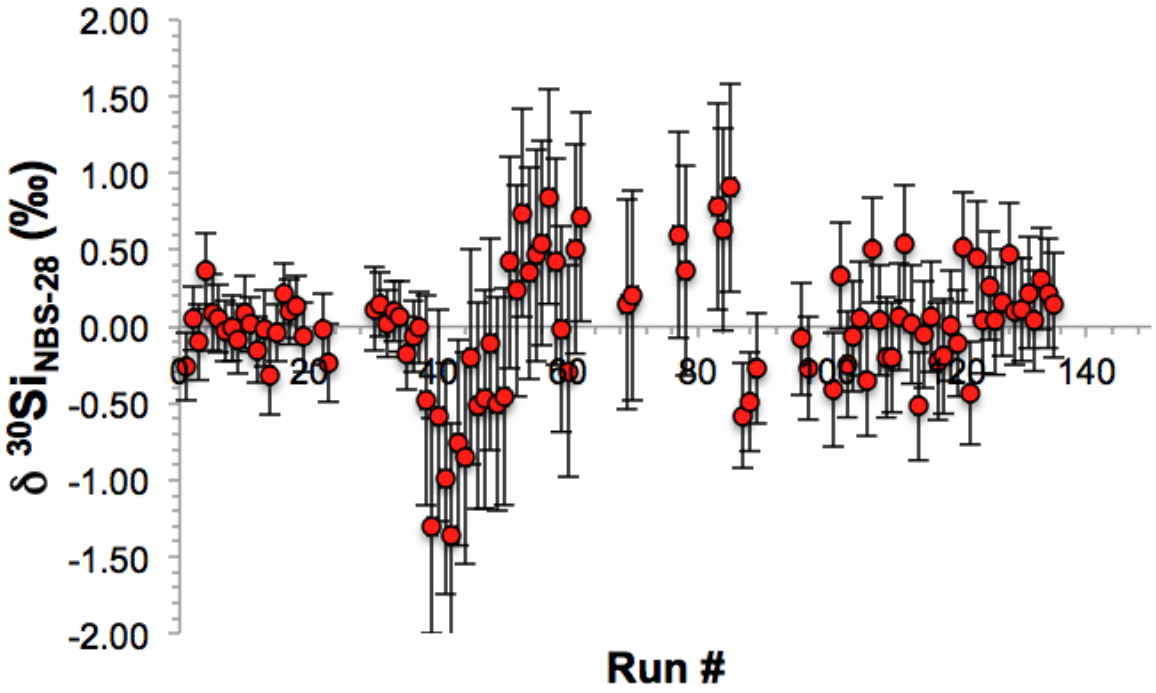


Figure 5-12. Plot showing δ^{30}Si isotope values of international standard (NBS-28; red filled circles) vs. run #.

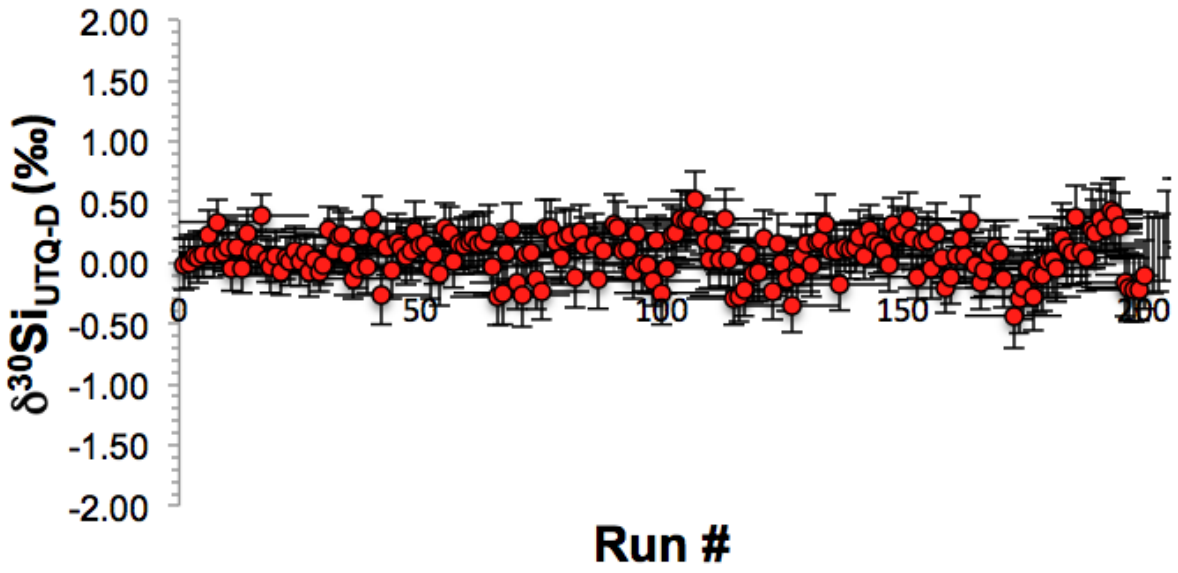


Figure 5-13. Plot showing δ^{30}Si isotope values of internal standard (UTQ-D red filled circles) vs. run #.

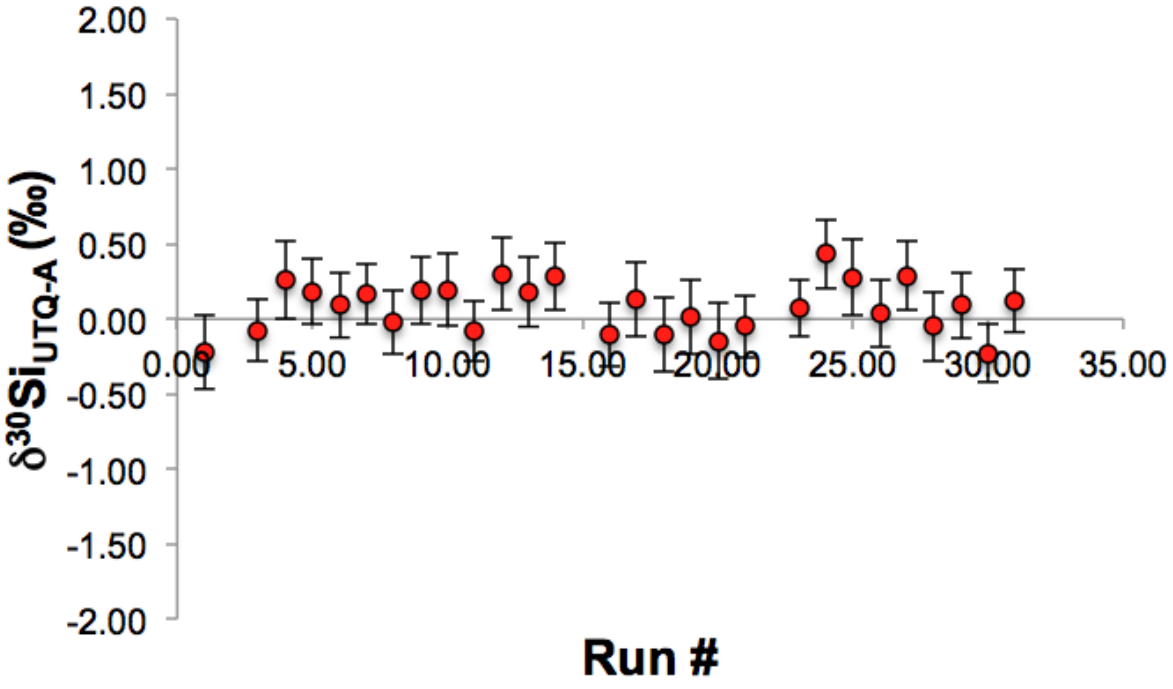


Figure 5-14. Plot showing δ^{30}Si isotope values of internal standard (UTQ-A red filled circles) vs. run #.

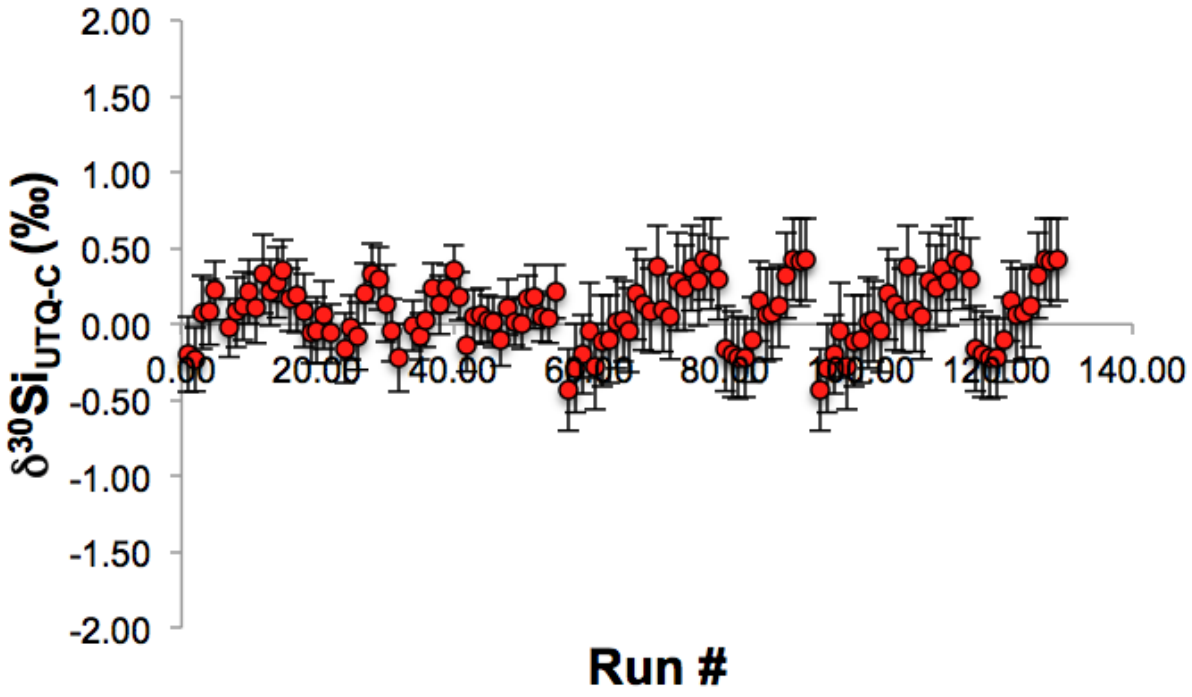
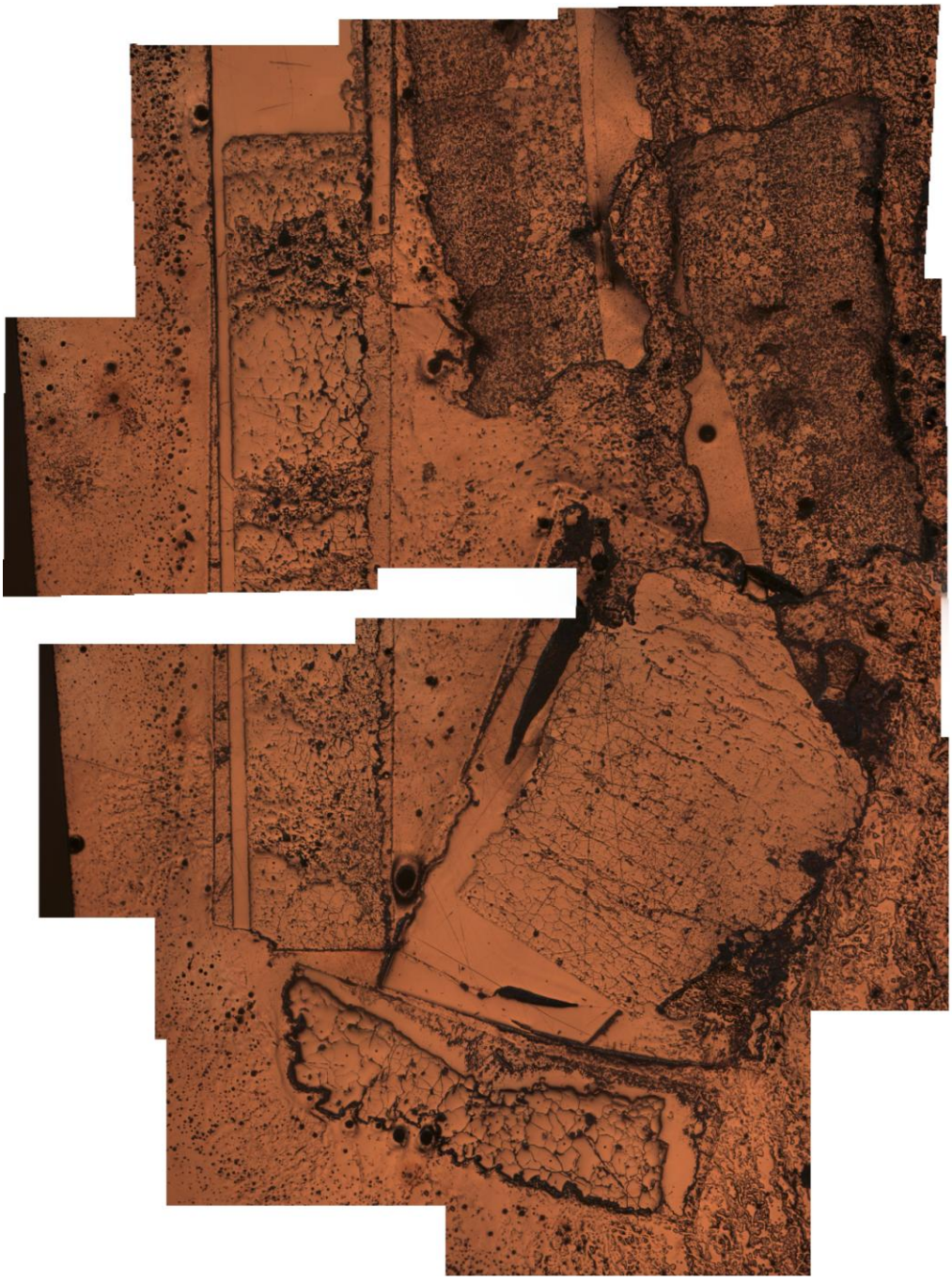


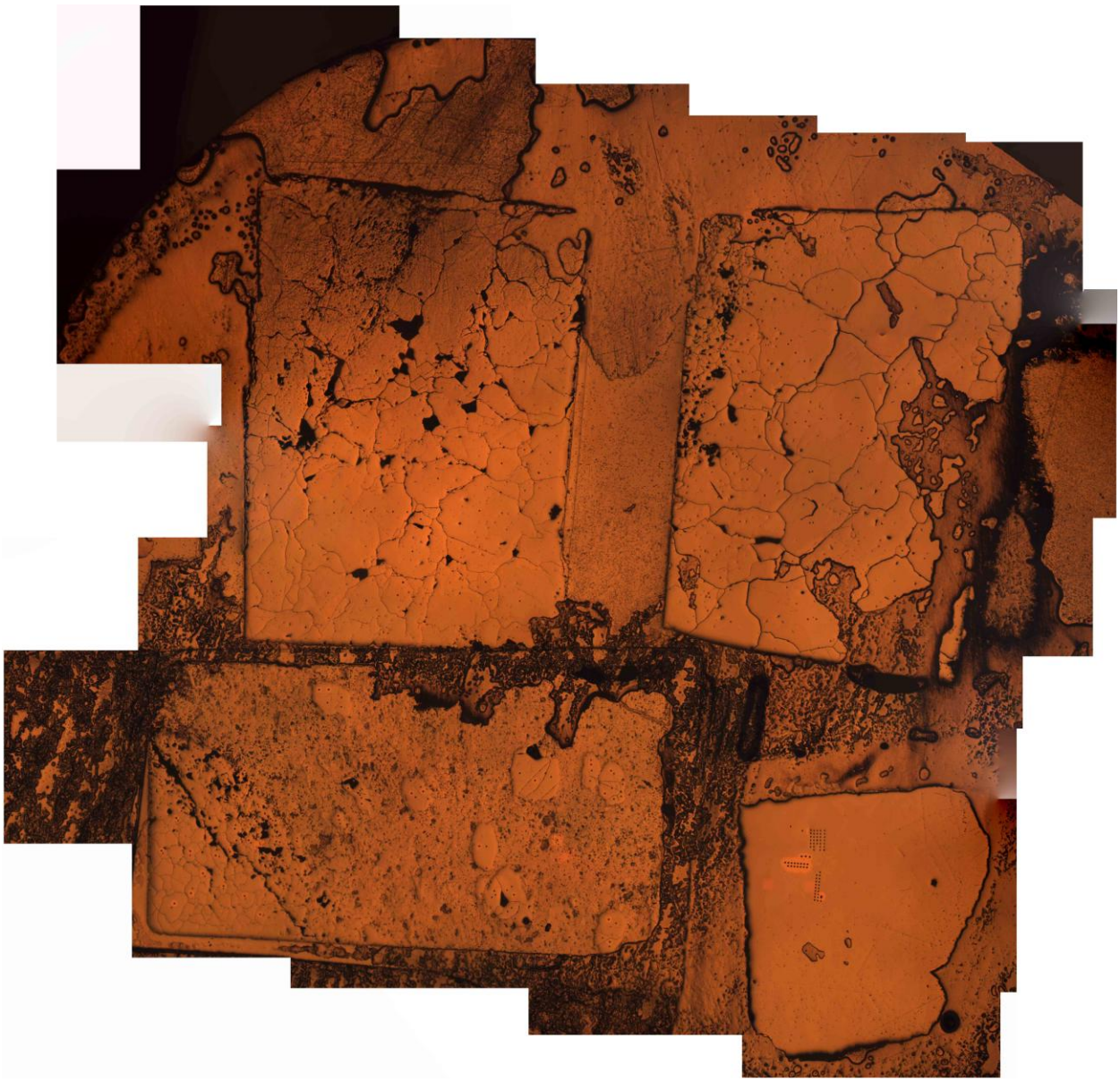
Figure 5.15. Plot showing δ^{30}Si isotope values of internal standard (UTQ-C red filled circles) vs. run #.

Sample information
Full mount maps, post-gold coat analyses



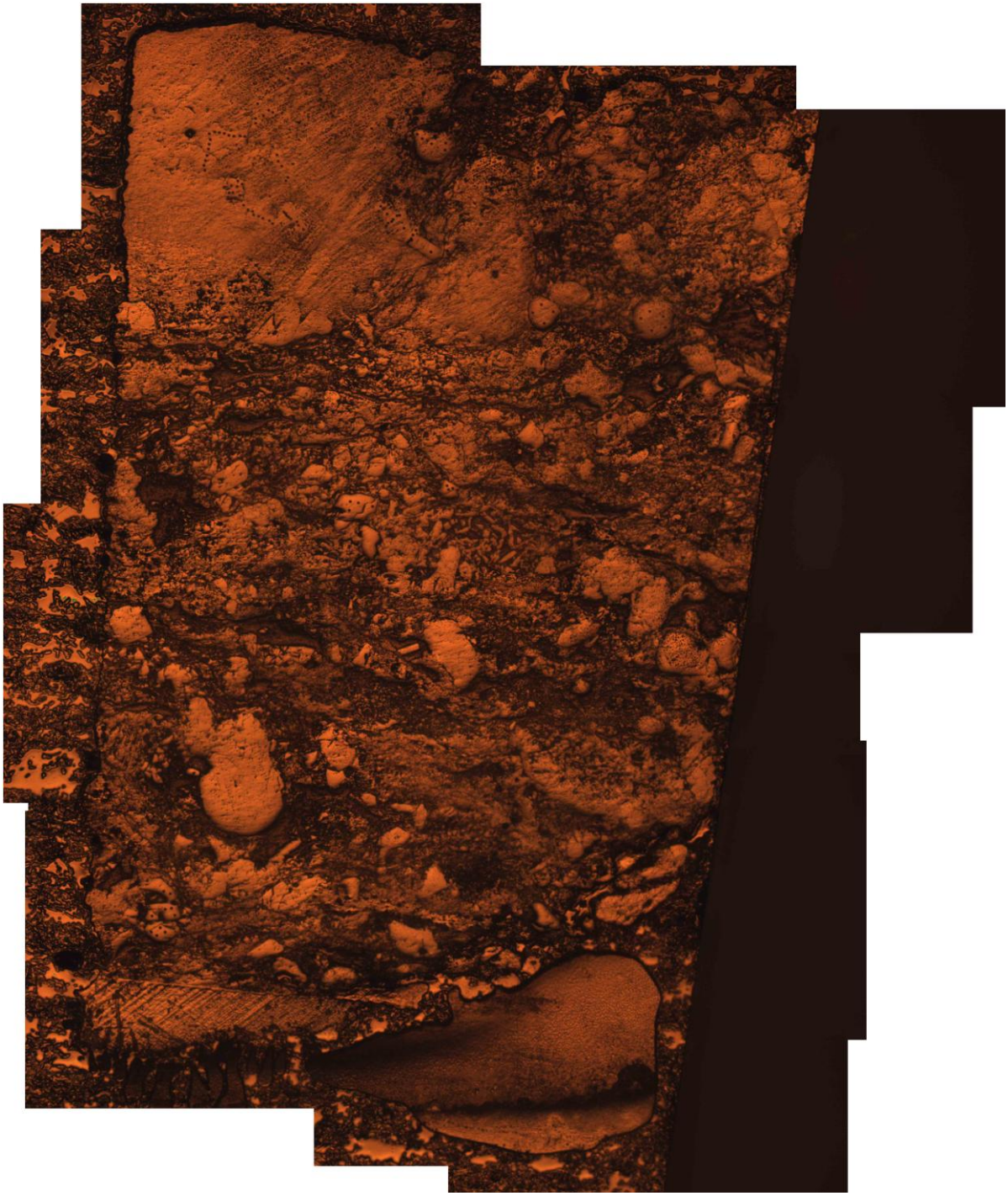
0.5 cm

Figure 5-16. Full gold coat, post-analysis map of samples ZB-169a, b, ZB-07, ZB-27, ZB-05 (in clock-wise order starting at North). Sample ZB 05 is ~ 1 cm in length for scale.



5 mm

Figure 5-17. Full gold coat, post-analysis map of samples ISB 26, ISB 28, UTQ, ISB-31b (in clock-wise order starting at Northwest). UTQ standard chip is ~5 mm in length for scale.



0.5 cm

Figure 5-18. Full gold coat, post-analysis map of sample AB-11-11. Length of sample is roughly ~ 1 cm for scale.

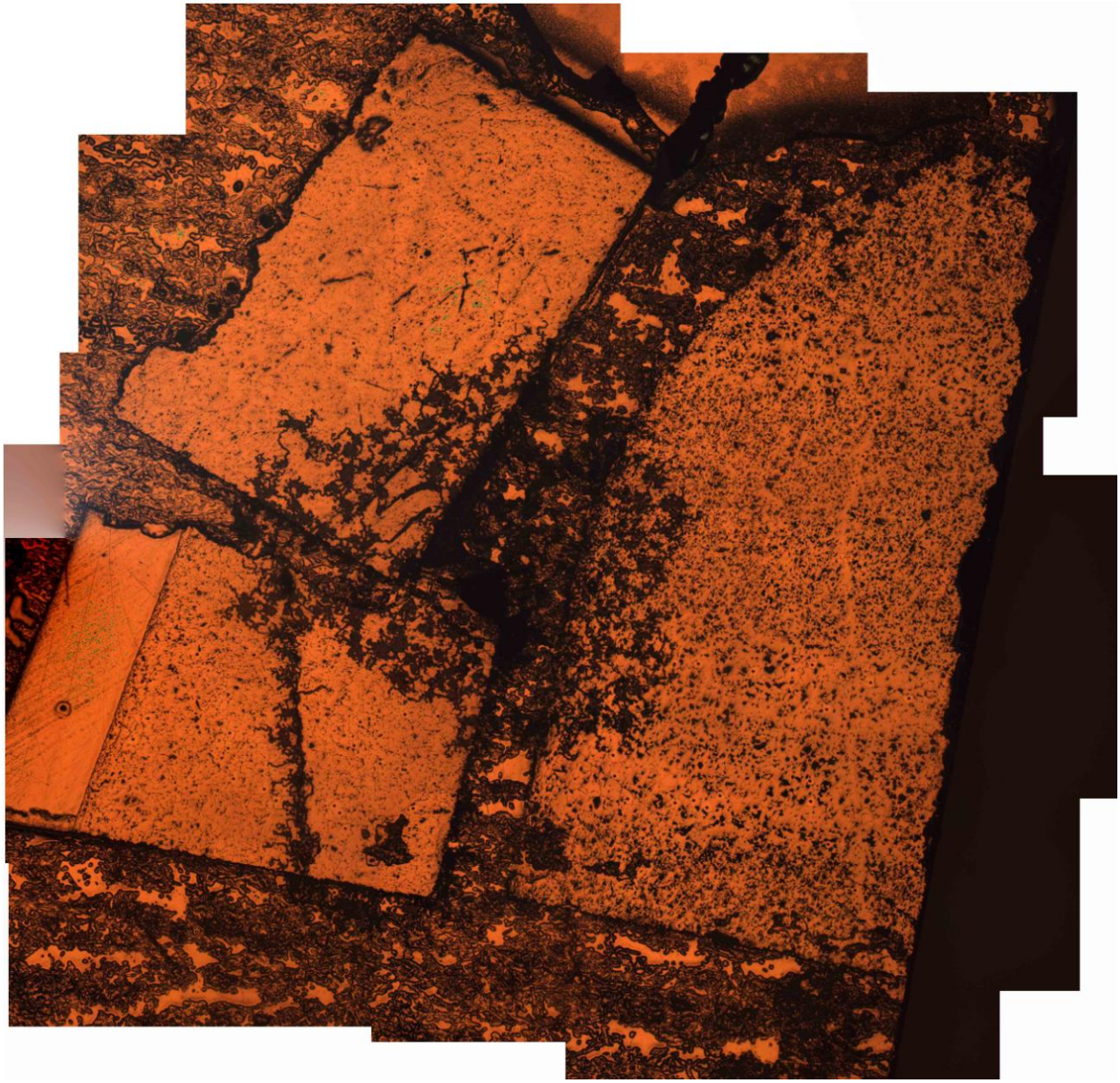
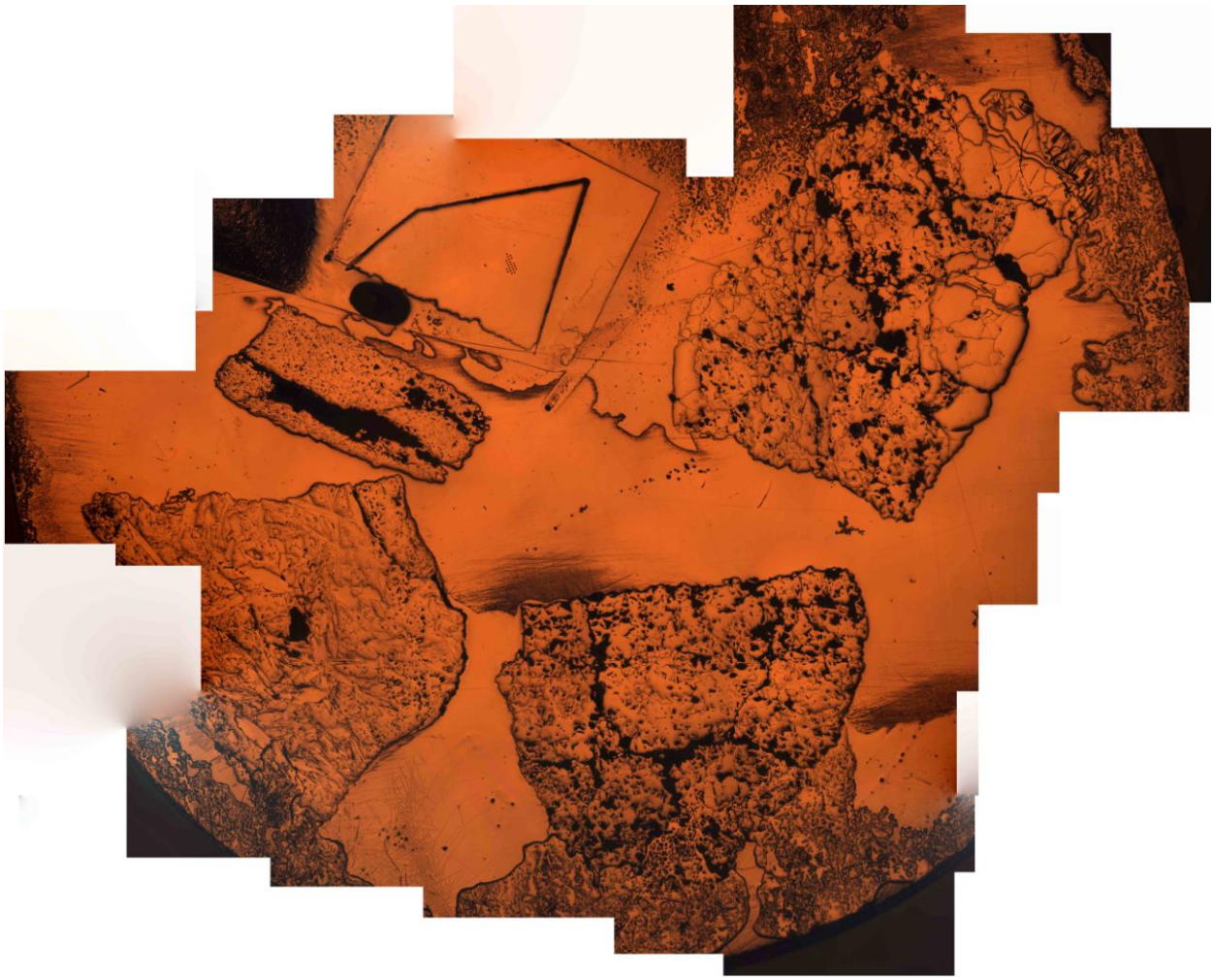
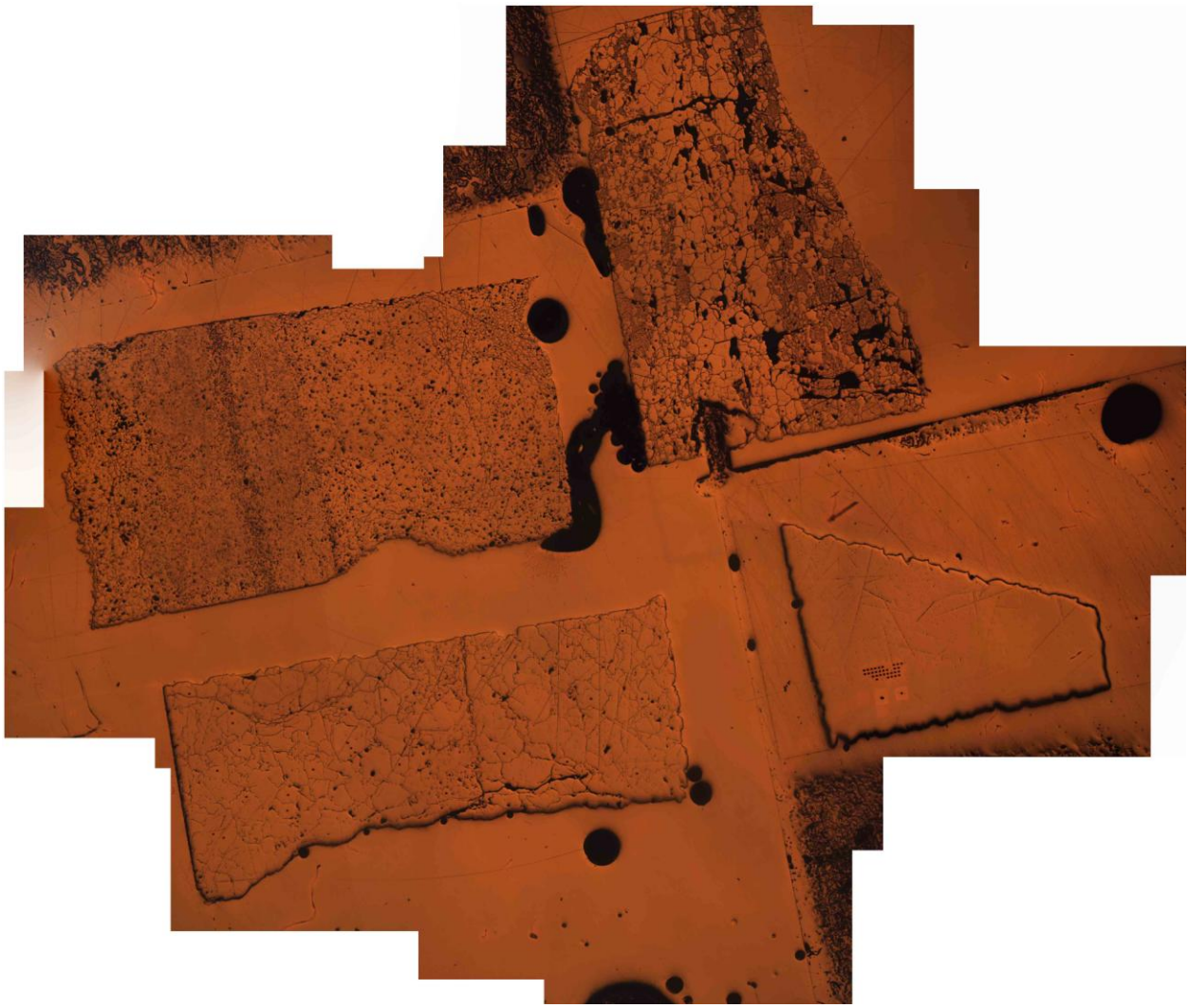


Figure 5-19. Full gold coat, post-analysis map of samples AB-11-12, TEM-cf, and AB-11-26 (in clock-wise order starting from Northwest). Length of TEM-cf sample is roughly ~7 mm for scale.



5 mm

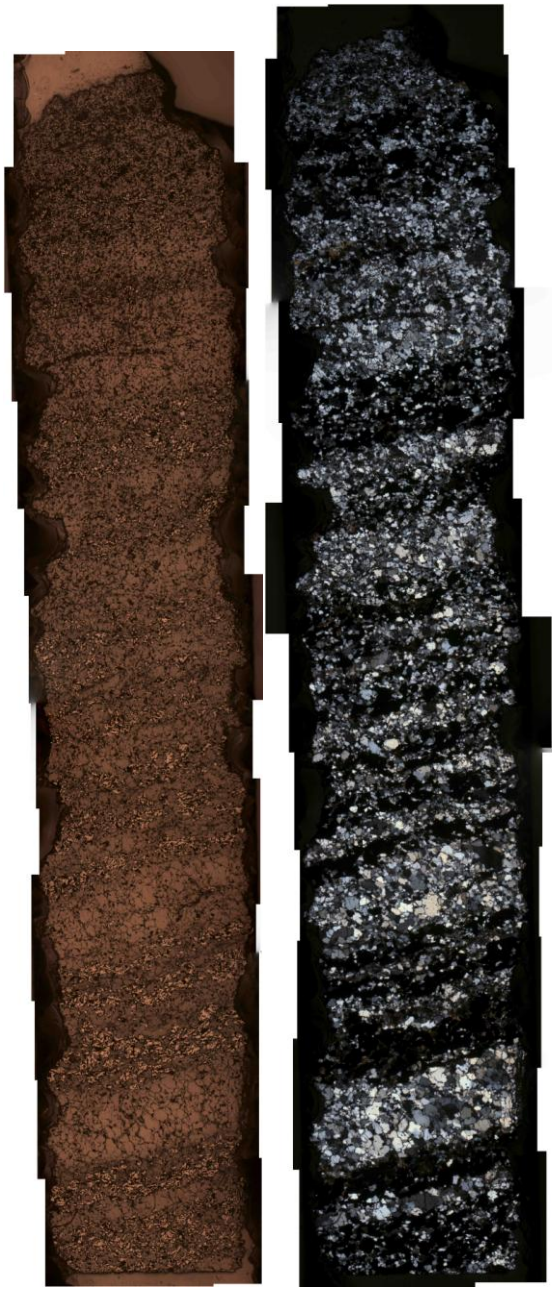
Figure 5-20. Full gold coat, post-analysis map of samples UTQ, sm-9796, IS-02-05, IS-02-06, IS-02-08 (in clock-wise order starting at Northwest with the clear standard). Length of UTQ standard is roughly ~5 mm for scale.



6 mm

Figure 5-21. Full gold coat, post-analysis map of samples ZB 23, ZB 117, UTQ, ZB 105 (in clock-wise order starting at Northwest).Length of UTQ standard is roughly ~ 6 mm for scale.

Individual sample maps



0.25 cm

Figure 5-22. Reflected light image of sample ZB-05 (left). Cross-polarized light image of sample ZB-05 (right). Length of ZB 05 sample is roughly ~1cm for scale.

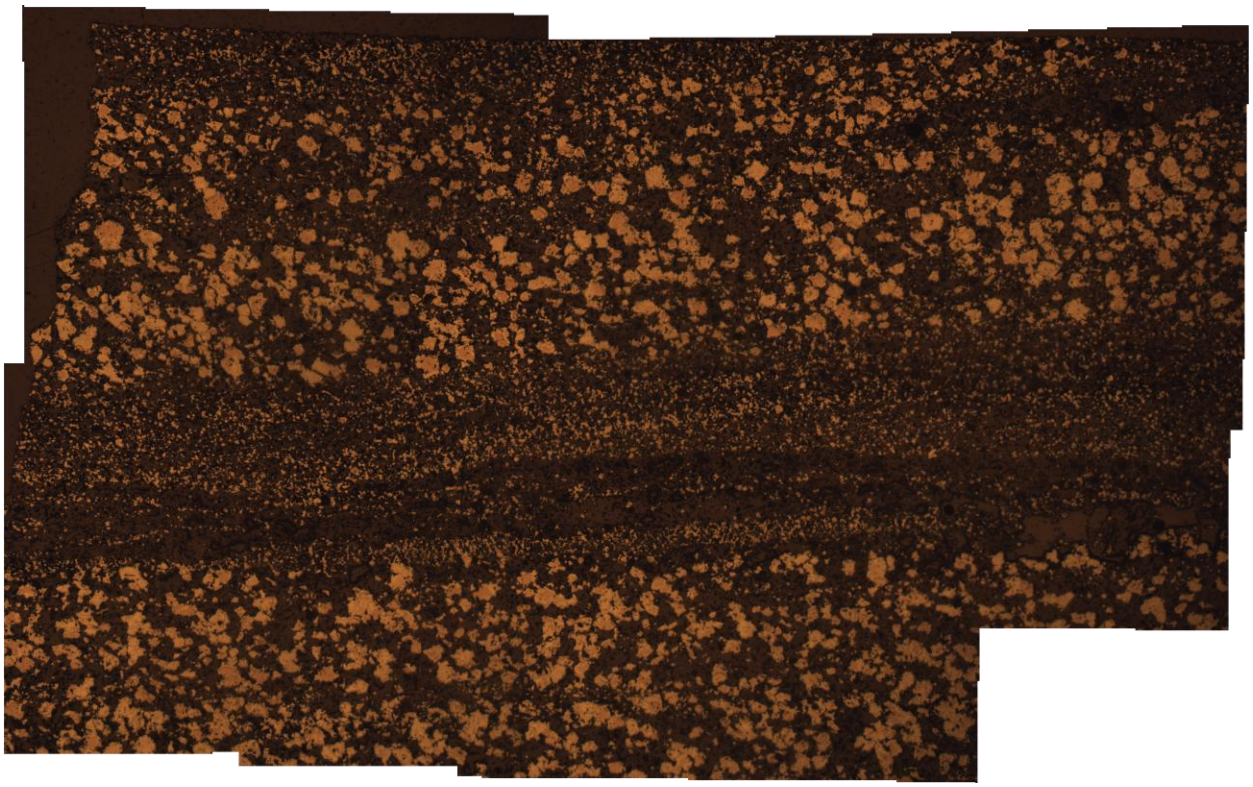
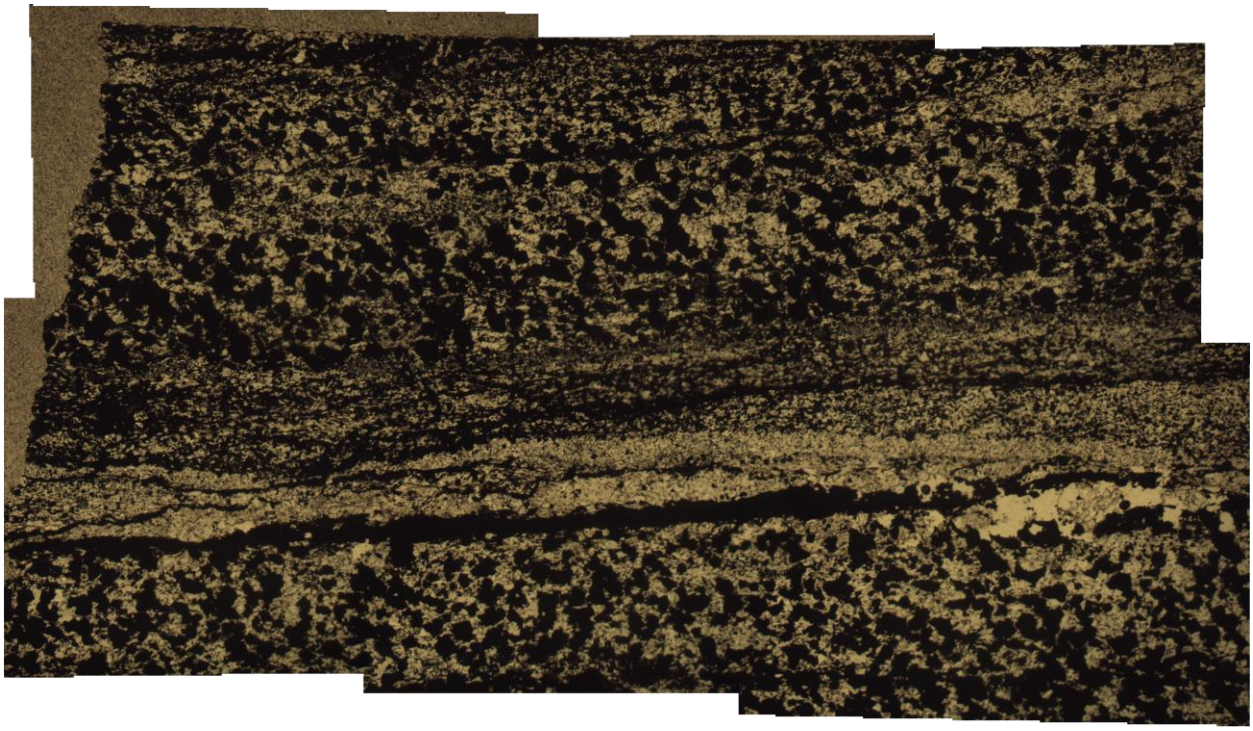
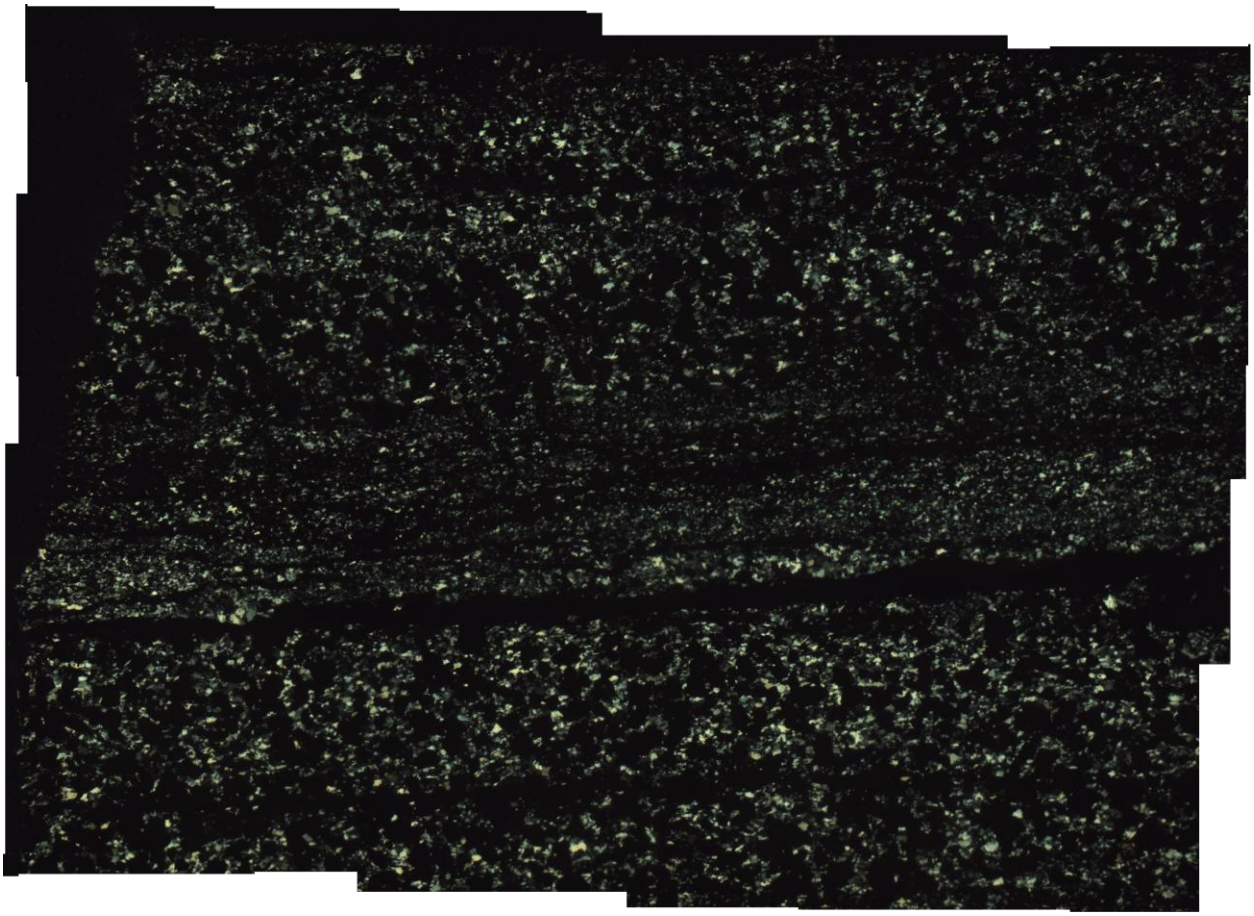


Figure 5-23. Reflected light image of sample ZB-169. Length of ZB 169 sample is roughly ~0.5 cm for scale.



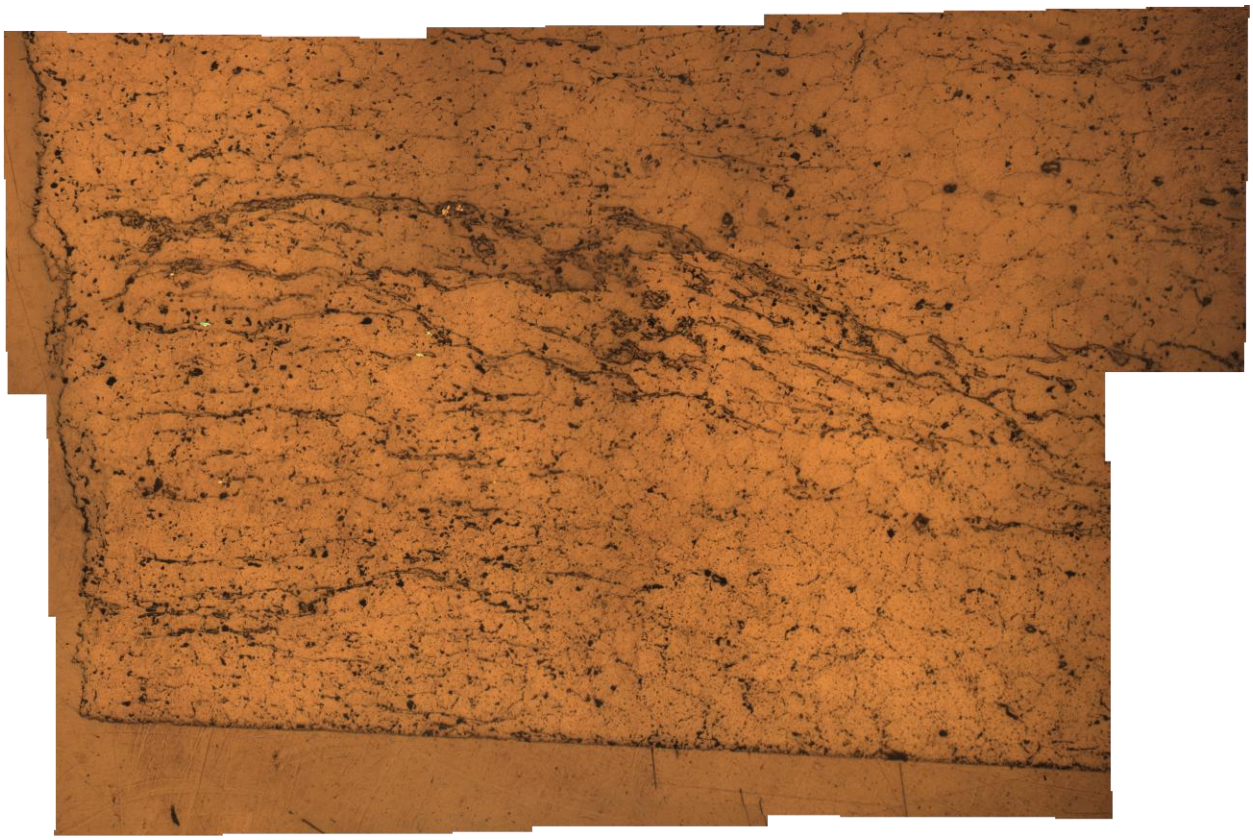
0.25 cm

Figure 5-24. Plane polarized light image of sample ZB-169. Length of ZB 169 sample is roughly ~0.5 cm for scale.



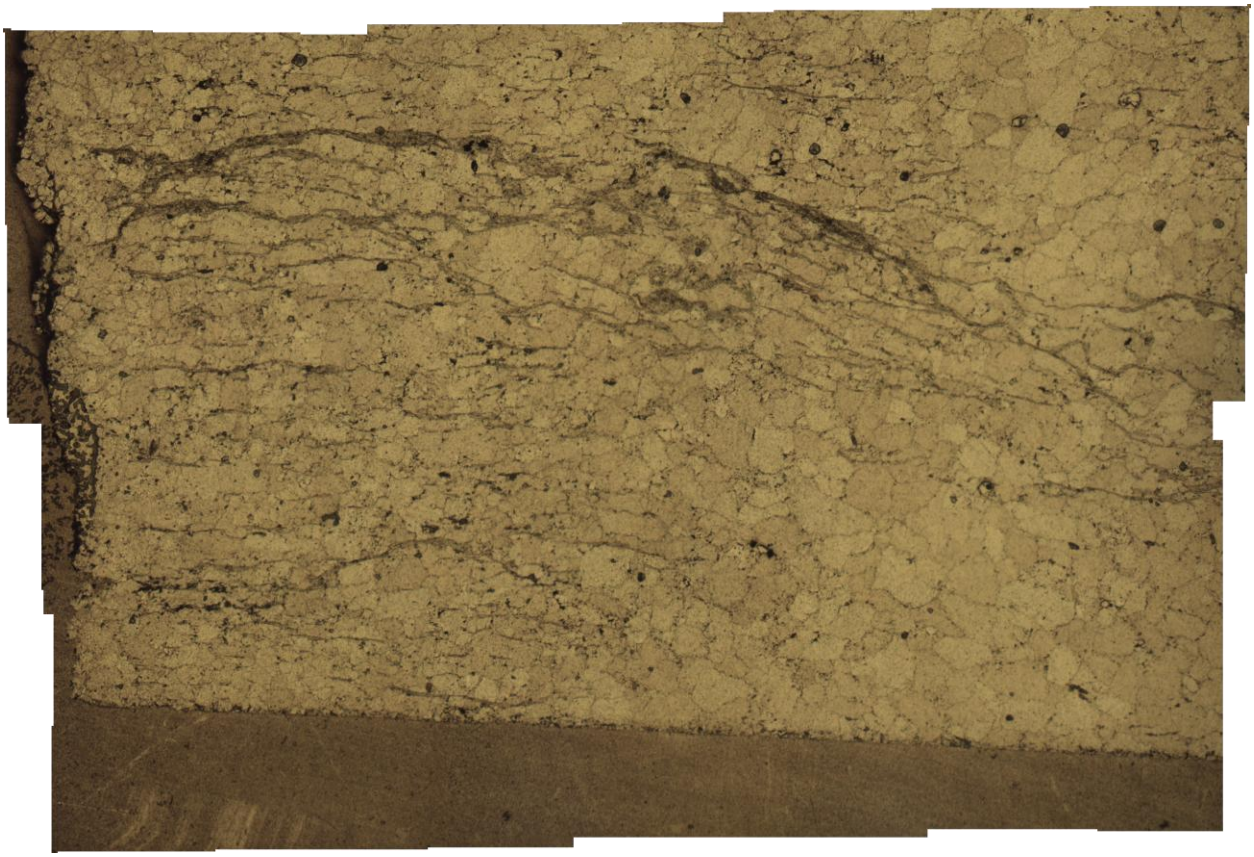
0.25 cm

Figure 5-25. Cross-polarized light image of sample ZB-169. Length of ZB 169 sample is roughly ~0.5 cm for scale.



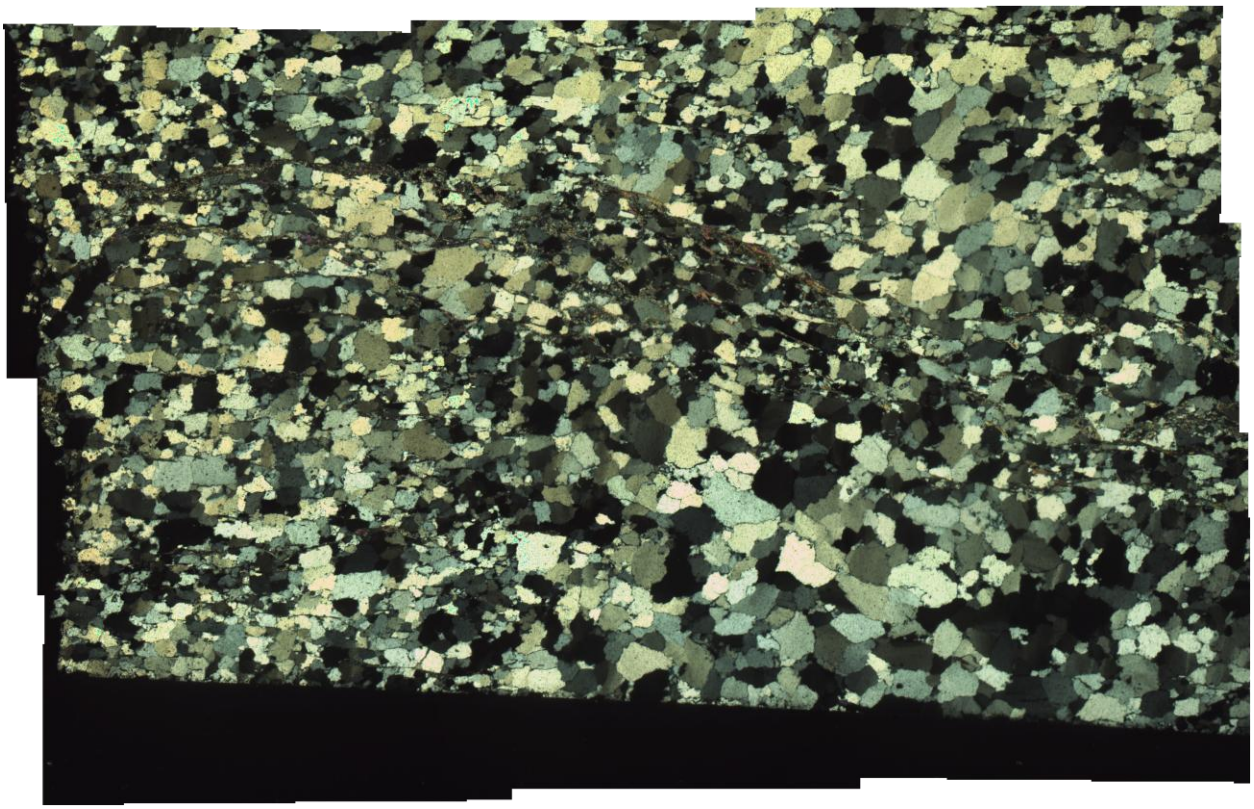
0.3 cm

Figure 5-26. Reflected light image of sample ZB-07. Length of ZB 07 sample is roughly ~0.6 cm for scale.



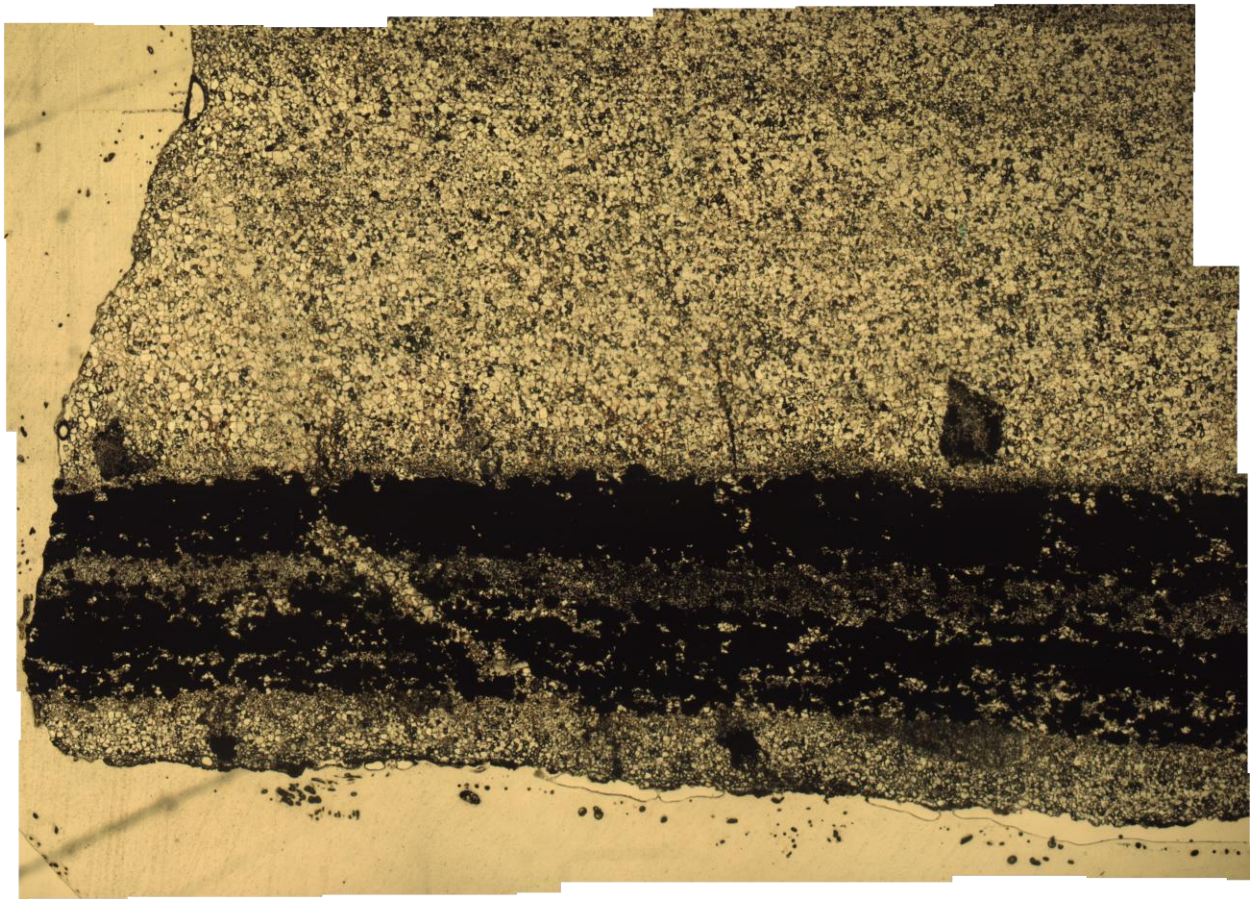
0.3 cm

Figure 5-27. Plane-polarized light image of sample ZB-07. Length of ZB 07 sample is roughly ~0.6 cm for scale.



0.3 cm

Figure 5-28. Cross-polarized light image of sample ZB-07. Length of ZB 07 sample is roughly ~0.6 cm for scale.



0.3 cm

Figure 5-29. Plane-polarized light image of sample ZB-23. Length of ZB 23 sample is roughly ~0.6 cm for scale.

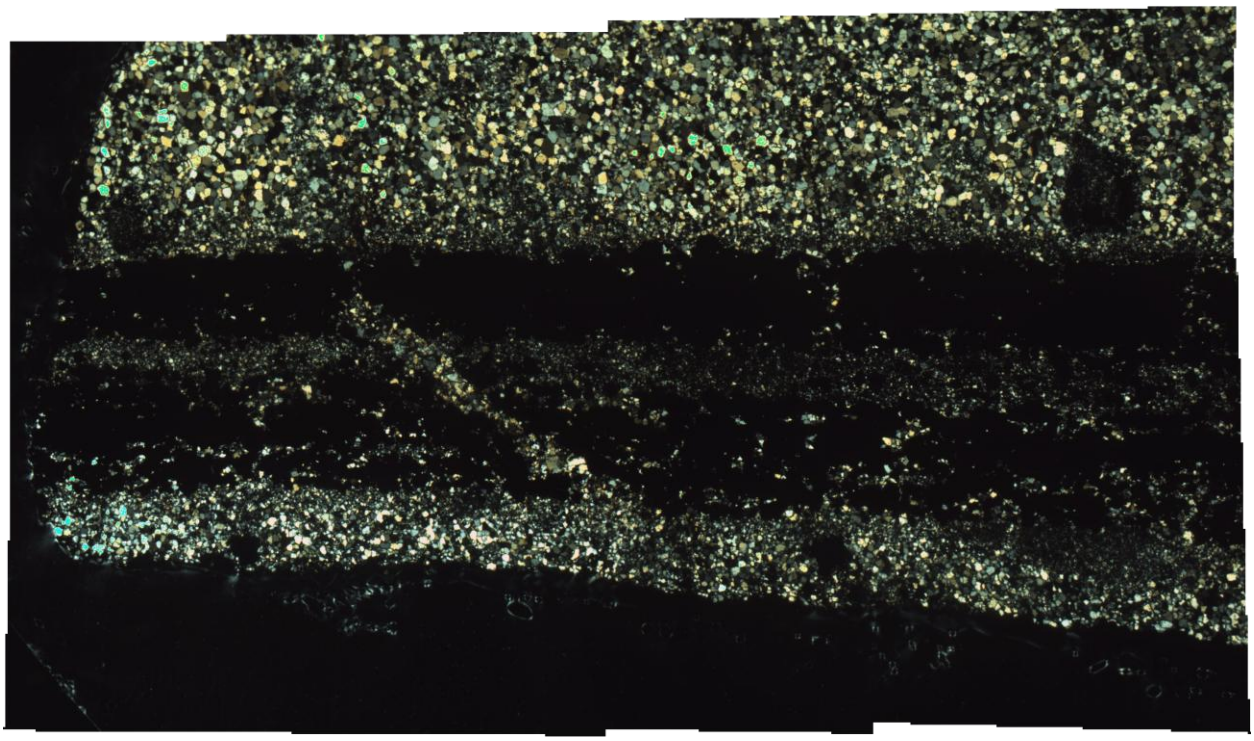
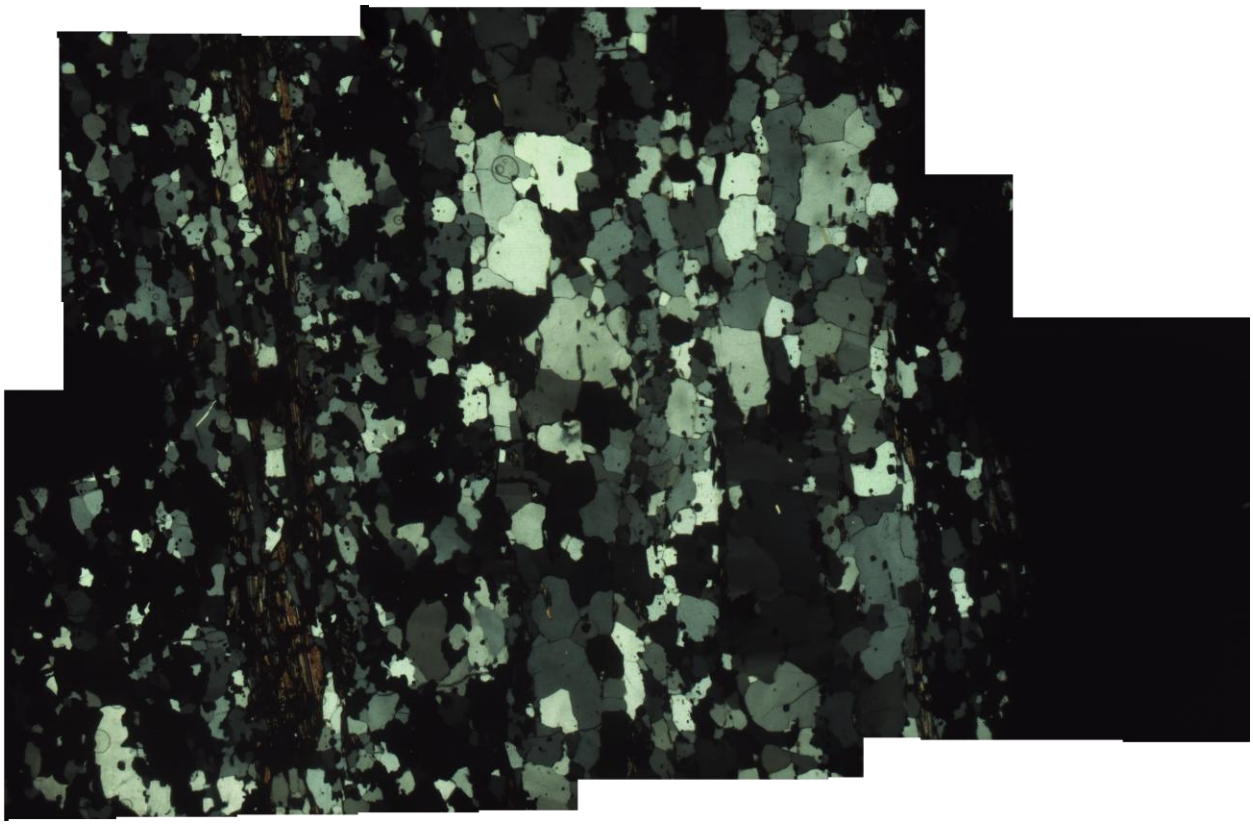


Figure 5-30. Cross-polarized light image of sample ZB-23. Length of ZB 23 sample is roughly ~0.6 cm for scale.



0.25 cm

Figure 5-31. Plane-polarized light image of sample ZB-117. Length of ZB 117 sample is roughly ~0.5 cm for scale.



0.25 cm

Figure 5-32. Cross-polarized light image of sample ZB-117. Length of ZB 117 sample is roughly ~0.5 cm for scale.

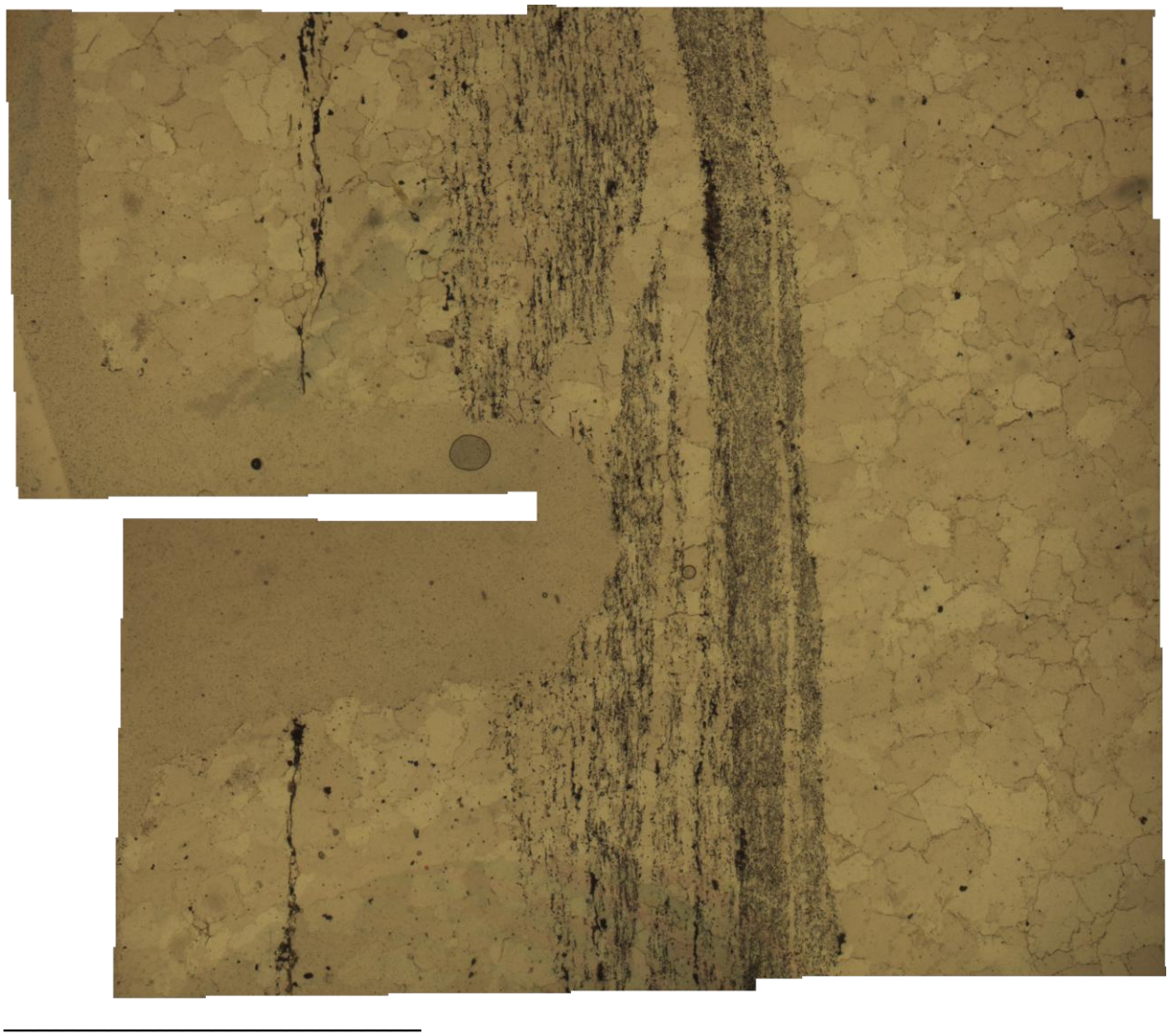
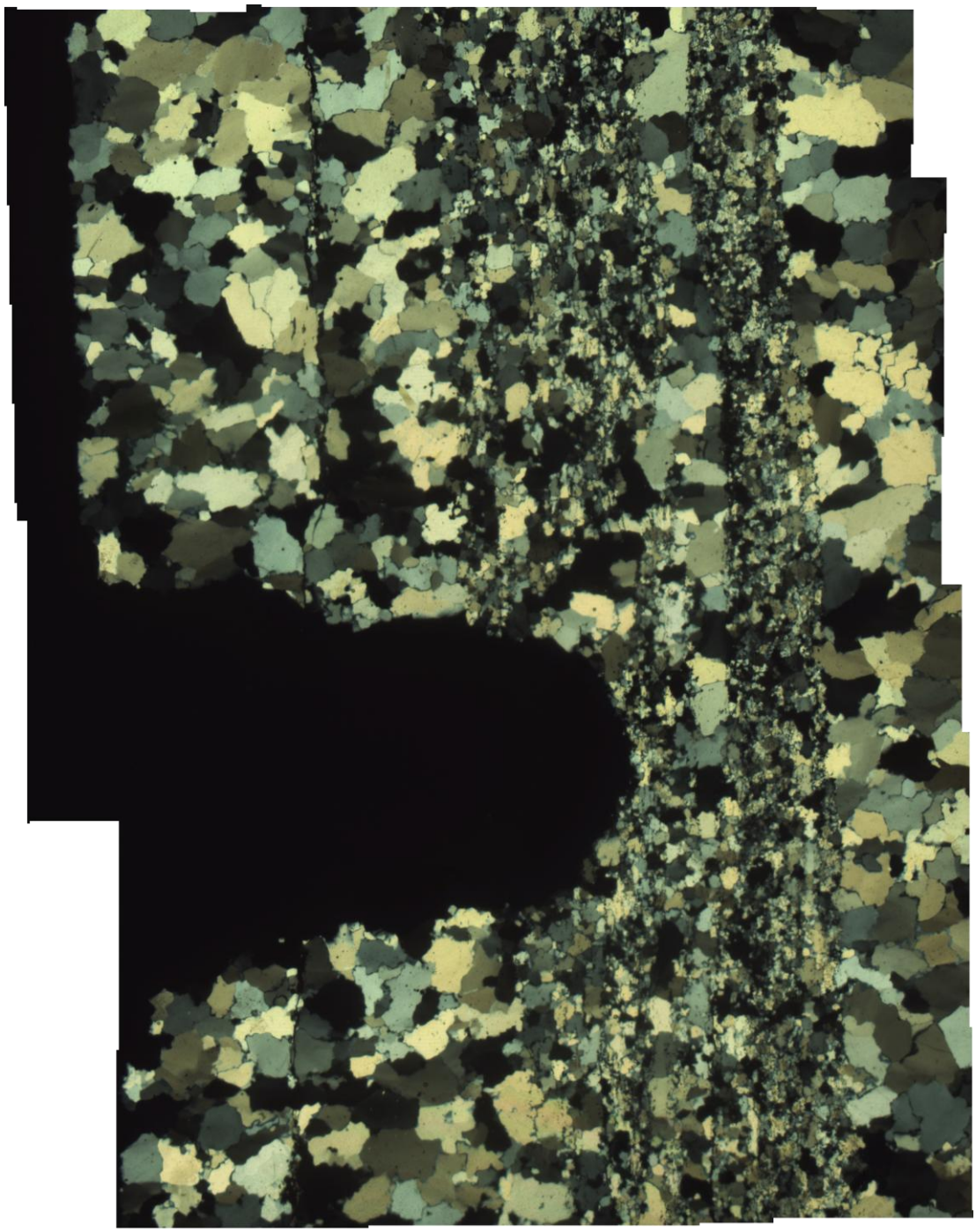


Figure 5-33. Plane-polarized light image of sample ZB-105. Length of ZB 105 sample is roughly ~0.6 cm for scale.



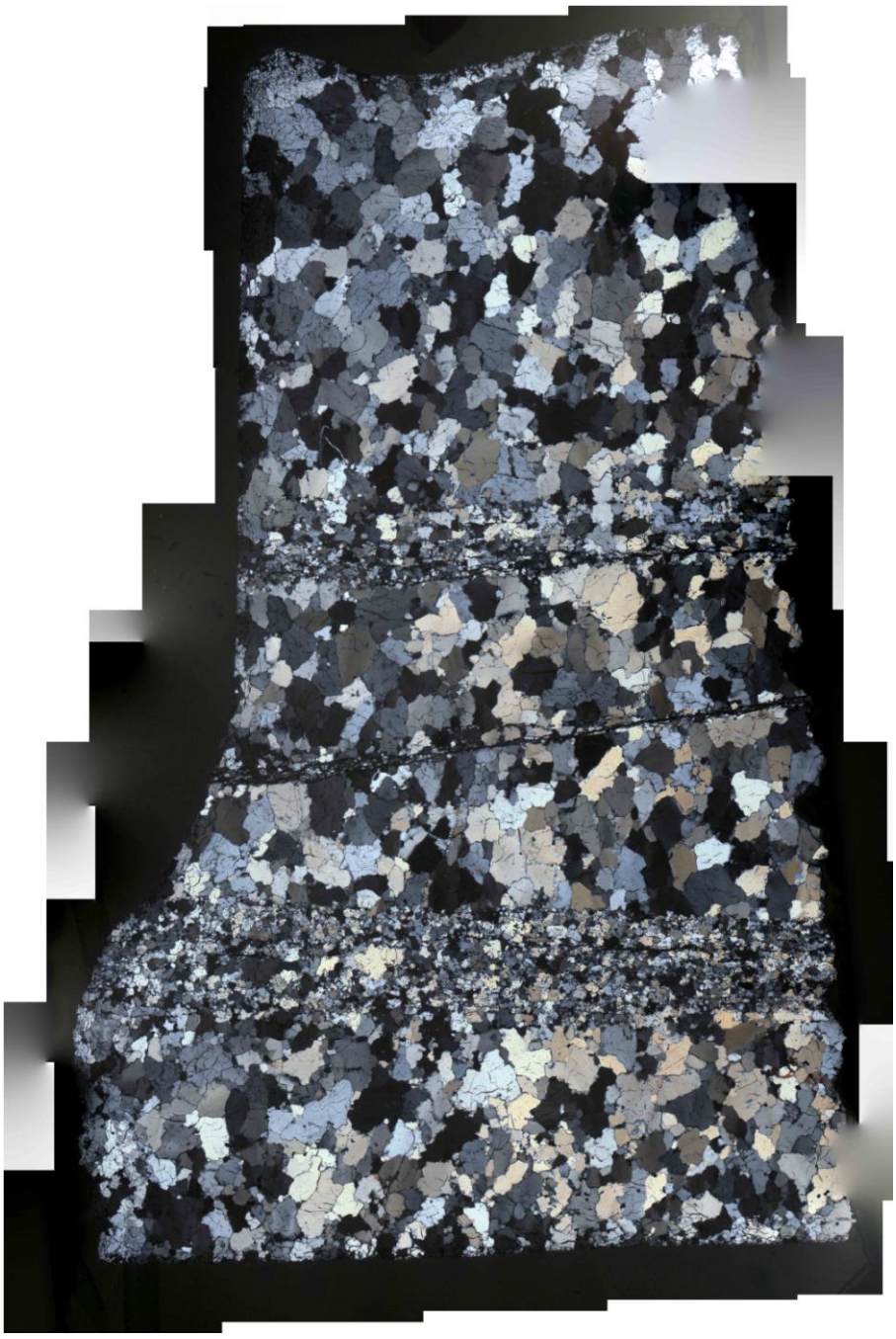
0.3 cm

Figure 5-34. Cross-polarized light image of sample ZB-105. Length of ZB 105 sample is roughly ~0.6 cm for scale.



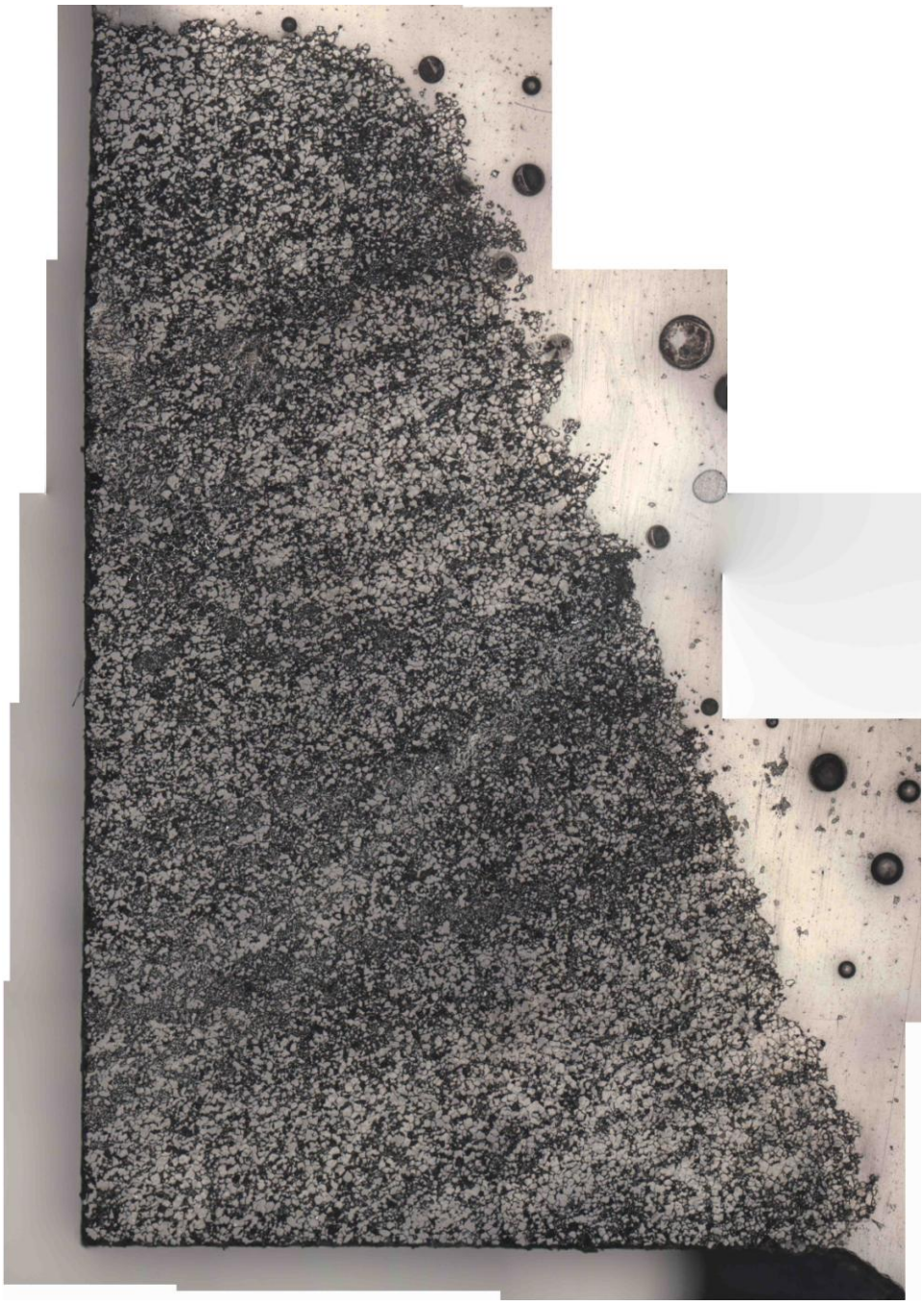
0.4 cm

Figure 5-35. Plane -polarized light image of sample ZB-105. Length of ZB 105 sample is roughly ~0.8 cm for scale.



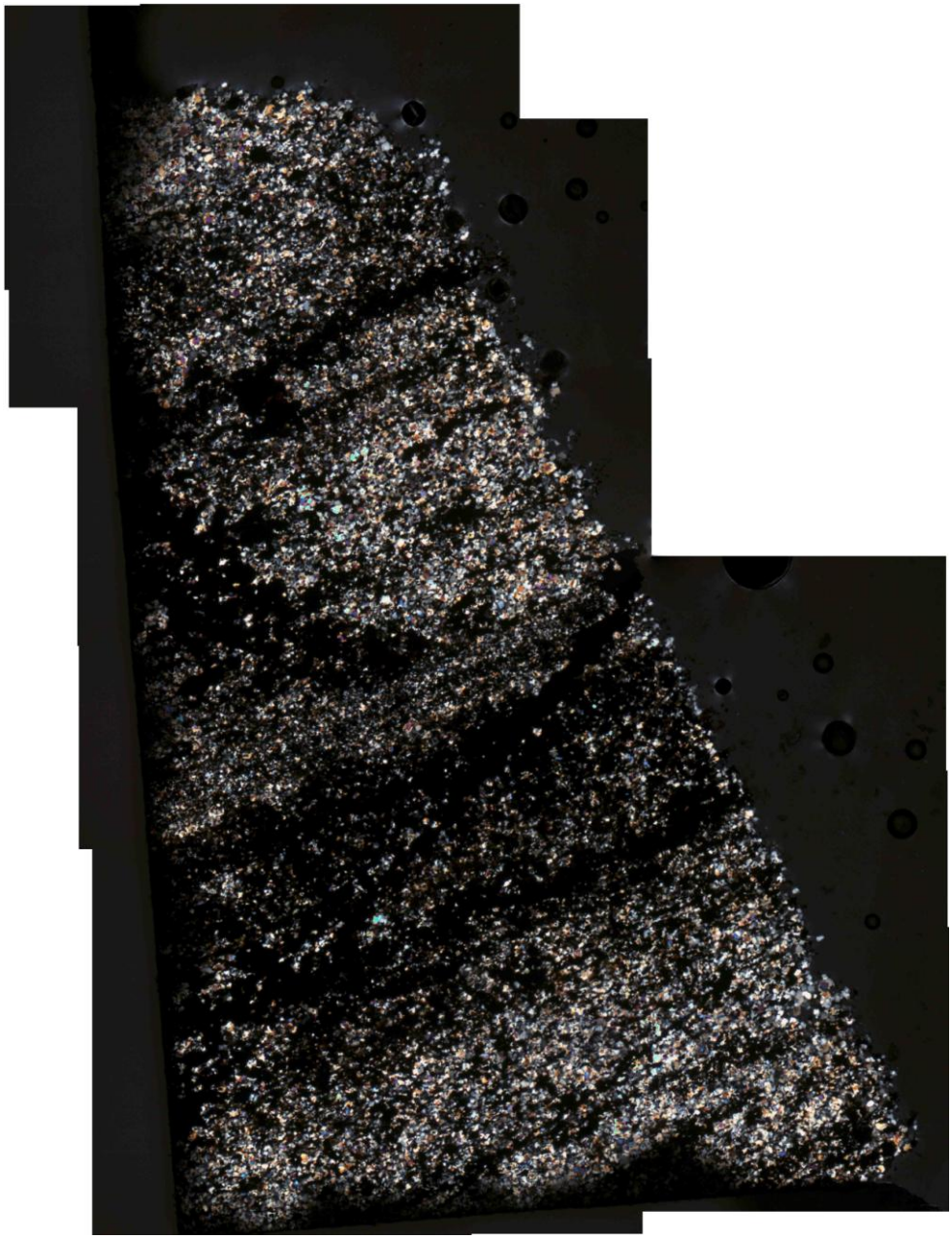
0.4 cm

Figure 5-36. Cross-polarized light image of sample ZB-105. Length of ZB 105 sample is roughly ~0.8 cm for scale.



0.25 cm

Figure 5-37. Plane-polarized light image of sample ZB-20. Length of ZB 20 sample is roughly ~0.5 cm for scale.



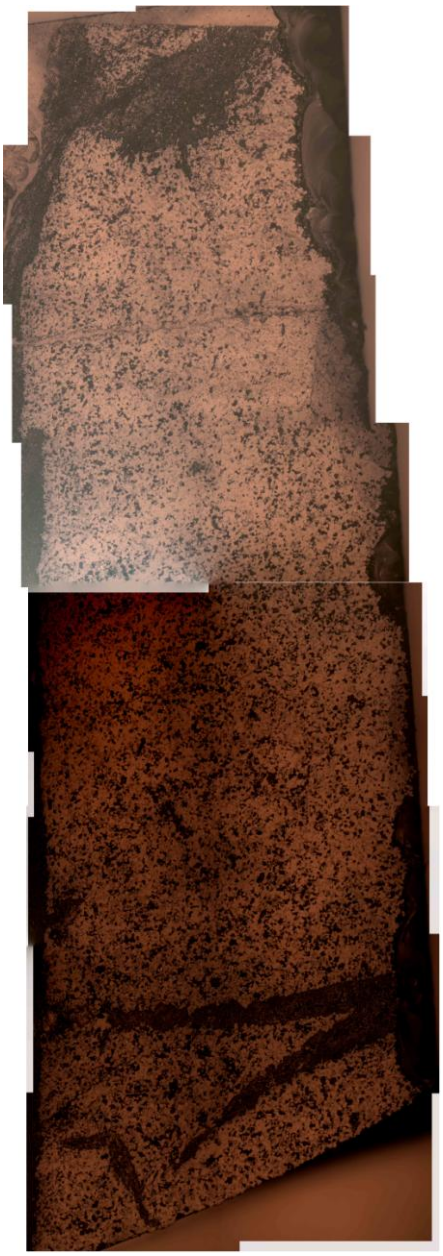
0.25 cm

Figure 5-38. Cross-polarized light image of sample ZB-20. Length of ZB 20 sample is roughly ~0.5 cm for scale.



0.25 cm

Figure 5-39. Plane-polarized light image (left) and cross-polarized image (right) of sample ZB-18. Length of ZB 18 sample is roughly ~1 cm for scale.



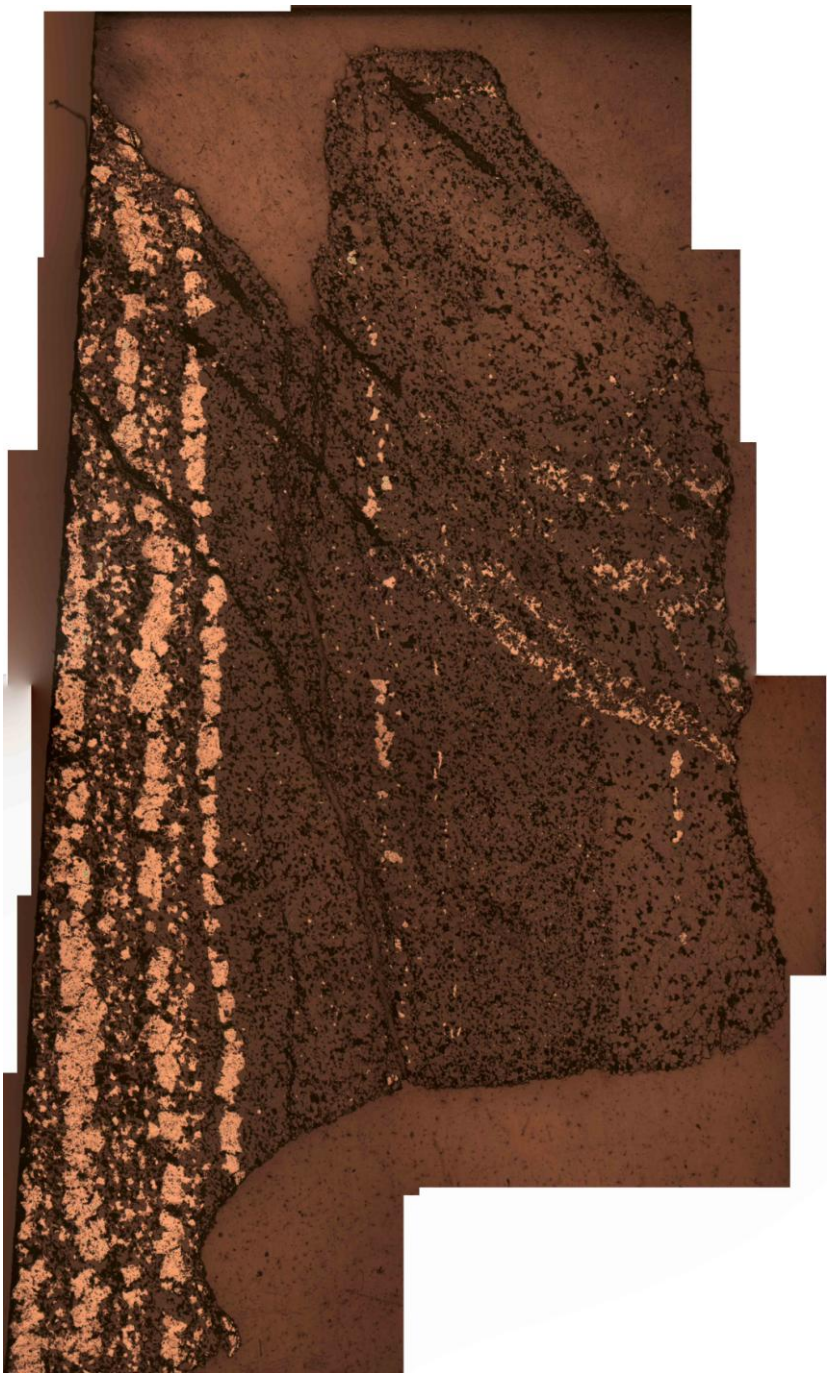
0.4 cm

Figure 5-40. Plane-polarized light image of sample ZB-17. Length of ZB 17 sample is roughly ~0.8 cm for scale.



0.4 cm

Figure 5-41. Cross-polarized light image of sample ZB-17. Length of ZB 17 sample is roughly ~0.8 cm for scale.



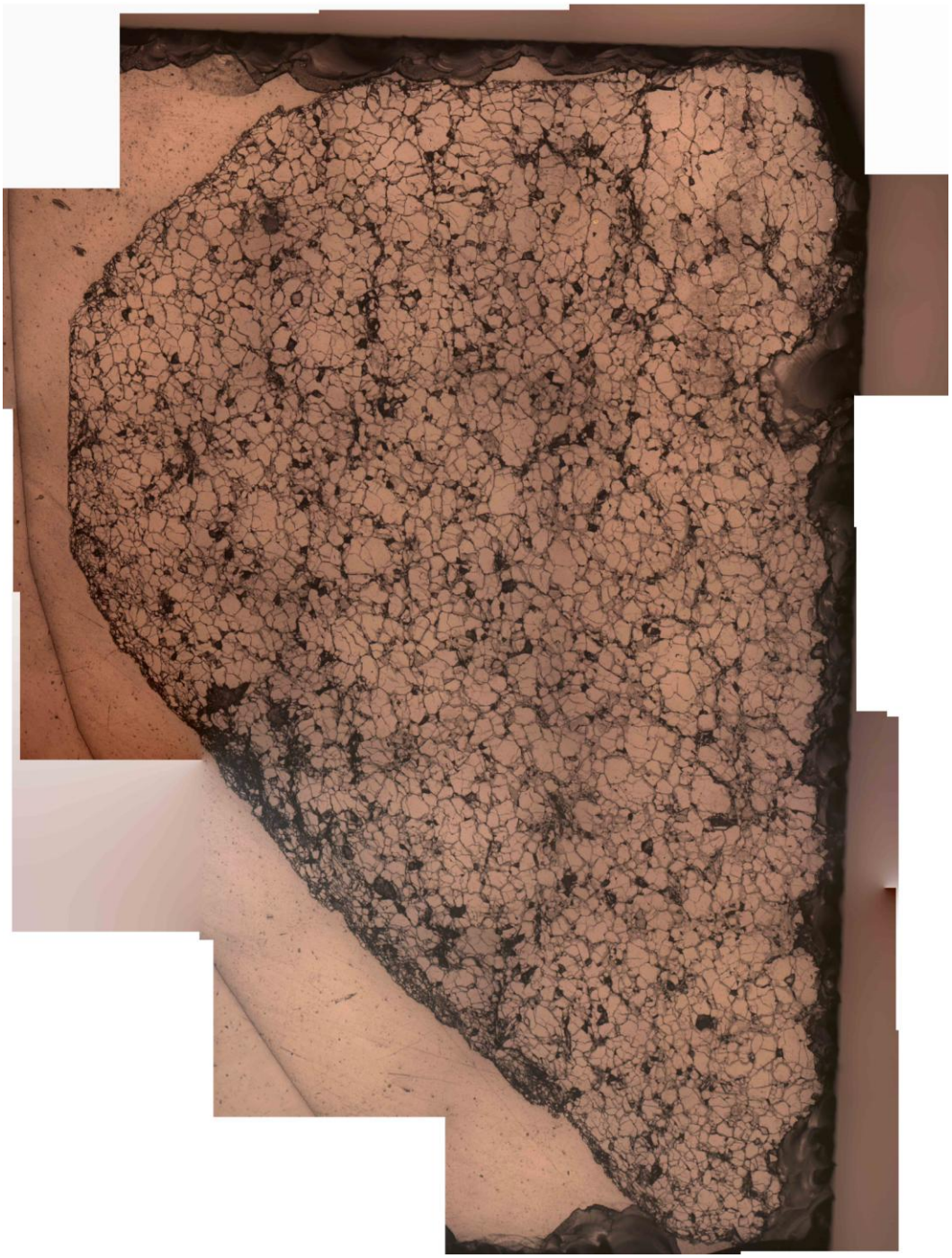
0.3 cm

Figure 5-42. Reflected–light image of sample ZB-143. Length of ZB 143 sample is roughly ~0.6 cm for scale.



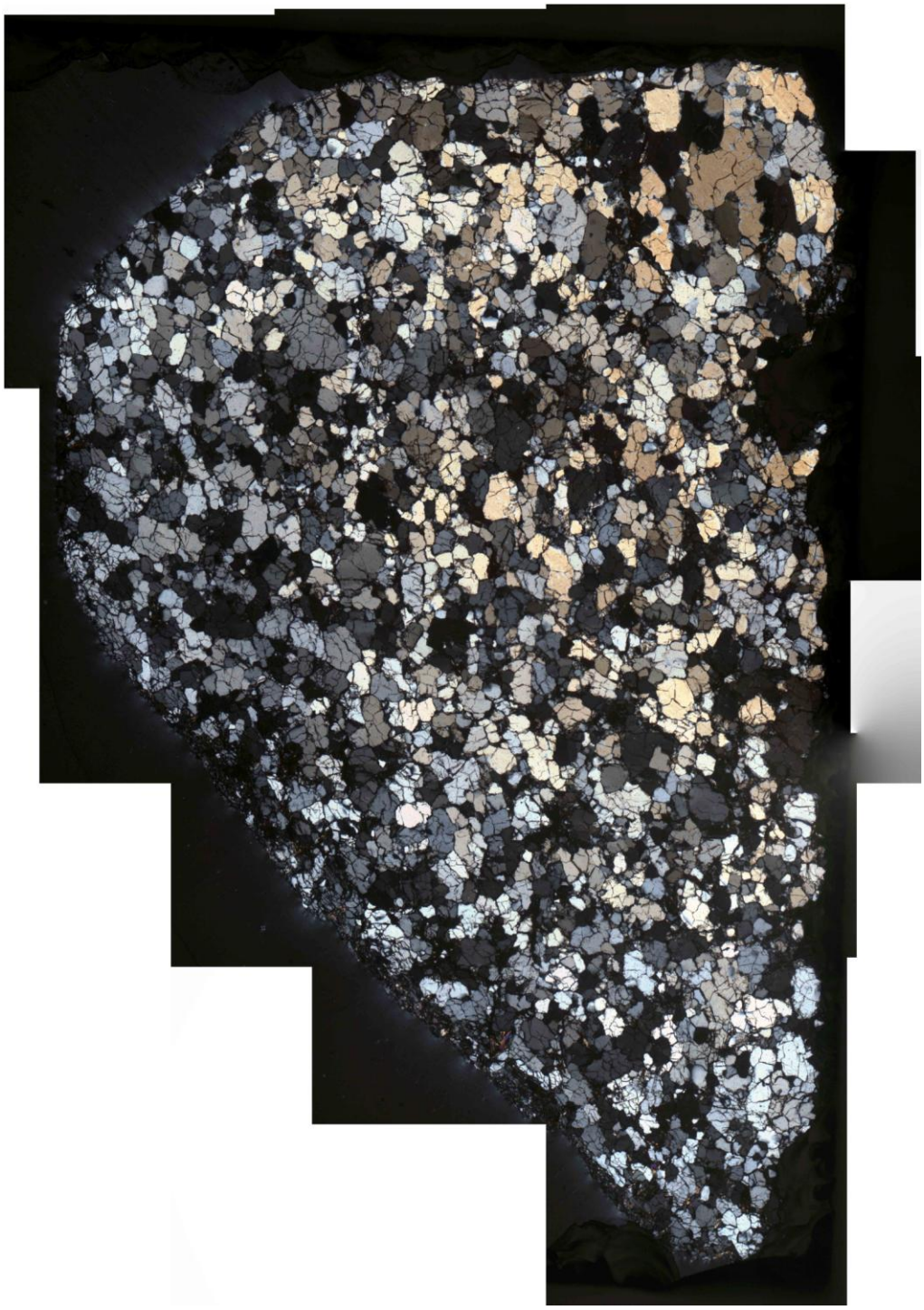
0.3 cm

Figure 5-43. Cross-polarized light image of sample ZB-143. Length of ZB 143 sample is roughly ~0.6 cm for scale.



0.35 cm

Figure 5-44. Reflected-light image of sample ZB-32. Length of ZB 32 sample is roughly ~0.7 cm for scale.



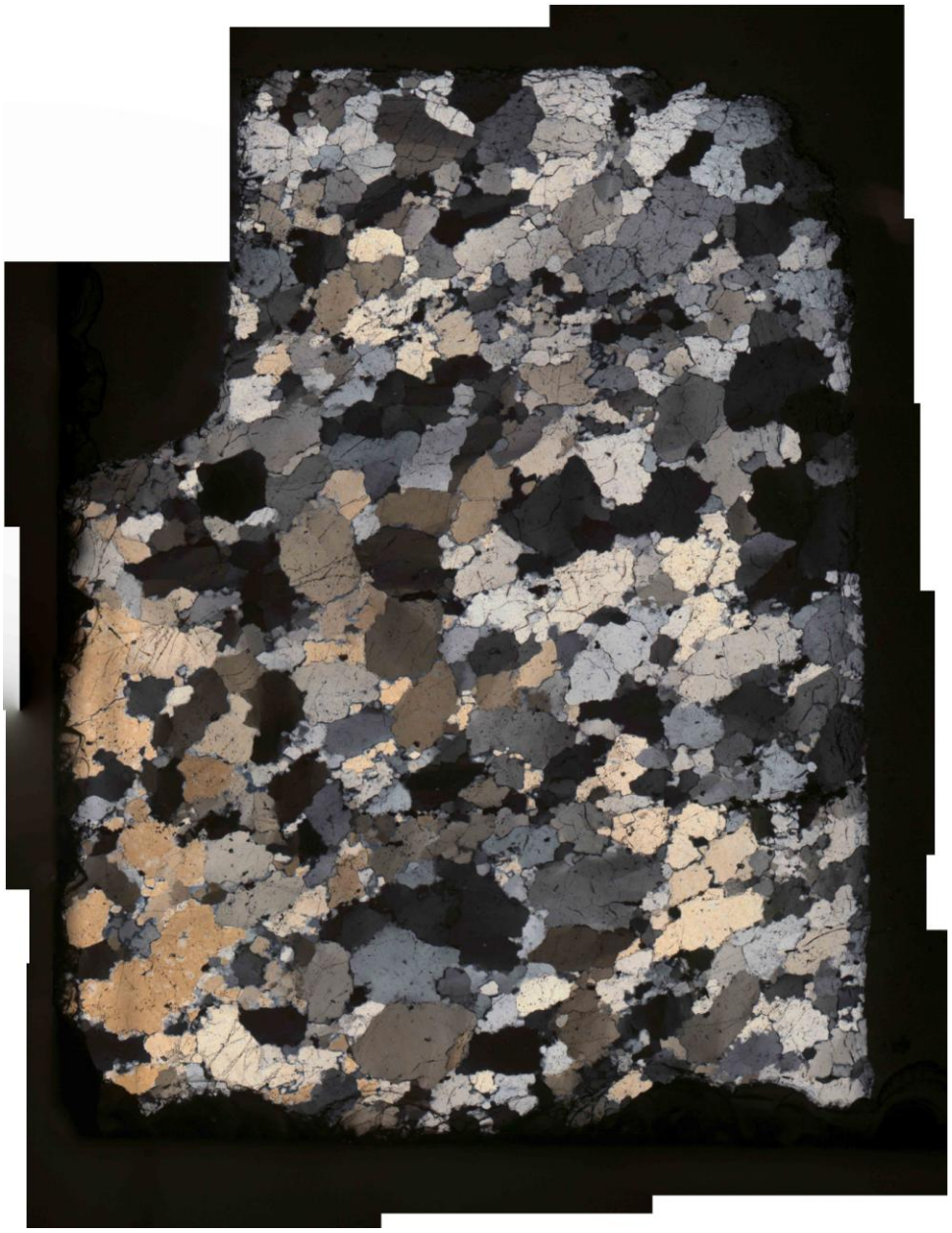
0.35 cm

Figure 5-45. Cross-polarized light image of sample ZB-32. Length of ZB 32 sample is roughly ~0.7 cm for scale.



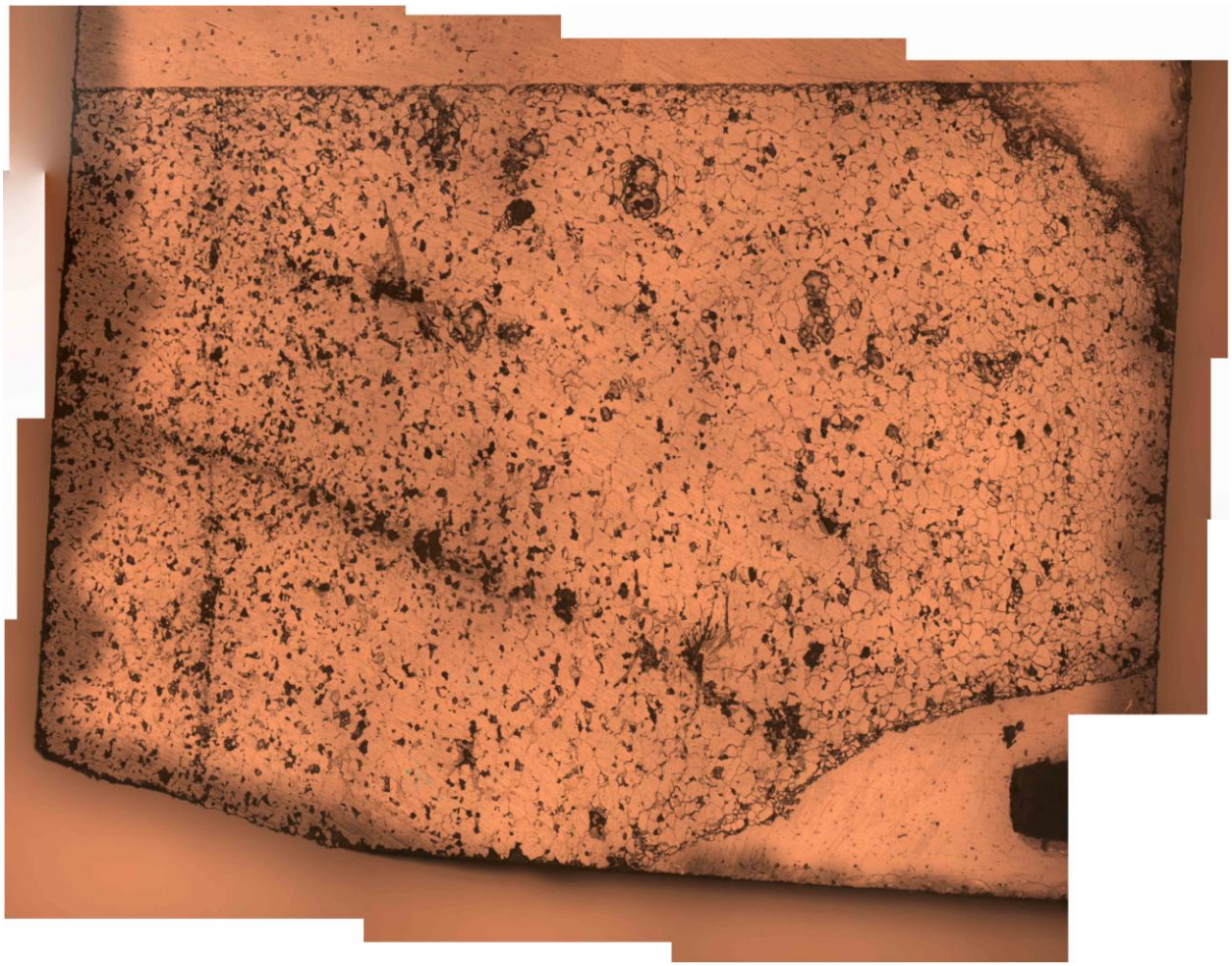
0.3 cm

Figure 5-46. Reflected-light image of sample ZB-03. Length of ZB 03 sample is roughly ~0.6 cm for scale.



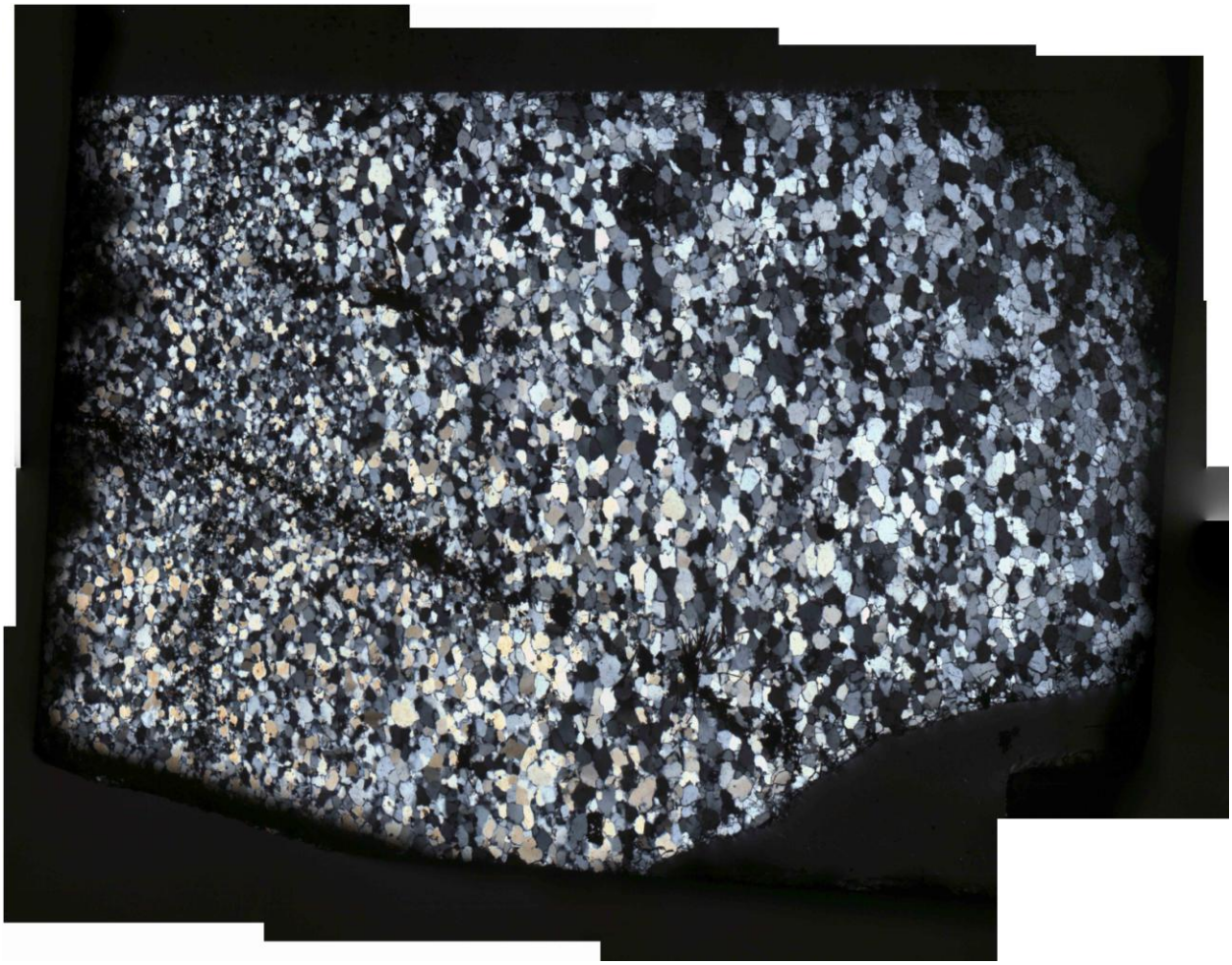
0.3 cm

Figure 5-47. Cross-polarized light image of sample ZB-03. Length of ZB 03 sample is roughly ~0.6 cm for scale.



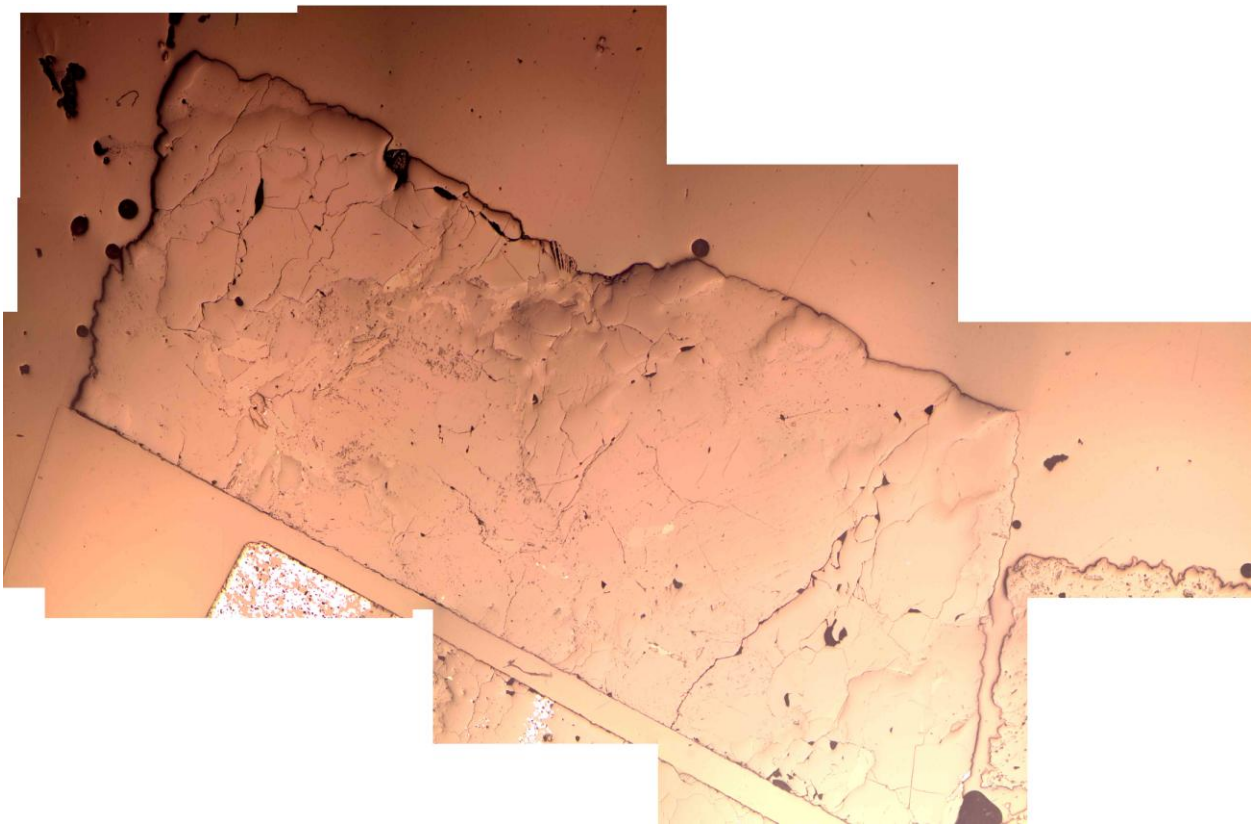
0.25 cm

Figure 5-48. Reflected-light light image of sample ZB-272. Length of ZB 272 sample is roughly ~0.5 cm for scale.



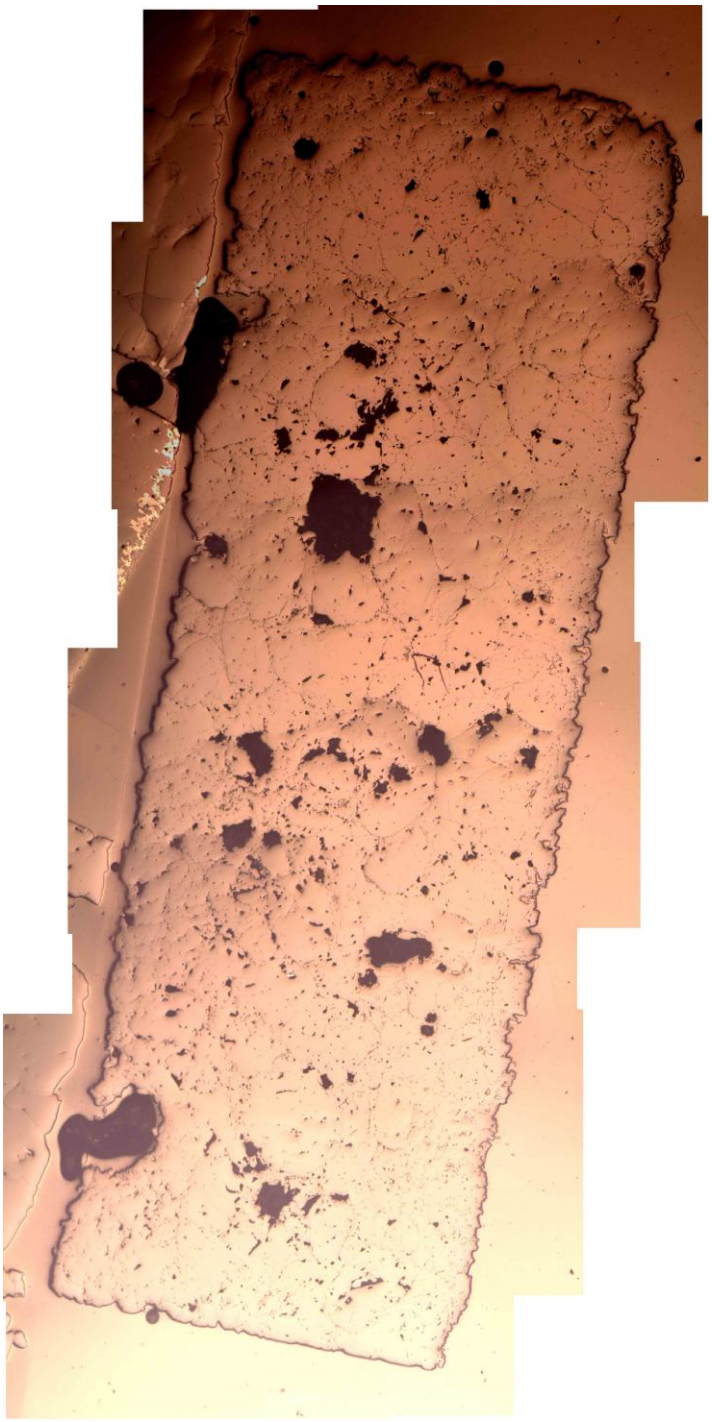
0.25 cm

Figure 5-49. Cross-polarized light image of sample ZB-272. Length of ZB 272 sample is roughly ~0.5 cm for scale.



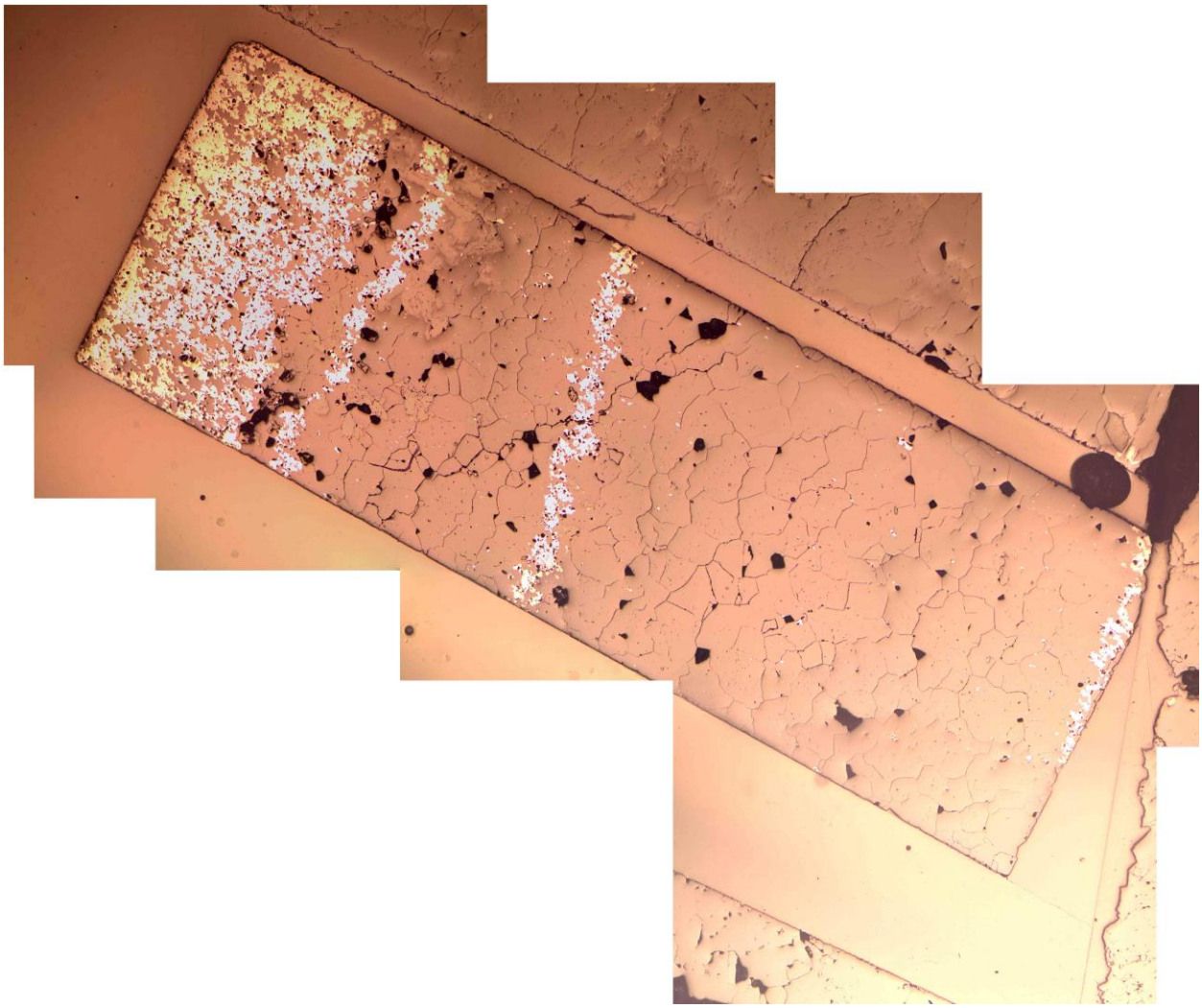
0.25 cm

Figure 5-50. Reflected-light image of sample ZB-182. Length of ZB 182 sample is roughly ~0.5 cm for scale.



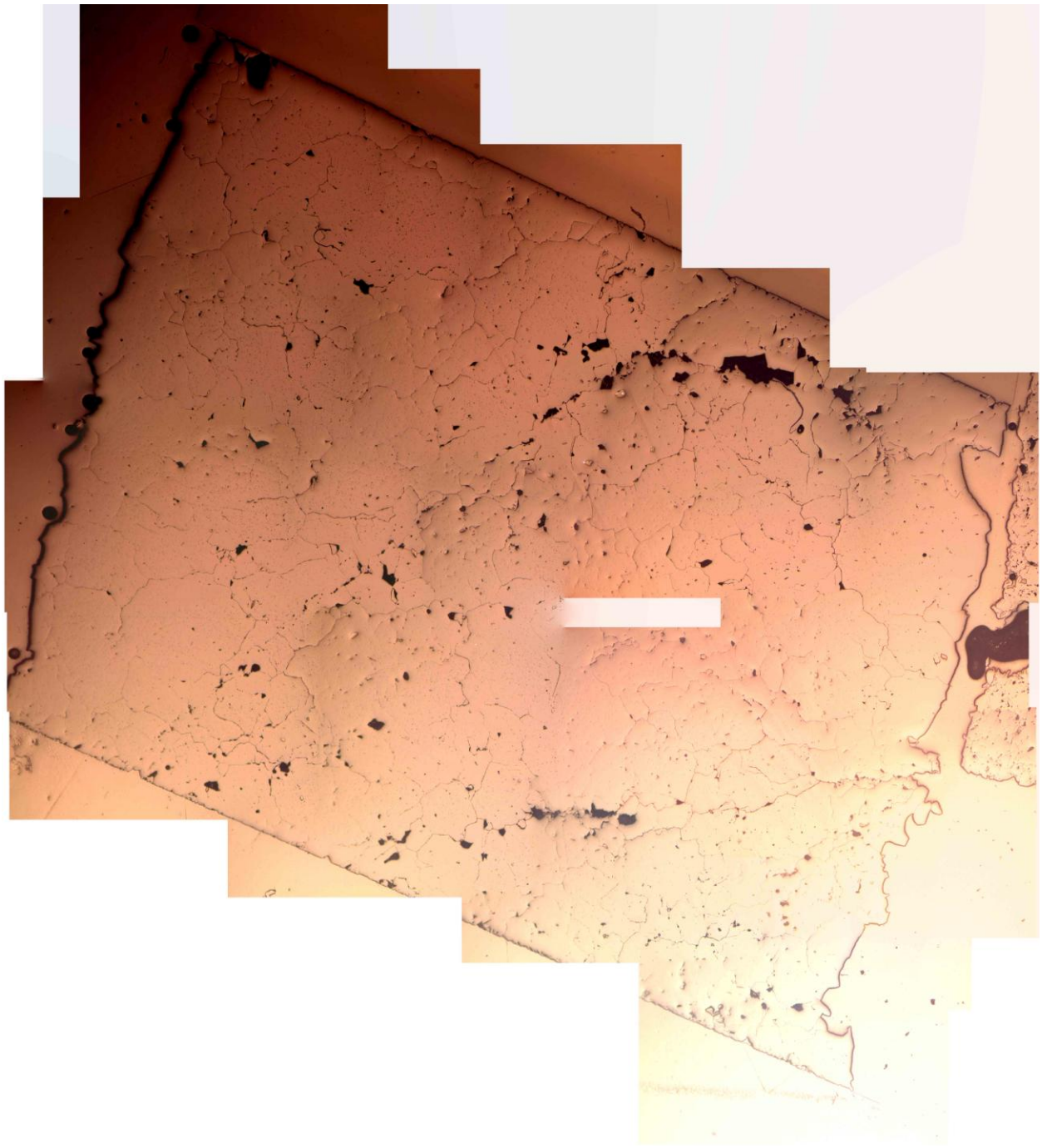
0.3 cm

Figure 5-51. Reflected-light image of sample ZB-240. Length of ZB 240 sample is roughly ~0.6 cm for scale.



0.3 cm

Figure 5-52. Reflected-light image of sample ISB-55. Length of ISB 55 sample is roughly ~0.6 cm for scale.



0.3 cm

Figure 5-53. Reflected-light image of sample ISB-26. Length of ISB 26 sample is roughly ~0.6 cm for scale.

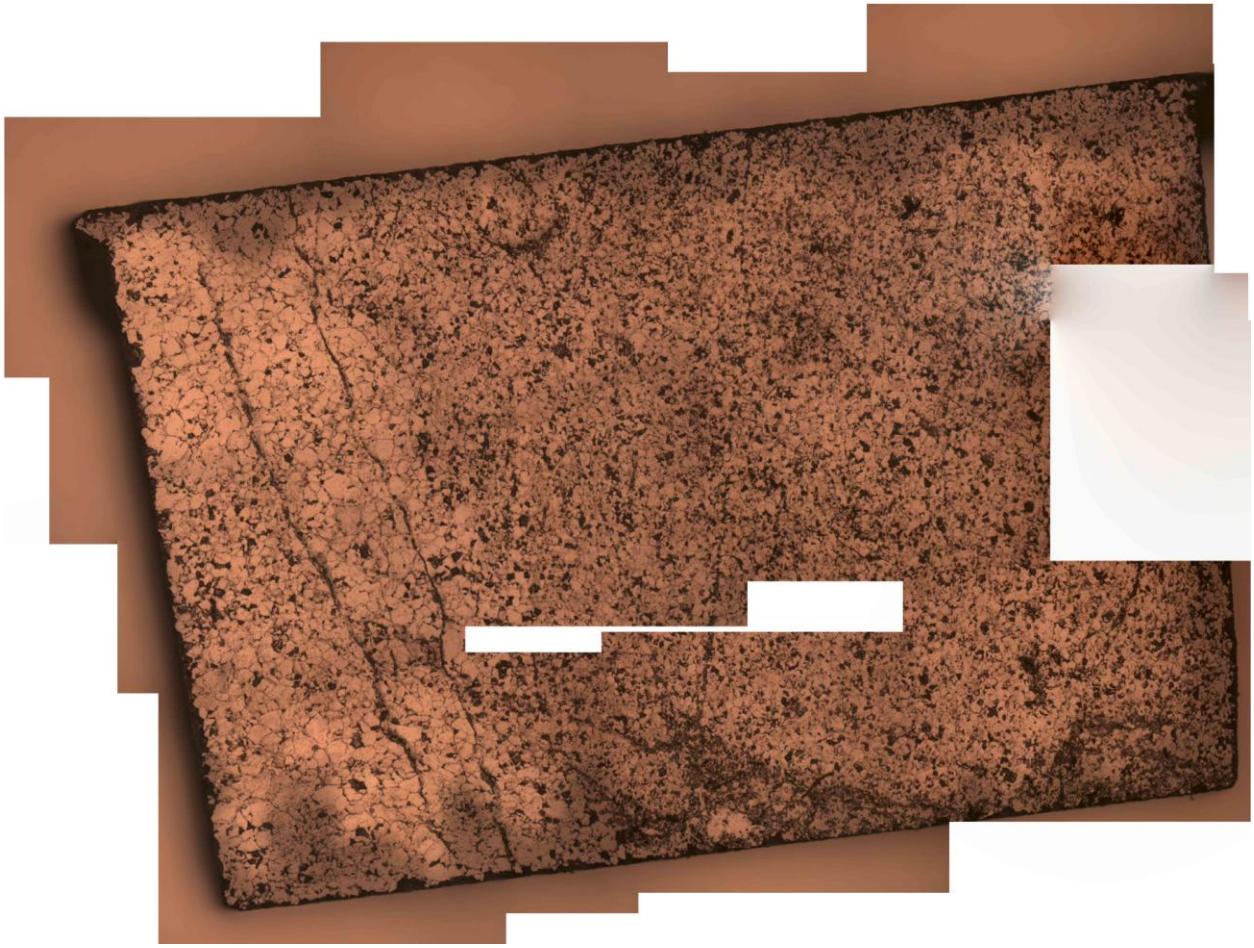


Figure 5-54. Reflected-light image of sample TEM-13-V2. Length of TEM-13-V2 sample is roughly ~0.5 cm for scale.



Figure 5-55. Reflected-light image of sample TEM-13-V2. Length of TEM-13-V2 sample is roughly ~0.5 cm for scale.

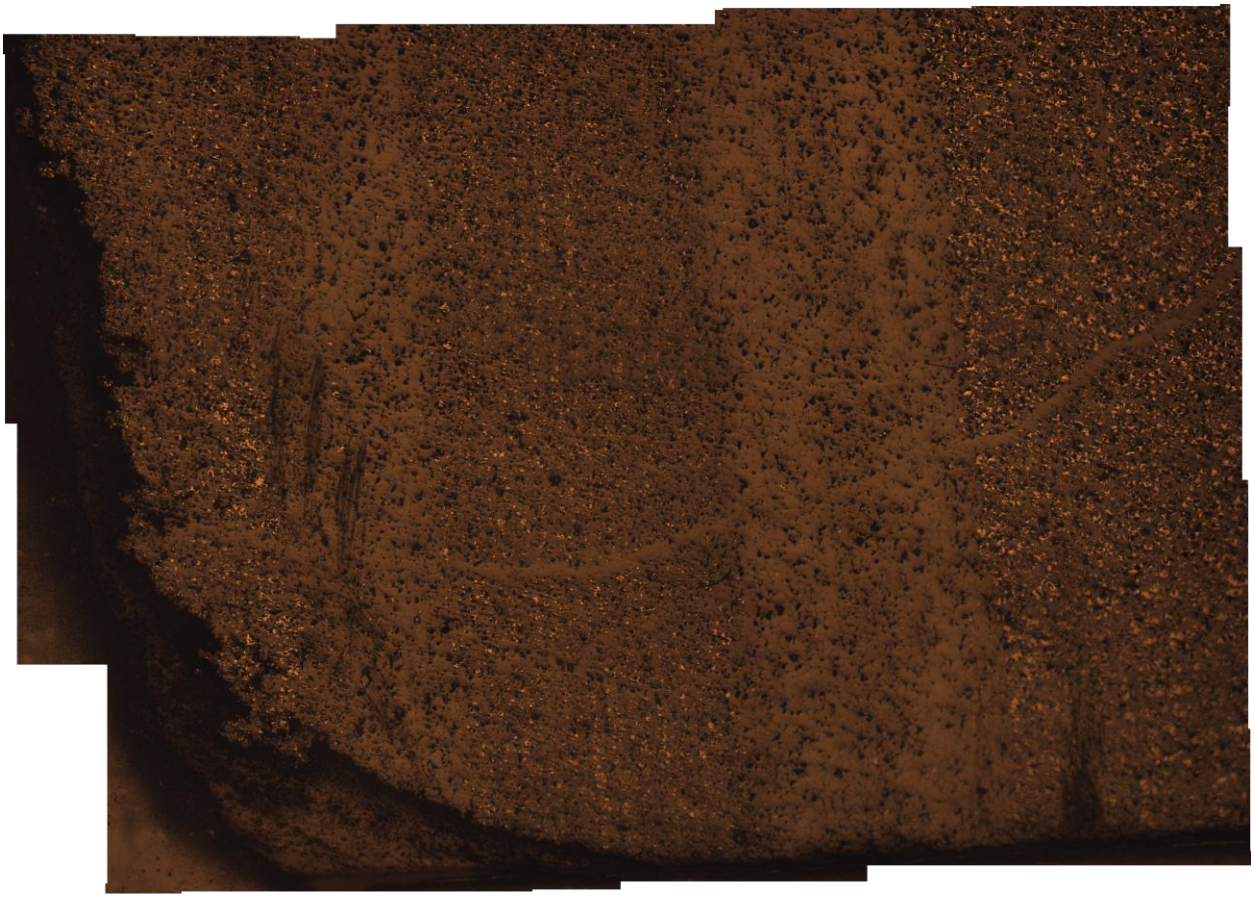


Figure 5-56. Reflected-light image of sample TEM-cf. Length of TEM-cf sample is roughly ~0.6 cm for scale.

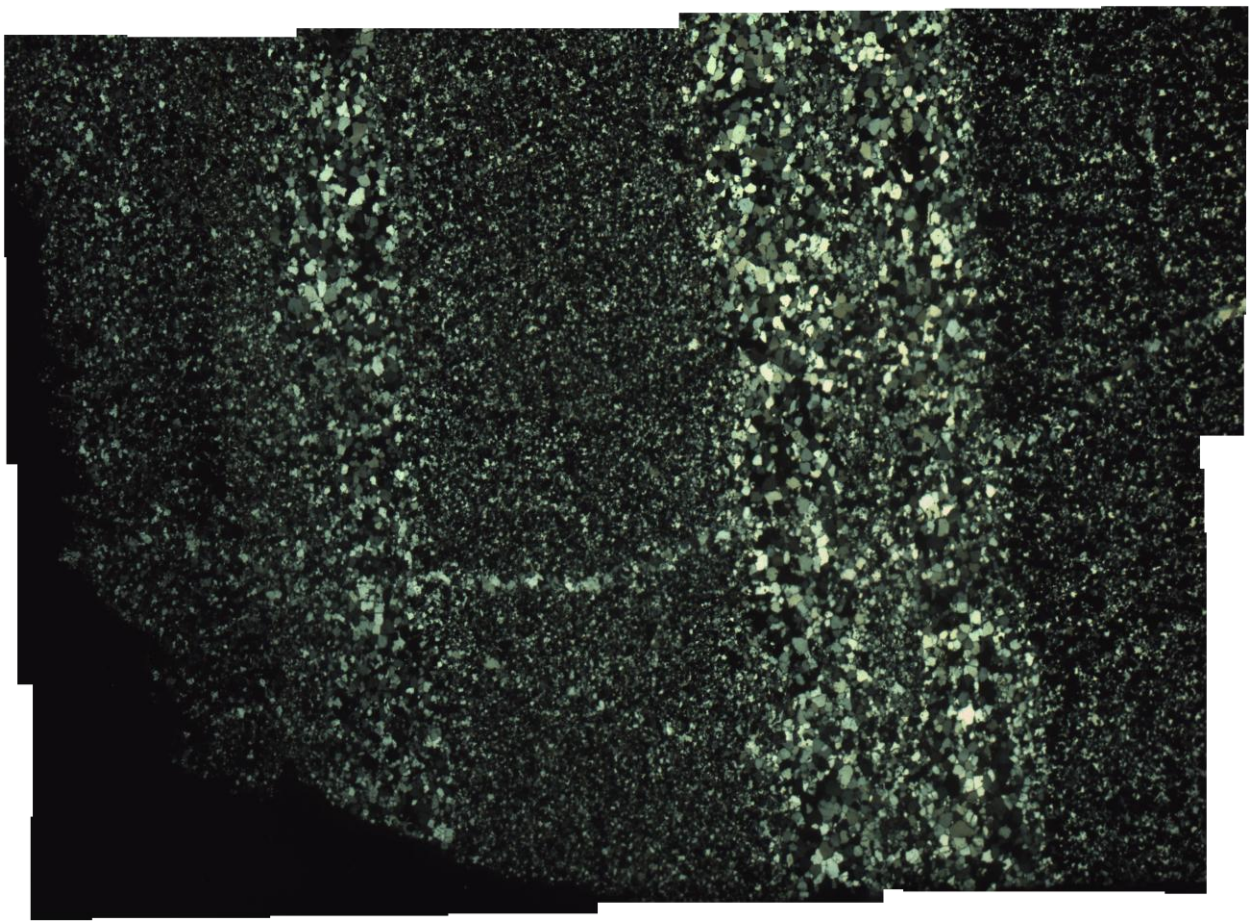


Figure 5-57. Reflected-light image of sample TEM-cf. Length of TEM-cf sample is roughly ~0.6 cm for scale.

Chapter II tables

Table 2-1. Criteria for defining lithologic groups 1, 2, 3

Felsic Volcanic Rocks: Group 1	AB-11-08	AB-11-11	AB-11-16	AB-11-17	AB-11-27	FCC	AB-13-A	AB-11-16	AB-11-17
By definition IF*	0	0	0	0	0	0	0	0	0
By mineralogy IF	0	0	0	0	0	0	0	0	0
By texture IF	0	0	0	0	0	0	0	0	0
By visual estimation IF	0	0	0	0	0	0	0	0	0
By chemistry IF	0	0	0	0	0	0	0	0	0
Score	0	0	0	0	0	0	0	0	0
Group 1: Scores 0	1 Felsic Volc.	1 Felsic Volc.	1 Felsic Volc.	1 Felsic Volc.	1 Felsic Volc.	1 Felsic Volc.	1 Felsic Volc.	1 Felsic Volc.	1 Felsic Volc.

Altered Volcanic Rocks: Group 2	AB-11-12	AB-11-26t	AB-11-34	AB-11-39	AB-11-41	AB-11-42
By definition IF	0	0	0	0	0	0
By mineralogy IF	1	0	1	1	1	1
By texture IF	0	1	0	1	0	0
By visual estimation IF	0	0	0	0	0	0
By chemistry IF	1	1	1	1	1	1
Score	2	2	2	3	2	2
Group 2: Scores 1-3	2 Altered Volc.	2 Altered Volc.	2 Altered Volc.	2 Altered Volc.	2 Altered Volc.	2 Altered Volc.

Jaspilite: Group 3	AB-11-19	AB-11-20	AB-11-22	AB-11-23	AB-11-24	AB-11-25	AB-11-26b	AB-11-30	AB-11-31	AB-11-32	AB-11-33	4.2 b
By definition IF	1	1	1	1	1	1	1	1	1	1	1	1
By mineralogy IF	1	1	1	1	1	1	1	1	1	1	1	1
By texture IF	0	1	1	0	1	0	0	0	0	0	1	0
By visual estimation IF	1	1	1	1	1	1	1	1	1	1	1	1
By chemistry IF	1	1	1	1	1	1	1	1	1	1	1	1
Score	4	5	5	4	5	4	4	4	4	4	5	4
Group 3: Scores 4-5	3 jaspilite	3 jaspilite	3 jaspilite	3 jaspilite	3 jaspilite	3 jaspilite	3 jaspilite	3 jaspilite	3 jaspilite	3 jaspilite	3 jaspilite	3 jaspilite

*IF = Algoma-type iron formation

Algoma-type IF definition Gross 1980, 1983: "Algoma-type iron formations, found in all ages of rock, are consistently associated with greywacke sedimentary units and volcanic rocks; they apparently formed close to volcanic centres and were produced by fumeroilic, effusive and exhalative hydrothermal processes related to volcanic centers"

Table 2-2. Major element data for Groups 1, 2, 3

Sample	SiO_2	Al_2O_3	Fe_2O_3(T)	MnO	MgO	CaO	Na_2O	K_2O	TiO_2	P_2O_5	LOI	Total
Group 1												
AB-11-08	79.24	9.42	4.74	0.063	1.94	0.49	3.34	0.09	0.208	0.04	1.42	101
AB-11-11	66.87	11.6	10.84	0.197	3.79	0.53	2.99	0.09	0.255	0.07	3.11	100.3
AB-11-16	74.15	7.83	6.92	0.138	4.57	0.75	1.51	0.04	0.147	0.01	3.09	99.16
AB-11-17	71.38	14.77	3.68	0.081	1.86	0.49	6.95	0.05	0.185	0.02	1.43	100.9
FCC	70	10.9	3.03	0.095	0.85	3.54	3.17	1.56	0.213	0.04	4.85	98.26
Group 2												
AB-11-27	76.54	9.5	2.62	0.085	0.48	1.87	5.04	0.06	0.215	0.05	2.73	99.19
AB-11-12	79.11	5.46	8.79	0.111	2.41	0.98	0.44	0.1	0.291	0.05	3.18	100.9
AB-11-26b	90.66	1.61	3.93	0.052	0.75	0.9	0.03	0.02	0.107	0.03	2	100.1
AB-11-34	76.33	4.95	11.01	0.08	2.69	0.48	0.05	0.07	0.254	0.03	2.51	98.45
AB-11-39	92.21	1.09	5.37	0.037	0.32	0.41	0.04	0.02	0.005	0.05	1.33	100.9
AB-11-41	59.41	14.02	7.66	0.129	3.16	7.11	2.52	0.63	0.646	0.11	4.97	100.4
Group 3												
AB-11-42	57.15	14.92	7.8	0.137	3.45	5.75	3.49	0.75	0.77	0.14	4.49	98.85
4.2 b	60.07	0.52	36.51	0.06	0.17	3	0.03	0.04	0.008	0.12	-0.06	100.5
AB-11-19	95.39	0.45	4.2	0.038	0.05	0.1	< 0.01	0.01	0.001	0.03	0.29	100.5
AB-11-20	69.09	0.55	29.02	0.017	0.11	0.54	< 0.01	0.03	0.01	0.08	-0.1	99.35
AB-11-22	72.54	0.45	26.11	0.025	0.09	0.44	0.04	0.04	0.002	0.12	-0.13	99.73
AB-11-23	48.67	0.71	46.45	0.105	0.31	2.83	< 0.01	0.06	0.017	0.15	0.07	99.38
AB-11-24	66.43	0.48	30.16	0.065	0.19	2.61	0.03	0.06	0.006	0.12	-0.15	100
AB-11-25	92.47	0.61	4.1	0.034	0.03	1.35	< 0.01	0.02	0.002	0.01	0.98	99.62

Table 2-3. Electron microprobe data for Group 1 feldspars inside silicification

AB-11-11 Wt. %	1	2	3	4	5	6	7	8	9	10	11	12	13	14
SiO_2	67.46	68.3	65.51	65.14	68.33	67.13	66.77	66.67	67.36	68.42	68.06	68.12	68.45	68.64
Al_2O_3	19.78	19.54	21.12	21.36	19.65	20.04	20.02	20.22	20.06	19.63	19.84	19.42	19.44	19.72
MgO	<0.03	<0.03	0.04	<0.03	<0.03	<0.03	<0.03	<0.03	<0.03	<0.03	<0.03	<0.03	<0.03	<0.03
CaO	0.27	<0.03	0.47	1.62	0.4	0.6	0.41	0.6	0.71	0.11	0.5	<0.03	0.37	0.43
FeO	<0.05	<0.05	0.07	0.08	<0.05	0.1	0.05	0.06	<0.05	<0.05	<0.05	<0.05	<0.05	0.05
Na_2O	11.43	11.64	10.40	9.69	11.09	10.91	10.86	11.14	11.38	11.31	11.23	11.38	11.51	11.26
K_2O	<0.05	<0.05	1.17	0.72	<0.05	0.44	0.27	0.15	0.08	<0.05	<0.05	<0.05	<0.05	<0.05
Total	98.96	99.51	98.78	98.61	99.47	99.24	98.40	98.86	99.61	99.47	99.63	98.94	99.79	100.14
Cation														
Si	2.977	2.995	2.915	2.9	2.994	2.962	2.965	2.951	2.96	2.997	2.982	3.001	2.995	2.991
Al	1.029	1.01	1.107	1.121	1.015	1.042	1.048	1.055	1.039	1.014	1.024	1.008	1.003	1.013
Mg	n.d.	n.d.	0.003	n.d	n.d	n.d	n.d	n.d	n.d	n.d	n.d.	n.d.	n.d.	n.d.
Ca	0.013	n.d	0.022	0.077	0.019	0.029	0.02	0.029	0.033	0.005	0.023	n.d.	0.018	0.02
Fe	n.d	n.d	0.003	0.003	n.d	0.004	0.002	0.002	n.d	n.d	n.d.	n.d.	n.d.	0.002
Na	0.978	0.99	0.897	0.836	0.942	0.934	0.935	0.956	0.969	0.96	0.954	0.972	0.976	0.951
K	n.d	n.d	0.066	0.041	n.d	0.025	0.015	0.008	0.005	n.d	n.d.	n.d.	n.d.	n.d.
Total	4.997	4.995	5.013	4.978	4.97	4.996	4.986	5.003	5.007	4.976	4.983	4.981	4.992	4.979
Ab	98.69	100.00	91.07	87.63	98.02	94.53	96.39	96.27	96.23	99.48	97.65	100.00	98.19	97.84
An	1.31	--	2.23	8.07	1.98	2.94	2.06	2.92	3.28	0.52	2.35	--	1.81	2.06
Or	--	--	6.70	4.30	--	2.53	1.55	0.81	0.5	--	--	--	--	0.10

n.d = not detected

Table 2-4. Electron microprobe data for Group 1 feldspars outside silicification

AB-11-11 Wt. %	1	2	3	4	5	6	7	8	9	10	11	12	13	14	15
SiO_2	67.19	68.29	68.37	67.59	67.78	67.95	68.61	68.36	67.48	67.69	68.80	68.40	68.77	67.76	68.67
Al_2O_3	19.58	19.87	19.68	20.21	20.12	19.73	19.55	19.50	19.60	19.59	19.75	19.52	19.46	19.83	19.38
MgO	<0.03	<0.03	<0.03	0.03	<0.03	<0.03	<0.03	<0.03	<0.03	<0.03	<0.03	<0.03	<0.03	<0.03	<0.03
CaO	0.28	0.25	<0.03	0.4	0.36	0.46	0.28	<0.03	0.29	0.18	0.35	0.26	0.19	0.45	0.30
FeO	<0.05	<0.05	<0.05	0.1	0.06	0.10	0.05	<0.05	0.16	0.20	0.23	0.27	0.14	0.05	0.10
Na_2O	11.41	11.74	11.52	11.35	11.10	11.25	11.54	11.71	11.36	11.27	11.55	11.58	11.46	11.24	11.37
K_2O	0.50	0.06	0.38	0.18	0.56	<0.05	<0.05	<0.05	0.30	<0.05	<0.05	<0.05	<0.05	0.31	<0.05
Total	99.00	100.23	100.00	99.85	99.99	99.50	100.01	99.56	99.2	98.96	100.68	100.04	100.21	99.64	99.84
Cation															
Si	2.974	2.978	2.989	2.962	2.968	2.982	2.994	2.996	2.978	2.986	2.987	2.989	2.997	2.975	3.001
Al	1.022	1.022	1.014	1.044	1.038	1.021	1.005	1.01	1.019	1.019	1.011	1.005	1.000	1.026	0.998
Mg	n.d.	n.d	n.d.	0.002	n.d	n.d	n.d	n.d	n.d	n.d	n.d.	n.d.	n.d.	n.d.	n.d.
Ca	0.013	0.012	n.d.	0.02	0.02	0.022	0.013	n.d.	0.014	0.009	0.016	0.012	0.009	0.021	0.014
Fe	n.d	n.d	n.d.	0.004	0.002	0.004	n.d.	n.d.	0.01	0.01	0.008	0.01	0.005	0.002	0.003
Na	0.98	0.993	0.976	0.964	0.943	0.958	0.977	0.995	0.972	0.964	0.972	0.981	0.984	0.956	0.964
K	0.028	0.004	0.021	0.01	0.031	n.d.	n.d.	n.d.	0.017	n.d	n.d.	n.d.	n.d.	0.017	n.d.
Total	5.019	5.009	5.003	5.003	5.000	4.986	4.991	4.998	5.007	4.987	4.994	4.999	4.995	4.998	4.982
Ab	95.98	98.41	97.89	97.08	95.16	97.76	98.69	100.00	96.91	99.08	98.69	99.09	96.18	98.19	98.57
An	1.27	1.19	--	1.91	1.72	2.24	1.31	--	1.40	0.92	1.21	0.91	2.11	1.50	1.43
Or	2.67	0.39	2.06	1.00	3.03	0.00	0.00	--	1.67	--	0.10	--	1.68	0.30	--

n.d = not detected

Table 2-5. Electron microprobe data for Group 1 quartz

AB-11-11 Wt. %	1	2	3	4	5	6	7	8	9	10
SiO_2	99.16	98.44	98.16	97.92	98.38	99.48	98.96	99.76	100.18	100.38
Al_2O_3	0.28	0.87	0.79	0.45	0.32	0.25	0.20	0.12	0.07	<0.03
MgO	<0.03	<0.03	0.03	0.05	0.17	0.06	0.10	<0.03	<0.03	<0.03
CaO	<0.03	<0.03	<0.03	<0.03	<0.03	0.25	0.12	<0.03	<0.03	<0.03
FeO	<0.05	0.07	0.28	0.48	0.47	0.28	0.32	0.13	0.03	0.05
Na_2O	<0.05	0.47	0.03	<0.05	<0.05	0.05	<0.05	<0.05	<0.05	<0.05
K_2O	0.08	0.10	<0.05	<0.05	<0.05	<0.05	<0.05	<0.05	<0.05	0.05
Total	99.54	99.96	99.28	98.92	99.37	100.37	99.72	99.72	100.31	100.50
Cation										
Si	3.989	3.957	3.966	3.974	3.975	3.978	3.981	3.994	3.996	3.998
Al	0.013	0.041	0.038	0.021	0.015	0.012	0.01	0.006	0.006	n.d.
Mg	n.d.	n.d.	0.002	0.003	0.01	0.003	0.006	n.d.	n.d.	n.d.
Ca	n.d.	n.d.	n.d.	n.d.	n.d.	0.011	0.005	n.d.	n.d.	n.d.
Fe	n.d.	n.d.	0.009	0.016	0.016	0.009	0.011	0.004	0.004	0.002
Na	n.d.	0.037	0.002	n.d.	n.d.	0.004	n.d.	n.d.	n.d.	n.d.
K	0.004	0.005	n.d.	n.d.	n.d.	n.d.	n.d.	n.d.	n.d.	0.003
Total	4.01	4.04	4.02	4.02	4.02	4.02	4.01	4.00	4.00	4

AB-11-11 Wt. %	11	12	13	14	15	16	17	18	19	20
SiO_2	100.17	100.03	99.85	99.96	99.83	99.62	99.48	99.46	99.79	100.01
Al_2O_3	0.05	0.05	0.02	<0.03	<0.03	0.03	0.03	0.03	<0.03	<0.03
MgO	0.03	<0.03	<0.03	<0.03	<0.03	<0.03	<0.03	<0.03	<0.03	<0.03
CaO	<0.03	<0.03	0.21	<0.03	<0.03	<0.03	<0.03	0.22	0.45	<0.03
FeO	0.07	<0.05	<0.05	<0.05	<0.05	0.06	<0.05	<0.05	<0.05	<0.05
Na_2O	<0.05	<0.05	<0.05	<0.05	<0.05	<0.05	<0.05	<0.05	<0.05	<0.05
K_2O	<0.05	<0.05	<0.05	0.11	<0.05	<0.05	<0.05	<0.05	<0.05	<0.05
Total	100.34	100.11	100.10	100.11	99.83	99.70	99.52	99.75	100.28	100.01
Cation										
Si	3.996	3.998	3.994	3.997	3.999	3.998	3.99	3.994	3.989	3.999
Al	0.002	0.002	0.001	n.d.	n.d.	0.001	n.d.	0.001	n.d.	n.d.
Mg	0.002	n.d.	n.d.	n.d.	n.d.	n.d.	n.d.	n.d.	n.d.	n.d.
Ca	n.d.	n.d.	0.009	n.d.	n.d.	n.d.	n.d.	0.01	0.019	n.d.
Fe	0.002	n.d.	n.d.	n.d.	n.d.	0.002	n.d.	n.d.	n.d.	n.d.
Na	n.d.	n.d.	n.d.	n.d.	n.d.	n.d.	n.d.	n.d.	n.d.	n.d.
K	0.004	n.d.	n.d.	0.006	n.d.	n.d.	n.d.	n.d.	n.d.	n.d.
Total	4.00	4.00	4.00	4.00	4.00	4.00	4.00	4.00	4.01	4.00

n.d = not detected

Table 2-6. Electron microprobe data for Group 2 feldspars outside silicification

AB-11-12											
Wt% Oxide	1	2	3	4	5	6	7	8	9	10	11
SiO2	67.3753	67.9067	67.8353	68.6815	68.4007	68.4777	67.4214	68.178	68.5301	67.6568	67.9824
Al2O3	19.7179	19.6275	20.1372	19.7307	19.6587	19.5671	19.9491	19.5008	19.3122	19.7202	19.5459
MgO	0.0072	0	0	0	0	0.0079	0	0	0.0094	0.0036	0
CaO	0.5576	0.4073	0.6048	0.2047	0	0.4527	0.3759	0.0087	0.3102	0.4726	0.2394
FeO	0.0237	0.0289	0.0863	0.0043	0.0463	0.0948	0.0903	0.0431	0.0635	0.1096	0.071
Na2O	11.4294	11.7875	11.4762	11.6459	11.5876	11.3446	11.1897	11.5241	11.6469	11.5284	11.614
K2O	0.1832	0	0	0.0417	0	0	1.0353	0.0408	0	0.0415	0.1707
Total	99.2943	99.7579	100.1397	100.3089	99.6934	99.9448	100.0617	99.2954	99.8724	99.5328	99.6234
Nb of Ions	1	2	3	4	5	6	7	8	9	10	11
Si	2.971	2.978	2.964	2.99	2.993	2.992	2.962	2.996	2.998	2.974	2.985
Al	1.025	1.015	1.037	1.012	1.014	1.007	1.033	1.01	0.996	1.022	1.011
Mg	0	0	0	0	0	0.001	0	0	0.001	0	0
Ca	0.026	0.019	0.028	0.01	0	0.021	0.018	0	0.015	0.022	0.011
Fe	0.001	0.001	0.003	0	0.002	0.003	0.003	0.002	0.002	0.004	0.003
Na	0.977	1.002	0.972	0.983	0.983	0.961	0.953	0.982	0.988	0.983	0.989
K	0.01	0	0	0.002	0	0	0.058	0.002	0	0.002	0.01
Total	5.011	5.016	5.004	4.997	4.992	4.985	5.027	4.991	4.998	5.007	5.009

Table 2-7. Trace element data for Groups 1, 2, 3

Sample	Sc	V	Cr	Co	Ni	Rb	Sr	Zr	Nb	Ba	Hf	Pb	Th	U
	ppm	ppm	ppm	ppm	ppm	ppm	ppm	ppm	ppm	ppm	ppm	ppm	ppm	ppm
AB-11-08	5	22	< 20	3	< 20	2	58	129	4.4	50	3.3	6	2.27	0.66
AB-11-11	7	11	< 20	2	< 20	2	68	212	7.8	63	5.3	< 5	3.52	1.06
AB-11-12	8	59	20	15	< 20	2	8	37	1.3	40	0.9	5	0.5	0.16
AB-11-16	8	57	< 20	18	20	< 1	25	155	5.8	28	4	< 5	2.55	0.73
AB-11-17	7	6	< 20	< 1	< 20	< 1	79	254	10.9	50	6.6	< 5	4.32	1.26
AB-11-18	< 1	9	< 20	5	< 20	< 1	2	7	< 0.2	24	0.1	< 5	0.06	0.07
AB-11-19	< 1	5	< 20	< 1	< 20	< 1	< 2	< 1	< 0.2	12	< 0.1	< 5	0.05	0.06
AB-11-20	< 1	< 5	< 20	< 1	< 20	< 1	3	< 1	< 0.2	7	< 0.1	< 5	< 0.05	< 0.01
AB-11-22	< 1	< 5	80	< 1	< 20	1	3	2	< 0.2	12	< 0.1	< 5	< 0.05	0.02
AB-11-23	< 1	< 5	< 20	< 1	< 20	3	7	2	< 0.2	23	< 0.1	< 5	< 0.05	< 0.01
AB-11-24	< 1	< 5	50	1	< 20	2	3	5	< 0.2	21	< 0.1	< 5	0.07	0.02
AB-11-25	< 1	< 5	< 20	< 1	< 20	2	3	30	1.3	9	0.8	< 5	0.18	0.06
AB-11-26b	3	20	< 20	5	< 20	< 1	3	16	0.6	6	0.4	< 5	0.19	0.06
AB-11-26t	6	51	< 20	18	< 20	< 1	< 2	33	1.3	18	0.8	< 5	0.4	0.13
AB-11-27	5	6	< 20	< 1	< 20	1	92	181	7.2	28	4.3	10	2.93	0.86
AB-11-30	< 1	< 5	< 20	1	< 20	3	8	3	< 0.2	5	< 0.1	< 5	< 0.05	< 0.01
AB-11-31	< 1	< 5	< 20	7	< 20	2	10	2	< 0.2	8	< 0.1	36	< 0.05	0.07
AB-11-32	< 1	< 5	< 20	2	< 20	2	7	2	< 0.2	4	< 0.1	< 5	< 0.05	< 0.01
AB-11-33	< 1	< 5	< 20	5	< 20	4	7	5	< 0.2	14	0.1	< 5	0.06	0.04
AB-11-34	5	19	< 20	4	< 20	2	9	56	2.5	19	1.3	< 5	0.93	0.19
AB-11-39	< 1	< 5	< 20	2	< 20	< 1	< 2	10	< 0.2	6	< 0.1	< 5	< 0.05	0.01
AB-11-41	15	140	80	22	50	17	127	88	3.5	152	2.2	< 5	1.04	0.34
AB-11-42	16	145	40	20	50	28	162	104	4.6	200	2.6	< 5	1.18	0.37
TEM-CHRIS	< 1	< 5	< 20	< 1	< 20	< 1	4	2	0.2	7	< 0.1	< 5	0.16	0.18
FCC	5	< 5	< 20	1	< 20	35	110	204	8.3	337	5.2	< 5	3.47	0.93
4.2 b	< 1	< 5	< 20	< 1	< 20	2	4	7	0.4	22	0.2	< 5	0.08	0.03

Table 2-7 continued. Trace element data for Groups 1, 2, 3

Sample	La	Ce	Pr	Nd	Sm	Eu	Gd	Tb	Dy	Y	Ho	Er	Yb	Lu	Tm
	ppm	ppm	ppm	ppm	ppm	ppm	ppm	ppm	ppm	ppm	ppm	ppm	ppm	ppm	ppm
AB-11-08	0.28	0.7	0.1	0.44	0.09	0.06	0.1	0.01	0.07	0.5	0.02	0.06	0.06	0.009	0.009
AB-11-11	31.8	65.9	7.76	30.2	6.05	1.13	4.92	0.77	4.62	23.8	0.92	2.82	2.92	0.478	0.431
AB-11-12	17.9	38	4.52	17.8	3.62	0.949	2.76	0.41	2.32	12.9	0.49	1.5	1.6	0.268	0.228
AB-11-16	19.5	34.1	4.1	16.9	3.91	0.747	3.34	0.52	3.15	17.8	0.67	2.17	2.41	0.418	0.356
AB-11-17	35.7	73.9	8.69	35	7.73	1.43	6.83	1.07	6.36	31.2	1.21	3.59	3.61	0.6	0.54
AB-11-18	8.36	13.3	1.3	4.72	0.69	0.338	0.59	0.06	0.33	1.9	0.07	0.17	0.17	0.03	0.024
AB-11-19	1.13	2	0.23	0.9	0.12	0.082	0.18	0.02	0.13	0.8	0.03	0.08	0.08	0.015	0.012
AB-11-20	2.2	2.41	0.21	0.81	0.1	0.1	0.1	0.01	0.09	0.5	0.02	0.06	0.06	0.014	0.008
AB-11-22	0.94	1.74	0.21	0.98	0.24	0.217	0.3	0.05	0.32	2.4	0.08	0.24	0.21	0.035	0.034
AB-11-23	1.96	3.5	0.42	1.95	0.47	0.593	0.61	0.11	0.71	5.7	0.17	0.53	0.54	0.098	0.08
AB-11-24	3.12	5.29	0.6	2.1	0.41	0.369	0.52	0.09	0.56	6.6	0.12	0.39	0.41	0.076	0.058
AB-11-25	1.42	2.45	0.24	0.92	0.2	0.064	0.27	0.05	0.37	2.3	0.09	0.33	0.39	0.062	0.052
AB-11-26b	3.07	6.19	0.78	3.35	0.68	0.243	0.59	0.08	0.45	2.6	0.09	0.31	0.31	0.065	0.044
AB-11-26t	6.83	14.7	1.76	7.23	1.4	0.356	1.13	0.16	0.89	4.8	0.18	0.58	0.61	0.114	0.085
AB-11-27	24.9	53.8	6.56	27.3	5.79	1.09	5.19	0.83	4.89	24.3	0.94	2.75	2.72	0.431	0.412
AB-11-30	0.55	1.24	0.16	0.71	0.18	0.14	0.22	0.04	0.25	1.6	0.06	0.19	0.21	0.044	0.03
AB-11-31	2.27	3.88	0.44	1.88	0.42	0.54	0.56	0.1	0.75	5.2	0.17	0.61	0.65	0.109	0.091
AB-11-32	0.45	0.91	0.12	0.57	0.15	0.144	0.19	0.03	0.23	1.7	0.05	0.18	0.19	0.029	0.027
AB-11-33	3.46	5.63	0.63	2.8	0.61	1.06	0.8	0.12	0.82	6.1	0.19	0.61	0.61	0.107	0.087
AB-11-34	1.03	2.07	0.23	0.9	0.27	0.155	0.3	0.06	0.38	2.6	0.09	0.28	0.34	0.069	0.044
AB-11-39	1.09	1.75	0.24	0.98	0.2	0.079	0.23	0.04	0.22	1.2	0.04	0.15	0.18	0.031	0.026
AB-11-41	11	21.6	2.54	10.6	2.44	0.863	2.3	0.35	2.02	10.2	0.39	1.15	1.09	0.179	0.17
AB-11-42	0.31	0.61	0.08	0.34	0.09	0.012	0.07	< 0.01	0.05	< 0.5	0.01	0.04	0.04	0.007	0.006
TEM-CHRIS	1.86	3.33	0.39	1.56	0.35	0.167	0.4	0.07	0.52	3.5	0.11	0.39	0.39	0.067	0.059
FCC	25.3	53.7	6.39	26	5.5	0.917	4.77	0.73	4.28	23.3	0.85	2.62	2.68	0.447	0.397
4.2 b	2.1	4.04	0.45	2.05	0.45	0.495	0.63	0.1	0.68	5.1	0.16	0.49	0.48	0.08	0.075

Table 2-7 continued. Trace element data for Groups 1, 2, 3

Upper crust norm.	Sc	V	Cr	Co	Ni	Rb	Sr	Zr	Nb	Ba	Hf	Pb	Th	U
AB-11-08	0.47	0.30	0.00	0.16	0.00	0.03	0.19	0.86	0.53	0.09	0.85	0.33	0.28	0.31
AB-11-11	0.65	0.15	0.00	0.11	0.00	0.03	0.23	1.41	0.94	0.11	1.36	0.00	0.43	0.50
AB-11-12	0.75	0.81	0.14	0.79	0.00	0.03	0.03	0.25	0.16	0.07	0.23	0.28	0.06	0.08
AB-11-16	0.75	0.78	0.00	0.95	0.26	0.00	0.08	1.03	0.70	0.05	1.03	0.00	0.31	0.35
AB-11-17	0.65	0.08	0.00	0.00	0.00	0.00	0.26	1.69	1.31	0.09	1.69	0.00	0.53	0.60
AB-11-19	0.00	0.07	0.00	0.00	0.00	0.00	0.00	0.00	0.00	0.02	0.00	0.00	0.01	0.03
AB-11-20	0.00	0.00	0.00	0.00	0.00	0.00	0.01	0.00	0.00	0.01	0.00	0.00	0.00	0.00
AB-11-22	0.00	0.00	0.57	0.00	0.00	0.01	0.01	0.01	0.00	0.02	0.00	0.00	0.00	0.01
AB-11-23	0.00	0.00	0.00	0.00	0.00	0.04	0.02	0.01	0.00	0.04	0.00	0.00	0.00	0.00
AB-11-24	0.00	0.00	0.36	0.05	0.00	0.03	0.01	0.03	0.00	0.04	0.00	0.00	0.01	0.01
AB-11-25	0.00	0.00	0.00	0.00	0.00	0.03	0.01	0.20	0.16	0.02	0.21	0.00	0.02	0.03
AB-11-26b	0.28	0.27	0.00	0.26	0.00	0.00	0.01	0.11	0.07	0.01	0.10	0.00	0.02	0.03
AB-11-26t	0.56	0.70	0.00	0.95	0.00	0.00	0.00	0.22	0.16	0.03	0.21	0.00	0.05	0.06
AB-11-27	0.47	0.08	0.00	0.00	0.00	0.01	0.31	1.21	0.87	0.05	1.10	0.56	0.36	0.41
AB-11-30	0.00	0.00	0.00	0.05	0.00	0.04	0.03	0.02	0.00	0.01	0.00	0.00	0.00	0.00
AB-11-31	0.00	0.00	0.00	0.37	0.00	0.03	0.03	0.01	0.00	0.01	0.00	2.00	0.00	0.03
AB-11-32	0.00	0.00	0.00	0.11	0.00	0.03	0.02	0.01	0.00	0.01	0.00	0.00	0.00	0.00
AB-11-33	0.00	0.00	0.00	0.26	0.00	0.05	0.02	0.03	0.00	0.02	0.03	0.00	0.01	0.02
AB-11-34	0.47	0.26	0.00	0.21	0.00	0.03	0.03	0.37	0.30	0.03	0.33	0.00	0.11	0.09
AB-11-39	0.00	0.00	0.00	0.11	0.00	0.00	0.00	0.07	0.00	0.01	0.00	0.00	0.00	0.00
AB-11-41	1.40	1.92	0.57	1.16	0.66	0.23	0.42	0.59	0.42	0.26	0.56	0.00	0.13	0.16
AB-11-42	1.50	1.99	0.29	1.05	0.66	0.38	0.54	0.69	0.55	0.35	0.67	0.00	0.15	0.18
TEM-CHRIS	0.00	0.00	0.00	0.00	0.00	0.00	0.01	0.01	0.02	0.01	0.00	0.00	0.02	0.09
FCC	0.47	0.00	0.00	0.05	0.00	0.48	0.37	1.36	1.00	0.59	1.33	0.00	0.43	0.44
4.2 b	0.00	0.00	0.00	0.00	0.00	0.03	0.01	0.05	0.05	0.04	0.05	0.00	0.01	0.01

Table 2-7 continued. Trace element data for Groups 1, 2, 3

AB-11-11 norm.	Sc	V	Cr	Co	Ni	Rb	Sr	Zr	Nb	Ba	Hf	Pb	Th	U
AB-11-08	0.71	2.00	--	1.50	--	1.00	0.85	0.61	0.56	0.79	0.62	--	0.64	0.62
AB-11-11	1.00	1.00	--	1.00	--	1.00	1.00	1.00	1.00	1.00	1.00	--	1.00	1.00
AB-11-12	1.14	5.36	--	7.50	--	1.00	0.12	0.17	0.17	0.63	0.17	--	0.14	0.15
AB-11-16	1.14	5.18	--	9.00	--	0.00	0.37	0.73	0.74	0.44	0.75	--	0.72	0.69
AB-11-17	1.00	0.55	--	0.00	--	0.00	1.16	1.20	1.40	0.79	1.25	--	1.23	1.19
AB-11-18														
AB-11-19	0.00	0.45	--	0.00	--	0.00	0.00	0.00	0.00	0.19	0.00	--	0.01	0.06
AB-11-20	0.00	0.00	--	0.00	--	0.00	0.04	0.00	0.00	0.11	0.00	--	0.00	0.00
AB-11-22	0.00	0.00	--	0.00	--	0.50	0.04	0.01	0.00	0.19	0.00	--	0.00	0.02
AB-11-23	0.00	0.00	--	0.00	--	1.50	0.10	0.01	0.00	0.37	0.00	--	0.00	0.00
AB-11-24	0.00	0.00	--	0.50	--	1.00	0.04	0.02	0.00	0.33	0.00	--	0.02	0.02
AB-11-25	0.00	0.00	--	0.00	--	1.00	0.04	0.14	0.17	0.14	0.15	--	0.05	0.06
AB-11-26b	0.43	1.82	--	2.50	--	0.00	0.04	0.08	0.08	0.10	0.08	--	0.05	0.06
AB-11-26t	0.86	4.64	--	9.00	--	0.00	0.00	0.16	0.17	0.29	0.15	--	0.11	0.12
AB-11-27	0.71	0.55	--	0.00	--	0.50	1.35	0.85	0.92	0.44	0.81	--	0.83	0.81
AB-11-30	0.00	0.00	--	0.50	--	1.50	0.12	0.01	0.00	0.08	0.00	--	0.00	0.00
AB-11-31	0.00	0.00	--	3.50	--	1.00	0.15	0.01	0.00	0.13	0.00	--	0.00	0.07
AB-11-32	0.00	0.00	--	1.00	--	1.00	0.10	0.01	0.00	0.06	0.00	--	0.00	0.00
AB-11-33	0.00	0.00	--	2.50	--	2.00	0.10	0.02	0.00	0.22	0.02	--	0.02	0.04
AB-11-34	0.71	1.73	--	2.00	--	1.00	0.13	0.26	0.32	0.30	0.25	--	0.26	0.18
AB-11-39	0.00	0.00	--	1.00	--	0.00	0.00	0.05	0.00	0.10	0.00	--	0.00	0.01
AB-11-41	2.14	12.73	--	11.00	--	8.50	1.87	0.42	0.45	2.41	0.42	--	0.30	0.32
AB-11-42	2.29	13.18	--	10.00	--	14.00	2.38	0.49	0.59	3.17	0.49	--	0.34	0.35
TEM-CHRIS	0.00	0.00	--	0.00	--	0.00	0.06	0.01	0.03	0.11	0.00	--	0.05	0.17
FCC	0.71	0.00	--	0.50	--	17.50	1.62	0.96	1.06	5.35	0.98	--	0.99	0.88
4.2 b	0.00	0.00	--	0.00	--	1.00	0.06	0.03	0.05	0.35	0.04	--	0.02	0.03

Table 2-8. Rare earth element data for Groups 1, 2, 3

PAAS norm.	La	Ce	Pr	Nd	Sm	Eu	Gd	Tb	Dy	Y	Ho	Er	Yb	Lu	Tm	Zr	Hf
AB-11-08	23.3	42.5	4.7	18.4	3.58	0.822	2.87	0.43	2.48	12.8	0.5	1.43	1.59	0.272	0.234	129	3.3
AB-11-11	31.8	65.9	7.76	30.2	6.05	1.13	4.92	0.77	4.62	23.8	0.92	2.82	2.92	0.478	0.431	212	5.3
AB-11-12	3.72	8.27	1.14	5.1	1.34	0.455	1.19	0.2	1.24	6.1	0.25	0.73	0.79	0.135	0.114	37	0.9
AB-11-16	19.5	34.1	4.1	16.9	3.91	0.747	3.34	0.52	3.15	17.8	0.67	2.17	2.41	0.418	0.356	155	4
AB-11-17	35.7	73.9	8.69	35	7.73	1.43	6.83	1.07	6.36	31.2	1.21	3.59	3.61	0.6	0.54	254	6.6
AB-11-18	8.36	13.3	1.3	4.72	0.69	0.338	0.59	0.06	0.33	1.9	0.07	0.17	0.17	0.03	0.024	7	0.1
AB-11-19	1.13	2	0.23	0.9	0.12	0.082	0.18	0.02	0.13	0.8	0.03	0.08	0.08	0.015	0.012	0	0
AB-11-20	1.12	1.79	0.2	0.84	0.16	0.177	0.2	0.03	0.21	1.6	0.05	0.15	0.15	0.031	0.022	0	0
AB-11-22	0.94	1.74	0.21	0.98	0.24	0.217	0.3	0.05	0.32	2.4	0.08	0.24	0.21	0.035	0.034	2	0
AB-11-23	1.96	3.5	0.42	1.95	0.47	0.593	0.61	0.11	0.71	5.7	0.17	0.53	0.54	0.098	0.08	2	0
AB-11-24	3.12	5.29	0.6	2.1	0.41	0.369	0.52	0.09	0.56	6.6	0.12	0.39	0.41	0.076	0.058	5	0
AB-11-25	1.42	2.45	0.24	0.92	0.2	0.064	0.27	0.05	0.37	2.3	0.09	0.33	0.39	0.062	0.052	30	0.8
AB-11-26b	3.07	6.19	0.78	3.35	0.68	0.243	0.59	0.08	0.45	2.6	0.09	0.31	0.31	0.065	0.044	16	0.4
AB-11-26t	6.83	14.7	1.76	7.23	1.4	0.356	1.13	0.16	0.89	4.8	0.18	0.58	0.61	0.114	0.085	33	0.8
AB-11-27	24.9	53.8	6.56	27.3	5.79	1.09	5.19	0.83	4.89	24.3	0.94	2.75	2.72	0.431	0.412	181	4.3
AB-11-30	0.55	1.24	0.16	0.71	0.18	0.14	0.22	0.04	0.25	1.6	0.06	0.19	0.21	0.044	0.03	3	0
AB-11-31	2.27	3.88	0.44	1.88	0.42	0.54	0.56	0.1	0.75	5.2	0.17	0.61	0.65	0.109	0.091	2	0
AB-11-32	0.45	0.91	0.12	0.57	0.15	0.144	0.19	0.03	0.23	1.7	0.05	0.18	0.19	0.029	0.027	2	0
AB-11-33	3.46	5.63	0.63	2.8	0.61	1.06	0.8	0.12	0.82	6.1	0.19	0.61	0.61	0.107	0.087	5	0.1
AB-11-34	7.74	18.1	2.26	9.31	2.13	0.817	1.79	0.27	1.65	7.9	0.33	0.94	0.96	0.166	0.14	56	1.3
AB-11-39	1.09	1.75	0.24	0.98	0.2	0.079	0.23	0.04	0.22	1.2	0.04	0.15	0.18	0.031	0.026	10	0
AB-11-41	11	21.6	2.54	10.6	2.44	0.863	2.3	0.35	2.02	10.2	0.39	1.15	1.09	0.179	0.17	88	2.2
AB-11-42	12.1	25.2	3.06	13	3.08	0.977	2.83	0.45	2.58	12.6	0.5	1.49	1.44	0.232	0.224	104	2.6
TEM-CHRIS	1.86	3.33	0.39	1.56	0.35	0.167	0.4	0.07	0.52	3.5	0.11	0.39	0.39	0.067	0.059	2	0
FCC	25.3	53.7	6.39	26	5.5	0.917	4.77	0.73	4.28	23.3	0.85	2.62	2.68	0.447	0.397	204	5.2
4.2 b	2.1	4.04	0.45	2.05	0.45	0.495	0.63	0.1	0.68	5.1	0.16	0.49	0.48	0.08	0.075	7	0.2

Chapter III tables

Table 3-1. $\delta^{18}O$ and $\delta^{30}Si$ isotope compositions of pillow basalt sample

Sample ID	^{16}O cps ($\times 10^9$)	$^{16}O_{samp/av.std}$	$^{18}O/^{16}O$ *drift corrected*	± abs	$\delta^{18}O$ *samples*	± ‰	$\delta^{18}O$ *standards*	± ‰	^{28}Si cps ($\times 10^9$)	$^{28}Si_{samp/av.std}$	$^{30}Si/^{28}Si$ *drift corrected*	± abs	$\delta^{30}Si$ *samples*	± ‰	$\delta^{30}Si$ *standards*	± ‰
(N 65° 10.752', W 049° 48.249')																
Quartz cement																
NBS_28_Isua1_ox@1a	2.47		0.00201759	0.00000013			9.43	0.43	0.17		0.03260728	0.00000530			-0.26	0.22
NBS_28_Isua1_ox@2a	2.48		0.00201791	0.00000017			9.60	0.43	0.17		0.03261756	0.00000470			0.05	0.20
NBS_28_Isua1_ox@3	2.45		0.00201760	0.00000015			9.44	0.43	0.17		0.03261265	0.00000663			-0.10	0.25
ISB31b_Isua1_ox@1	2.37	0.99	0.00203296	0.00000015	17.12	0.43			0.16	0.96	0.03262099	0.00000476	0.16	0.21		
ISB31b_Isua1_ox@02	2.36	0.99	0.00203321	0.00000022	17.25	0.44			0.16	0.96	0.03262494	0.00000447	0.28	0.20		
ISB31b_Isua1_ox@03	2.40	1.01	0.00203416	0.00000018	17.73	0.44			0.17	1.01	0.03264138	0.00000555	0.78	0.22		
ISB31b_Isua1_ox@04	2.38	1.00	0.00203430	0.00000019	17.79	0.44			0.17	1.00	0.03263633	0.00000443	0.63	0.20		
ISB31b_Isua1_ox@05	2.38	1.00	0.00203349	0.00000019	17.39	0.44			0.17	1.01	0.03263380	0.00000478	0.55	0.21		
ISB31b_Isua1_ox@06	2.35	0.99	0.00203395	0.00000023	17.62	0.44			0.17	0.99	0.03264128	0.00000512	0.78	0.21		
NBS_28_Isua1_ox@4	2.49		0.00201665	0.00000012			8.96	0.43	0.17		0.03262776	0.00000662			0.37	0.25
NBS_28_Isua1_ox@5	2.48		0.00201675	0.00000018			9.02	0.43	0.17		0.03261889	0.00000678			0.09	0.25
ISB31b_Isua1_ox@07	2.36	0.99	0.00203489	0.00000015	18.09	0.43			0.17	0.99	0.03264298	0.00000531	0.83	0.22		
ISB31b_Isua1_ox@08	2.35	0.98	0.00203390	0.00000018	17.60	0.44			0.17	1.00	0.03263552	0.00000457	0.60	0.20		
ISB31b_Isua1_ox@09	2.34	0.98	0.00203395	0.00000019	17.62	0.44			0.16	0.98	0.03263836	0.00000560	0.69	0.22		
ISB31b_Isua1_ox@10	2.32	0.97	0.00203402	0.00000014	17.66	0.43			0.17	0.98	0.03263863	0.00000574	0.70	0.23		
ISB31b_Isua1_ox@11	2.29	0.96	0.00203323	0.00000028	17.26	0.45			0.16	0.97	0.03263948	0.00000414	0.72	0.19		
ISB31b_Isua1_ox@12	2.35	0.98	0.00203401	0.00000022	17.65	0.44			0.16	0.98	0.03263682	0.00000492	0.64	0.21		
NBS_28_Isua1_ox@6	2.48		0.00201860	0.00000018			9.94	0.43	0.17		0.03261758	0.00000552			0.05	0.22
NBS_28_Isua1_ox@7	2.49		0.00201855	0.00000021			9.92	0.44	0.17		0.03261490	0.00000451			-0.03	0.20
ISB31b_Isua1_ox@13	2.38	1.00	0.00203450	0.00000020	17.90	0.44			0.16	0.97	0.03263500	0.00000533	0.59	0.22		
ISB31b_Isua1_ox@14	2.35	0.99	0.00203334	0.00000019	17.31	0.44			0.16	0.96	0.03261608	0.00000548	0.01	0.22		
ISB31b_Isua1_ox@15	2.34	0.98	0.00203301	0.00000022	17.15	0.44			0.16	0.96	0.03261766	0.00000485	0.06	0.21		
ISB31b_Isua1_ox@16	2.33	0.97	0.00203289	0.00000026	17.09	0.45			0.16	0.95	0.03262725	0.00000684	0.35	0.25		

Table 3-1. Continued.

Sample ID	^{16}O cps (x 10^9)	$^{16}O_{samp/av.std}$	$^{18}O/^{16}O$ *drift corrected*	± abs	$\delta^{18}O$ *samp*	± ‰	$\delta^{18}O$ *stand.*	± ‰	^{28}Si cps (x 10^9)	$^{28}Si_{samp/av.std}$	$^{30}Si/^{28}Si$ *drift corrected*	± abs	$\delta^{30}Si$ *samp*	± ‰	$\delta^{30}Si$ *stand*	± ‰
ISB31b_Isua1_ox@17	2.33	0.98	0.00203358	0.00000021	17.44	0.44			0.16	0.96	0.03262498	0.00000666	0.28	0.25		
ISB31b_Isua1_ox@18	2.33	0.97	0.00203310	0.00000018	17.20	0.44			0.16	0.97	0.03263698	0.00000449	0.65	0.20		
NBS_28_Isua1_ox@8	2.41		0.00201949	0.00000017			10.39	0.43	0.17		0.03261556	0.00000508			-0.01	0.21
NBS_28_Isua1_ox@9	2.41		0.00201923	0.00000016			10.26	0.43	0.17		0.03261321	0.00000555			-0.08	0.22
ISB31b_Isua1_ox@19	2.28	0.96	0.00203314	0.00000019	17.22	0.44			0.17	0.99	0.03261687	0.00000758	0.03	0.27		
ISB31b_Isua1_ox@20	2.29	0.96	0.00203322	0.00000019	17.26	0.44			0.16	0.97	0.03263744	0.00000480	0.66	0.21		
ISB31b_Isua1_ox@21	2.28	0.95	0.00203331	0.00000013	17.30	0.43			0.16	0.97	0.03263178	0.00000602	0.49	0.23		
ISB31b_Isua1_ox@22	2.26	0.95	0.00203249	0.00000019	16.89	0.44			0.17	0.99	0.03263748	0.00000315	0.66	0.17		
Quartz amygdules																
ISB31b_Isua1_ox@23	2.29	0.96	0.00203285	0.00000019	17.07	0.44			0.17	1.00	0.03259585	0.00000582	-0.61	0.23		
ISB31b_Isua1_ox@24	2.26	0.95	0.00203312	0.00000017	17.20	0.44			0.17	1.01	0.03260516	0.00000634	-0.33	0.24		
NBS_28_Isua1_ox@10	2.32		0.00201741	0.00000020			9.34	0.43	0.17		0.03261890	0.00000601			0.09	0.23
NBS_28_Isua1_ox@11	2.29		0.00201691	0.00000020			9.10	0.43	0.17		0.03261628	0.00000329			0.01	0.18
ISB31b_Isua1_ox@25	2.22	0.93	0.00203333	0.00000018	17.31	0.44			0.17	1.02	0.03261292	0.00000543	-0.09	0.22		
ISB31b_Isua1_ox@26	2.24	0.94	0.00203388	0.00000017	17.59	0.44			0.17	1.00	0.03257218	0.00000524	-1.34	0.22		
ISB31b_Isua1_ox@27	2.34	0.98	0.00203431	0.00000015	17.80	0.43			0.17	1.01	0.03262231	0.00000472	0.20	0.20		
ISB31b_Isua1_ox@28	2.36	0.99	0.00203443	0.00000016	17.86	0.43			0.17	1.00	0.03262038	0.00000562	0.14	0.23		
ISB31b_Isua1_ox@29	2.35	0.99	0.00203425	0.00000026	17.77	0.45			0.17	1.02	0.03251335	0.00000286	-3.14	0.17		
ISB31b_Isua1_ox@30	2.35	0.98	0.00203432	0.00000019	17.81	0.44			0.17	1.02	0.03260879	0.00000650	-0.22	0.25		
NBS_28_Isua1_ox@12	2.39		0.00201682	0.00000020			9.05	0.43	0.17		0.03261088	0.00000527			-0.15	0.22
NBS_28_Isua1_ox@13	2.40		0.00201800	0.00000023			9.64	0.44	0.17		0.03261549	0.00000660			-0.01	0.25
ISB31b_Isua1_ox@31	2.32	0.97	0.00203450	0.00000016	17.90	0.43			0.17	1.02	0.03261422	0.00000683	-0.05	0.25		
ISB31b_Isua1_ox@32	2.33	0.98	0.00203313	0.00000025	17.21	0.44			0.17	1.01	0.03259153	0.00000465	-0.75	0.20		
ISB31b_Isua1_ox@33	2.32	0.97	0.00203337	0.00000030	17.33	0.45			0.17	1.00	0.03262003	0.00000396	0.13	0.19		
ISB31b_Isua1_ox@34	2.25	0.94	0.00203252	0.00000018	16.90	0.44			0.16	0.98	0.03260465	0.00000589	-0.34	0.23		

Table 3-1. Continued.

Sample ID	^{16}O cps (x 10^9)	$^{16}O_{samp/av.std}$	$^{18}O/^{16}O$ *drift corrected*	± abs	$\delta^{18}O$ *samp*	± ‰	$\delta^{18}O$ *stand.*	± ‰	^{28}Si cps (x 10^9)	$^{28}Si_{samp/av.std}$	$^{30}Si/^{28}Si$ *drift corrected*	± abs	$\delta^{30}Si$ *samp*	± ‰	$\delta^{30}Si$ *stand*	± ‰
ISB31b_Isua1_ox@35	2.29	0.96	0.00203264	0.00000021	16.97	0.44			0.17	1.00	0.03246756	0.00000402	-4.55	0.19		
ISB31b_Isua1_ox@36	2.28	0.96	0.00203364	0.00000021	17.47	0.44			0.17	1.00	0.03248431	0.00000523	-4.03	0.22		
NBS_28_Isua1_ox@14	2.33		0.00201800	0.00000020			9.64	0.43	0.17		0.03260531	0.00000667			-0.32	0.25
NBS_28_Isua1_ox@15	2.32		0.00201649	0.00000015			8.89	0.43	0.17		0.03261460	0.00000388			-0.04	0.19
ISB31b_Isua1_ox@37	2.20	0.92	0.00203286	0.00000013	17.08	0.43			0.17	0.99	0.03246076	0.00000491	-4.75	0.21		
ISB31b_Isua1_ox@38	2.26	0.95	0.00203279	0.00000015	17.04	0.43			0.17	0.99	0.03244968	0.00000549	-5.09	0.22		
ISB31b_Isua1_ox@39	2.27	0.95	0.00203251	0.00000019	16.90	0.44			0.16	0.97	0.03246109	0.00000620	-4.75	0.24		
ISB31b_Isua1_ox@40	2.27	0.95	0.00203325	0.00000023	17.27	0.44			0.16	0.98	0.03252171	0.00000507	-2.89	0.21		
ISB31b_Isua1_ox@41	2.26	0.94	0.00203385	0.00000022	17.57	0.44			0.16	0.97	0.03246003	0.00000372	-4.78	0.18		
ISB31b_Isua1_ox@42	2.25	0.94	0.00203295	0.00000013	17.12	0.43			0.16	0.98	0.03253775	0.00000555	-2.39	0.22		
NBS_28_Isua1_ox@16	2.34		0.00201780	0.00000014			9.54	0.43	0.17		0.03262286	0.00000434			0.21	0.20
NBS_28_Isua1_ox@17	2.32		0.00201786	0.00000014			9.57	0.43	0.17		0.03261895	0.00000497			0.10	0.21
ISB31b_Isua1_ox@43	2.23	0.93	0.00203295	0.00000014	17.12	0.43			0.16	0.98	0.03253201	0.00000560	-2.57	0.22		
ISB31b_Isua1_ox@44	2.23	0.93	0.00203256	0.00000020	16.92	0.44			0.16	0.98	0.03246311	0.00000603	-4.68	0.23		
ISB31b_Isua1_ox@45	2.22	0.93	0.00203233	0.00000017	16.81	0.43			0.16	0.97	0.03247569	0.00000529	-4.30	0.22		
ISB31b_Isua1_ox@46	2.24	0.94	0.00203317	0.00000017	17.23	0.43			0.16	0.97	0.03251087	0.00000572	-3.22	0.23		
ISB31b_Isua1_ox@47	2.21	0.93	0.00203324	0.00000017	17.27	0.43			0.16	0.97	0.03250147	0.00000736	-3.51	0.27		
ISB31b_Isua1_ox@48	2.23	0.93	0.00203289	0.00000013	17.09	0.43			0.17	0.98	0.03251223	0.00000415	-3.18	0.19		
NBS_28_Isua1_ox@18	2.34		0.00201644	0.00000021			8.86	0.44	0.17		0.03262009	0.00000482			0.13	0.21
NBS_28_Isua1_ox@19	2.30		0.00201654	0.00000022			8.91	0.44	0.17		0.03261364	0.00000568			-0.07	0.23
ISB31b_Isua1_ox@49	2.22	0.93	0.00203401	0.00000016	17.65	0.43			0.17	0.99	0.03248426	0.00000389	-4.03	0.19		
ISB31b_Isua1_ox@50	2.24	0.94	0.00203398	0.00000028	17.63	0.45			0.17	0.99	0.03248415	0.00000436	-4.04	0.20		
ISB31b_Isua1_ox@51	2.24	0.94	0.00203426	0.00000017	17.78	0.44			0.17	1.00	0.03254208	0.00000554	-2.26	0.22		
ISB31b_Isua1_ox@52	2.27	0.95	0.00203474	0.00000021	18.02	0.44			0.17	1.01	0.03248665	0.00000574	-3.96	0.23		

Table 3-2: Si isotope compositions of chert and chert clast samples

Point #	^{28}Si	$^{28}Si_{samp/av.stnd}$	$^{30}Si/^{28}Si$	± abs	$\delta^{30}Si$	± ‰	$\delta^{30}Si$	± ‰	$\delta^{30}Si$	± ‰
	cps x 10^9		*drift corrected*		*samples measured*		*samples corrected*		*standard*	
ISB 26 (Greenstone chert, >3.7 Ga Isua Greenstone Belt; N 65° 10.752', W 049° 48.249')										
UTQ_D_mt_3_Si@26†	0.14		0.03264118	0.00000481					0.36	0.22
UTQ_D_mt_3_Si@27	0.14		0.03263567	0.00000631					0.19	0.25
ISB_26_mt_6_Si@1	0.14	0.94	0.03261545	0.00000496	-0.42	0.22	0.59	0.40		
ISB_26_mt_6_Si@02	0.14	0.95	0.03257924	0.00000284	-1.53	0.18	-0.52	0.35		
ISB_26_mt_6_Si@03	0.14	0.94	0.03260938	0.00000353	-0.61	0.19	0.40	0.36		
ISB_26_mt_6_Si@04	0.14	0.94	0.03261694	0.00000631	-0.38	0.25	0.63	0.44		
ISB_26_mt_6_Si@05	0.14	0.93	0.03260377	0.00000518	-0.78	0.23	0.23	0.40		
ISB_26_mt_6_Si@06	0.14	0.93	0.03258325	0.00000507	-1.41	0.22	-0.40	0.40		
UTQ_D_mt_3_Si@28	0.14		0.03262557	0.00000254					-0.11	0.18
UTQ_D_mt_3_Si@29	0.14		0.03263480	0.00000406					0.17	0.20
ISB_26_mt_6_Si@07	0.14	0.93	0.03260450	0.00000380	-0.76	0.20	0.25	0.37		
ISB_26_mt_6_Si@08	0.14	0.93	0.03258973	0.00000439	-1.21	0.21	-0.20	0.38		
ISB_26_mt_6_Si@09	0.14	0.93	0.03258739	0.00000398	-1.29	0.20	-0.28	0.37		
ISB_26_mt_6_Si@10	0.14	0.92	0.03257961	0.00000383	-1.52	0.20	-0.51	0.37		
ISB_26_mt_6_Si@11	0.14	0.93	0.03259544	0.00000530	-1.04	0.23	-0.03	0.41		
ISB_26_mt_6_Si@12	0.14	0.94	0.03259319	0.00000409	-1.11	0.20	-0.10	0.37		
UTQ_D_mt_3_Si@30	0.14		0.03263554	0.00000497					0.19	0.22
UTQ_D_mt_3_Si@31	0.14		0.03262773	0.00000623					-0.05	0.25
ISB_26_mt_6_Si@13	0.14	0.95	0.03260431	0.00000526	-0.77	0.23	0.24	0.41		
ISB_26_mt_6_Si@14	0.14	0.93	0.03261041	0.00000562	-0.58	0.24	0.43	0.42		
ISB_26_mt_6_Si@15	0.14	0.93	0.03262977	0.00000409	0.01	0.20	1.02	0.37		
ISB_26_mt_6_Si@16	0.14	0.92	0.03261563	0.00000470	-0.42	0.22	0.59	0.39		
ISB_26_mt_6_Si@17	0.13	0.91	0.03262202	0.00000485	-0.22	0.22	0.79	0.39		
ISB_26_mt_6_Si@18	0.13	0.91	0.03262780	0.00000388	-0.05	0.20	0.96	0.37		
UTQ_D_mt_3_Si@32	0.13		0.03263743	0.00000594					0.25	0.24

Table 3-2. Continued.

Point #	^{28}Si *cps x 10^9*	$^{28}Si_{samp/av.stnd}$	$^{30}Si/^{28}Si$ *drift corrected*	± abs	$\delta^{30}Si$ *samples measured*	± ‰	$\delta^{30}Si$ *samples corrected*	± ‰	$\delta^{30}Si$ *standard*	± ‰
UTQ_D_mt_3_Si@33	0.13		0.03263073	0.00000427					0.04	0.21
ISB_26_mt_6_Si@19	0.13	0.90	0.03262771	0.00000390	-0.05	0.20	0.96	0.37		
ISB_26_mt_6_Si@20	0.13	0.90	0.03263057	0.00000467	0.04	0.22	1.05	0.39		
ISB_26_mt_6_Si@21	0.13	0.90	0.03262590	0.00000404	-0.10	0.20	0.91	0.37		
ISB_26_mt_6_Si@22	0.13	0.90	0.03262032	0.00000254	-0.28	0.18	0.73	0.34		
ISB_26_mt_6_Si@23	0.13	0.90	0.03262292	0.00000302	-0.20	0.19	0.81	0.35		
ISB_26_mt_6_Si@24	0.13	0.89	0.03262766	0.00000241	-0.05	0.18	0.96	0.34		
UTQ_D_mt_3_Si@34	0.13		0.03262259	0.00000417					-0.21	0.21
UTQ_D_mt_3_Si@35	0.13		0.03262530	0.00000457					-0.12	0.21
ISB_26_mt_6_Si@25	0.13	0.88	0.03262818	0.00000572	-0.03	0.24	0.98	0.42		
ISB_26_mt_6_Si@26	0.13	0.88	0.03258922	0.00000573	-1.23	0.24	-0.22	0.42		
ISB_26_mt_6_Si@27	0.13	0.87	0.03260710	0.00000379	-0.68	0.20	0.33	0.37		
ISB_26_mt_6_Si@28	0.13	0.87	0.03262463	0.00000472	-0.14	0.22	0.87	0.39		
ISB_26_mt_6_Si@29	0.13	0.87	0.03262266	0.00000446	-0.20	0.21	0.81	0.38		
ISB_26_mt_6_Si@30	0.13	0.86	0.03263679	0.00000352	0.23	0.19	1.24	0.36		
UTQ_D_mt_3_Si@36	0.13		0.03263100	0.00000461					0.05	0.21
UTQ_D_mt_3_Si@37	0.13		0.03263597	0.00000434					0.20	0.21
ISB_26_mt_6_Si@31	0.13	0.85	0.03262497	0.00000270	-0.13	0.18	0.88	0.34		
ISB_26_mt_6_Si@32	0.13	0.85	0.03261124	0.00000412	-0.55	0.20	0.46	0.38		
ISB_26_mt_6_Si@33	0.12	0.85	0.03260879	0.00000504	-0.63	0.22	0.38	0.40		
ISB_26_mt_6_Si@34	0.13	0.85	0.03260676	0.00000225	-0.69	0.17	0.32	0.34		
ISB_26_mt_6_Si@35	0.13	0.86	0.03260645	0.00000418	-0.70	0.21	0.31	0.38		
ISB_26_mt_6_Si@36	0.12	0.85	0.03259960	0.00000496	-0.91	0.22	0.10	0.40		
UTQ_D_mt_3_Si@38	0.12		0.03263111	0.00000499					0.05	0.22
UTQ_D_mt_3_Si@39	0.12		0.03264076	0.00000375					0.35	0.20
ISB_26_mt_6_Si@37	0.12	0.84	0.03259446	0.00000433	-1.07	0.21	-0.06	0.38		
ISB_26_mt_6_Si@38	0.12	0.84	0.03257490	0.00000326	-1.67	0.19	-0.66	0.35		

Table 3-2. Continued.

Point #	^{28}Si *cps x 10^9*	$^{28}Si_{samp/av.stnd}$	$^{30}Si/^{28}Si$ *drift corrected*	± abs	$\delta^{30}Si$ *samples measured*	± ‰	$\delta^{30}Si$ *samples corrected*	± ‰	$\delta^{30}Si$ *standard*	± ‰
ISB_26_mt_6_Si@39	0.12	0.84	0.03260607	0.00000298	-0.71	0.18	0.30	0.35		
ISB_26_mt_6_Si@40	0.12	0.85	0.03260395	0.00000424	-0.78	0.21	0.23	0.38		
ISB_26_mt_6_Si@41	0.13	0.87	0.03260772	0.00000601	-0.66	0.24	0.35	0.43		
ISB_26_mt_6_Si@42	0.12	0.89	0.03256626	0.00000360	-1.93	0.19	-0.92	0.36		
UTQ_D_mt_3_Si@40	0.13		0.03262893	0.00000315					-0.01	0.19
UTQ_D_mt_3_Si@41	0.13		0.03262418	0.00000505					-0.16	0.22
ISB_26_mt_6_Si@43	0.13	0.88	0.03258477	0.00000384	-1.37	0.20	-0.36	0.37		
ISB_26_mt_6_Si@44	0.13	0.88	0.03258106	0.00000443	-1.48	0.21	-0.47	0.38		
ISB_26_mt_6_Si@45	0.13	0.88	0.03259873	0.00000597	-0.94	0.24	0.07	0.43		
ISB_26_mt_6_Si@46	0.14	0.93	0.03256312	0.00000346	-2.03	0.19	-1.02	0.36		
UTQ_D_mt_3_Si@42	0.13		0.03262752	0.00000487					-0.05	0.22
UTQ_D_mt_3_Si@43	0.14		0.03263141	0.00000416					0.06	0.20
ISB_26_mt_6_Si@47	0.13	0.91	0.03258021	0.00000547	-1.51	0.23	-0.50	0.41		
ISB_26_mt_6_Si@48	0.13	0.91	0.03258909	0.00000307	-1.23	0.19	-0.22	0.35		
ISB_26_mt_6_Si@49	0.13	0.91	0.03259604	0.00000323	-1.02	0.19	-0.01	0.35		
ISB_26_mt_6_Si@50	0.13	0.90	0.03260064	0.00000330	-0.88	0.19	0.13	0.36		
UTQ_D_mt_3_Si@44	0.13		0.03263369	0.00000451					0.13	0.21
UTQ_D_mt_3_Si@45	0.13		0.03263185	0.00000536					0.08	0.23
UTQ_D_mt_3_Si@46	0.13		0.03262479	0.00000542					-0.14	0.23
ISB 28 (Greenstone chert, >3.7 Ga Isua Greenstone Belt; N 65° 10.752', W 049° 48.249')										
NBS_28_Isua_mt_1_re_run_Mar_2014_Si@22	0.17		0.03261963	0.00000744					0.12	0.27
NBS_28_Isua_mt_1_re_run_Mar_2014_Si@23	0.17		0.03262062	0.00000494					0.15	0.21
ISB_28_Isua_mt_1_re_run_Mar_2014_Si@1	0.16	0.96	0.03257838	0.00000483	-1.15	0.21	-1.15	0.21		
ISB_28_Isua_mt_1_re_run_Mar_2014_Si@2	0.16	0.96	0.03260322	0.00000608	-0.39	0.24	-0.39	0.24		

Table 3-2. Continued.

Point #	^{28}Si *cps x 10^9*	$^{28}Si_{samp/av.stnd}$	$^{30}Si/^{28}Si$ *drift corrected*	± abs	$\delta^{30}Si$ *samples measured*	± ‰	$\delta^{30}Si$ *samples corrected*	± ‰	$\delta^{30}Si$ *standard*	± ‰
ISB_28_Isua_mt_1_re_run_Mar_2014_Si@3	0.16	0.97	0.03259337	0.00000500	-0.69	0.21	-0.69	0.21		
ISB_28_Isua_mt_1_re_run_Mar_2014_Si@4	0.17	0.99	0.03260091	0.00000603	-0.46	0.23	-0.46	0.23		
ISB_28_Isua_mt_1_re_run_Mar_2014_Si@5	0.16	0.97	0.03255984	0.00000444	-1.72	0.20	-1.72	0.20		
ISB_28_Isua_mt_1_re_run_Mar_2014_Si@6	0.16	0.97	0.03256331	0.00000502	-1.61	0.21	-1.61	0.21		
NBS_28_Isua_mt_1_re_run_Mar_2014_Si@24	0.16		0.03261652	0.00000531					0.02	0.22
NBS_28_Isua_mt_1_re_run_Mar_2014_Si@25	0.16		0.03261910	0.00000419					0.10	0.19
ISB_28_Isua_mt_1_re_run_Mar_2014_Si@7	0.16	0.97	0.03260990	0.00000466	-0.18	0.20	-0.18	0.20		
ISB 5Bc (Recrystallized chert clast, >3.7 Ga Isua Greenstone Belt; N 65° 10.120', W 049° 49.568')										
ISB_5Bc_Isua_mt_1_re_run_Mar_2014_Si@1	0.16	0.97	0.03259561	0.00000510	-0.62	0.21	-0.62	0.21		
ISB_5Bc_Isua_mt_1_re_run_Mar_2014_Si@02	0.16	0.98	0.03259047	0.00000438	-0.78	0.20	-0.78	0.20		
ISB_5Bc_Isua_mt_1_re_run_Mar_2014_Si@03	0.16	0.97	0.03259520	0.00000414	-0.63	0.19	-0.63	0.19		
NBS_28_Isua_mt_1_re_run_Mar_2014_Si@26	0.17		0.03261811	0.00000588					0.07	0.23
NBS_28_Isua_mt_1_re_run_Mar_2014_Si@27	0.16		0.03261016	0.00000604					-0.17	0.24
ISB_5Bc_Isua_mt_1_re_run_Mar_2014_Si@04	0.16	0.95	0.03259711	0.00000504	-0.57	0.21	-0.57	0.21		
ISB_5Bc_Isua_mt_1_re_run_Mar_2014_Si@05	0.16	0.96	0.03260844	0.00000551	-0.23	0.22	-0.23	0.22		
ISB_5Bc_Isua_mt_1_re_run_Mar_2014_Si@06	0.16	0.96	0.03260738	0.00000589	-0.26	0.23	-0.26	0.23		
ISB_5Bc_Isua_mt_1_re_run_Mar_2014_Si@07	0.18	1.06	0.03254921	0.00000185	outlier	--	--	--		
NBS_28_Isua_mt_1_re_run_Mar_2014_Si@28	0.16		0.03261389	0.00000601					-0.06	0.23
NBS_28_Isua_mt_1_re_run_Mar_2014_Si@29	0.16		0.03261578	0.00000603					0.00	0.24

† UTQ-D internal standard, corrected to NBS-28 values

Chapter IV tables

Table 4-1. Comparison of NBS-28 (international stnd.) with UTQ (internal stnd.)

Run #	Sample ID	Seq. in run	^{28}Si cps (x 10^9)	$^{28}Si_{samp/av.std}$	$^{30}Si/^{28}Si$ *drift corrected*	± abs	δ^{30}Si *samples*	± ‰	δ^{30}Si *standards*	± ‰
1	NBS_28_stnd_test_2_Si_@1	1	0.20		0.03261751	0.00000651			-0.14	0.28
2	NBS_28_stnd_test_2_Si_@2	2	0.20		0.03262043	0.00000506			-0.05	0.25
3	UTQ_C_stnd_test_Si@1	3	0.20	0.99	0.03264979	0.00000346	0.85	0.22		
4	UTQ_C_stnd_test_Si@2	4	0.20	0.99	0.03265333	0.00000383	0.96	0.23		
5	NBS_28_stnd_test_2_Si_@3	5	0.20		0.03261827	0.00000516			-0.12	0.25
6	NBS_28_stnd_test_2_Si_@4	6	0.20		0.03262018	0.00000280			-0.06	0.21
7	UTQ_C_stnd_test_Si@3	7	0.20	0.98	0.03265929	0.00000474	1.14	0.24		
8	UTQ_C_stnd_test_Si@4	8	0.20	0.98	0.03265165	0.00000484	0.91	0.24		
9	NBS_28_stnd_test_2_Si_@5	9	0.20		0.03263009	0.00000274			0.24	0.21
10	NBS_28_stnd_test_2_Si_@6	10	0.20		0.03263288	0.00000405			0.33	0.23
11	UTQ_C_stnd_test_Si@5	11	0.20	0.98	0.03266031	0.00000326	1.17	0.22		
12	UTQ_C_stnd_test_Si@6	12	0.20	0.99	0.03265728	0.00000554	1.08	0.26		
13	NBS_28_stnd_test_2_Si_@7	13	0.21		0.03262579	0.00000385			0.11	0.23
14	NBS_28_stnd_test_2_Si_@8	14	0.21		0.03262494	0.00000663			0.09	0.28
15	UTQ_C_stnd_test_Si@7	15	0.20	0.99	0.03265570	0.00000474	1.03	0.24		
16	UTQ_C_stnd_test_Si@8	16	0.20	0.99	0.03265939	0.00000559	1.14	0.26		
17	NBS_28_stnd_test_2_Si_@9	17	0.20		0.03261156	0.00000363			-0.32	0.22
18	NBS_28_stnd_test_2_Si_@10	18	0.20		0.03261932	0.00000363			-0.09	0.22
19	NBS_28_stnd_test_Si@1	1	0.19		0.03261074	0.00000298			0.01	0.13
20	NBS_28_stnd_test_Si@2	2	0.19		0.03261265	0.00000558			0.07	0.20
21	UTQ_D_stnd_test_Si@1	3	0.20	1.02	0.03264580	0.00000419	1.09	0.16		
22	UTQ_D_stnd_test_Si@2	4	0.20	1.03	0.03264517	0.00000489	1.07	0.18		
23	NBS_28_stnd_test_Si@3	5	0.19		0.03260862	0.00000444			-0.05	0.17

Table 4-1. Continued.

Run #	Sample ID	Seq. in run	^{28}Si cps (x 10^9)	$^{28}Si_{samp/av.std}$	$^{30}Si/^{28}Si$ *drift corrected*	± abs	$\delta^{30}Si$ *samples*	± ‰ *standards*	$\delta^{30}Si$	± ‰
24	NBS_28_stnd_test_Si@4	6	0.19		0.03260506	0.00000396			-0.16	0.16
25	UTQ_D_stnd_test_Si@3	7	0.20	1.02	0.03264498	0.00000716	1.06	0.24		
26	UTQ_D_stnd_test_Si@4	8	0.20	1.03	0.03264298	0.00000346	1.00	0.15		
27	NBS_28_stnd_test_Si@5	9	0.19		0.03261390	0.00000550			0.11	0.20
28	NBS_28_stnd_test_Si@6	10	0.19		0.03260886	0.00000591			-0.05	0.21
29	UTQ_D_stnd_test_Si@5	11	0.20	1.03	0.03263001	0.00000507	0.60	0.18		
30	UTQ_D_stnd_test_Si@6	12	0.20	1.02	0.03262732	0.00000642	0.52	0.22		
31	NBS_28_stnd_test_Si@7	13	0.19		0.03261032	0.00000546			0.00	0.19
32	NBS_28_stnd_test_Si@8	14	0.20		0.03261596	0.00000536			0.17	0.19
33	UTQ_D_stnd_test_Si@7	15	0.20	1.03	0.03262976	0.00000467	0.60	0.17		
34	UTQ_D_stnd_test_Si@8	16	0.20	1.02	0.03263567	0.00000594	0.78	0.21		
35	NBS_28_stnd_test_Si@9	17	0.20		0.03261041	0.00000524			0.00	0.19
36	NBS_28_stnd_test_Si@10	18	0.20		0.03260695	0.00000445			-0.10	0.17
--										
37	NBS_28_Mmount_Si@1	1	0.19		0.03258086	0.00000545			-0.58	0.34
38	NBS_28_Mmount_Si@2	2	0.18		0.03258377	0.00000392			-0.49	0.32
39	NBS_28_Mmount_Si@3	3	0.18		0.03259082	0.00000662			-0.28	0.36
40	UTQ_Isua_3_Mmount_Si@1	4	0.18	1.07	0.03259282	0.00000740	-0.21	0.37		
41	UTQ_Isua_3_Mmount_Si@2	5	0.18	1.07	0.03259719	0.00000656	-0.08	0.36		
42	UTQ_Isua_3_Mmount_Si@3	6	0.18	1.06	0.03259744	0.00000637	-0.07	0.35		
43	UTQ_Isua_3_Mmount_Si@4	7	0.18	1.06	0.03260381	0.00000584	0.12	0.35		
44	UTQ_Isua_3_Mmount_Si@5	8	0.18	1.04	0.03260069	0.00000563	0.03	0.34		
45	UTQ_Isua_3_Mmount_Si@6	9	0.18	1.05	0.03260645	0.00000726	0.20	0.37		

Table 4-2. Measured $\delta^{30}Si$ values for standard runs

Sample ID	Seq. in run	^{28}Si cps (x 10^9)	$^{28}Si_{samp/av.std}$	$^{30}Si/^{28}Si$ *drift corrected*	± abs	$\delta^{30}Si$ *samples*	± ‰	$\delta^{30}Si$ *standards*	± ‰
NBS_28_Isua_mt_1_re_run_Mar_2014_Si@1	1	0.1674627		0.03260728	5.30173E-06			-0.262813191	0.217765689
NBS_28_Isua_mt_1_re_run_Mar_2014_Si@2	2	0.1672929		0.032617557	4.70288E-06			0.052282963	0.204458153
NBS_28_Isua_mt_1_re_run_Mar_2014_Si@3	3	0.167705		0.032612654	6.62925E-06			-0.098038744	0.249634903
NBS_28_Isua_mt_1_re_run_Mar_2014_Si@4	10	0.1672853		0.032627764	6.62207E-06			0.36523005	0.249494859
NBS_28_Isua_mt_1_re_run_Mar_2014_Si@5	11	0.1685805		0.032618891	6.78484E-06			0.093188389	0.253549922
NBS_28_Isua_mt_1_re_run_Mar_2014_Si@6	18	0.1667753		0.032617581	5.52411E-06			0.053020999	0.222930984
NBS_28_Isua_mt_1_re_run_Mar_2014_Si@7	19	0.1657216		0.032614898	4.5083E-06			-0.029235645	0.200286945
NBS_28_Isua_mt_1_re_run_Mar_2014_Si@8	26	0.1693413		0.032615558	5.07636E-06			-0.009002957	0.212682524
NBS_28_Isua_mt_1_re_run_Mar_2014_Si@9	27	0.1700855		0.032613205	5.55255E-06			-0.081141822	0.223581501
NBS_28_Isua_mt_1_re_run_Mar_2014_Si@10	34	0.1705274		0.032618895	6.01131E-06			0.093310355	0.234484504
NBS_28_Isua_mt_1_re_run_Mar_2014_Si@11	35	0.1723686		0.032616282	3.29347E-06			0.013199907	0.176655561
NBS_28_Isua_mt_1_re_run_Mar_2014_Si@12	42	0.1708434		0.032610882	5.26837E-06			-0.15236663	0.217013837
NBS_28_Isua_mt_1_re_run_Mar_2014_Si@13	43	0.1706986		0.032615489	6.59746E-06			-0.011112325	0.248849279
NBS_28_Isua_mt_1_re_run_Mar_2014_Si@14	50	0.1735916		0.032605309	6.67191E-06			-0.323233366	0.250682265
NBS_28_Isua_mt_1_re_run_Mar_2014_Si@15	51	0.1715884		0.032614596	3.88393E-06			-0.038490551	0.187586915
NBS_28_Isua_mt_1_re_run_Mar_2014_Si@16	58	0.1697171		0.032622856	4.33913E-06			0.214757667	0.19676942
NBS_28_Isua_mt_1_re_run_Mar_2014_Si@17	59	0.1706133		0.032618954	4.96775E-06			0.095095898	0.210268478
NBS_28_Isua_mt_1_re_run_Mar_2014_Si@18	66	0.169169		0.032620093	4.81954E-06			0.130045357	0.207003975
NBS_28_Isua_mt_1_re_run_Mar_2014_Si@19	67	0.1689517		0.032613641	5.67848E-06			-0.067799254	0.226536421
UTQ_Isua_mt_1_re_run_Mar_2014_Si@1	72	0.1609428	0.960185043	0.032598606	5.10113E-06	-0.528751574	0.213187855		
UTQ_Isua_mt_1_re_run_Mar_2014_Si@2	73	0.1609892	0.960461866	0.032600123	5.35975E-06	-0.482236478	0.219075703		
NBS_28_Isua_mt_1_re_run_Mar_2014_Si@20	74	0.1672938		0.03261532	6.05337E-06			-0.016293429	0.235489729
NBS_28_Isua_mt_1_re_run_Mar_2014_Si@21	75	0.1676509		0.032608178	6.81331E-06			-0.235293397	0.254239482
UTQ_Isua_mt_1_re_run_Mar_2014_Si@3	76	0.1589263	0.9481546	0.032595725	4.10451E-06	-0.617097637	0.191887852		
UTQ_Isua_mt_1_re_run_Mar_2014_Si@4	77	0.1591861	0.949704568	0.032603262	5.77142E-06	-0.386009713	0.228704621		

Table 4-2. Continued.

Sample ID	Seq. in run	^{28}Si cps (x 10^9)	$^{28}Si_{samp/av.std}$	$^{30}Si/^{28}Si$ *drift corrected*	± abs	$\delta^{30}Si$ *samples*	± ‰	$\delta^{30}Si$ *standards*	± ‰
UTQ_Isua_mt_1_re_run_Mar_2014_Si@5	78	0.1600892	0.955092464	0.032600859	4.02356E-06	-0.459681575	0.190286934		
UTQ_Isua_mt_1_re_run_Mar_2014_Si@6	79	0.1614532	0.963230091	0.032594816	5.30091E-06	-0.644955611	0.217709996		
UTQ_Isua_mt_1_re_run_Mar_2014_Si@7	80	0.1591945	0.949754682	0.032606153	5.6877E-06	-0.297359923	0.226732462		
UTQ_Isua_mt_1_re_run_Mar_2014_Si@8	81	0.1600881	0.955085901	0.03260071	4.92113E-06	-0.464237996	0.209179145		
NBS_28_Isua_mt_1_re_run_Mar_2014_Si@22	82	0.1653561		0.032619627	7.44425E-06			0.115760023	0.270386175
NBS_28_Isua_mt_1_re_run_Mar_2014_Si@23	83	0.1671045		0.032620625	4.94359E-06			0.146331951	0.209737638
NBS_28_Isua_mt_1_re_run_Mar_2014_Si@24	90	0.1645425		0.032616525	5.30827E-06			0.020623334	0.21794261
NBS_28_Isua_mt_1_re_run_Mar_2014_Si@25	91	0.1636136		0.032619102	4.18532E-06			0.099637964	0.193599728
NBS_28_Isua_mt_1_re_run_Mar_2014_Si@26	96	0.1655164		0.032618107	5.87965E-06			0.069151175	0.231322882
NBS_28_Isua_mt_1_re_run_Mar_2014_Si@27	97	0.1638086		0.032610164	6.03572E-06			-0.174376743	0.235049113
NBS_28_Isua_mt_1_re_run_Mar_2014_Si@28	102	0.1599044		0.03261389	6.01177E-06			-0.060148625	0.234481871
NBS_28_Isua_mt_1_re_run_Mar_2014_Si@29	103	0.1577668		0.032615777	6.03339E-06			-0.002289352	0.235008373
NBS_28_Mmount_2_Si@5a	1	0.1493735		0.03248906	7.61341E-06			-0.47789399	0.687373433
NBS_28_Mmount_2_Si@5b	2	0.1517793		0.03246234	8.82958E-06			-1.299931644	0.700516068
NBS_28_Mmount_2_Si@5c	3	0.1462497		0.03248566	7.7399E-06			-0.58249459	0.688645674
NBS_28_Mmount_2_Si@6	8	0.1292963		0.0324724	1.26436E-05			-0.990436929	0.753987261
NBS_28_Mmount_2_Si@7	9	0.1347377		0.0324603	1.15174E-05			-1.362692004	0.736499869
NBS_28_Mmount_2_Si@8	16	0.1347878		0.03248006	5.82007E-06			-0.75477793	0.670409908
NBS_28_Mmount_2_Si@9	17	0.1358112		0.03247676	7.83402E-06			-0.856302042	0.689486365
NBS_28_Mmount_2_Si@10	24	0.1350735		0.03249806	8.81057E-06			-0.20101005	0.700944556
NBS_28_Mmount_2_Si@11	25	0.1304442		0.03248786	6.25039E-06			-0.514811849	0.674215133
NBS_28_Mmount_2_Si@12	32	0.1325852		0.03248926	9.69992E-06			-0.471741014	0.711813325
NBS_28_Mmount_2_Si@13	33	0.1438738		0.03250093	8.05567E-06			-0.112714837	0.692348361
NBS_28_Mmount_2_Si@14	40	0.1426449		0.03248815	8.2642E-06			-0.505890033	0.694434128
NBS_28_Mmount_2_Si@15	41	0.1393318		0.03248984	9.40033E-06			-0.453897382	0.70800931

Table 4-2. Continued.

Sample ID	Seq. in run	^{28}Si cps (x 10^9)	$^{28}Si_{samp/av.std}$	$^{30}Si/^{28}Si$ *drift corrected*	± abs	$\delta^{30}Si$ *samples*	± ‰	$\delta^{30}Si$ *standards*	± ‰
NBS_28_Mmount_2_Si@16	48	0.1375741		0.03251823	8.12803E-06			0.419517626	0.69346935
NBS_28_Mmount_2_Si@17	49	0.1416903		0.03251221	7.65599E-06			0.234313035	0.688253565
NBS_28_Mmount_2_Si@18	56	0.1386532		0.03252866	6.35027E-06			0.740395348	0.675874808
NBS_28_Mmount_2_Si@19	57	0.1367401		0.03251599	8.07232E-06			0.35060429	0.692811506
NBS_28_Mmount_2_Si@20	64	0.1362771		0.03251972	7.93891E-06			0.4653573	0.691420372
NBS_28_Mmount_2_Si@21	65	0.1355692		0.03252226	5.13968E-06			0.543500101	0.665940636
NBS_28_Mmount_2_Si@22	72	0.133587		0.03253209	8.4113E-06			0.845918894	0.696915195
NBS_28_Mmount_2_Si@23	73	0.1354396		0.03251841	6.19184E-06			0.425055305	0.674286511
NBS_28_Mmount_2_Si@24	80	0.1302938		0.03250409	5.69794E-06			-0.015497809	0.669877462
NBS_28_Mmount_2_Si@25	81	0.1317055		0.03249517	8.08176E-06			-0.289920559	0.692529142
NBS_28_Mmount_2_Si@26	88	0.1310609		0.0325211	7.08631E-06			0.507812838	0.682621952
NBS_28_Mmount_2_Si@27	89	0.1304115		0.0325278	6.64187E-06			0.713937549	0.678505975
UTQ_Isua_2_Mmount_Si@1	90	0.1312709	0.969141987	0.03254373	7.54288E-06	1.204022124	0.687660558		
UTQ_Isua_2_Mmount_Si@2	91	0.1308343	0.965918673	0.03255824	7.00742E-06	1.650420566	0.682551566		
UTQ_Isua_2_Mmount_Si@3	92	0.1310652	0.967623353	0.03256773	7.92596E-06	1.942379298	0.692173332		
UTQ_Isua_2_Mmount_Si@4	93	0.1297002	0.957545881	0.03255904	8.60725E-06	1.675032471	0.699672093		
UTQ_Isua_2_Mmount_Si@5	94	0.1295915	0.956743375	0.03256367	9.60072E-06	1.817473876	0.711885708		
UTQ_Isua_2_Mmount_Si@6	95	0.1296372	0.957080767	0.03252855	8.42799E-06	0.737011211	0.697040606		
NBS_28_Mmount_2_Si@28	96	0.1305798		0.03250938	7.32147E-06			0.147248418	0.684746666
NBS_28_Mmount_2_Si@29	97	0.1312731		0.03251128	7.45289E-06			0.205701694	0.686122832
UTQ_Isua_2_Mmount_Si@7	98	0.1298774	0.958854107	0.03254988	8.67525E-06	1.39322615	0.700298146		
UTQ_Isua_2_Mmount_Si@8	99	0.130006	0.95980353	0.03254372	8.67542E-06	1.203714475	0.700186833		
UTQ_ZIM_1_Mmount_Si@1	100	0.1318091	0.97311539	0.03255095	7.29107E-06	1.426144574	0.685220818		
UTQ_ZIM_1_Mmount_Si@2	101	0.1314868	0.970735926	0.03253647	6.90041E-06	0.980669079	0.681107445		
UTQ_ZIM_1_Mmount_Si@3	102	0.1339474	0.988901953	0.0325527	9.10482E-06	1.479983118	0.705492057		

Table 4-2. Continued.

Sample ID	Seq. in run	^{28}Si cps (x 10^9)	$^{28}Si_{samp/av.std}$	$^{30}Si/^{28}Si$ *drift corrected*	± abs	$\delta^{30}Si$ *samples*	± ‰	$\delta^{30}Si$ *standards*	± ‰
UTQ_ZIM_1_Mmount_Si@4	103	0.1340005	0.989293978	0.03254786	4.68254E-06	1.331081088	0.663239133		
NBS_28_Mmount_2_Si@30	104	0.1321954		0.03252399	5.57127E-06			0.596723348	0.669250933
NBS_28_Mmount_2_Si@31	105	0.1298331		0.03251654	7.41826E-06			0.367524975	0.685866261
UTQ_ZIM_1_Mmount_Si@5	106	0.1316087	0.971635885	0.03256912	6.16947E-06	1.985142485	0.67506033		
UTQ_ZIM_1_Mmount_Si@6	107	0.1298544	0.958684303	0.03257123	6.86318E-06	2.050056386	0.681408682		
UTQ_ZIM_1_Mmount_Si@7	108	0.1306751	0.964743337	0.03256644	5.17814E-06	1.9026926	0.667075872		
UTQ_ZIM_1_Mmount_Si@8	109	0.1309201	0.966552114	0.03255467	5.55683E-06	1.540589936	0.669727313		
NBS_28_Mmount_2_Si@32	110	0.1284629		0.03253011	6.25941E-06			0.785004427	0.675099818
NBS_28_Mmount_2_Si@33	111	0.1276607		0.03252527	4.38011E-06			0.636102397	0.660840693
NBS_28_Mmount_2_Si@34	112	0.1294242		0.03253402	6.51186E-06			0.905295117	0.677430401
NBS_28_Mmount_Si@1	1	0.1889395		0.03258086	5.45437E-06			-0.580762895	0.339800447
NBS_28_Mmount_Si@2	2	0.184816		0.03258377	3.9217E-06			-0.491498523	0.319308623
NBS_28_Mmount_Si@3	3	0.1849995		0.03259082	6.61716E-06			-0.27523948	0.358783701
UTQ_Isua_3_Mmount_Si@1	4	0.1837027	1.072294513	0.03259282	7.39716E-06	-0.213889397	0.372856898		
UTQ_Isua_3_Mmount_Si@2	5	0.1833084	1.069992937	0.03259719	6.55809E-06	-0.079839465	0.357809457		
UTQ_Isua_3_Mmount_Si@3	6	0.1818205	1.061307888	0.03259744	6.37184E-06	-0.072170704	0.354630804		
UTQ_Isua_3_Mmount_Si@4	7	0.1811102	1.057161782	0.03260381	5.84227E-06	0.123229311	0.345992506		
UTQ_Isua_3_Mmount_Si@5	8	0.1788174	1.043778436	0.03260069	5.63111E-06	0.027523181	0.342657867		
UTQ_Isua_3_Mmount_Si@6	9	0.1794515	1.047479753	0.03260645	7.26284E-06	0.204211421	0.370462656		
NBS_28_Mmount_Si@4	10	0.1850989		0.03259728	7.10556E-06			-0.077078711	0.367514504
NBS_28_Mmount_Si@5	11	0.1864827		0.03259108	5.30612E-06			-0.267263969	0.337665811
UTQ_Isua_3_Mmount_Si@8	12	0.1782568	1.040506147	0.03260321	6.64443E-06	0.104824286	0.359350207		
UTQ_Isua_3_Mmount_Si@9	13	0.1801279	1.05142798	0.03259168	6.75435E-06	-0.248858944	0.361187615		
UTQ_Isua_3_Mmount_Si@10	14	0.1788692	1.044080799	0.03260222	5.02266E-06	0.074455995	0.333651054		

Table 4-2. Continued.

Sample ID	Seq. in run	^{28}Si cps (x 10^9)	$^{28}Si_{samp/av.std}$	$^{30}Si/^{28}Si$ *drift corrected*	± abs	δ^{30}Si *samples*	± ‰	δ^{30}Si *standards*	± ‰
NBS_28_Mmount_Si@6	18	0.1859398		0.03258651	7.44816E-06			-0.407448909	0.373765615
NBS_28_Mmount_Si@7	19	0.1854589		0.03261063	5.87463E-06			0.332433095	0.346560664
NBS_28_Mmount_Si@8	26	0.1844203		0.03259187	5.95707E-06			-0.243030686	0.347737446
NBS_28_Mmount_Si@9	27	0.1846996		0.03259778	6.82304E-06			-0.06174119	0.362445552
NBS_28_Mmount_Si@10	34	0.1836554		0.03260147	7.4641E-06			0.051449714	0.374172069
NBS_28_Mmount_Si@11	35	0.1820584		0.03258819	6.46422E-06			-0.355914839	0.356130602
NBS_28_Mmount_Si@12	42	0.1800741		0.03261613	5.76147E-06			0.501145824	0.344811348
NBS_28_Mmount_Si@13	43	0.1798226		0.03260121	6.66317E-06			0.043474203	0.359661667
NBS_28_Mmount_Si@14	50	0.180359		0.03259332	8.44613E-06			-0.198551876	0.393271932
NBS_28_Mmount_Si@15	51	0.1802342		0.03259322	6.45874E-06			-0.20161938	0.356074997
NBS_28_Mmount_Si@16	58	0.1760241		0.0326018	6.08462E-06			0.061572477	0.349885468
NBS_28_Mmount_Si@17	59	0.1767097		0.03261754	7.3668E-06			0.544397633	0.372469227
NBS_28_Mmount_Si@18	66	0.1763585		0.03260028	8.06441E-06			0.014946414	0.385707101
NBS_28_Mmount_Si@19	67	0.1768699		0.03258289	6.22367E-06			-0.51849256	0.352035123
NBS_28_Mmount_Si@20	75	0.169432		0.03259802	5.91513E-06			-0.05437918	0.347110587
NBS_28_Mmount_Si@21	76	0.1704373		0.0326019	6.70343E-06			0.064639981	0.360370031
NBS_28_Mmount_Si@22	83	0.1657669		0.03259236	7.93526E-06			-0.227999916	0.3831227
NBS_28_Mmount_Si@23	84	0.1683848		0.03259358	7.58234E-06			-0.190576365	0.376346161
NBS_28_Mmount_Si@24	91	0.1637805		0.03259996	6.54216E-06			0.005130401	0.357555788
NBS_28_Mmount_Si@25	92	0.164203		0.03259625	5.76951E-06			-0.108674004	0.34478284
NBS_28_Mmount_Si@26	99	0.1632667		0.03261667	6.60427E-06			0.517710346	0.358753681
NBS_28_Mmount_Si@27	100	0.1642584		0.03258569	5.0998E-06			-0.432602443	0.334617681
NBS_28_Mmount_Si@28	107	0.1619027		0.03261434	7.53634E-06			0.446237499	0.375624259
NBS_28_Mmount_Si@29	108	0.160392		0.03260128	6.02737E-06			0.045621456	0.348947859
NBS_28_Mmount_Si@30	115	0.1598466		0.03260843	6.27743E-06			0.264948003	0.353126392

Table 4-2. Continued.

Sample ID	Seq. in run	^{28}Si cps (x 10^9)	$^{28}Si_{samp/av.std}$	$^{30}Si/^{28}Si$ *drift corrected*	± abs	δ^{30}Si *samples*	± ‰	δ^{30}Si *standards*	± ‰
NBS_28_Mmount_Si@31	116	0.1612642		0.03260108	6.24138E-06			0.039486447	0.352468625
NBS_28_Mmount_Si@32	123	0.1592452		0.03260488	5.96546E-06			0.156051606	0.347973102
NBS_28_Mmount_Si@33	124	0.1611165		0.03261495	5.29789E-06			0.464949275	0.337734071
NBS_28_Mmount_Si@34	131	0.157401		0.03260297	5.96305E-06			0.097462276	0.347919483
NBS_28_Mmount_Si@35	132	0.1581183		0.03260342	5.08775E-06			0.111266045	0.33458739
NBS_28_Mmount_Si@36	139	0.1579359		0.03260698	6.70252E-06			0.220469193	0.360392001
NBS_28_Mmount_Si@37	140	0.155378		0.03260102	4.51261E-06			0.037645945	0.326711307
NBS_28_Mmount_Si@38	147	0.1548551		0.03260992	4.90488E-06			0.310653815	0.33206057
NBS_28_Mmount_Si@39	148	0.1554384		0.03260688	6.46582E-06			0.217401689	0.356298878
NBS_28_Mmount_Si@40	149	0.1572511		0.03260448	5.70721E-06			0.143781589	0.343870172
UTQ_D_run_2_ab_11_mt_Si@1	1	0.1753267		0.032622572	5.5683E-06			-0.014193617	0.213000057
UTQ_D_run_2_ab_11_mt_Si@2	2	0.1746806		0.032622943	5.15931E-06			-0.002805089	0.203094961
UTQ_D_run_2_ab_11_mt_Si@3	3	0.1756417		0.032624685	3.88963E-06			0.050578306	0.174514949
UTQ_D_run_2_ab_11_mt_Si@4	10	0.1737351		0.032624525	5.5073E-06			0.045695205	0.211509488
UTQ_D_run_2_ab_11_mt_Si@5	11	0.1740422		0.032625487	4.47741E-06			0.075169114	0.187287398
UTQ_D_run_2_ab_11_mt_Si@6	18	0.1744931		0.032630408	5.0337E-06			0.226004207	0.200130212
UTQ_D_run_2_ab_11_mt_Si@7	19	0.173573		0.032625159	4.363E-06			0.06512182	0.184732302
UTQ_D_run_2_ab_11_mt_Si@8	26	0.1714411		0.03263403	4.00545E-06			0.337037004	0.176985327
UTQ_D_run_2_ab_11_mt_Si@9	27	0.1696932		0.032625971	3.07211E-06			0.09001916	0.158461004
UTQ_D_run_2_ab_11_mt_Si@10	34	0.1725824		0.032627282	6.22813E-06			0.130196245	0.229534875
UTQ_D_run_2_ab_11_mt_Si@11	35	0.1715615		0.032621693	4.51352E-06			-0.041108225	0.188089947
UTQ_D_run_2_ab_11_mt_Si@12	42	0.1702099		0.032627164	4.28573E-06			0.126586121	0.183030475
UTQ_D_run_2_ab_11_mt_Si@13	43	0.1693057		0.032621576	5.13262E-06			-0.044718349	0.20245526
UTQ_D_run_2_ab_11_mt_Si@14	50	0.1678695		0.032631225	4.88878E-06			0.251059472	0.19672836

Table 4-2. Continued.

Sample ID	Seq. in run	^{28}Si cps (x 10^9)	$^{28}Si_{samp/av.std}$	$^{30}Si/^{28}Si$ *drift corrected*	± abs	δ^{30}Si *samples*	± ‰	δ^{30}Si *standards*	± ‰
UTQ_D_run_2_ab_11_mt_Si@15	51	0.1677659		0.032625686	3.9717E-06			0.081287661	0.176245824
UTQ_D_run_2_ab_11_mt_Si@16	58	0.1621398		0.032625807	4.51849E-06			0.084987453	0.188212865
UTQ_D_run_2_ab_11_mt_Si@17	59	0.1627287		0.032635749	3.63894E-06			0.389726987	0.169391228
UTQ_D_run_2_ab_11_mt_Si@18	66	0.162145		0.032623789	4.11818E-06			0.023136272	0.179371117
UTQ_D_run_2_ab_11_mt_Si@19	67	0.1619869		0.032622011	5.66093E-06			-0.031379554	0.215280579
UTQ_D_run_2_ab_11_mt_Si@20	74	0.1560644		0.032625012	5.7009E-06			0.060601419	0.216276078
UTQ_D_run_2_ab_11_mt_Si@21	75	0.1565695		0.032620513	4.40078E-06			-0.077291077	0.185559925
UTQ_D_run_2_ab_11_mt_Si@22	82	0.1528804		0.032624214	3.95105E-06			0.036147126	0.175805032
UTQ_D_run_2_ab_11_mt_Si@23	83	0.1532426		0.032623525	5.02633E-06			0.015043276	0.199939002
UTQ_D_run_2_ab_11_mt_Si@24	90	0.1465664		0.032626446	4.87302E-06			0.104571993	0.196348541
UTQ_D_run_2_ab_11_mt_Si@25	91	0.1477806		0.032623178	4.71093E-06			0.004382918	0.192587672
UTQ_D_run_2_ab_11_mt_Si@26	98	0.1423674		0.032626018	2.93645E-06			0.09145938	0.156026259
UTQ_D_run_2_ab_11_mt_Si@27	99	0.14291		0.03262036	4.82803E-06			-0.081990813	0.195285995
UTQ_D_run_2_ab_11_mt_Si@28	106	0.1383588		0.03262411	4.37373E-06			0.03298005	0.184967659
UTQ_D_run_2_ab_11_mt_Si@29	107	0.1377656		0.032620602	3.35371E-06			-0.07456579	0.163720953
UTQ_D_run_2_ab_11_mt_Si@30	114	0.1322011		0.032622243	3.14581E-06			-0.024273153	0.159802107
UTQ_D_run_2_ab_11_mt_Si@31	115	0.1320638		0.032632074	4.48965E-06			0.27709453	0.187579898
UTQ_D_run_2_ab_11_mt_Si@32	122	0.1378412		0.032626325	4.60098E-06			0.10086011	0.19008245
UTQ_D_run_2_ab_11_mt_Si@33	123	0.1360669		0.032630236	6.07786E-06			0.220760923	0.225725361
UTQ_D_run_2_ab_11_mt_Si@34	130	0.126259		0.032630497	4.70459E-06			0.228752161	0.192461097
UTQ_D_run_2_ab_11_mt_Si@35	131	0.1270641		0.032625529	3.44355E-06			0.076452667	0.165478523
UTQ_D_run_2_ab_11_mt_Si@36	137	0.1243545		0.032618838	3.55478E-06			-0.128642598	0.167653843
UTQ_D_run_2_ab_11_mt_Si@37	138	0.1237755		0.032621569	3.50118E-06			-0.044912547	0.166599001
UTQ_D_run_2_ab_11_mt_Si@38	143	0.1181527		0.032630217	2.72844E-06			0.220165238	0.152451009
UTQ_D_run_2_ab_11_mt_Si@39	144	0.1188267		0.032621789	5.55798E-06			-0.038194285	0.212744903

Table 4-2. Continued.

Sample ID	Seq. in run	^{28}Si cps (x 10^9)	$^{28}Si_{samp/av.std}$	$^{30}Si/^{28}Si$ *drift corrected*	± abs	δ^{30}Si *samples*	± ‰	δ^{30}Si *standards*	± ‰
UTQ_D_run_2_ab_11_mt_Si@40	145	0.118648		0.03263472	4.87813E-06			0.35819828	0.196488692
UTQ-A_mt1_@1	1	0.1338503	1.071109564	0.03264596	5.23516E-06				
UTQ-A_mt1_@2	2	0.1335223	1.068484811	0.032644022	4.83543E-06				
UTQ-A_mt1_@3	3	0.1345702	1.076870416	0.032639364	4.06853E-06				
UTQ-A_mt1_@4	4	0.133514	1.068418392	0.032649866	3.48338E-06				
UTQ-A_mt1_@5	5	0.1328359	1.062992036	0.032650258	2.82722E-06				
UTQ-A_mt1_@6	6	0.1326654	1.061627644	0.03264723	4.69498E-06				
UTQ-A_mt1_@7	7	0.1322951	1.058664395	0.032653512	5.46483E-06				
UTQ-A_mt1_@8	8	0.132278	1.058527555	0.032645274	4.39504E-06				
UTQ-A_mt1_@9	9	0.1253687		0.032664766	5.82292E-06			-0.219401877	0.246927362
UTQ-A_mt1_@10	10	0.1263743	1.011284407	0.032653138	5.3723E-06				
UTQ-A_mt1_@11	11	0.1260621		0.03266948	3.8264E-06			-0.075117664	0.207211796
UTQ-A_mt1_@12	18	0.1251914		0.032680344	6.38457E-06			0.257404897	0.259659396
UTQ-A_mt1_@13	19	0.1252269		0.032677876	4.36672E-06			0.181866737	0.217021321
UTQ-A_mt1_@14	26	0.1238592		0.032674931	4.24999E-06			0.091702358	0.214827658
UTQ-A_mt1_@15	27	0.1238568		0.032677363	3.66161E-06			0.166140013	0.204438395
UTQ-A_mt1_@16	34	0.1280345		0.032671277	4.10436E-06			-0.020131317	0.21214333
UTQ-A_mt1_@17	35	0.1274918		0.032678119	4.60152E-06			0.189284572	0.221519817
UTQ-A_mt1_@18	42	0.1267375		0.032678303	5.4595E-06			0.19492107	0.239074881
UTQ-A_mt1_@19	43	0.1262079		0.032669385	3.49778E-06			-0.078034234	0.201698271
UTQ-A_mt1_@20	50	0.124726		0.032681759	5.61444E-06			0.300705364	0.242425395
UTQ-A_mt1_@21	51	0.1249606		0.032677861	5.14345E-06			0.181398751	0.232416002
UTQ-A_mt1_@22	58	0.1257634		0.032681195	4.86905E-06			0.283448274	0.226825428
UTQ-A_mt1_@23	59	0.1260792	1.00892293	0.032687207	3.30714E-06				
UTQ-A_mt1_@24	66	0.125086		0.032668471	4.16515E-06			-0.105993695	0.213238473

Table 4-2. Continued.

Sample ID	Seq. in run	^{28}Si cps (x 10^9)	$^{28}Si_{samp/av.std}$	$^{30}Si/^{28}Si$ *drift corrected*	± abs	δ^{30}Si *samples*	± ‰	δ^{30}Si *standards*	± ‰
UTQ-A_mt1_@25	67	0.1256264		0.032676153	5.92824E-06			0.129132333	0.249304469
UTQ-A_mt1_@26	74	0.1252117		0.032668488	5.69291E-06			-0.105498546	0.244084791
UTQ-A_mt1_@27	75	0.1246763		0.03267248	5.94967E-06			0.016686512	0.249768906
UTQ-A_mt1_@28	82	0.1250167		0.032667194	6.09077E-06			-0.145098971	0.252915778
UTQ-A_mt1_@29	83	0.1251342		0.032670326	3.87945E-06			-0.0492362	0.208137392
UTQ-A_mt1_@30	90	0.1250863	1.000977452	0.03265899	4.43272E-06				
UTQ-A_mt1_@31	91	0.125114		0.032674292	2.86965E-06			0.072157822	0.192210044
UTQ-A_mt1_@32	98	0.1241478		0.032686146	5.05913E-06			0.434981618	0.230708022
UTQ-A_mt1_@33	99	0.1240173		0.032681008	6.12981E-06			0.277721943	0.253846294
UTQ-A_mt1_@34	106	0.123599		0.032673102	4.69769E-06			0.03574531	0.223382443
UTQ-A_mt1_@35	107	0.1235994		0.032681254	4.99356E-06			0.285256774	0.22934704
UTQ-A_mt1_@36	112	0.1235466		0.032670344	5.06873E-06			-0.048665574	0.230844065
UTQ-A_mt1_@37	113	0.1230269		0.032674966	4.57084E-06			0.092802088	0.220911416
UTQ-A_mt1_@38	118	0.1239167		0.032664477	2.81253E-06			-0.22826519	0.191371715
UTQ-A_mt1_@39	119	0.1237905		0.032675989	4.05418E-06			0.124086833	0.211257581
UTQ-D_mt2_@1	1	0.1596519		0.03267519	2.52578E-06			0.179851607	0.201788982
UTQ-D_mt2_@2	2	0.1606231		0.032660515	4.73718E-06			-0.269338538	0.236080344
UTQ-D_mt2_@3	3	0.1596091		0.032673411	4.04386E-06			0.125382508	0.223736472
UTQ-D_mt2_@4	10	0.1605231		0.032667227	4.57294E-06			-0.063881897	0.233057473
UTQ-D_mt2_@5	11	0.160044		0.032674723	5.04875E-06			0.165546424	0.242116688
UTQ-D_mt2_@6	18	0.1600945		0.03267367	3.34055E-06			0.133310107	0.212587048
UTQ-D_mt2_@7	19	0.1592367		0.032671065	4.48713E-06			0.053579813	0.231507223
UTQ-D_mt2_@8	26	0.1601344		0.032672332	4.8622E-06			0.092358148	0.23850236
UTQ-D_mt2_@9	27	0.1599613		0.032677727	5.60529E-06			0.257505965	0.253340891

Table 4-2. Continued.

Sample ID	Seq. in run	^{28}Si cps (x 10^9)	$^{28}Si_{samp/av.std}$	$^{30}Si/^{28}Si$ *drift corrected*	± abs	δ^{30}Si *samples*	± ‰	δ^{30}Si *standards*	± ‰
UTQ-D_mt2_@10	34	0.1599327		0.032673974	4.11611E-06			0.142623286	0.224969963
UTQ-D_mt2_@11	35	0.1595352		0.032674389	3.70602E-06			0.155334478	0.218191108
UTQ-D_mt2_@12	42	0.1591559		0.032667886	5.48509E-06			-0.043725052	0.250822279
UTQ-D_mt2_@13	43	0.1591682		0.032671551	5.03518E-06			0.068467873	0.241837773
UTQ-D_mt2_@14	50	0.1602933		0.032666148	5.64743E-06			-0.096920916	0.254167538
UTQ-D_mt2_@15	51	0.1601336		0.032678873	2.7777E-06			0.29259647	0.204885993
UTQ-D_mt2_@16	58	0.1586801		0.03267741	3.88232E-06			0.24781015	0.221058835
UTQ-D_mt2_@17	59	0.1595835		0.032669795	3.62787E-06			0.014724938	0.216934579
UTQ-D_mt2_@18	66	0.1614963		0.032674372	3.12622E-06			0.154821592	0.209514437
UTQ-D_mt2_@19	67	0.1611779		0.032673928	4.76348E-06			0.141208388	0.236635947
UTQ-D_mt2_@20	74	0.1613685		0.032674974	3.55364E-06			0.173252576	0.215806009
UTQ-D_mt2_@21	75	0.1617187		0.03267583	3.96246E-06			0.199432064	0.222379422
UTQ-D_mt2_@22	82	0.1610113		0.032674297	4.65242E-06			0.152503061	0.234558487
UTQ-D_mt2_@23	83	0.1617986		0.032674832	5.31665E-06			0.168887425	0.247431073
UTQ-D_mt2_@24	90	0.1621182		0.032677439	4.16859E-06			0.248682844	0.22588985
UTQ-D_mt2_@25	91	0.1632098		0.032668344	4.91131E-06			-0.029704818	0.239425388
UTQ-D_mt2_@26	98	0.162395		0.032660111	4.34082E-06			-0.28171924	0.228828139
UTQ-D_mt2_@27	99	0.1613931		0.032661276	5.91564E-06			-0.246050724	0.259800335
UTQ-D_mt2_@28	106	0.162114		0.032671873	4.87294E-06			0.078316709	0.23870556
UTQ-D_mt2_@29	107	0.1621191		0.032678038	4.47276E-06			0.267034044	0.231278688
UTQ-D_mt2_@30	114	0.1641751		0.032664025	3.72691E-06			-0.161904813	0.218473708
UTQ-D_mt2_@31	115	0.1639634		0.03266051	5.70582E-06			-0.269489993	0.255362865
UTQ-D_mt2_@32	122	0.1644646		0.032671667	4.65728E-06			0.072018908	0.234636821
UTQ-D_mt2_@33	123	0.1641539		0.032672062	4.44992E-06			0.084117905	0.230837958
UTQ-D_mt2_@34	130	0.1641662		0.032664929	5.55623E-06			-0.134225776	0.252272448

Table 4-2. Continued.

Sample ID	Seq. in run	^{28}Si cps (x 10^9)	$^{28}Si_{samp/av.std}$	$^{30}Si/^{28}Si$ *drift corrected*	± abs	$\delta^{30}Si$ *samples*	± ‰	$\delta^{30}Si$ *standards*	± ‰
UTQ-D_mt2_@35	131	0.1641346		0.032661615	4.38968E-06			-0.235689003	0.229706615
UTQ-D_mt2_@36	138	0.1645536		0.032678731	4.4228E-06			0.28825409	0.230379963
UTQ-D_mt2_@37	139	0.1643121		0.032678697	4.29688E-06			0.287190889	0.228136572
UTQ-D_mt2_@38	146	0.1649096		0.032675004	5.28489E-06			0.174144796	0.246793624
UTQ-D_mt2_@39	147	0.1641451		0.032670819	4.17503E-06			0.046051074	0.225970039
UTQ-D_mt2_@40	154	0.164731		0.032676036	4.90458E-06			0.205737977	0.239330198
UTQ-D_mt2_@41	155	0.1641297		0.032676901	2.77562E-06			0.232223564	0.204849263
UTQ-D_mt2_@42	163	0.1646775		0.032665283	5.15695E-06			-0.123396768	0.244202475
UTQ-D_mt2_@43	164	0.163636		0.032677678	3.7784E-06			0.256019396	0.219366888
UTQ-D_mt2_@44	165	0.1638846		0.032673744	4.88282E-06			0.135578116	0.238902949
UTQ-D_mt2_@45	166	0.1756055	1.082172792	0.032612859	3.60049E-06				
UTQ-D_mt2_@46	167	0.1642796		0.032674514	5.10205E-06			0.159163915	0.243160265
UTQ-D_mt2_@47	168	0.1642457		0.032664759	4.79837E-06			-0.139426191	0.237254265
UTQ-D_mt2_@48	169	0.1646298		0.032672715	3.86379E-06			0.104082621	0.220731931
UTQ-D_mt2_@49	170	0.1669563	1.028871905	0.03264312	4.80411E-06				
UTQ-D_mt2_@50	171	0.1637453		0.032679685	5.3027E-06			0.317448957	0.24717142
UTQ-D_mt2_@51	172	0.1636543		0.03267866	3.80707E-06			0.286082089	0.219835526
UTQ-D_mt2_@52	173	0.1637978		0.032672426	4.44234E-06			0.095238352	0.23070278
UTQ-D_mt2_@53	174	0.1636065		0.032673081	5.14629E-06			0.115295888	0.244025713
UTQ-D_mt2_@54	175	0.1645481		0.032666796	4.0351E-06			-0.077078338	0.223556795
UTQ-D_mt2_@55	176	0.1646447		0.032677272	3.46271E-06			0.24356708	0.214428178
UTQ-D_mt2_@56	177	0.1641644		0.032668997	4.09844E-06			-0.009720576	0.224644108
UTQ-D_mt2_@57	178	0.1644342		0.032668752	4.84161E-06			-0.017211827	0.238093515
UTQ-D_mt2_@58	179	0.1628111		0.032664497	3.16082E-06			-0.147448232	0.209950137
UTQ-D_mt2_@59	180	0.1636039		0.032675473	2.77918E-06			0.188502067	0.204887157

Table 4-2. Continued.

Sample ID	Seq. in run	^{28}Si cps (x 10^9)	$^{28}Si_{samp/av.std}$	$^{30}Si/^{28}Si$ *drift corrected*	± abs	δ^{30}Si *samples*	± ‰	δ^{30}Si *standards*	± ‰
UTQ-D_mt2_@60	181	0.1633984		0.032661248	5.8915E-06			-0.246913684	0.259285853
UTQ-D_mt2_@61	182	0.1634207		0.032667913	3.14353E-06			-0.042891467	0.209724187
UTQ-D_mt2_@62	183	0.162406		0.032676698	5.30965E-06			0.22602345	0.247298333
UTQ-D_mt2_@63	184	0.1627652		0.032677284	2.14696E-06			0.243938302	0.197648603
UTQ-D_mt2_@64	185	0.1624773		0.032681029	4.3228E-06			0.358580009	0.228605629
UTQ-D_mt2_@65	186	0.1631506		0.032680524	5.28458E-06			0.343130219	0.246811073
UTQ-D_mt2_@66	187	0.163575		0.032680979	2.92023E-06			0.357065802	0.206745109
UTQ-D_mt2_@67	188	0.1629612		0.032686305	4.82744E-06			0.520070935	0.237902434
UTQ-D_mt2_@68	189	0.1627462		0.03267946	5.13943E-06			0.310555242	0.243918103
UTQ-D_mt2_@69	190	0.1625263		0.032675625	4.22E-06			0.193174938	0.226773708
UTQ-D_mt2_@70	191	0.1620533		0.032670151	4.55109E-06			0.025594621	0.232669748
UTQ-D_mt2_@71	192	0.1619175		0.032675076	4.5898E-06			0.176355849	0.233403524
UTQ-D_mt2_@72	193	0.1613524		0.032670201	3.6815E-06			0.02714139	0.217781375
UTQ-D_mt2_@73	194	0.1606427		0.032681186	4.82229E-06			0.363397788	0.237781572
UTQ-D_mt2_@74	195	0.1599758		0.032670382	4.57927E-06			0.032667429	0.233188232
UTQ-D_mt2_@75	196	0.1616554		0.032659487	2.9077E-06			-0.300817808	0.206468901
UTQ-D_mt2_@76	197	0.1606719		0.032660402	3.39268E-06			-0.272801734	0.213292901
UTQ-D_mt2_@77	198	0.1610448		0.032662167	3.66002E-06			-0.21876736	0.217402619
UTQ-D_mt2_@78	199	0.1607023		0.032671523	5.58847E-06			0.067595122	0.252966461
UTQ-D_mt2_@79	200	0.1609575		0.032666138	4.09098E-06			-0.097230316	0.224503078
UTQ-D_mt2_@80	201	0.1600354	0	0.032666623	4.67608E-06			-0.08237644	0.234964129
UTQ-D_mt2_@81	202	0.1612951	0	0.032675868	4.71E-06			0.200618968	0.235639578
UTQ-D_mt2_@82	203	0.1606726	0	0.032689454	5.29683E-06				
UTQ-D_mt2_@83	204	0.1612744	0	0.032661409	4.05491E-06			-0.241981937	0.223866777
UTQ-D_mt2_@84	205	0.1607458	0	0.032674674	4.75418E-06			0.164064722	0.236464015

Table 4-2. Continued.

Sample ID	Seq. in run	^{28}Si cps (x 10^9)	$^{28}Si_{samp/av.std}$	$^{30}Si/^{28}Si$ *drift corrected*	± abs	$\delta^{30}Si$ *samples*	± ‰	$\delta^{30}Si$ *standards*	± ‰
UTQ-D_mt2_@85	206	0.1607072	0	0.03266921	3.96325E-06			-0.003209497	0.222361026
UTQ_C_mt_3_Si@1	1	0.1458148		0.0326279	5.93905E-06			-0.201228496	0.247770288
UTQ_C_mt_3_Si@2	2	0.1467975		0.032626908	4.08825E-06			-0.231621252	0.209679498
UTQ_C_mt_3_Si@3	3	0.1458688		0.032636876	5.59344E-06			0.073827236	0.240132943
UTQ_C_mt_3_Si@4	10	0.1465484		0.032637183	4.51908E-06			0.083235699	0.217863887
UTQ_C_mt_3_Si@5	11	0.145658		0.032641721	3.20233E-06			0.222295687	0.19474984
UTQ_C_mt_3_Si@6	18	0.145248	1.045657126	0.032652049	3.25961E-06				
UTQ_C_mt_3_Si@7	19	0.145046		0.032633667	2.94737E-06			-0.024523457	0.190896621
UTQ_C_mt_3_Si@8	26	0.1447199		0.032637074	5.21436E-06			0.079876599	0.231986687
UTQ_C_mt_3_Si@9	27	0.143553		0.032638312	4.75541E-06			0.117816504	0.22254067
UTQ_C_mt_3_Si@10	34	0.1410103		0.032641439	4.08031E-06			0.213636675	0.209594296
UTQ_C_mt_3_Si@11	35	0.1398343		0.032637887	5.08232E-06			0.104799248	0.229222389
UTQ_C_mt_3_Si@12	42	0.1382347		0.032645244	6.34925E-06			0.330236979	0.257201018
UTQ_C_mt_3_Si@13	43	0.1430202		0.032641302	4.49367E-06			0.209448997	0.217386332
UTQ_C_mt_3_Si@14	50	0.146819		0.032643469	5.24431E-06			0.275852416	0.232643506
UTQ_C_mt_3_Si@15	51	0.1381035		0.032646007	3.91738E-06			0.353627506	0.206674452
UTQ_C_mt_3_Si@16	58	0.1493042		0.032639754	3.92522E-06			0.162021501	0.206787917
UTQ_C_mt_3_Si@17	59	0.1483131		0.032640513	5.59202E-06			0.185253031	0.240115067
UTQ_C_mt_3_Si@18	66	0.1422216		0.03263732	5.59245E-06			0.087412922	0.240112866
UTQ_C_mt_3_Si@19	67	0.1405905		0.032632598	3.78474E-06			-0.05727617	0.204284084
UTQ_C_mt_3_Si@20	74	0.1405271		0.032633145	4.4203E-06			-0.040513519	0.215936697
UTQ_C_mt_3_Si@21	75	0.1369727		0.032636433	5.01969E-06			0.060243407	0.227917545
UTQ_C_mt_3_Si@22	82	0.1369976		0.03263252	3.30808E-06			-0.059659266	0.196361687
UTQ_C_mt_3_Si@23	83	0.1355855	0.976095673	0.032621118	3.52244E-06				
UTQ_C_mt_3_Si@24	90	0.1277678		0.032629195	5.05928E-06			-0.161539625	0.228710455

Table 4-2. Continued.

Sample ID	Seq. in run	^{28}Si cps (x 10^9)	$^{28}Si_{samp/av.std}$	$^{30}Si/^{28}Si$ *drift corrected*	± abs	$\delta^{30}Si$ *samples*	± ‰	$\delta^{30}Si$ *standards*	± ‰
UTQ_C_mt_3_Si@25	91	0.1270288		0.032633733	4.42591E-06			-0.022479637	0.216046877
UTQ_C_mt_3_Si@26	98	0.1243606		0.03263198	4.8148E-06			-0.076194619	0.223711854
UTQ_C_mt_3_Si@27	99	0.122617		0.032641189	3.62713E-06			0.205965607	0.201618944
UTQ_C_mt_3_Si@28	106	0.1154371		0.032645426	3.19961E-06			0.335798896	0.194724381
UTQ_C_mt_3_Si@29	107	0.1154156		0.032644204	3.96109E-06			0.298358377	0.207447735
UTQ_C_mt_3_Si@30	113	0.1442217		0.032638923	6.29092E-06			0.13653228	0.255830439
UTQ_C_mt_3_Si@31	114	0.1444347		0.032633071	3.79714E-06			-0.04278278	0.204502027
UTQ_C_mt_3_Si@32	115	0.1399401		0.032627339	4.8493E-06			-0.218420746	0.224392388
UTQ_C_mt_4_Si@1	1	0.1854298		0.03263515	3.8078E-06			-0.010555884	0.168381179
UTQ_C_mt_4_Si@2	2	0.1845962		0.032632927	3.07529E-06			-0.078657345	0.153678388
UTQ_C_mt_4_Si@3	3	0.1855734		0.032636475	4.32841E-06			0.03004256	0.179804821
UTQ_C_mt_4_Si@4	10	0.1846569		0.032643097	3.67216E-06			0.232960461	0.165550434
UTQ_C_mt_4_Si@5	11	0.1853159		0.032639665	4.88227E-06			0.127782803	0.192669712
UTQ_C_mt_4_Si@6	18	0.1837269		0.032643087	3.15205E-06			0.232647953	0.155161179
UTQ_C_mt_4_Si@7	19	0.1847194		0.032647165	3.61464E-06			0.357587845	0.16436894
UTQ_C_mt_4_Si@8	26	0.1832478		0.032641407	3.24246E-06			0.181164167	0.156895452
UTQ_C_mt_4_Si@9	27	0.185207		0.032631114	4.19982E-06			-0.134214075	0.17690503
UTQ_C_mt_4_Si@10	34	0.1844291		0.032637117	4.32821E-06			0.049706105	0.179801796
UTQ_C_mt_4_Si@11	35	0.185144		0.032637394	4.10901E-06			0.058208356	0.174907947
UTQ_C_mt_4_Si@12	42	0.1838682		0.032636476	3.43137E-06			0.030089463	0.160609111
UTQ_C_mt_4_Si@13	43	0.1847375		0.032635854	3.5298E-06			0.011014377	0.162597379
UTQ_C_mt_4_Si@14	50	0.1833549		0.032632176	3.99268E-06			-0.101675013	0.172346615
UTQ_C_mt_4_Si@15	51	0.1836078		0.032639214	4.58185E-06			0.113963672	0.185612929
UTQ_C_mt_4_Si@16	58	0.1836097		0.032635996	3.36562E-06			0.015369365	0.159296154

Table 4-2. Continued.

Sample ID	Seq. in run	^{28}Si cps (x 10^9)	$^{28}Si_{samp/av.std}$	$^{30}Si/^{28}Si$ *drift corrected*	± abs	$\delta^{30}Si$ *samples*	± ‰	$\delta^{30}Si$ *standards*	± ‰
UTQ_C_mt_4_Si@17	59	0.181831		0.032635564	3.81005E-06			0.002116161	0.168430019
UTQ_C_mt_4_Si@18	64	0.1804379		0.032640871	3.10974E-06			0.164742033	0.154351123
UTQ_C_mt_4_Si@19	65	0.1780927		0.032641378	5.52523E-06			0.180291825	0.208338277
UTQ_C_mt_4_Si@20	70	0.1764676		0.032637096	3.50552E-06			0.049065859	0.162107012
UTQ_C_mt_4_Si@21	71	0.1744167		0.032636583	3.24604E-06			0.033361337	0.156951099
UTQ_C_mt_4_Si@22	72	0.1752112		0.032642511	4.10914E-06			0.214987975	0.174924117
UTQ_D_mt_3_Si@1	1	0.1559949		0.03262504	7.05655E-06			-0.13112024	0.269311217
UTQ_D_mt_3_Si@2	2	0.157125		0.032617855	5.0663E-06			-0.351305678	0.223290983
UTQ_D_mt_3_Si@3	3	0.1758527		0.032625701	4.30243E-06			-0.11086243	0.207727017
UTQ_D_mt_3_Si@4	10	0.1834062		0.032631259	6.09558E-06			0.059490344	0.246311061
UTQ_D_mt_3_Si@5	11	0.173827		0.032634675	5.51811E-06			0.164166121	0.233187442
UTQ_D_mt_3_Si@6	18	0.166645		0.032628543	6.3551E-06			-0.02374786	0.25238718
UTQ_D_mt_3_Si@7	19	0.1665059		0.032635059	4.95939E-06			0.175934499	0.221086866
UTQ_D_mt_3_Si@8	26	0.1638683		0.032635267	5.24893E-06			0.182324301	0.227278462
UTQ_D_mt_3_Si@9	27	0.1631937		0.032639483	6.22041E-06			0.311517906	0.24925073
UTQ_D_mt_3_Si@10	34	0.1614846		0.032632531	4.6908E-06			0.098473152	0.215502591
UTQ_D_mt_3_Si@11	35	0.1618708		0.032632557	4.67976E-06			0.099254635	0.215277123
UTQ_D_mt_3_Si@12	42	0.1593883		0.032623395	4.34215E-06			-0.181520617	0.208493131
UTQ_D_mt_3_Si@13	43	0.160516		0.032633591	3.99913E-06			0.130943748	0.201986322
UTQ_D_mt_3_Si@14	50	0.1591773		0.032632839	5.75831E-06			0.107912157	0.238573007
UTQ_D_mt_3_Si@15	51	0.1578808		0.032633475	4.35321E-06			0.127388484	0.208747632
UTQ_D_mt_3_Si@16	58	0.1561422		0.032636193	4.8651E-06			0.21070297	0.219114859
UTQ_D_mt_3_Si@17	59	0.1553342		0.032631039	3.30497E-06			0.05273152	0.189823438
UTQ_D_mt_3_Si@18	66	0.1534961		0.032638147	4.55057E-06			0.270587585	0.212680967

Table 4-2. Continued.

Sample ID	Seq. in run	^{28}Si cps (x 10^9)	$^{28}Si_{samp/av.std}$	$^{30}Si/^{28}Si$ *drift corrected*	± abs	δ^{30}Si *samples*	± ‰	δ^{30}Si *standards*	± ‰
UTQ_D_mt_3_Si@19	67	0.1529643		0.032635093	4.62863E-06			0.176975432	0.214245897
UTQ_D_mt_3_Si@20	74	0.1508319		0.032633901	5.2265E-06			0.140459036	0.226787681
UTQ_D_mt_3_Si@21	75	0.1497981		0.032632767	2.98882E-06			0.10568967	0.184843395
UTQ_D_mt_3_Si@22	82	0.1468722		0.032628805	5.04632E-06			-0.015719704	0.22290444
UTQ_D_mt_3_Si@23	83	0.147084		0.032639441	5.1211E-06			0.310229467	0.22453782
UTQ_D_mt_3_Si@24	90	0.1430517		0.032636769	5.83036E-06			0.22835509	0.240223753
UTQ_D_mt_3_Si@25	91	0.1424035		0.032637535	3.22613E-06			0.251815563	0.188572648
UTQ_D_mt_3_Si@26	98	0.1405743		0.032641183	4.80517E-06			0.363632024	0.217887396
UTQ_D_mt_3_Si@27	99	0.1416472		0.032635669	6.30865E-06			0.194627552	0.251312679
UTQ_D_mt_3_Si@28	106	0.1381023		0.032625567	2.53823E-06			-0.114956149	0.178372971
UTQ_D_mt_3_Si@29	107	0.1380146		0.032634803	4.05694E-06			0.168086824	0.203070764
UTQ_D_mt_3_Si@30	114	0.1394024		0.032635541	4.96629E-06			0.190719687	0.221234109
UTQ_D_mt_3_Si@31	115	0.1398367		0.032627727	6.22513E-06			-0.048773539	0.249323987
UTQ_D_mt_3_Si@32	122	0.1346175		0.032637425	5.94377E-06			0.248458992	0.242821902
UTQ_D_mt_3_Si@33	123	0.1329785		0.032630731	4.26872E-06			0.043290724	0.207092193
UTQ_D_mt_3_Si@34	130	0.1313551		0.032622589	4.17441E-06			-0.206224299	0.205247436
UTQ_D_mt_3_Si@35	131	0.1309617		0.032625305	4.57071E-06			-0.12300162	0.213038668
UTQ_D_mt_3_Si@36	138	0.12586		0.032631003	4.61401E-06			0.051641773	0.213934361
UTQ_D_mt_3_Si@37	139	0.1258598		0.032635969	4.34145E-06			0.203820841	0.20852692
UTQ_D_mt_3_Si@38	146	0.1235505		0.032631107	4.98622E-06			0.054828912	0.221638857
UTQ_D_mt_3_Si@39	147	0.1234151		0.032640763	3.75084E-06			0.350743744	0.197491106
UTQ_D_mt_3_Si@40	154	0.1313435		0.032628931	3.15324E-06			-0.011859758	0.187374967
UTQ_D_mt_3_Si@41	155	0.1327734		0.032624177	5.04811E-06			-0.157572295	0.22292601
UTQ_D_mt_3_Si@42	160	0.1342903		0.032627524	4.86873E-06			-0.054980622	0.219159232
UTQ_D_mt_3_Si@43	161	0.1387036		0.03263141	4.1561E-06			0.064099379	0.20493222

Table 4-2. Continued.

Sample ID	Seq. in run	^{28}Si cps (x 10^9)	$^{28}Si_{samp/av.std}$	$^{30}Si/^{28}Si$ *drift corrected*	± abs	δ^{30}Si *samples*	± ‰	δ^{30}Si *standards*	± ‰
UTQ_D_mt_3_Si@44	166	0.1316819		0.032633687	4.51101E-06			0.133898458	0.211871513
UTQ_D_mt_3_Si@45	167	0.1308016		0.032631853	5.362E-06			0.077675992	0.229732124
UTQ_D_mt_3_Si@46	168	0.1307168		0.032624788	5.41989E-06			-0.138831771	0.230980105
UTQ_C_mt_8_Si@1	1	0.1544064		0.03260638	3.70805E-06			-0.434510303	0.267388899
UTQ_C_mt_8_Si@2	2	0.1538006		0.03261119	5.22342E-06			-0.287057259	0.290226205
UTQ_C_mt_8_Si@3	3	0.1547955		0.03261396	3.26718E-06			-0.202141472	0.261981965
UTQ_C_mt_8_Si@4	10	0.1549911		0.03261913	6.28412E-06			-0.043652441	0.309400622
UTQ_C_mt_8_Si@5	11	0.1558655		0.03261131	4.52166E-06			-0.283378596	0.278937145
UTQ_C_mt_8_Si@6	18	0.153449		0.03261692	5.89186E-06			-0.111401137	0.30204815
UTQ_C_mt_8_Si@7	19	0.1542406		0.03261721	5.48091E-06			-0.102511036	0.294690826
UTQ_C_mt_8_Si@8	26	0.1528869		0.03262091	5.83053E-06			0.010914383	0.300951597
UTQ_C_mt_8_Si@9	27	0.1527811		0.03262119	4.03471E-06			0.019497928	0.271894342
UTQ_C_mt_8_Si@10	34	0.1501589		0.0326192	4.46376E-06			-0.041506554	0.278110482
UTQ_C_mt_8_Si@11	35	0.1511195		0.03262701	5.64442E-06			0.197913046	0.297635999
UTQ_C_mt_8_Si@12	42	0.1505162		0.03262473	5.88285E-06			0.128018464	0.301929535
UTQ_C_mt_8_Si@13	43	0.1548094		0.03262352	4.49936E-06			0.090925286	0.278676941
UTQ_C_mt_8_Si@14	50	0.1502821		0.03263284	3.57531E-06			0.37663472	0.265863686
UTQ_C_mt_8_Si@15	51	0.1509134		0.03262397	4.27458E-06			0.10472027	0.275334892
UTQ_C_mt_8_Si@16	58	0.1469887		0.03262207	4.50126E-06			0.046474784	0.278696431
UTQ_C_mt_8_Si@17	59	0.1473151		0.03262966	6.91982E-06			0.279150171	0.321952433
UTQ_C_mt_8_Si@18	66	0.1461915		0.03262843	4.73514E-06			0.241443883	0.282354915
UTQ_C_mt_8_Si@19	67	0.1467823		0.03263248	4.73391E-06			0.365598733	0.282361222
UTQ_C_mt_8_Si@20	74	0.1460395		0.03262997	5.90311E-06			0.288653381	0.302332048
UTQ_C_mt_8_Si@21	75	0.1478684		0.03263456	3.98918E-06			0.429362212	0.271350912

Table 4-2. Continued.

Sample ID	Seq. in run	^{28}Si cps (x 10^9)	$^{28}Si_{samp/av.std}$	$^{30}Si/^{28}Si$ *drift corrected*	± abs	δ^{30}Si *samples*	± ‰	δ^{30}Si *standards*	± ‰
UTQ_C_mt_8_Si@22	82	0.1437708		0.03263359	5.71497E-06			0.399626359	0.29893788
UTQ_C_mt_8_Si@23	83	0.1448573		0.03263044	4.0439E-06			0.303061475	0.272083769
UTQ_C_mt_8_Si@24	90	0.1407927		0.0326153	4.66864E-06			-0.161063077	0.281228474
UTQ_C_mt_8_Si@25	91	0.1423992		0.03261405	4.68835E-06			-0.199382475	0.281528558
UTQ_C_mt_8_Si@26	99	0.1404014		0.03261349	3.59104E-06			-0.216549566	0.265932088
UTQ_C_mt_8_Si@27	100	0.1418237		0.03261348	2.9523E-06			-0.216856121	0.258442918
UTQ_C_mt_8_Si@28	107	0.1403523		0.03261737	4.61398E-06			-0.097606153	0.280392986
UTQ_C_mt_8_Si@29	108	0.1450373		0.03262559	3.41061E-06			0.15438221	0.263773317
UTQ_C_mt_8_Si@30	115	0.1454913		0.0326225	6.37088E-06			0.059656657	0.311082782
UTQ_C_mt_8_Si@31	116	0.1473433		0.03262282	6.03492E-06			0.069466423	0.304725161
UTQ_C_mt_8_Si@32	123	0.1441722		0.03262459	4.19084E-06			0.123726691	0.274126777
UTQ_C_mt_8_Si@33	124	0.1444932		0.03263096	4.36288E-06			0.319002345	0.276678651
UTQ_C_mt_8_Si@34	131	0.1432928		0.03263467	3.72729E-06			0.432734319	0.267830051
UTQ_C_mt_8_Si@35	132	0.1437269		0.03263404	5.05632E-06			0.413421342	0.287574983
UTQ_C_mt_8_Si@36	133	0.1426505		0.03263436	4.17226E-06			0.423231108	0.273924422

Table 4-3. Whole-rock $\delta^{30}Si$ and $\delta^{18}O$ data

Sample ID	Sample weight (mg)	$\delta^{17}O_{VSMOW}$ MAT253 (‰)	$\delta^{18}O_{VSMOW}$ MAT253 (‰)	Yield mmol/mg	$\delta^{29}Si_{NBS-28}$ MAT253 (‰)	$\delta^{30}Si_{NBS-28}$ MAT253 (‰)	Yield mmol/mg
Abitibi Greenstone Belt, Canada							
AB-11-11-WR	1.18	5.14	10.02	16.54	0.360	-0.029	12.65
AB-11-11-1	1.25	7.04	13.47	16.97	-0.140	-0.137	16.33
AB-11-11-2	1.09	7.18	13.66	17.99	-0.069	-0.082	16.90
AB-11-12-1	0.93	7.08	13.57	16.81	-0.050	-0.017	15.31
AB-11-12-2	1.04	6.80	12.82	17.71	0.097	0.162	16.37
AB-11-19	1.01	7.27	14.09	15.57	-0.026	0.046	14.19
AB-11-19-2	1.08	7.61	14.67	15.49	-0.178	-0.224	14.75
AB-11-25-1	1.00	6.87	13.42	16.43	-0.299	-0.276	16.03
AB-11-25-2	0.98	6.43	12.48	16.96	-0.249	-0.289	16.15
AB-11-34-1	1.07	5.92	11.28	16.47	0.178	0.248	15.54
AB-11-34-2	0.93	5.59	10.53	17.02	0.172	0.257	15.52
AB-11-37-1	0.97	5.46	10.51	17.14	0.156	0.370	16.32
AB-11-37-2	1.08	5.98	11.54	17.24	0.163	0.488	16.32
AB-13-61	1.07	6.22	12.24	15.63	-0.040	0.041	11.35
AB-13-61-2	1.00	6.68	13.20	15.33	0.064	0.069	11.34
AB-13-65	1.06	5.73	11.36	14.84	-0.599	-0.991	13.90
AB-13-65-2	1.09	5.90	11.72	15.16	-0.704	-1.127	13.88
AB-13-72	1.14	6.49	12.91	15.89	0.284	0.604	15.89
AB-13-72-2	1.05	6.33	12.60	16.50	0.279	0.644	16.88
TEM-CF-1	1.05	6.21	12.05	16.69	-0.333	-0.745	16.50
TEM-CF-2	1.11	6.58	12.78	16.86	-0.445	-0.894	16.68

Table 4-3. Continued.

Sample ID	Sample weight (mg)	$\delta^{17}O_{VSMOW}$ MAT253 (‰)	$\delta^{18}O_{VSMOW}$ MAT253 (‰)	Yield mmol/mg	$\delta^{29}Si_{NBS-28}$ MAT253 (‰)	$\delta^{30}Si_{NBS-28}$ MAT253 (‰)	Yield mmol/mg
Buhwa Greenstone Belt, Zimbabwe							
ZB-05	1.03	4.88	9.41	16.24	-1.369	-2.591	15.27
ZB-05	1.22	6.10	11.95	15.83	-1.167	-2.268	15.51
ZB-05	1.03	5.86	11.57	16.04	-1.150	-2.272	15.85
ZB-05-L	1.07	6.17	12.07	16.75	-1.200	-2.306	16.56
ZB-17	1.14	7.03	13.58	16.77	-0.159	-0.480	16.24
ZB-18	1.03	6.37	12.20	16.43	-0.442	-1.003	13.53
ZB-20	1.11	6.90	13.42	15.25	-0.429	-1.027	13.09
ZB-23-1	1.20	6.76	12.97	16.59	-0.739	-1.500	16.76
ZB-23-2	1.07	6.92	13.38	16.75	-0.824	-1.599	16.93
ZB-27	1.21	5.86	11.44	16.62	-1.039	-1.893	15.47
ZB-27-L	1.06	6.10	11.96	14.84	-0.917	-1.634	12.96
ZB-105-1	1.03	7.77	15.10	16.91	-0.310	-0.603	16.53
ZB-105-2	0.98	6.81	13.28	17.78	-0.765	-1.084	17.57
ZB-143	1.00	5.38	10.38	16.53	-0.838	-1.563	15.33
ZB-169-1	1.14	5.99	11.82	13.97	-0.399	-0.850	11.52
ZB-169-2	1.11	5.90	11.75	14.53	-0.497	-0.933	12.37
ZB-169-L	1.01	6.03	11.85	14.98	-0.607	-1.051	12.22
ZB-169-L-2	1.02	5.79	11.41	14.44	-0.606	-1.033	11.90
ZB-178-F	1.05	7.35	14.17	12.32	1.099	1.394	9.67
ZB-267-F	1.06	4.88	9.45	15.78	0.218	0.363	14.46
ZB-272	1.00	7.05	13.61	17.12	-0.656	-1.125	17.32

Table 4-3. Continued.

Sample ID	Sample weight (mg)	$\delta^{17}O_{VSMOW}$ MAT253 (‰)	$\delta^{18}O_{VSMOW}$ MAT253 (‰)	Yield mmol/mg	$\delta^{29}Si_{NBS-28}$ MAT253 (‰)	$\delta^{30}Si_{NBS-28}$ MAT253 (‰)	Yield mmol/mg
Isua Greenstone Belt, SW Greenland							
ISB-28-1	1.05	9.22	18.06	16.88	-0.148	-0.260	16.88
ISB-28-2	1.04	9.70	18.88	16.85	-0.167	-0.208	16.85
ISB-55	1.02	7.33	14.18	16.59	-0.704	-1.205	16.20
462604	1.02	7.18	13.89	16.59	-0.531	-1.046	16.01
462637	1.09	6.01	11.77	15.53	1.747	-1.454	15.34
465915	1.07	3.28	6.34	13.77	-1.080	-1.985	9.11
Mesabi Iron Range, Superior Province, Canada							
LC-7	1.16	7.51	14.54	14.42	-0.644	-1.184	10.98
GF-07-13	1.06	4.54	8.93	13.71	-0.744	-1.467	8.63
UTQ-1	0.96	10.37	20.01	17.32	-0.064	0.056	17.73
UTQ-2	1.16	9.91	19.22	17.42	-0.047	0.024	17.42

Table 4-4. $\delta^{30}Si$ isotope data for all chart and iron formation samples in Chapter IV

Point #	^{28}Si	$^{28}Si_{samp/av.stnd}$	$^{30}Si/^{28}Si$	± abs	$\delta^{30}Si$	± ‰	$\delta^{30}Si$	± ‰
	cps x 10^9		*drift corrected*		*samples measured*		*samples corrected*	
IS-02-05 (Algoma BIF, >3.7 Ga Isua Greenstone Belt; N 65° 10.350', W 049° 49.263')								
IS_02_05_@1	0.18	1.05	0.03265683	0.00000375	-0.64	0.18	-0.64	0.18
IS_02_05_@2	0.18	1.04	0.03264082	0.00000240	-1.13	0.16	-1.13	0.16
IS_02_05_@3	0.18	1.02	0.03264576	0.00000482	-0.98	0.20	-0.98	0.20
IS_02_05_@4	0.18	1.02	0.03262893	0.00000318	-1.50	0.17	-1.50	0.17
IS_02_05_@5	0.18	1.00	0.03261389	0.00000616	-1.96	0.23	-1.96	0.23
IS_02_05_@6	0.00	0.00	-0.01238354		*omitted as outlier*		*omitted as outlier*	
IS_02_05_@7	0.17	0.99	0.03260866	0.00000198	-2.12	0.15	-2.12	0.15
IS_02_05_@8	0.17	0.96	0.03263122	0.00000572	-1.43	0.22	-1.43	0.22
IS_02_05_@9	0.18	1.00	0.03263142	0.00000267	-1.42	0.16	-1.42	0.16
IS_02_05_@10	0.18	1.00	0.03262946	0.00000289	-1.48	0.16	-1.48	0.16
IS_02_05_@11	0.18	1.00	0.03263782	0.00000272	-1.23	0.16	-1.23	0.16
IS_02_05_@12	0.18	1.00	0.03262093	0.00000332	-1.74	0.17	-1.74	0.17
IS_02_05_@13	0.17	0.99	0.03264293	0.00000504	-1.07	0.21	-1.07	0.21
IS_02_05_@14	0.17	0.99	0.03263224	0.00000300	-1.40	0.17	-1.40	0.17
IS_02_05_@15	0.18	1.01	0.03265713	0.00000354	-0.64	0.18	-0.64	0.18
IS_02_05_@16	0.18	1.00	0.03267233	0.00000322	-0.17	0.17	-0.17	0.17
IS_02_05_@17	0.17	0.96	0.03271274	0.00000334	*omitted as outlier*		*omitted as outlier*	
IS_02_05_@18	0.17	1.00	0.03263299	0.00000333	-1.37	0.17	-1.37	0.17
IS_02_05_@19	0.17	0.99	0.03264345	0.00000423	-1.05	0.19	-1.05	0.19
IS_02_05_@20	0.17	0.98	0.03262774	0.00000355	-1.53	0.18	-1.53	0.18
IS_02_05_@21	0.17	0.97	0.03262003	0.00000498	-1.77	0.21	-1.77	0.21

Table 4-4. Continued.

Point #	^{28}Si	$^{28}Si_{samp/av.stnd}$	$^{30}Si/^{28}Si$	± abs	$\delta^{30}Si$	± ‰	$\delta^{30}Si$	± ‰
	cps x 10^9		*drift corrected*		*samples measured*		*samples corrected*	
IS-02-06 (Algoma BIF, >3.7 Ga Isua Greenstone Belt; N 65° 10.353', W 049° 49.200')								
IS_02_06_@22	0.16	0.94	0.03258530	0.00000437	-2.83	0.19	-2.83	0.19
IS_02_06_@23	0.17	0.96	0.03258863	0.00000577	-2.73	0.22	-2.73	0.22
IS_02_06_@24	0.16	0.91	0.03300845	0.00000297	*omitted as outlier*		*omitted as outlier*	
IS_02_06_@25	0.17	0.96	0.03262307	0.00000384	-1.68	0.18	-1.68	0.18
IS_02_06_@26	0.17	0.97	0.03262055	0.00000379	-1.75	0.18	-1.75	0.18
IS_02_06_@27	0.17	0.96	0.03259679	0.00000243	-2.48	0.16	-2.48	0.16
IS_02_06_@28	0.17	0.95	0.03259496	0.00000294	-2.54	0.17	-2.54	0.17
IS_02_06_@29	0.17	0.95	0.03260121	0.00000323	-2.35	0.17	-2.35	0.17
IS_02_06_@30	0.17	0.96	0.03260222	0.00000257	-2.32	0.16	-2.32	0.16
IS_02_06_@31	0.16	0.94	0.03258818	0.00000474	-2.75	0.20	-2.75	0.20
IS_02_06_@32	0.16	0.93	0.03257232	0.00000323	-3.23	0.17	-3.23	0.17
IS_02_06_@33	0.16	0.92	0.03258135	0.00000553	-2.95	0.22	-2.95	0.22
IS_02_06_@34	0.16	0.92	0.03258965	0.00000397	-2.70	0.18	-2.70	0.18
IS_02_06_@35	0.17	0.96	0.03259637	0.00000507	-2.49	0.21	-2.49	0.21
IS_02_06_@36	0.16	0.93	0.03256802	0.00000456	-3.36	0.20	-3.36	0.20
IS_02_06_@37	0.16	0.91	0.03257200	0.00000322	-3.24	0.17	-3.24	0.17
IS_02_06_@38	0.16	0.90	0.03256762	0.00000308	-3.37	0.17	-3.37	0.17

Table 4-4. Continued.

Point #	^{28}Si	$^{28}Si_{samp/av.stnd}$	$^{30}Si/^{28}Si$	± abs	$\delta^{30}Si$	± ‰	$\delta^{30}Si$	± ‰
	cps x 10^9		*drift corrected*		*samples measured*		*samples corrected*	
IS-02-08 (Algoma BIF, >3.7 Ga Isua Greenstone Belt; N 65° 12.531', W 049° 45.504')								
IS_02_08_Mmount_Si@1	0.16	0.94	0.03255829	0.00000804	-1.27	0.38	-1.27	0.38
IS_02_08_Mmount_Si@02	0.16	0.96	0.03254796	0.00000612	-1.59	0.35	-1.59	0.35
IS_02_08_Mmount_Si@03	0.17	0.97	0.03254730	0.00000609	-1.61	0.35	-1.61	0.35
IS_02_08_Mmount_Si@04	0.16	0.95	0.03253906	0.00000713	-1.86	0.37	-1.86	0.37
IS_02_08_Mmount_Si@05	0.15	0.86	0.03251418	0.00000696	-2.63	0.36	-2.63	0.36
IS_02_08_Mmount_Si@06	0.00	0.01	0.03207700	0.00027997	-16.04	8.59	omitted as outlier	
IS_02_08_Mmount_Si@07	0.00	0.02	0.03201506	0.00006806	-17.94	2.11	omitted as outlier	
IS_02_08_Mmount_Si@08	0.17	0.98	0.03253938	0.00000820	-1.85	0.39	-1.85	0.39
IS_02_08_Mmount_Si@09	0.17	0.98	0.03253252	0.00000574	-2.06	0.34	-2.06	0.34
IS_02_08_Mmount_Si@10	0.17	0.97	0.03253859	0.00001000	-1.88	0.43	-1.88	0.43
IS_02_08_Mmount_Si@11	0.16	0.96	0.03252619	0.00000722	-2.26	0.37	-2.26	0.37
IS_02_08_Mmount_Si@12	0.16	0.95	0.03251333	0.00000691	-2.65	0.36	-2.65	0.36
IS_02_08_Mmount_Si@13	0.16	0.96	0.03253766	0.00000719	-1.91	0.37	-1.91	0.37
IS_02_08_Mmount_Si@14	0.00	0.01	0.03248620	0.00014575	-3.48	4.48	omitted as outlier	
IS_02_08_Mmount_Si@15	0.16	0.96	0.03252770	0.00000656	-2.21	0.36	-2.21	0.36
IS_02_08_Mmount_Si@16	0.11	0.65	0.03244975	0.00001115	-4.60	0.45	-4.60	0.45
IS_02_08_Mmount_Si@17	0.16	0.91	0.03253496	0.00000666	-1.99	0.36	-1.99	0.36
IS_02_08_Mmount_Si@18	0.00	0.00	0.03133914	0.00059469	-38.67	18.24	omitted as outlier	
IS_02_08_Mmount_Si@19	0.16	0.93	0.03252998	0.00000591	-2.14	0.35	-2.14	0.35
IS_02_08_Mmount_Si@20	0.15	0.90	0.03254559	0.00000575	-1.66	0.34	-1.66	0.34
IS_02_08_Mmount_Si@21	0.16	0.92	0.03254184	0.00000644	-1.78	0.36	-1.78	0.36
IS_02_08_Mmount_Si@22	0.15	0.90	0.03253324	0.00000600	-2.04	0.35	-2.04	0.35
IS_02_08_Mmount_Si@23	0.00	0.00	1.99266800	1.27315982	60125.17	39054.23	omitted as outlier	

Table 4-4. Continued.

Point #	^{28}Si	$^{28}Si_{samp/av.stnd}$	$^{30}Si/^{28}Si$	± abs	$\delta^{30}Si$	± ‰	$\delta^{30}Si$	± ‰
	cps x 10^9		*drift corrected*		*samples measured*		*samples corrected*	
ISB 55 (Algoma BIF, >3.7 Ga Isua Greenstone Belt; Iron Mountain, no GPS)								
ISB_55_mt_6_Si@1	0.14	0.96	0.03259884	0.00000485	-0.93	0.22	0.08	0.35
ISB_55_mt_6_Si@02	0.17	1.18	0.03257908	0.00000531	-1.54	0.23	-0.53	0.36
ISB_55_mt_6_Si@03	0.18	1.20	0.03257763	0.00000545	-1.58	0.23	-0.57	0.37
ISB_55_mt_6_Si@04	0.17	1.18	0.03258640	0.00000535	-1.32	0.23	-0.31	0.37
ISB_55_mt_6_Si@05	0.17	1.17	0.03257708	0.00000539	-1.60	0.23	-0.59	0.37
ISB_55_mt_6_Si@06	0.17	1.16	0.03258125	0.00000471	-1.47	0.22	-0.46	0.35
ISB_55_mt_6_Si@07	0.17	1.16	0.03258362	0.00000548	-1.40	0.23	-0.39	0.37
ISB_55_mt_6_Si@08	0.17	1.15	0.03257594	0.00000530	-1.64	0.23	-0.63	0.36
ISB_55_mt_6_Si@09	0.16	1.11	0.03260278	0.00000680	-0.81	0.26	0.20	0.41
ISB_55_mt_6_Si@10	0.17	1.13	0.03258916	0.00000499	-1.23	0.22	-0.22	0.36
UTQ_D_mt_3_Si@6	0.17		0.03262854	0.00000636				
UTQ_D_mt_3_Si@7	0.17		0.03263506	0.00000496				
ISB_55_mt_6_Si@11	0.16	1.12	0.03259258	0.00000409	-1.13	0.20	-0.12	0.33
ISB_55_mt_6_Si@12	0.16	1.11	0.03259890	0.00000636	-0.93	0.25	0.08	0.40
ISB_55_mt_6_Si@13	0.16	1.11	0.03258685	0.00000504	-1.30	0.22	-0.29	0.36
ISB_55_mt_6_Si@14	0.16	1.11	0.03258178	0.00000479	-1.46	0.22	-0.45	0.35
ISB_55_mt_6_Si@15	0.16	1.11	0.03259395	0.00000504	-1.08	0.22	-0.07	0.36
ISB_55_mt_6_Si@16	0.16	1.12	0.03260537	0.00000516	-0.73	0.23	0.28	0.36
ISB_55_mt_6_Si@17	0.16	1.10	0.03258539	0.00000429	-1.35	0.21	-0.34	0.34
ISB_55_mt_6_Si@18	0.16	1.10	0.03258666	0.00000590	-1.31	0.24	-0.30	0.38
ISB_55_mt_6_Si@19	0.16	1.10	0.03258123	0.00000599	-1.47	0.24	-0.46	0.38
ISB_55_mt_6_Si@20	0.16	1.08	0.03258243	0.00000564	-1.44	0.24	-0.43	0.37
ISB_55_mt_6_Si@21	0.16	1.07	0.03258794	0.00000562	-1.27	0.24	-0.26	0.37
ISB_55_mt_6_Si@22	0.16	1.08	0.03260905	0.00000403	-0.62	0.20	0.39	0.33

Table 4-4. Continued.

Point #	^{28}Si	$^{28}Si_{samp/av.stnd}$	$^{30}Si/^{28}Si$	± abs	$\delta^{30}Si$	± ‰	$\delta^{30}Si$	± ‰
	cps x 10^9		*drift corrected*		*samples measured*		*samples corrected*	
ISB_55_mt_6_Si@23	0.16	1.07	0.03258141	0.00000461	-1.47	0.21	-0.46	0.35
ISB_55_mt_6_Si@24	0.16	1.08	0.03259038	0.00000498	-1.19	0.22	-0.18	0.36
ISB_55_mt_6_Si@25	0.16	1.08	0.03258539	0.00000495	-1.35	0.22	-0.34	0.35
ISB 26 (Greenstone chert, >3.7 Ga Isua Greenstone Belt; N 65° 10.752', W 049° 48.249')								
ISB_26_mt_6_Si@1	0.14	0.94	0.03261545	0.00000496	-0.42	0.22	0.59	0.40
ISB_26_mt_6_Si@02	0.14	0.95	0.03257924	0.00000284	-1.53	0.18	-0.52	0.35
ISB_26_mt_6_Si@03	0.14	0.94	0.03260938	0.00000353	-0.61	0.19	0.40	0.36
ISB_26_mt_6_Si@04	0.14	0.94	0.03261694	0.00000631	-0.38	0.25	0.63	0.44
ISB_26_mt_6_Si@05	0.14	0.93	0.03260377	0.00000518	-0.78	0.23	0.23	0.40
ISB_26_mt_6_Si@06	0.14	0.93	0.03258325	0.00000507	-1.41	0.22	-0.40	0.40
ISB_26_mt_6_Si@07	0.14	0.93	0.03260450	0.00000380	-0.76	0.20	0.25	0.37
ISB_26_mt_6_Si@08	0.14	0.93	0.03258973	0.00000439	-1.21	0.21	-0.20	0.38
ISB_26_mt_6_Si@09	0.14	0.93	0.03258739	0.00000398	-1.29	0.20	-0.28	0.37
ISB_26_mt_6_Si@10	0.14	0.92	0.03257961	0.00000383	-1.52	0.20	-0.51	0.37
ISB_26_mt_6_Si@11	0.14	0.93	0.03259544	0.00000530	-1.04	0.23	-0.03	0.41
ISB_26_mt_6_Si@12	0.14	0.94	0.03259319	0.00000409	-1.11	0.20	-0.10	0.37
ISB_26_mt_6_Si@13	0.14	0.95	0.03260431	0.00000526	-0.77	0.23	0.24	0.41
ISB_26_mt_6_Si@14	0.14	0.93	0.03261041	0.00000562	-0.58	0.24	0.43	0.42
ISB_26_mt_6_Si@15	0.14	0.93	0.03262977	0.00000409	0.01	0.20	1.02	0.37
ISB_26_mt_6_Si@16	0.14	0.92	0.03261563	0.00000470	-0.42	0.22	0.59	0.39
ISB_26_mt_6_Si@17	0.13	0.91	0.03262202	0.00000485	-0.22	0.22	0.79	0.39
ISB_26_mt_6_Si@18	0.13	0.91	0.03262780	0.00000388	-0.05	0.20	0.96	0.37
ISB_26_mt_6_Si@19	0.13	0.90	0.03262771	0.00000390	-0.05	0.20	0.96	0.37

Table 4-4. Continued.

Point #	^{28}Si	$^{28}Si_{samp/av.stnd}$	$^{30}Si/^{28}Si$	± abs	$\delta^{30}Si$	± ‰	$\delta^{30}Si$	± ‰
	cps x 10^9		*drift corrected*		*samples measured*		*samples corrected*	
ISB_26_mt_6_Si@20	0.13	0.90	0.03263057	0.00000467	0.04	0.22	1.05	0.39
ISB_26_mt_6_Si@21	0.13	0.90	0.03262590	0.00000404	-0.10	0.20	0.91	0.37
ISB_26_mt_6_Si@22	0.13	0.90	0.03262032	0.00000254	-0.28	0.18	0.73	0.34
ISB_26_mt_6_Si@23	0.13	0.90	0.03262292	0.00000302	-0.20	0.19	0.81	0.35
ISB_26_mt_6_Si@24	0.13	0.89	0.03262766	0.00000241	-0.05	0.18	0.96	0.34
ISB_26_mt_6_Si@25	0.13	0.88	0.03262818	0.00000572	-0.03	0.24	0.98	0.42
ISB_26_mt_6_Si@26	0.13	0.88	0.03258922	0.00000573	-1.23	0.24	-0.22	0.42
ISB_26_mt_6_Si@27	0.13	0.87	0.03260710	0.00000379	-0.68	0.20	0.33	0.37
ISB_26_mt_6_Si@28	0.13	0.87	0.03262463	0.00000472	-0.14	0.22	0.87	0.39
ISB_26_mt_6_Si@29	0.13	0.87	0.03262266	0.00000446	-0.20	0.21	0.81	0.38
ISB_26_mt_6_Si@30	0.13	0.86	0.03263679	0.00000352	0.23	0.19	1.24	0.36
ISB_26_mt_6_Si@31	0.13	0.85	0.03262497	0.00000270	-0.13	0.18	0.88	0.34
ISB_26_mt_6_Si@32	0.13	0.85	0.03261124	0.00000412	-0.55	0.20	0.46	0.38
ISB_26_mt_6_Si@33	0.12	0.85	0.03260879	0.00000504	-0.63	0.22	0.38	0.40
ISB_26_mt_6_Si@34	0.13	0.85	0.03260676	0.00000225	-0.69	0.17	0.32	0.34
ISB_26_mt_6_Si@35	0.13	0.86	0.03260645	0.00000418	-0.70	0.21	0.31	0.38
ISB_26_mt_6_Si@36	0.12	0.85	0.03259960	0.00000496	-0.91	0.22	0.10	0.40
ISB_26_mt_6_Si@37	0.12	0.84	0.03259446	0.00000433	-1.07	0.21	-0.06	0.38
ISB_26_mt_6_Si@38	0.12	0.84	0.03257490	0.00000326	-1.67	0.19	-0.66	0.35
ISB_26_mt_6_Si@39	0.12	0.84	0.03260607	0.00000298	-0.71	0.18	0.30	0.35
ISB_26_mt_6_Si@40	0.12	0.85	0.03260395	0.00000424	-0.78	0.21	0.23	0.38
ISB_26_mt_6_Si@41	0.13	0.87	0.03260772	0.00000601	-0.66	0.24	0.35	0.43
ISB_26_mt_6_Si@42	0.13	0.89	0.03256626	0.00000360	-1.93	0.19	-0.92	0.36
ISB_26_mt_6_Si@43	0.13	0.88	0.03258477	0.00000384	-1.37	0.20	-0.36	0.37
ISB_26_mt_6_Si@44	0.13	0.88	0.03258106	0.00000443	-1.48	0.21	-0.47	0.38

Table 4-4. Continued.

Point #	^{28}Si	$^{28}Si_{samp/av.stnd}$	$^{30}Si/^{28}Si$	± abs	$\delta^{30}Si$	± ‰	$\delta^{30}Si$	± ‰
	cps x 10^9		*drift corrected*		*samples measured*		*samples corrected*	
ISB_26_mt_6_Si@45	0.13	0.88	0.03259873	0.00000597	-0.94	0.24	0.07	0.43
ISB_26_mt_6_Si@46	0.14	0.93	0.03256312	0.00000346	-2.03	0.19	-1.02	0.36
ISB_26_mt_6_Si@47	0.13	0.91	0.03258021	0.00000547	-1.51	0.23	-0.50	0.41
ISB_26_mt_6_Si@48	0.13	0.91	0.03258909	0.00000307	-1.23	0.19	-0.22	0.35
ISB_26_mt_6_Si@49	0.13	0.91	0.03259604	0.00000323	-1.02	0.19	-0.01	0.35
ISB_26_mt_6_Si@50	0.13	0.90	0.03260064	0.00000330	-0.88	0.19	0.13	0.36
ISB 28 (Greenstone chert, >3.7 Ga Isua Greenstone Belt; N 65° 10.752', W 049° 48.249')								
ISB_28_Isua_mt_1_re_run_Mar_2014_Si@1	0.16	0.96	0.03257838	0.00000483	-1.15	0.21	-1.15	0.21
ISB_28_Isua_mt_1_re_run_Mar_2014_Si@2	0.16	0.96	0.03260322	0.00000608	-0.39	0.24	-0.39	0.24
ISB_28_Isua_mt_1_re_run_Mar_2014_Si@3	0.16	0.97	0.03259337	0.00000500	-0.69	0.21	-0.69	0.21
ISB_28_Isua_mt_1_re_run_Mar_2014_Si@4	0.17	0.99	0.03260091	0.00000603	-0.46	0.23	-0.46	0.23
ISB_28_Isua_mt_1_re_run_Mar_2014_Si@5	0.16	0.97	0.03255984	0.00000444	-1.72	0.20	-1.72	0.20
ISB_28_Isua_mt_1_re_run_Mar_2014_Si@6	0.16	0.97	0.03256331	0.00000502	-1.61	0.21	-1.61	0.21
ISB_28_Isua_mt_1_re_run_Mar_2014_Si@7	0.16	0.97	0.03260990	0.00000466	-0.18	0.20	-0.18	0.20
ZB 182 (Tokwe Gneiss, ~3 Ga Buhwa Greenstone Belt; probably location, S 20° 11' 48.36'', E 30° 15' 16.7'')								
ZB_182_Mt_6_Si@1	0.15	1.04	0.03262212	0.00000457	-0.22	0.21	0.79	0.39
ZB_182_Mt_6_Si@02	0.15	1.05	0.03261890	0.00000450	-0.32	0.21	0.69	0.39
ZB_182_Mt_6_Si@03	0.16	1.06	0.03263079	0.00000438	0.05	0.21	1.06	0.38
ZB_182_Mt_6_Si@04	0.15	1.03	0.03262941	0.00000595	0.00	0.24	1.01	0.43

Table 4-4. Continued.

Point #	^{28}Si	$^{28}Si_{samp/av.stnd}$	$^{30}Si/^{28}Si$	± abs	$\delta^{30}Si$	± ‰	$\delta^{30}Si$	± ‰
	cps x 10^9		*drift corrected*		*samples measured*		*samples corrected*	
ZB_182_Mt_6_Si@05	0.15	1.05	0.03262847	0.00000554	-0.03	0.23	0.98	0.41
ZB_182_Mt_6_Si@06	0.16	1.06	0.03263584	0.00000608	0.20	0.25	1.21	0.43
ZB_182_Mt_6_Si@07	0.16	1.08	0.03262929	0.00000592	0.00	0.24	1.01	0.43
ZB_182_Mt_6_Si@08	0.16	1.08	0.03262669	0.00000484	-0.08	0.22	0.93	0.39
ZB_182_Mt_6_Si@09	0.15	1.03	0.03264368	0.00000382	0.44	0.20	1.45	0.37
ZB_182_Mt_6_Si@10	0.15	1.03	0.03263194	0.00000547	0.08	0.23	1.09	0.41
ZB_182_Mt_6_Si@11	0.15	1.00	0.03261707	0.00000423	-0.38	0.21	0.63	0.38
ZB_182_Mt_6_Si@12	0.15	1.00	0.03263134	0.00000622	0.06	0.25	1.07	0.43
ZB_182_Mt_6_Si@13	0.11	0.77	0.03289304	0.00000441	8.08	0.21	*omitted as outlier*	0.38
ZB_182_Mt_6_Si@14	0.15	0.99	0.03261405	0.00000347	-0.47	0.19	0.54	0.36
ZB_182_Mt_6_Si@15	0.12	0.79	0.03288359	0.00000383	7.79	0.20	*omitted as outlier*	0.37
ZB_182_Mt_6_Si@16	0.15	1.00	0.03262244	0.00000589	-0.21	0.24	0.80	0.42
ZB 240 (Quartz arenite, ~3 Ga Buhwa Greenstone Belt; S 20° 37' 12.54'', E 30° 17' 55.31'')								
ZB_240_Mt_6_Si@1	0.15	1.00	0.03259937	0.00000259	-0.92	0.18	0.09	0.34
ZB_240_Mt_6_Si@02	0.15	1.01	0.03261085	0.00000409	-0.57	0.20	0.44	0.37
ZB_240_Mt_6_Si@03	0.15	1.02	0.03261169	0.00000641	-0.54	0.25	0.47	0.44
ZB_240_Mt_6_Si@04	0.15	1.03	0.03262031	0.00000325	-0.28	0.19	0.73	0.36
ZB_240_Mt_6_Si@05	0.15	1.03	0.03262590	0.00000574	-0.10	0.24	0.91	0.42
ZB_240_Mt_6_Si@06	0.15	1.02	0.03261651	0.00000485	-0.39	0.22	0.62	0.39
ZB_240_Mt_6_Si@07	0.15	1.00	0.03258856	0.00000316	-1.25	0.19	-0.24	0.35
ZB_240_Mt_6_Si@08	0.15	1.02	0.03263554	0.00000513	0.19	0.22	1.20	0.40
ZB_240_Mt_6_Si@09	0.15	1.01	0.03262220	0.00000555	-0.22	0.23	0.79	0.41
ZB_240_Mt_6_Si@10	0.15	1.01	0.03262969	0.00000382	0.01	0.20	1.02	0.37

Table 4-4. Continued.

Point #	^{28}Si	$^{28}Si_{samp/av.stnd}$	$^{30}Si/^{28}Si$	± abs	$\delta^{30}Si$	± ‰	$\delta^{30}Si$	± ‰
	cps x 10^9		*drift corrected*		*samples measured*		*samples corrected*	
ZB_240_Mt_6_Si@11	0.15	1.01	0.03261940	0.00000633	-0.30	0.25	0.71	0.44
ZB_240_Mt_6_Si@12	0.14	0.98	0.03262597	0.00000619	-0.10	0.25	0.91	0.43
ZB_240_Mt_6_Si@13	0.15	0.99	0.03261261	0.00000376	-0.51	0.20	0.50	0.37
ZB_240_Mt_6_Si@14	0.15	1.00	0.03262424	0.00000361	-0.16	0.19	0.85	0.36
ZB_240_Mt_6_Si@15	0.15	0.99	0.03262874	0.00000327	-0.02	0.19	0.99	0.36
ZB_240_Mt_6_Si@16	0.15	0.99	0.03261068	0.00000488	-0.57	0.22	0.44	0.39
ZB_240_Mt_6_Si@17	0.15	0.99	0.03261472	0.00000508	-0.45	0.22	0.56	0.40
ZB_240_Mt_6_Si@18	0.14	0.98	0.03261277	0.00000424	-0.51	0.21	0.50	0.38
ZB_240_Mt_6_Si@19	0.14	0.98	0.03261088	0.00000411	-0.57	0.20	0.44	0.37
ZB_240_Mt_6_Si@20	0.14	0.98	0.03262214	0.00000411	-0.22	0.20	0.79	0.38
ZB_240_Mt_6_Si@21	0.14	0.96	0.03260780	0.00000689	-0.66	0.27	0.35	0.46
ZB_240_Mt_6_Si@22	0.14	0.96	0.03260621	0.00000357	-0.71	0.19	0.30	0.36
ZB_240_Mt_6_Si@23	0.14	0.96	0.03262016	0.00000524	-0.28	0.23	0.73	0.41
ZB_240_Mt_6_Si@24	0.14	0.94	0.03260911	0.00000207	-0.62	0.17	0.39	0.33
ZB_240_Mt_6_Si@25	0.14	0.95	0.03262113	0.00000546	-0.25	0.23	0.76	0.41
ZB_240_Mt_6_Si@26	0.14	0.95	0.03261166	0.00000487	-0.54	0.22	0.47	0.39
ZB_240_Mt_6_Si@27	0.14	0.94	0.03261025	0.00000333	-0.58	0.19	0.43	0.36
ZB_240_Mt_6_Si@28	0.14	0.96	0.03261938	0.00000520	-0.30	0.23	0.71	0.40
ZB_240_Mt_6_Si@29	0.14	0.94	0.03261833	0.00000395	-0.34	0.20	0.67	0.37

Table 4-4. Continued.

Point #	^{28}Si	$^{28}Si_{samp/av.stnd}$	$^{30}Si/^{28}Si$	± abs	$\delta^{30}Si$	± ‰	$\delta^{30}Si$	± ‰
	cps x 10^9		*drift corrected*		*samples measured*		*samples corrected*	
ZB 105 (Greenstone Chert, ~3 Ga Buhwa Greenstone Belt; S 20° 34.85', E 30° 26.892660')								
ZB_105_mt_3_Si@1	0.15	1.05	0.03260589	0.00000589	-0.88	0.25	0.15	0.36
ZB_105_mt_3_Si@02	0.14	1.03	0.03259303	0.00000429	-1.27	0.21	-0.24	0.31
ZB_105_mt_3_Si@03	0.14	1.03	0.03263565	0.00000500	0.04	0.23	1.07	0.33
ZB_105_mt_3_Si@04	0.14	1.03	0.03261580	0.00000545	-0.57	0.24	0.46	0.34
ZB_105_mt_3_Si@05	0.14	1.03	0.03261991	0.00000414	-0.45	0.21	0.58	0.31
ZB_105_mt_3_Si@06	0.14	1.03	0.03262037	0.00000502	-0.43	0.23	0.60	0.33
ZB_105_mt_3_Si@07	0.14	1.03	0.03261811	0.00000479	-0.50	0.22	0.53	0.33
ZB_105_mt_3_Si@08	0.14	1.03	0.03262652	0.00000624	-0.24	0.25	0.79	0.37
ZB_105_mt_3_Si@09	0.14	1.04	0.03259741	0.00000424	-1.14	0.21	-0.11	0.31
ZB_105_mt_3_Si@10	0.15	1.05	0.03262993	0.00000440	-0.14	0.22	0.89	0.32
ZB_105_mt_3_Si@11	0.15	1.05	0.03263962	0.00000377	0.16	0.20	1.19	0.30
ZB_105_mt_3_Si@12	0.15	1.06	0.03264023	0.00000474	0.18	0.22	1.21	0.32
ZB_105_mt_3_Si@13	0.15	1.04	0.03264244	0.00000590	0.24	0.25	1.27	0.36
ZB_105_mt_3_Si@14	0.15	1.05	0.03259879	0.00000567	-1.09	0.24	-0.06	0.35
ZB_105_mt_3_Si@15	0.14	1.03	0.03263422	0.00000562	-0.01	0.24	1.02	0.35
ZB_105_mt_3_Si@16	0.15	1.04	0.03265022	0.00000469	0.48	0.22	1.51	0.32
ZB_105_mt_3_Si@17	0.15	1.05	0.03264854	0.00000647	0.43	0.26	1.46	0.37
ZB_105_mt_3_Si@18	0.14	1.04	0.03258593	0.00000408	-1.49	0.21	-0.46	0.31
ZB_105_mt_3_Si@19	0.14	1.03	0.03263203	0.00000467	-0.07	0.22	0.96	0.32
ZB_105_mt_3_Si@20	0.14	1.03	0.03254558	0.00000480	-2.72	0.22	-1.69	0.33
ZB_105_mt_3_Si@21	0.14	1.02	0.03255465	0.00000416	-2.45	0.21	-1.42	0.31
ZB_105_mt_3_Si@22	0.14	1.02	0.03265336	0.00000436	0.58	0.21	1.61	0.32
ZB_105_mt_3_Si@23	0.14	1.01	0.03264552	0.00000515	0.34	0.23	1.37	0.34
ZB_105_mt_3_Si@24	0.14	1.02	0.03261847	0.00000519	-0.49	0.23	0.54	0.34

Table 4-4. Continued.

Point #	^{28}Si	$^{28}Si_{samp/av.stnd}$	$^{30}Si/^{28}Si$	± abs	$\delta^{30}Si$	± ‰	$\delta^{30}Si$	± ‰
	cps x 10^9		*drift corrected*		*samples measured*		*samples corrected*	
ZB_105_mt_3_Si@25	0.14	1.01	0.03262932	0.00000572	-0.16	0.24	0.87	0.35
ZB_105_mt_3_Si@26	0.14	1.02	0.03262412	0.00000484	-0.32	0.22	0.71	0.33
ZB_105_mt_3_Si@27	0.14	1.00	0.03261728	0.00000268	-0.53	0.19	0.50	0.28
ZB_105_mt_3_Si@28	0.14	1.01	0.03260670	0.00000465	-0.85	0.22	0.18	0.32
ZB_105_mt_3_Si@29	0.14	1.00	0.03259551	0.00000364	-1.19	0.20	-0.16	0.30
ZB_105_mt_3_Si@30	0.14	0.99	0.03262287	0.00000272	-0.36	0.19	0.67	0.28
ZB_105_mt_3_Si@31	0.15	1.05	0.03262927	0.00000353	-0.16	0.20	0.87	0.30
ZB_105_mt_3_Si@32	0.14	1.03	0.03262124	0.00000518	-0.41	0.23	0.62	0.34
ZB_105_mt_3_Si@33	0.15	1.05	0.03263956	0.00000518	0.16	0.23	1.19	0.34
ZB_105_mt_3_Si@34	0.15	1.06	0.03261917	0.00000318	-0.47	0.19	0.56	0.29
ZB_105_mt_3_Si@35	0.15	1.05	0.03260122	0.00000368	-1.02	0.20	0.01	0.30
ZB_105_mt_3_Si@36	0.15	1.07	0.03261435	0.00000540	-0.62	0.24	0.41	0.34
ZB_105_mt_3_Si@37	0.14	0.99	0.03262487	0.00000422	-0.29	0.21	0.74	0.31
ZB_105_mt_3_Si@38	0.13	0.95	0.03263127	0.00000237	-0.10	0.18	0.93	0.27
ZB_105_mt_3_Si@39	0.14	0.99	0.03263293	0.00000375	-0.05	0.20	0.98	0.30
ZB_105_mt_3_Si@40	0.14	0.98	0.03263687	0.00000425	0.07	0.21	1.10	0.31
ZB_105_mt_3_Si@41	0.14	1.03	0.03262030	0.00000396	-0.43	0.21	0.60	0.31
ZB_105_mt_3_Si@42	0.15	1.05	0.03262749	0.00000484	-0.21	0.22	0.82	0.33
ZB_105_mt_3_Si@43	0.15	1.08	0.03260761	0.00000469	-0.82	0.22	0.21	0.32
ZB_105_mt_3_Si@44	0.15	1.07	0.03254523	0.00000362	-2.73	0.20	-1.70	0.30
ZB_105_mt_3_Si@45	0.15	1.07	0.03256148	0.00000433	-2.24	0.21	-1.21	0.31
ZB_105_mt_3_Si@46	0.15	1.06	0.03259893	0.00000464	-1.09	0.22	-0.06	0.32
ZB_105_mt_3_Si@47	0.15	1.06	0.03260300	0.00000350	-0.96	0.20	0.07	0.29
ZB_105_mt_3_Si@48	0.15	1.05	0.03263359	0.00000634	-0.03	0.26	1.00	0.37
ZB_105_mt_3_Si@49	0.14	1.03	0.03260858	0.00000621	-0.79	0.25	0.24	0.37

Table 4-4. Continued.

Point #	^{28}Si	$^{28}Si_{samp/av.stnd}$	$^{30}Si/^{28}Si$	± abs	$\delta^{30}Si$	± ‰	$\delta^{30}Si$	± ‰
	cps x 10^9		*drift corrected*		*samples measured*		*samples corrected*	
ZB_105_mt_3_Si@50	0.14	1.03	0.03259839	0.00000563	-1.11	0.24	-0.08	0.35
ZB_105_mt_3_Si@51	0.14	1.03	0.03263396	0.00000358	-0.02	0.20	1.01	0.30
ZB_105_mt_3_Si@52	0.14	1.03	0.03262131	0.00000691	-0.40	0.27	0.63	0.39
ZB_105_mt_3_Si@53	0.15	1.04	0.03262357	0.00000530	-0.33	0.23	0.70	0.34
ZB_105_mt_3_Si@54	0.15	1.05	0.03259686	0.00000577	-1.15	0.24	-0.12	0.35
ZB_105_mt_3_Si@55	0.14	1.02	0.03263833	0.00000401	0.12	0.21	1.15	0.31
ZB_105_mt_3_Si@56	0.14	1.02	0.03262439	0.00000615	-0.31	0.25	0.72	0.36
ZB_105_mt_3_Si@57	0.14	1.03	0.03263284	0.00000521	-0.05	0.23	0.98	0.34
ZB_105_mt_3_Si@58	0.14	1.03	0.03261252	0.00000706	-0.67	0.27	0.36	0.39
ZB_105_mt_3_Si@59	0.14	1.03	0.03258826	0.00000390	-1.42	0.21	-0.39	0.30
ZB_105_mt_3_Si@60	0.14	1.02	0.03260312	0.00000366	-0.96	0.20	0.07	0.30
ZB_105_mt_3_Si@61	0.14	0.98	0.03258665	0.00000416	-1.47	0.21	-0.44	0.31
ZB_105_mt_3_Si@62	0.14	0.98	0.03259610	0.00000445	-1.18	0.22	-0.15	0.32
ZB_105_mt_3_Si@63	0.14	0.97	0.03259517	0.00000386	-1.20	0.21	-0.17	0.30
ZB_105_mt_3_Si@64	0.13	0.97	0.03260862	0.00000485	-0.79	0.22	0.24	0.33
ZB_105_mt_3_Si@65	0.13	0.97	0.03260396	0.00000489	-0.93	0.23	0.10	0.33
ZB_105_mt_3_Si@66	0.13	0.95	0.03259457	0.00000392	-1.22	0.21	-0.19	0.30
ZB_105_mt_3_Si@67	0.13	0.93	0.03259452	0.00000448	-1.22	0.22	-0.19	0.32
ZB_105_mt_3_Si@68	0.13	0.93	0.03264283	0.00000449	0.26	0.22	1.29	0.32

Table 4-4. Continued.

Point #	^{28}Si	$^{28}Si_{samp/av.stnd}$	$^{30}Si/^{28}Si$	± abs	$\delta^{30}Si$	± ‰	$\delta^{30}Si$	± ‰
	cps x 10^9		*drift corrected*		*samples measured*		*samples corrected*	
ZB 105 (Greenstone Chert, ~3 Ga Buhwa Greenstone Belt; S 20° 34.85', E 30° 26.892660')								
ZB07_mt_1_Si@1	0.13	1.03	0.03263529	0.00000414	-1.12	0.21	-0.09	0.31
ZB07_mt_1_Si@02	0.13	1.02	0.03263598	0.00000445	-1.10	0.22	-0.07	0.32
ZB07_mt_1_Si@03	0.13	1.01	0.03262575	0.00000320	-1.41	0.20	-0.38	0.29
ZB07_mt_1_Si@04	0.12	0.99	0.03262312	0.00000340	-1.49	0.20	-0.46	0.30
ZB07_mt_1_Si@05	0.12	0.99	0.03261290	0.00000417	-1.81	0.21	-0.78	0.31
ZB07_mt_1_Si@06	0.12	0.99	0.03261677	0.00000506	-1.69	0.23	-0.66	0.34
ZB07_mt_1_Si@07	0.12	0.97	0.03262671	0.00000294	-1.38	0.19	-0.35	0.29
ZB07_mt_1_Si@08	0.12	0.95	0.03260150	0.00000465	-2.16	0.22	-1.13	0.32
ZB07_mt_1_Si@09	0.12	0.95	0.03260535	0.00000303	-2.04	0.19	-1.01	0.29
ZB07_mt_1_Si@10	0.12	0.98	0.03262206	0.00000464	-1.53	0.22	-0.50	0.32
ZB07_mt_1_Si@11	0.12	0.98	0.03262300	0.00000475	-1.50	0.22	-0.47	0.33
ZB07_mt_1_Si@12	0.13	1.01	0.03263187	0.00000437	-1.23	0.22	-0.20	0.32
ZB07_mt_1_Si@13	0.13	1.01	0.03259792	0.00000282	-2.27	0.19	-1.24	0.28
ZB07_mt_1_Si@14	0.13	1.02	0.03258904	0.00000529	-2.54	0.24	-1.51	0.34
ZB07_mt_1_Si@15	0.13	1.01	0.03262114	0.00000410	-1.55	0.21	-0.52	0.31

Table 4-4. Continued.

Point #	^{28}Si	$^{28}Si_{samp/av.stnd}$	$^{30}Si/^{28}Si$	± abs	$\delta^{30}Si$	± ‰	$\delta^{30}Si$	± ‰
	cps x 10^9		*drift corrected*		*samples measured*		*samples corrected*	
ZB 17 (Superior-type BIF, ~3 Ga Buhwa Greenstone Belt; S 20° 36' 24.10'', E 30° 23' 57.9'')								
ZB_17_mt_4_Si@1	0.18	0.96	0.03258268	0.00000442	-1.62	0.18	-0.59	0.27
ZB_17_mt_4_Si@02	0.17	0.95	0.03258066	0.00000355	-1.68	0.16	-0.65	0.25
ZB_17_mt_4_Si@03	0.17	0.96	0.03258365	0.00000385	-1.59	0.17	-0.56	0.25
ZB_17_mt_4_Si@04	0.17	0.95	0.03258758	0.00000396	-1.47	0.17	-0.44	0.26
ZB_17_mt_4_Si@05	0.18	0.98	0.03257627	0.00000256	-1.81	0.14	-0.78	0.22
ZB_17_mt_4_Si@06	0.17	0.95	0.03258030	0.00000312	-1.69	0.15	-0.66	0.24
ZB_17_mt_4_Si@07	0.17	0.94	0.03257470	0.00000349	-1.86	0.16	-0.83	0.25
ZB_17_mt_4_Si@08	0.17	0.94	0.03257277	0.00000374	-1.92	0.17	-0.89	0.25
ZB_17_mt_4_Si@09	0.17	0.94	0.03257980	0.00000427	-1.71	0.18	-0.68	0.27
ZB_17_mt_4_Si@10	0.18	0.96	0.03258626	0.00000333	-1.51	0.16	-0.48	0.24
ZB_17_mt_4_Si@11	0.18	0.97	0.03257800	0.00000273	-1.76	0.15	-0.73	0.23
ZB_17_mt_4_Si@12	0.18	0.97	0.03257476	0.00000226	-1.86	0.14	-0.83	0.22
ZB_17_mt_4_Si@13	0.18	0.98	0.03258148	0.00000335	-1.66	0.16	-0.63	0.24
ZB_17_mt_4_Si@14	0.18	0.99	0.03259062	0.00000347	-1.38	0.16	-0.35	0.24
ZB_17_mt_4_Si@15	0.18	0.99	0.03259134	0.00000368	-1.35	0.17	-0.32	0.25
ZB_17_mt_4_Si@16	0.18	0.99	0.03259029	0.00000310	-1.39	0.15	-0.36	0.23
ZB_17_mt_4_Si@17	0.18	0.97	0.03258446	0.00000343	-1.56	0.16	-0.53	0.24
ZB_17_mt_4_Si@18	0.17	0.94	0.03258168	0.00000288	-1.65	0.15	-0.62	0.23
ZB_17_mt_4_Si@19	0.17	0.95	0.03258090	0.00000381	-1.67	0.17	-0.64	0.25
ZB_17_mt_4_Si@20	0.17	0.95	0.03258165	0.00000199	-1.65	0.14	-0.62	0.21

Table 4-4. Continued.

Point #	^{28}Si	$^{28}Si_{samp/av.stnd}$	$^{30}Si/^{28}Si$	± abs	$\delta^{30}Si$	± ‰	$\delta^{30}Si$	± ‰
	cps x 10^9		*drift corrected*		*samples measured*		*samples corrected*	
ZB 18 (Superior-type BIF, ~3 Ga Buhwa Greenstone Belt; S 20° 36' 24.10'', E 30° 23' 57.9')								
ZB_18_mt_3_Si@1	0.13	0.90	0.03259432	0.00000440	-1.23	0.22	-0.20	0.32
ZB_18_mt_3_Si@02	0.13	0.96	0.03257600	0.00000502	-1.79	0.23	-0.76	0.33
ZB_18_mt_3_Si@03	0.14	1.01	0.03258621	0.00000344	-1.48	0.20	-0.45	0.29
ZB_18_mt_3_Si@04	0.13	0.96	0.03257716	0.00000499	-1.76	0.23	-0.73	0.33
ZB_18_mt_3_Si@05	0.12	0.88	0.03258768	0.00000473	-1.43	0.22	-0.40	0.32
ZB_18_mt_3_Si@06	0.12	0.87	0.03258010	0.00000630	-1.67	0.26	-0.64	0.37
ZB_18_mt_3_Si@07	0.12	0.86	0.03257967	0.00000529	-1.68	0.23	-0.65	0.34
ZB_18_mt_3_Si@08	0.12	0.86	0.03258572	0.00000461	-1.49	0.22	-0.46	0.32
ZB_18_mt_3_Si@09	0.12	0.85	0.03259044	0.00000314	-1.35	0.19	-0.32	0.29
ZB_18_mt_3_Si@10	0.12	0.85	0.03258336	0.00000639	-1.57	0.26	-0.54	0.37
ZB_18_mt_3_Si@11	0.13	0.92	0.03254622	0.00000320	-2.70	0.19	-1.67	0.29
ZB_18_mt_3_Si@12	0.12	0.84	0.03258519	0.00000416	-1.51	0.21	-0.48	0.31
ZB_18_mt_3_Si@13	0.12	0.86	0.03258969	0.00000427	-1.37	0.21	-0.34	0.31
ZB_18_mt_3_Si@14	0.12	0.84	0.03258851	0.00000719	-1.41	0.28	-0.38	0.40
ZB_18_mt_3_Si@15	0.12	0.89	0.03259080	0.00000383	-1.34	0.20	-0.31	0.30

Table 4-4. Continued.

Point #	^{28}Si	$^{28}Si_{samp/av.stnd}$	$^{30}Si/^{28}Si$	± abs	$\delta^{30}Si$	± ‰	$\delta^{30}Si$	± ‰
	cps x 10^9		*drift corrected*		*samples measured*		*samples corrected*	
ZB 20 (Superior-type BIF, ~3 Ga Buhwa Greenstone Belt; S 20° 36' 24.10'', E 30° 23' 57.9')								
ZB_20_mt_2_Si@1	0.16	0.97	0.03259113	0.00000514	-2.39	0.24	-1.38	0.43
ZB_20_mt_2_Si@02	0.16	0.97	0.03258716	0.00000247	-2.51	0.20	-1.50	0.37
ZB_20_mt_2_Si@03	0.16	0.98	0.03258309	0.00000431	-2.64	0.23	-1.63	0.41
ZB_20_mt_2_Si@04	0.16	0.98	0.03258447	0.00000299	-2.60	0.21	-1.59	0.38
ZB_20_mt_2_Si@05	0.16	0.97	0.03260088	0.00000443	-2.09	0.23	-1.08	0.41
ZB_20_mt_2_Si@06	0.16	0.96	0.03257498	0.00000442	-2.89	0.23	-1.88	0.41
ZB_20_mt_2_Si@07	0.15	0.95	0.03257602	0.00000492	-2.86	0.24	-1.85	0.42
ZB_20_mt_2_Si@08	0.15	0.95	0.03258305	0.00000497	-2.64	0.24	-1.63	0.42
ZB_20_mt_2_Si@09	0.16	0.97	0.03260956	0.00000316	-1.83	0.21	-0.82	0.38
ZB_20_mt_2_Si@10	0.16	0.96	0.03260973	0.00000326	-1.82	0.21	-0.81	0.38
ZB_20_mt_2_Si@11	0.15	0.95	0.03259709	0.00000460	-2.21	0.23	-1.20	0.41
ZB_20_mt_2_Si@12	0.15	0.95	0.03259792	0.00000311	-2.19	0.21	-1.18	0.38
ZB_20_mt_2_Si@13	0.15	0.93	0.03258703	0.00000438	-2.52	0.23	-1.51	0.41
ZB_20_mt_2_Si@14	0.15	0.95	0.03258543	0.00000519	-2.57	0.24	-1.56	0.43
ZB_20_mt_2_Si@15	0.15	0.94	0.03258472	0.00000546	-2.59	0.25	-1.58	0.44
ZB_20_mt_2_Si@16	0.15	0.95	0.03257547	0.00000457	-2.87	0.23	-1.86	0.41
ZB_20_mt_2_Si@17	0.15	0.95	0.03257910	0.00000330	-2.76	0.21	-1.75	0.38
ZB_20_mt_2_Si@18	0.15	0.95	0.03257186	0.00000411	-2.98	0.22	-1.97	0.40
ZB_20_mt_2_Si@19	0.15	0.95	0.03257823	0.00000484	-2.79	0.24	-1.78	0.42
ZB_20_mt_2_Si@20	0.15	0.93	0.03257382	0.00000238	-2.92	0.20	-1.91	0.37
ZB_20_mt_2_Si@21	0.15	0.93	0.03257743	0.00000388	-2.81	0.22	-1.80	0.40
ZB_20_mt_2_Si@22	0.15	0.92	0.03256884	0.00000303	-3.08	0.21	-2.07	0.38
ZB_20_mt_2_Si@23	0.15	0.92	0.03258150	0.00000359	-2.69	0.22	-1.68	0.39
ZB_20_mt_2_Si@24	0.15	0.92	0.03257463	0.00000369	-2.90	0.22	-1.89	0.39
ZB_20_mt_2_Si@25	0.15	0.92	0.03256888	0.00000470	-3.07	0.23	-2.06	0.42

Table 4-4. Continued.

Point #	^{28}Si	$^{28}Si_{samp/av.stnd}$	$^{30}Si/^{28}Si$	± abs	$\delta^{30}Si$	± ‰	$\delta^{30}Si$	± ‰
	cps x 10^9		*drift corrected*		*samples measured*		*samples corrected*	
ZB 23 (Superior BIF, ~3.0 Ga Buhwa Greenstone Belt; S 20° 37.03', E 30° 21.68')								
ZB_23_Mmount_Si@1	0.18	1.06	0.03256221	0.00000562	-1.15	0.34	-1.15	0.34
ZB_23_Mmount_Si@02	0.18	1.07	0.03256381	0.00000772	-1.10	0.38	-1.10	0.38
ZB_23_Mmount_Si@03	0.18	1.06	0.03255979	0.00000752	-1.23	0.37	-1.23	0.37
ZB_23_Mmount_Si@04	0.18	1.06	0.03257026	0.00000530	-0.91	0.34	-0.91	0.34
ZB_23_Mmount_Si@05	0.18	1.06	0.03257812	0.00000757	-0.66	0.38	-0.66	0.38
ZB_23_Mmount_Si@06	0.18	1.06	0.03255649	0.00000714	-1.33	0.37	-1.33	0.37
ZB_23_Mmount_Si@07	0.18	1.05	0.03256052	0.00000521	-1.20	0.34	-1.20	0.34
ZB_23_Mmount_Si@08	0.17	1.00	0.03255254	0.00000626	-1.45	0.35	-1.45	0.35
ZB_23_Mmount_Si@09	0.18	1.07	0.03253213	0.00000508	-2.08	0.33	-2.08	0.33
ZB_23_Mmount_Si@10	0.18	1.06	0.03255155	0.00000617	-1.48	0.35	-1.48	0.35
ZB_23_Mmount_Si@11	0.18	1.06	0.03256200	0.00000680	-1.16	0.36	-1.16	0.36
ZB_23_Mmount_Si@12	0.18	1.06	0.03254784	0.00000625	-1.59	0.35	-1.59	0.35
ZB_23_Mmount_Si@13	0.19	1.08	0.03251477	0.00000689	-2.61	0.36	-2.61	0.36
ZB_23_Mmount_Si@14	0.19	1.10	0.03253495	0.00000608	-1.99	0.35	-1.99	0.35
ZB_23_Mmount_Si@15	0.18	1.03	0.03253387	0.00000691	-2.02	0.36	-2.02	0.36
ZB_23_Mmount_Si@16	0.17	0.97	0.03258863	0.00000793	-0.34	0.38	-0.34	0.38
ZB_23_Mmount_Si@17	0.18	1.02	0.03254527	0.00000598	-1.67	0.35	-1.67	0.35
ZB_23_Mmount_Si@18	0.18	1.03	0.03252638	0.00000702	-2.25	0.37	-2.25	0.37
ZB_23_Mmount_Si@19	0.17	1.00	0.03252162	0.00000514	-2.40	0.33	-2.40	0.33
ZB_23_Mmount_Si@20	0.17	1.00	0.03254070	0.00000561	-1.81	0.34	-1.81	0.34
ZB_23_Mmount_Si@21	0.15	0.89	0.03252690	0.00000513	-2.24	0.33	-2.24	0.33
ZB_23_Mmount_Si@22	0.17	0.99	0.03254283	0.00000528	-1.75	0.34	-1.75	0.34
ZB_23_Mmount_Si@23	0.16	0.96	0.03252681	0.00000745	-2.24	0.37	-2.24	0.37
ZB_23_Mmount_Si@24	0.17	0.99	0.03254022	0.00000550	-1.83	0.34	-1.83	0.34

Table 4-4. Continued.

Point #	^{28}Si	$^{28}Si_{samp/av.stnd}$	$^{30}Si/^{28}Si$	± abs	$\delta^{30}Si$	± ‰	$\delta^{30}Si$	± ‰
	cps x 10^9		*drift corrected*		*samples measured*		*samples corrected*	
ZB_23_Mmount_Si@25	0.17	1.02	0.03256216	0.00000691	-1.15	0.36	-1.15	0.36
ZB_23_Mmount_Si@26	0.17	1.01	0.03257206	0.00000752	-0.85	0.38	-0.85	0.38
ZB_23_Mmount_Si@27	0.18	1.03	0.03256741	0.00000692	-0.99	0.36	-0.99	0.36
ZB_23_Mmount_Si@28	0.18	1.03	0.03256847	0.00000633	-0.96	0.35	-0.96	0.35
ZB_23_Mmount_Si@29	0.17	1.00	0.03257693	0.00000669	-0.70	0.36	-0.70	0.36
ZB_23_Mmount_Si@30	0.17	0.98	0.03257405	0.00000809	-0.79	0.39	-0.79	0.39
ZB_23_Mmount_Si@31	0.16	0.95	0.03258012	0.00000646	-0.60	0.36	-0.60	0.36
ZB_23_Mmount_Si@32	0.18	1.04	0.03254988	0.00000618	-1.53	0.35	-1.53	0.35
ZB 169 (Superior BIF, ~3.0 Ga Buhwa Greenstone Belt; S 20° 37.08', E 30° 20.20')								
ZB_169b_mt_1_Si@1	0.13	1.00	0.03259170	0.00000574	-2.46	0.24	-1.45	0.43
ZB_169b_mt_1_Si@02	0.13	1.00	0.03259217	0.00000465	-2.44	0.22	-1.43	0.40
ZB_169b_mt_1_Si@03	0.12	0.97	0.03256593	0.00000422	-3.24	0.21	-2.23	0.39
ZB_169b_mt_1_Si@04	0.12	0.97	0.03255438	0.00000552	-3.60	0.24	-2.59	0.42
ZB_169b_mt_1_Si@05	0.12	0.97	0.03258702	0.00000431	-2.60	0.22	-1.59	0.39
ZB_169b_mt_1_Si@06	0.12	0.95	0.03257376	0.00000449	-3.00	0.22	-1.99	0.39
ZB_169b_mt_1_Si@07	0.12	0.95	0.03258378	0.00000298	-2.70	0.19	-1.69	0.36
ZB_169b_mt_1_Si@08	0.12	0.95	0.03254504	0.00000327	-3.88	0.20	-2.87	0.37
ZB_169b_mt_1_Si@09	0.12	0.98	0.03259425	0.00000279	-2.38	0.19	-1.37	0.36
ZB_169b_mt_1_Si@10	0.12	0.97	0.03258864	0.00000265	-2.55	0.19	-1.54	0.35
ZB_169b_mt_1_Si@11	0.12	0.97	0.03258013	0.00000399	-2.81	0.21	-1.80	0.38
ZB_169b_mt_1_Si@12	0.12	0.97	0.03258129	0.00000497	-2.77	0.23	-1.76	0.41
ZB_169b_mt_1_Si@13	0.12	0.97	0.03258040	0.00000293	-2.80	0.19	-1.79	0.36
ZB_169b_mt_1_Si@14	0.09	0.75	0.03256984	0.00000595	-3.12	0.25	-2.11	0.43

Table 4-4. Continued.

Point #	^{28}Si	$^{28}Si_{samp/av.stnd}$	$^{30}Si/^{28}Si$	± abs	$\delta^{30}Si$	± ‰	$\delta^{30}Si$	± ‰
	cps x 10^9		*drift corrected*		*samples measured*		*samples corrected*	
ZB 143 (Superior-type BIF, ~3 Ga Buhwa Greenstone Belt; S 20° 37' 04.02'', E 30° 22' 01.61'')								
ZB_143_mt_4_Si@1	0.18	1.00	0.03254189	0.00000462	-2.87	0.19	-1.84	0.35
ZB_143_mt_4_Si@02	0.18	1.01	0.03254990	0.00000293	-2.62	0.15	-1.59	0.30
ZB_143_mt_4_Si@03	0.18	1.00	0.03256070	0.00000391	-2.29	0.17	-1.26	0.33
ZB_143_mt_4_Si@04	0.19	1.02	0.03252498	0.00000296	-3.39	0.15	-2.36	0.31
ZB_143_mt_4_Si@05	0.18	0.99	0.03255197	0.00000398	-2.56	0.17	-1.53	0.33
ZB_143_mt_4_Si@06	0.19	1.01	0.03254255	0.00000440	-2.85	0.18	-1.82	0.34
ZB_143_mt_4_Si@07	0.18	1.00	0.03257089	0.00000417	-1.98	0.18	-0.95	0.34
ZB_143_mt_4_Si@08	0.18	0.98	0.03257937	0.00000486	-1.72	0.19	-0.69	0.36
ZB_143_mt_4_Si@09	0.18	1.01	0.03257634	0.00000566	-1.81	0.21	-0.78	0.38
ZB_143_mt_4_Si@10	0.09	0.48	0.03249290	0.00001456	-4.37	0.46	-3.34	0.71
ZB_143_mt_4_Si@11	0.18	0.99	0.03256540	0.00000462	-2.15	0.19	-1.12	0.35
ZB_143_mt_4_Si@12	0.20	1.07	0.03257798	0.00000279	-1.76	0.15	-0.73	0.30
ZB_143_mt_4_Si@13	0.18	0.99	0.03257346	0.00000397	-1.90	0.17	-0.87	0.33
ZB_143_mt_4_Si@14	0.19	1.02	0.03258531	0.00000276	-1.54	0.15	-0.51	0.30
ZB_143_mt_4_Si@15	0.18	0.99	0.03257096	0.00000273	-1.98	0.15	-0.95	0.30

Table 4-4. Continued.

Point #	^{28}Si	$^{28}Si_{samp/av.stnd}$	$^{30}Si/^{28}Si$	± abs	$\delta^{30}Si$	± ‰	$\delta^{30}Si$	± ‰
	cps x 10^9		*drift corrected*		*samples measured*		*samples corrected*	
ZB 05 (Algoma BIF, ~3.0 Ga Buhwa Greenstone Belt; S 20° 34.85', E 30° 26.892660')								
ZB05_mt_1_Si@26	0.12	0.96	0.03258956	0.00000363	-2.52	0.20	-1.49	0.30
ZB05_mt_1_Si@27	0.11	0.90	0.03260546	0.00000495	-2.03	0.23	-1.00	0.33
ZB05_mt_1_Si@28	0.12	0.97	0.03252792	0.00000636	-4.41	0.26	-3.38	0.37
ZB05_mt_1_Si@29	0.12	0.96	0.03255615	0.00000461	-3.54	0.22	-2.51	0.32
ZB05_mt_1_Si@30	0.12	0.98	0.03256895	0.00000399	-3.15	0.21	-2.12	0.31
ZB05_mt_1_Si@31	0.12	0.99	0.03256877	0.00000397	-3.16	0.21	-2.13	0.31
ZB05_mt_1_Si@32	0.13	1.00	0.03254405	0.00000521	-3.91	0.23	-2.88	0.34
ZB05_mt_1_Si@33	0.13	1.07	0.03254187	0.00000350	-3.98	0.20	-2.95	0.30
ZB05_mt_1_Si@34	0.13	1.00	0.03256431	0.00000356	-3.29	0.20	-2.26	0.30
ZB05_mt_1_Si@35	0.12	0.98	0.03255646	0.00000429	-3.53	0.22	-2.50	0.32
ZB05_mt_1_Si@36	0.12	0.97	0.03255231	0.00000410	-3.66	0.21	-2.63	0.31
ZB05_mt_1_Si@1	0.13	1.05	0.03252414	0.00000337	-4.52	0.20	-3.49	0.29
ZB05_mt_1_Si@02	0.13	1.03	0.03253941	0.00000389	-4.06	0.21	-3.03	0.31
ZB05_mt_1_Si@03	0.13	1.04	0.03253103	0.00000368	-4.31	0.20	-3.28	0.30
ZB05_mt_1_Si@04	0.13	1.04	0.03253994	0.00000515	-4.04	0.23	-3.01	0.34
ZB05_mt_1_Si@05	0.13	1.03	0.03255404	0.00000516	-3.61	0.23	-2.58	0.34
ZB05_mt_1_Si@06	0.13	1.05	0.03255691	0.00000375	-3.52	0.21	-2.49	0.30
ZB05_mt_1_Si@07	0.13	1.02	0.03254863	0.00000637	-3.77	0.26	-2.74	0.37
ZB05_mt_1_Si@08	0.13	1.01	0.03254565	0.00000442	-3.87	0.22	-2.84	0.32
ZB05_mt_1_Si@09	0.13	1.02	0.03254854	0.00000461	-3.78	0.22	-2.75	0.32
ZB05_mt_1_Si@10	0.13	1.01	0.03256774	0.00000518	-3.19	0.23	-2.16	0.34
ZB05_mt_1_Si@11	0.13	1.02	0.03255751	0.00000435	-3.50	0.22	-2.47	0.32
ZB05_mt_1_Si@12	0.13	1.00	0.03256635	0.00000471	-3.23	0.22	-2.20	0.33
ZB05_mt_1_Si@13	0.12	0.99	0.03253696	0.00000376	-4.13	0.21	-3.10	0.30

Table 4-4. Continued.

Point #	^{28}Si	$^{28}Si_{samp/av.stnd}$	$^{30}Si/^{28}Si$	± abs	$\delta^{30}Si$	± ‰	$\delta^{30}Si$	± ‰
	cps x 10^9		*drift corrected*		*samples measured*		*samples corrected*	
ZB05_mt_1_Si@14	0.13	1.01	0.03255581	0.00000503	-3.55	0.23	-2.52	0.33
ZB05_mt_1_Si@15	0.13	1.04	0.03252679	0.00000409	-4.44	0.21	-3.41	0.31
ZB05_mt_1_Si@16	0.13	1.00	0.03252388	0.00000349	-4.53	0.20	-3.50	0.30
ZB05_mt_1_Si@17	0.13	1.01	0.03255630	0.00000469	-3.54	0.22	-2.51	0.33
ZB05_mt_1_Si@18	0.13	1.01	0.03253725	0.00000462	-4.12	0.22	-3.09	0.32
ZB05_mt_1_Si@19	0.12	0.98	0.03251587	0.00000344	-4.78	0.20	-3.75	0.30
ZB05_mt_1_Si@20	0.12	0.98	0.03254430	0.00000509	-3.91	0.23	-2.88	0.34
ZB05_mt_1_Si@21	0.13	1.00	0.03255211	0.00000387	-3.67	0.21	-2.64	0.31
ZB05_mt_1_Si@22	0.13	1.02	0.03253276	0.00000538	-4.26	0.24	-3.23	0.34
ZB05_mt_1_Si@23	0.13	1.03	0.03257173	0.00000548	-3.07	0.24	-2.04	0.35
ZB05_mt_1_Si@24	0.13	1.02	0.03255309	0.00000354	-3.64	0.20	-2.61	0.30
ZB05_mt_1_Si@25	0.12	1.00	0.03253598	0.00000360	-4.16	0.20	-3.13	0.30
ZB05_mt_2_Si@1	0.16	0.98	0.03258552	0.00000388	-2.57	0.22	-1.54	0.32
ZB05_mt_2_Si@02	0.16	0.97	0.03255930	0.00000424	-3.37	0.23	-2.34	0.33
ZB05_mt_2_Si@03	0.16	0.97	0.03256661	0.00000407	-3.14	0.22	-2.11	0.33
ZB05_mt_2_Si@04	0.16	0.96	0.03255328	0.00000397	-3.55	0.22	-2.52	0.32
ZB05_mt_2_Si@05	0.15	0.95	0.03256736	0.00000382	-3.12	0.22	-2.09	0.32
ZB05_mt_2_Si@06	0.15	0.94	0.03256371	0.00000313	-3.23	0.21	-2.20	0.31
ZB05_mt_2_Si@07	0.15	0.95	0.03257265	0.00000463	-2.96	0.23	-1.93	0.34
ZB05_mt_2_Si@08	0.16	0.96	0.03257448	0.00000480	-2.90	0.24	-1.87	0.34
ZB05_mt_2_Si@09	0.16	0.96	0.03256360	0.00000210	-3.24	0.20	-2.21	0.29
ZB05_mt_2_Si@10	0.16	0.97	0.03257187	0.00000460	-2.98	0.23	-1.95	0.34
ZB05_mt_2_Si@11	0.16	0.96	0.03256799	0.00000375	-3.10	0.22	-2.07	0.32
ZB05_mt_2_Si@12	0.16	0.97	0.03257817	0.00000433	-2.79	0.23	-1.76	0.33
ZB05_mt_2_Si@13	0.16	0.96	0.03256182	0.00000377	-3.29	0.22	-2.26	0.32

Table 4-4. Continued.

Point #	^{28}Si	$^{28}Si_{samp/av.stnd}$	$^{30}Si/^{28}Si$	± abs	$\delta^{30}Si$	± ‰	$\delta^{30}Si$	± ‰
	cps x 10^9		*drift corrected*		*samples measured*		*samples corrected*	
ZB05_mt_2_Si@14	0.15	0.95	0.03256189	0.00000371	-3.29	0.22	-2.26	0.32
ZB05_mt_2_Si@15	0.15	0.95	0.03256971	0.00000493	-3.05	0.24	-2.02	0.35
ZB05_mt_2_Si@16	0.15	0.95	0.03256248	0.00000434	-3.27	0.23	-2.24	0.33
ZB05_mt_2_Si@17	0.15	0.95	0.03256262	0.00000442	-3.27	0.23	-2.24	0.33
ZB05_mt_2_Si@18	0.15	0.94	0.03255045	0.00000414	-3.64	0.22	-2.61	0.33
ZB05_mt_2_Si@19	0.15	0.95	0.03256215	0.00000523	-3.28	0.25	-2.25	0.36
ZB05_mt_2_Si@20	0.16	0.96	0.03256850	0.00000241	-3.09	0.20	-2.06	0.30
ZB05_mt_2_Si@21	0.16	0.97	0.03258922	0.00000343	-2.45	0.21	-1.42	0.31
ZB05_mt_2_Si@22	0.16	0.96	0.03257889	0.00000494	-2.77	0.24	-1.74	0.35
ZB05_mt_2_Si@23	0.16	0.96	0.03257316	0.00000329	-2.94	0.21	-1.91	0.31
ZB05_mt_2_Si@24	0.16	0.96	0.03257169	0.00000536	-2.99	0.25	-1.96	0.36
ZB05_mt_2_Si@25	0.16	0.96	0.03255589	0.00000316	-3.47	0.21	-2.44	0.31
ZB05_mt_2_Si@26	0.16	0.97	0.03256845	0.00000550	-3.09	0.25	-2.06	0.36
ZB05_mt_2_Si@27	0.16	0.96	0.03257279	0.00000408	-2.95	0.22	-1.92	0.33
ZB05_mt_2_Si@28	0.16	0.98	0.03255905	0.00000369	-3.38	0.22	-2.35	0.32
ZB05_mt_2_Si@29	0.16	0.97	0.03256042	0.00000414	-3.33	0.22	-2.30	0.33
ZB05_mt_2_Si@30	0.16	0.96	0.03257669	0.00000444	-2.84	0.23	-1.81	0.34
ZB05_mt_2_Si@31	0.16	0.97	0.03255730	0.00000209	-3.43	0.20	-2.40	0.29
ZB05_mt_2_Si@32	0.16	0.97	0.03256656	0.00000231	-3.15	0.20	-2.12	0.29
ZB05_mt_2_Si@33	0.16	0.97	0.03256271	0.00000411	-3.26	0.22	-2.23	0.33
ZB05_mt_2_Si@34	0.16	0.96	0.03256948	0.00000422	-3.06	0.23	-2.03	0.33
ZB05_mt_2_Si@35	0.15	0.94	0.03255958	0.00000363	-3.36	0.22	-2.33	0.32
ZB05_mt_2_Si@36	0.16	0.98	0.03256073	0.00000325	-3.32	0.21	-2.29	0.31
ZB05_mt_2_Si@37	0.15	0.93	0.03253600	0.00000368	-4.08	0.22	-3.05	0.32
ZB05_mt_2_Si@38	0.15	0.94	0.03252459	0.00000329	-4.43	0.21	-3.40	0.31

Table 4-4. Continued.

Point #	^{28}Si	$^{28}Si_{samp/av.stnd}$	$^{30}Si/^{28}Si$	± abs	$\delta^{30}Si$	± ‰	$\delta^{30}Si$	± ‰
	cps x 10^9		*drift corrected*		*samples measured*		*samples corrected*	
ZB05_mt_2_Si@39	0.16	0.97	0.03254436	0.00000353	-3.82	0.21	-2.79	0.32
ZB05_mt_2_Si@40	0.16	0.97	0.03254172	0.00000418	-3.91	0.23	-2.88	0.33
ZB05_mt_2_Si@41	0.16	0.97	0.03255192	0.00000378	-3.59	0.22	-2.56	0.32
ZB05_mt_2_Si@42	0.16	0.98	0.03255282	0.00000428	-3.57	0.23	-2.54	0.33
ZB05_mt_2_Si@43	0.16	0.98	0.03256007	0.00000352	-3.34	0.21	-2.31	0.31
ZB05_mt_2_Si@44	0.16	0.98	0.03256501	0.00000538	-3.19	0.25	-2.16	0.36
ZB05_mt_2_Si@45	0.16	0.97	0.03255558	0.00000384	-3.48	0.22	-2.45	0.32
ZB05_mt_2_Si@46	0.16	0.99	0.03256239	0.00000598	-3.27	0.26	-2.24	0.38
ZB05_mt_2_Si@47	0.16	1.00	0.03255591	0.00000259	-3.47	0.20	-2.44	0.30
ZB05_mt_2_Si@48	0.16	0.98	0.03257831	0.00000323	-2.79	0.21	-1.76	0.31
ZB05_mt_2_Si@49	0.16	0.97	0.03258126	0.00000506	-2.70	0.24	-1.67	0.35
ZB05_mt_2_Si@50	0.16	0.99	0.03256360	0.00000429	-3.24	0.23	-2.21	0.33
ZB05_mt_2_Si@51	0.16	0.99	0.03258009	0.00000442	-2.73	0.23	-1.70	0.33
ZB05_mt_2_Si@52	0.16	1.00	0.03257389	0.00000457	-2.92	0.23	-1.89	0.34
ZB05_mt_2_Si@53	0.16	0.97	0.03258892	0.00000586	-2.46	0.26	-1.43	0.37
ZB05_mt_2_Si@54	0.16	1.00	0.03255654	0.00000391	-3.45	0.22	-2.42	0.32
ZB05_mt_2_Si@55	0.16	1.00	0.03257026	0.00000485	-3.03	0.24	-2.00	0.35
ZB05_mt_2_Si@56	0.16	0.96	0.03257619	0.00000302	-2.85	0.21	-1.82	0.31
ZB05_mt_2_Si@57	0.16	0.97	0.03257143	0.00000441	-3.00	0.23	-1.97	0.33
ZB05_mt_2_Si@58	0.16	0.99	0.03257028	0.00000595	-3.03	0.26	-2.00	0.37
ZB05_mt_2_Si@59	0.16	1.00	0.03258718	0.00000340	-2.51	0.21	-1.48	0.31
ZB05_mt_2_Si@60	0.16	1.00	0.03258406	0.00000378	-2.61	0.22	-1.58	0.32
ZB05_mt_2_Si@61	0.16	0.99	0.03257708	0.00000461	-2.82	0.23	-1.79	0.34
ZB05_mt_2_Si@62	0.16	1.02	0.03257942	0.00000399	-2.75	0.22	-1.72	0.33
ZB05_mt_2_Si@63	0.16	1.00	0.03258054	0.00000444	-2.72	0.23	-1.69	0.34

Table 4-4. Continued.

Point #	^{28}Si	$^{28}Si_{samp/av.stnd}$	$^{30}Si/^{28}Si$	± abs	$\delta^{30}Si$	± ‰	$\delta^{30}Si$	± ‰
	cps x 10^9		*drift corrected*		*samples measured*		*samples corrected*	
ZB05_mt_2_Si@64	0.16	0.96	0.03256888	0.00000555	-3.07	0.25	-2.04	0.36
ZB05_mt_2_Si@65	0.16	0.98	0.03257573	0.00000401	-2.86	0.22	-1.83	0.33
ZB05_mt_2_Si@66	0.16	1.01	0.03256133	0.00000481	-3.31	0.24	-2.28	0.34
ZB05_mt_2_Si@67	0.16	1.00	0.03257143	0.00000344	-3.00	0.21	-1.97	0.31
ZB05_mt_2_Si@68	0.16	1.00	0.03257417	0.00000424	-2.91	0.23	-1.88	0.33
ZB05_mt_2_Si@69	0.16	1.00	0.03257480	0.00000444	-2.89	0.23	-1.86	0.34
ZB05_mt_2_Si@70	0.16	1.01	0.03258583	0.00000421	-2.56	0.23	-1.53	0.33
ZB05_mt_2_Si@71	0.16	1.01	0.03258494	0.00000362	-2.58	0.22	-1.55	0.32
ZB05_mt_2_Si@72	0.16	0.98	0.03258052	0.00000433	-2.72	0.23	-1.69	0.33
ZB05_mt_2_Si@73	0.16	1.01	0.03256610	0.00000446	-3.16	0.23	-2.13	0.34
ZB05_mt_2_Si@74	0.16	1.02	0.03257394	0.00000329	-2.92	0.21	-1.89	0.31
ZB05_mt_2_Si@75	0.16	0.96	0.03258072	0.00000418	-2.71	0.23	-1.68	0.33
ZB05_mt_2_Si@76	0.16	1.01	0.03256354	0.00000396	-3.24	0.22	-2.21	0.32
ZB05_mt_2_Si@77	0.16	1.01	0.03257297	0.00000507	-2.95	0.24	-1.92	0.35
ZB05_mt_2_Si@78	0.16	1.00	0.03257881	0.00000409	-2.77	0.22	-1.74	0.33
Temj (Algoma-type BIF, 2.7 Ga Abitibi Greenstone Belt; N 47° 04.173', W 079° 47.434')								
Temj_mt_8_Si@1	0.16	1.06	0.03257529	0.00000522	-1.39	0.29	-0.36	0.41
Temj_mt_8_Si@02	0.16	1.06	0.03256600	0.00000478	-1.67	0.28	-0.64	0.40
Temj_mt_8_Si@03	0.16	1.05	0.03256274	0.00000576	-1.77	0.30	-0.74	0.43
Temj_mt_8_Si@04	0.16	1.06	0.03255995	0.00000689	-1.86	0.32	-0.83	0.45
Temj_mt_8_Si@05	0.16	1.05	0.03253445	0.00000502	-2.64	0.29	-1.61	0.41
Temj_mt_8_Si@06	0.16	1.05	0.03251549	0.00000460	-3.22	0.28	-2.19	0.40
Temj_mt_8_Si@07	0.15	1.04	0.03256371	0.00000544	-1.74	0.29	-0.71	0.42

Table 4-4. Continued.

Point #	^{28}Si	$^{28}Si_{samp/av.stnd}$	$^{30}Si/^{28}Si$	± abs	$\delta^{30}Si$	± ‰	$\delta^{30}Si$	± ‰
	cps x 10^9		*drift corrected*		*samples measured*		*samples corrected*	
Temj_mt_8_Si@08	0.15	1.04	0.03254647	0.00000509	-2.27	0.29	-1.24	0.41
Temj_mt_8_Si@09	0.15	1.04	0.03257156	0.00000697	-1.50	0.32	-0.47	0.46
Temj_mt_8_Si@10	0.15	1.03	0.03255259	0.00000513	-2.08	0.29	-1.05	0.41
Temj_mt_8_Si@11	0.15	1.03	0.03255487	0.00000304	-2.01	0.26	-0.98	0.37
Temj_mt_8_Si@12	0.15	1.04	0.03258125	0.00000559	-1.20	0.30	-0.17	0.42
Temj_mt_8_Si@13	0.15	1.02	0.03253470	0.00000528	-2.63	0.29	-1.60	0.42
Temj_mt_8_Si@14	0.15	1.02	0.03254874	0.00000660	-2.20	0.32	-1.17	0.45
Temj_mt_8_Si@15	0.15	1.02	0.03260394	0.00000445	-0.51	0.28	0.52	0.40
Temj_mt_8_Si@16	0.15	1.02	0.03258884	0.00000663	-0.97	0.32	0.06	0.45
Temj_mt_8_Si@17	0.15	1.03	0.03256715	0.00000570	-1.64	0.30	-0.61	0.43
Temj_mt_8_Si@18	0.15	1.02	0.03255692	0.00000612	-1.95	0.31	-0.92	0.43
Temj_mt_8_Si@19	0.15	1.03	0.03257479	0.00000421	-1.40	0.27	-0.37	0.39
Temj_mt_8_Si@20	0.15	1.04	0.03256410	0.00000491	-1.73	0.28	-0.70	0.41
Temj_mt_8_Si@21	0.15	1.03	0.03258011	0.00000431	-1.24	0.28	-0.21	0.40
Temj_mt_8_Si@22	0.15	1.03	0.03256244	0.00000638	-1.78	0.31	-0.75	0.44
Temj_mt_8_Si@23	0.15	1.01	0.03256044	0.00000632	-1.84	0.31	-0.81	0.44
Temj_mt_8_Si@24	0.15	1.02	0.03255279	0.00000576	-2.08	0.30	-1.05	0.43
Temj_mt_8_Si@25	0.15	1.00	0.03256266	0.00000429	-1.77	0.28	-0.74	0.39
Temj_mt_8_Si@26	0.15	1.00	0.03254225	0.00000639	-2.40	0.31	-1.37	0.44
Temj_mt_8_Si@27	0.15	1.00	0.03255232	0.00000360	-2.09	0.27	-1.06	0.38
Temj_mt_8_Si@28	0.15	0.99	0.03255464	0.00000565	-2.02	0.30	-0.99	0.42
Temj_mt_8_Si@29	0.15	0.99	0.03255979	0.00000486	-1.86	0.28	-0.83	0.41
Temj_mt_8_Si@30	0.14	0.98	0.03254755	0.00000594	-2.24	0.30	-1.21	0.43
Temj_mt_8_Si@31	0.15	1.00	0.03255937	0.00000461	-1.88	0.28	-0.85	0.40
Temj_mt_8_Si@32	0.15	1.01	0.03255023	0.00000555	-2.16	0.30	-1.13	0.42

Table 4-4. Continued.

Point #	^{28}Si	$^{28}Si_{samp/av.stnd}$	$^{30}Si/^{28}Si$	± abs	$\delta^{30}Si$	± ‰	$\delta^{30}Si$	± ‰
	cps x 10^9		*drift corrected*		*samples measured*		*samples corrected*	
Temj_mt_8_Si@33	0.15	1.02	0.03259572	0.00000640	-0.76	0.31	0.27	0.44
Temj_mt_8_Si@34	0.15	1.02	0.03258531	0.00000471	-1.08	0.28	-0.05	0.40
Temj_mt_8_Si@35	0.15	1.00	0.03259192	0.00000546	-0.88	0.29	0.15	0.42
Temj_mt_8_Si@36	0.15	1.02	0.03260232	0.00000445	-0.56	0.28	0.47	0.40
Temj_mt_8_Si@37	0.15	1.01	0.03258001	0.00000419	-1.24	0.27	-0.21	0.39
Temj_mt_8_Si@38	0.15	1.01	0.03258657	0.00000459	-1.04	0.28	-0.01	0.40
Temj_mt_8_Si@39	0.15	1.01	0.03257804	0.00000491	-1.30	0.28	-0.27	0.41
Temj_mt_8_Si@40	0.15	1.00	0.03255788	0.00000662	-1.92	0.32	-0.89	0.45
Temj_mt_8_Si@41	0.15	0.98	0.03257047	0.00000606	-1.54	0.30	-0.51	0.43
Temj_mt_8_Si@42	0.14	0.97	0.03256899	0.00000375	-1.58	0.27	-0.55	0.38
Temj_mt_8_Si@43	0.14	0.97	0.03254829	0.00000395	-2.22	0.27	-1.19	0.39
Temj_mt_8_Si@44	0.15	0.98	0.03257215	0.00000520	-1.48	0.29	-0.45	0.41
Temj_mt_8_Si@45	0.15	0.98	0.03256497	0.00000590	-1.70	0.30	-0.67	0.43
TEM13Db (Algoma-type BIF, 2.7 Ga Abitibi Greenstone Belt; N 47° 04.173', W 079° 47.434')								
TEM13Db_mt_8_Si_1	0.14	0.98	0.03258471	0.00000685	-1.10	0.32	-0.07	0.45
TEM13Db_mt_8_Si_1@00	0.14	0.96	0.03257070	0.00000356	-1.53	0.27	-0.50	0.38
TEM13Db_mt_8_Si_1@01	0.14	0.96	0.03257758	0.00000519	-1.32	0.29	-0.29	0.41
TEM13Db_mt_8_Si_1@02	0.14	0.97	0.03258140	0.00000498	-1.20	0.29	-0.17	0.41
TEM13Db_mt_8_Si_1@03	0.14	0.97	0.03257365	0.00000389	-1.44	0.27	-0.41	0.39
TEM13Db_mt_8_Si_1@04	0.15	1.01	0.03252760	0.00000767	-2.85	0.34	-1.82	0.48
TEM13Db_mt_8_Si_1@05	0.14	0.97	0.03255507	0.00000451	-2.01	0.28	-0.98	0.40
TEM13Db_mt_8_Si_1@06	0.15	1.00	0.03253772	0.00000628	-2.54	0.31	-1.51	0.44
TEM13Db_mt_8_Si_1@07	0.15	0.99	0.03257203	0.00000439	-1.49	0.28	-0.46	0.40

Table 4-4. Continued.

Point #	^{28}Si	$^{28}Si_{samp/av.stnd}$	$^{30}Si/^{28}Si$	± abs	$\delta^{30}Si$	± ‰	$\delta^{30}Si$	± ‰
	cps x 10^9		*drift corrected*		*samples measured*		*samples corrected*	
TEM13Db_mt_8_Si_1@08	0.14	0.97	0.03255244	0.00000495	-2.09	0.29	-1.06	0.41
TEM13Db_mt_8_Si_1@09	0.14	0.97	0.03256612	0.00000464	-1.67	0.28	-0.64	0.40
TEM13Db_mt_8_Si_1@10	0.14	0.95	0.03257316	0.00000452	-1.45	0.28	-0.42	0.40
TEM13Db_mt_8_Si_1@11	0.14	0.97	0.03256406	0.00000417	-1.73	0.27	-0.70	0.39
TEM13Db_mt_8_Si_1@12	0.14	0.96	0.03259628	0.00000501	-0.74	0.29	0.29	0.41
TEM13Db_mt_8_Si_1@13	0.14	0.96	0.03254925	0.00000456	-2.19	0.28	-1.16	0.40
TEM13Db_mt_8_Si_1@14	0.14	0.96	0.03256211	0.00000536	-1.79	0.29	-0.76	0.42
TEM13Db_mt_8_Si_1@15	0.14	0.96	0.03258056	0.00000370	-1.23	0.27	-0.20	0.38
TEM13Db_mt_8_Si_1@16	0.14	0.96	0.03260853	0.00000543	-0.37	0.29	0.66	0.42
TEM CF (Algoma BIF, 2.7 Ga Abitibi Greenstone Belt; N 47° 04.173', W 079° 47.434')								
TEM_cf_Mmount_Si@1	0.16	0.91	0.03260666	0.00000593	0.21	0.35	0.21	0.49
TEM_cf_Mmount_Si@02	0.16	0.94	0.03259370	0.00000657	-0.19	0.36	-0.19	0.50
TEM_cf_Mmount_Si@03	0.16	0.96	0.03258478	0.00000639	-0.46	0.35	-0.46	0.50
TEM_cf_Mmount_Si@04	0.16	0.92	0.03258683	0.00000662	-0.40	0.36	-0.40	0.50
TEM_cf_Mmount_Si@05	0.16	0.94	0.03259935	0.00000691	-0.01	0.36	-0.01	0.51
TEM_cf_Mmount_Si@06	0.16	0.95	0.03259044	0.00000583	-0.29	0.35	-0.29	0.49
TEM_cf_Mmount_Si@07	0.16	0.92	0.03256906	0.00000625	-0.94	0.35	-0.94	0.50
TEM_cf_Mmount_Si@08	0.16	0.94	0.03258904	0.00000712	-0.33	0.37	-0.33	0.52
TEM_cf_Mmount_Si@09	0.16	0.93	0.03257487	0.00000489	-0.76	0.33	-0.76	0.47
TEM_cf_Mmount_Si@10	0.16	0.93	0.03257275	0.00000594	-0.83	0.35	-0.83	0.49
TEM_cf_Mmount_Si@11	0.16	0.93	0.03258230	0.00000655	-0.54	0.36	-0.54	0.50
TEM_cf_Mmount_Si@12	0.16	0.94	0.03257501	0.00000687	-0.76	0.36	-0.76	0.51
TEM_cf_Mmount_Si@13	0.16	0.96	0.03257523	0.00000608	-0.75	0.35	-0.75	0.49

Table 4-4. Continued.

Point #	^{28}Si	$^{28}Si_{samp/av.stnd}$	$^{30}Si/^{28}Si$	± abs	$\delta^{30}Si$	± ‰	$\delta^{30}Si$	± ‰
	cps x 10^9		*drift corrected*		*samples measured*		*samples corrected*	
TEM_cf_Mmount_Si@14	0.16	0.93	0.03257061	0.00000487	-0.90	0.33	-0.90	0.47
TEM_cf_Mmount_Si@15	0.16	0.94	0.03258388	0.00000522	-0.49	0.34	-0.49	0.48
TEM_cf_Mmount_Si@16	0.16	0.95	0.03257208	0.00000738	-0.85	0.37	-0.85	0.52
TEM_cf_Mmount_Si@17	0.16	0.93	0.03259474	0.00000625	-0.15	0.35	-0.15	0.50
TEM_cf_Mmount_Si@18	0.16	0.93	0.03257370	0.00000759	-0.80	0.38	-0.80	0.53
TEM_cf_Mmount_Si@19	0.16	0.94	0.03258332	0.00000546	-0.51	0.34	-0.51	0.48
TEM_cf_Mmount_Si@20	0.16	0.94	0.03259420	0.00000461	-0.17	0.33	-0.17	0.46
TEM_cf_Mmount_Si@21	0.16	0.94	0.03258639	0.00000611	-0.41	0.35	-0.41	0.49
TEM_cf_Mmount_Si@22	0.16	0.92	0.03257634	0.00000730	-0.72	0.37	-0.72	0.52
TEM_cf_Mmount_Si@23	0.16	0.92	0.03259129	0.00000351	-0.26	0.31	-0.26	0.45
TEM_cf_Mmount_Si@24	0.16	0.92	0.03259212	0.00000580	-0.24	0.35	-0.24	0.49
TEM_cf_Mmount_Si@25	0.16	0.92	0.03258273	0.00000530	-0.52	0.34	-0.52	0.48
TEM_cf_Mmount_Si@26	0.16	0.92	0.03259721	0.00000378	-0.08	0.32	-0.08	0.45
TEM_cf_Mmount_Si@27	0.16	0.92	0.03260501	0.00000379	0.16	0.32	0.16	0.45
TEM_cf_Mmount_Si@28	0.16	0.93	0.03258584	0.00000571	-0.43	0.34	-0.43	0.48
TEM_cf_Mmount_Si@29	0.16	0.93	0.03259196	0.00000595	-0.24	0.35	-0.24	0.49
TEM_cf_Mmount_Si@30	0.15	0.88	0.03258661	0.00000502	-0.40	0.33	-0.40	0.47
TEM_cf_Mmount_Si@31	0.16	0.92	0.03259440	0.00000603	-0.17	0.35	-0.17	0.49
AB-11-12 (Silicified volcanic rock 2.7 Ga Abitibi Greenstone Belt; N 48° 35.268, W 079° 20.604')								
AB_11_12_Mmount_Si@1	0.18	1.03	0.03258766	0.00000934	-0.37	0.41	-0.37	0.41
AB_11_12_Mmount_Si@02	0.18	1.03	0.03259968	0.00000614	0.00	0.35	0.00	0.35
AB_11_12_Mmount_Si@03	0.17	1.00	0.03261781	0.00000657	0.55	0.36	0.55	0.36
AB_11_12_Mmount_Si@04	0.18	1.03	0.03261512	0.00000674	0.47	0.36	0.47	0.36

Table 4-4. Continued.

Point #	^{28}Si	$^{28}Si_{samp/av.stnd}$	$^{30}Si/^{28}Si$	± abs	$\delta^{30}Si$	± ‰	$\delta^{30}Si$	± ‰
	cps x 10^9		*drift corrected*		*samples measured*		*samples corrected*	
AB_11_12_Mmount_Si@05	0.18	1.02	0.03262550	0.00000410	0.79	0.32	0.79	0.32
AB_11_12_Mmount_Si@06	0.18	1.03	0.03259940	0.00000678	-0.01	0.36	-0.01	0.36
AB_11_12_Mmount_Si@07	0.17	1.02	0.03261826	0.00000555	0.57	0.34	0.57	0.34
AB_11_12_Mmount_Si@08	0.18	1.03	0.03262663	0.00000521	0.82	0.34	0.82	0.34
AB_11_12_Mmount_Si@09	0.17	1.01	0.03261428	0.00000533	0.44	0.34	0.44	0.34
AB_11_12_Mmount_Si@10	0.17	1.01	0.03261060	0.00000689	0.33	0.36	0.33	0.36
AB_11_12_Mmount_Si@11	0.17	1.00	0.03260235	0.00000547	0.08	0.34	0.08	0.34
AB_11_12_Mmount_Si@12	0.17	1.02	0.03260035	0.00000655	0.02	0.36	0.02	0.36
AB_11_12_Mmount_Si@13	0.17	0.99	0.03257619	0.00000736	-0.72	0.37	-0.72	0.37
AB_11_12_Mmount_Si@14	0.17	0.99	0.03262008	0.00000657	0.62	0.36	0.62	0.36

† ISB3 standard equivalent to ISUA3, separate analytical run

Table 4-5. Calculated peak values for each sample

Age	Locality	Sample	Rock type	$\delta^{30}Si$	± ‰
					peak
> 3.7 Ga	Isua Greenstone Belt	IS-02-05	Algoma-type BIF	-1.41	0.43
		IS-02-06	Algoma-type BIF	-2.56	0.32
		IS-02-08	Algoma-type BIF	-1.79	0.80
		ISB 55	Greenstone chert	-0.35	0.34
		ISB 28	Greenstone chert	-0.41	0.48
		ISB 26	Greenstone chert	0.29	0.82
~ 3.0 Ga	Buhwa Greenstone Belt	ZB 182	Bedrock gneiss	0.94	0.41
		ZB 240	Quartz arenite	0.59	0.44
		ZB 105	Greenstone chert	0.79	1.13*
		ZB 07	Greenstone chert	-0.42	0.46
		ZB 17	Superior-type BIF	-0.64	0.25
		ZB 18	Superior-type BIF	-0.44	0.35
		ZB 20	Superior-type BIF	-1.74	0.37
		ZB 23	Superior-type BIF	-1.23	0.71
		ZB 143	Superior-type BIF	-0.86	0.61
		ZB 169	Superior-type BIF	-1.66	0.45
		ZB 05	Algoma-type BIF	-2.14	0.57
2.7 Ga	Abitibi Greenstone Belt	TEM CF	Algoma-type BIF	-0.41	0.58
		TEM 13 Db	Algoma-type BIF	-0.46	0.67
		TEMj	Algoma-type BIF	-0.79	0.74
		AB-11-12	Silicified volcanic rock	0.41	0.56

*higher than others due to 4 spurious data points

Table 4-6. Compiled sources and sample locations for others $\delta^{30}Si$ data

Age (Ga)	Locality	Formation / Unit name	Chert types	Reference	Method
>3.7	Isua Greenstone Belt, SW Greenland	N/A*	Silicified rock	Andre et al. (2006)	MC-ICP-MS
>3.7	Isua Greenstone Belt, SW Greenland	N/A*	Algoma-type BIF	Heck et al. (2011)	SIMS
>3.7	Isua Greenstone Belt, SW Greenland	N/A*	Algoma-type BIF	This study	SIMS
3.545	Pilbara Craton, Warrawoona Group, Western Australia	Apex Formation, Apex chert	Silicified rock	Van den Boorn et al. (2007)	MC-ICP-MS
3.545	Pilbara Craton, Warrawoona Group, Western Australia	Apex Formation, Apex chert	Bedded (gs-assoc) chert	Van den Boorn et al. (2007)	MC-ICP-MS
3.54	Barberton Greenstone Belt, Kapvaal Craton, S.Africa, Swaziland	Swaziland Supergroup, Onverwacht Group, Theespruit Formation	Silicified rock	Abraham et al. (2011)	P2Q-ICP-MS
3.5	Pilbara Craton, Warrawoona Group, Western Australia	Kittys Gap Chert	Silicified rock	Van den Boorn et al. (2010)	MC-ICP-MS
3.5	Pilbara Craton, Warrawoona Group, Western Australia	Kittys Gap Chert	Bedded (gs-assoc) chert	Van den Boorn et al. (2010)	MC-ICP-MS
3.5	Pilbara Craton, Warrawoona Group, Western Australia	Marble Bar Chert	Bedded (gs-assoc) chert	Van den Boorn et al. (2010)	MC-ICP-MS
3.5	Pilbara Craton, Warrawoona Group, Western Australia	Marble Bar Chert	Silicified rock	Van den Boorn et al. (2010)	MC-ICP-MS
3.5	Pilbara Craton, Warrawoona Group, Western Australia	North Pole Chert	Silicified rock	Van den Boorn et al. (2010)	MC-ICP-MS
3.5	Barberton Greenstone Belt, S. Africa	Onverwacht Group	Silicified rock	Robert and Chaussidon (2006)†	SIMS
3.49	Pilbara Craton, Warrawoona Group, Western Australia	Dresser Formation McPhee Chert	Silicified rock	Van den Boorn et al. (2007)	MC-ICP-MS
3.49	Pilbara Craton, Warrawoona Group, Western Australia	Dresser Formation, North Pole chert-barite unit	Bedded (gs-assoc) chert	Van den Boorn et al. (2007)	MC-ICP-MS
3.48	Pilbara Craton, Warrawoona Group, Western Australia	Dresser Formation	Bedded (gs-assoc) chert	Marin-Carbonne et al. (2012)	SIMS
3.46	Pilbara Craton, Warrawoona Group, Western Australia	Towers Formation, Marble Bar Chert	Bedded (gs-assoc) chert	Van den Boorn et al. (2007)	MC-ICP-MS
3.45	Pilbara Craton, Warrawoona Group, Western Australia	Panorama Formation, Kitty's Gap volcano-sedimentary unit	Silicified rock	Van den Boorn et al. (2007)	MC-ICP-MS
3.45	Kapvaal Craton, S.Africa, Swaziland	Swaziland Supergroup, Onverwacht Group, Hooggenoeg Formation	Silicified rock	Abraham et al. (2011)	P2Q-ICP-MS
3.33	Kapvaal Craton, S.Africa, Swaziland	Swaziland Supergroup, Onverwacht Group, Kromberg Formation	Silicified rock	Abraham et al. (2011)	P2Q-ICP-MS
3.29	Barberton Greenstone Belt, Kapvaal Craton, S.Africa, Swaziland	Swaziland Supergroup, Onverwacht Group, Mendon Formation	Bedded (gs-assoc) chert	Marin-Carbonne et al. (2012)	SIMS
3.26	Pilbara Craton, Western Australia	Kangaroo Caves Formation Sulphur Spring Chert	Silicified rock	Van den Boorn et al. (2007)	MC-ICP-MS
3.02	Pilbara Craton, Western Australia	Cleaverville formation, Dixon Island chert	Bedded (gs-assoc) chert	Van den Boorn et al. (2007)	MC-ICP-MS
3.02	Pilbara Craton, Western Australia	Cleaverville formation, Snapper Beach BIF	Superior-type BIF	Van den Boorn et al. (2007)	MC-ICP-MS
3.02	Pilbara Craton, Western Australia	Cleavervillle formation, Point Samson chert	Bedded (gs-assoc) chert	Van den Boorn et al. (2007)	MC-ICP-MS
3	Buhwa Greenstone Belt, Zimbabwe	N/A*	Algoma-type BIF	This study	SIMS

Table 4-6. Continued.

Age (Ga)	Locality	Formation / Unit name	Chert types	Reference	Method
3	Buhwa Greenstone Belt, Zimbabwe	IF 1	Superior-type BIF	This study	SIMS
2.985	Kapvaal Craton, S.Africa, Swaziland	Mozaan jaspilitic IF, Pongola Supergroup	Superior-type BIF	Delvigne et al. (2012)	MC-iCP-MS
2.75	Shurugwi Greenstone Belt, Zimbabwe	Wanderer IF, Bulawayan Supergroup	Algoma-type BIF	Steinhoefel et al. (2010)	Femtosecond LA-ICP-MS
2.72	Abitibi Greenstone Belt, Canada	Hunter Mine Group	Silicified rock	This study	SIMS
2.7	Hamersley Basin, W. Australia	Tumbiana Formation, Forescue Group	Bedded chert	Marin-Carbonne et al. (2012)	SIMS
2.7	Abitibi Greenstone Belt, Canada	Temagami Iron Formation	Algoma-type BIF	This study	SIMS
2.7	NW, Ontario	Wabigoon Belt	Algoma-type BIF	Robert and Chaussidon (2006)†	SIMS
2.65	Ventersdorp Basin, S. Africa	Ventersdorp Supergroup, Rietgat Formation	Bedded (carb-assoc) chert	Robert and Chaussidon (2006)†	SIMS
2.63	Belingwe Greenstone Belt , Zimbabwe	Manjeri Formation	Bedded (carb-assoc) chert	Robert and Chaussidon (2006)†	SIMS
2.57	Western Australia	Wittenoom Formation, Hamersley Group	Bedded (carb-assoc) chert	Chakrabarti et al. (2012)	MC-ICP-MS
2.53	Transvaal Supergroup, S. Africa	Griqualand West	Superior-type BIF	Chakrabarti et al. (2012)	MC-ICP-MS
2.53	Transvaal Supergroup, S. Africa	Griqualand West	Bedded (carb-assoc) chert	Chakrabarti et al. (2012)	MC-ICP-MS
2.5	Transvaal Supergroup, S. Africa	Transvaal Iron Formation	Superior-type BIF	Heck et al. (2011)	SIMS
2.5	Hamersley Group, Western Australia	Dales Gorge Member, Brockman Iron Formation	Superior-type BIF	Heck et al. (2011)	SIMS
2.5	Hamersley Group, Western Australia	Dales Gorge Member, Brockman Iron Formation	Superior-type BIF	Chakrabarti et al. (2012)	MC-ICP-MS
2.5	Superior Province, Canada	Keewatin Iron Formation	Superior-type BIF	Robert and Chaussidon (2006)†	SIMS
2.2	Yuanjiacun Formation, Lvliang Group, North China Craton	Jianshan, Hugushan, and Yuanjiacun banded iron formation	Superior-type BIF	Kejun, et al., (2014)	ICP-MS
2	Austrailia	Wyloo Group, Ashburton Trough	Bedded (carb-assoc) chert	Robert and Chaussidon (2006)†	SIMS
1.88	Superior Province, Minnesota, USA	Mesabi Iron Range, Biwabik Iron formation	Superior-type BIF	Heck et al. (2011)	SIMS
1.88	Superior Province, Minnesota, USA	Mesabi Iron Range, Biwabik Iron formation	Superior-type BIF	Chakrabarti et al. (2012)	MC-ICP-MS
1.88	Superior Province, Canada	Mesabi Iron Range, Gunflint Iron Formation	Superior-type BIF	Marin-Carbonne et al. (2012)	SIMS
1.88	Superior Province, Canada	Mesabi Iron Range, Gunflint Iron Formation	Bedded (carb-assoc) chert	Chakrabarti et al. (2012)	MC-ICP-MS
1.88	Superior Province, Canada	Mesabi Iron Range, Gunflint Iron Formation	Superior-type BIF	Chakrabarti et al. (2012)	MC-ICP-MS
1.88	Western Australia	Duck Creek Formation	Superior-type BIF	Chakrabarti et al. (2012)	MC-ICP-MS

Table 4-6. Continued.

Age (Ga)	Locality	Formation / Unit name	Chert types	Reference	Method
1.8	Western Australia	Frere Formation	Superior-type BIF	Chakrabarti et al. (2012)	MC-ICP-MS
1.78	China	Jixian Group	Bedded (carb-assoc) chert	Robert and Chaussidon (2006)†	SIMS
1.5	Australia	MacArthur Group, Amelia Dolomite	Bedded (carb-assoc) chert	Robert and Chaussidon (2006)†	SIMS
1.5	China	Jixian Group	Bedded (carb-assoc) chert	Robert and Chaussidon (2006)†	SIMS
1.45 - 1.5	Siberia	Kotuikan Formation, Billyakh Group	Bedded (carb-assoc) chert	Chakrabarti et al. (2012)	MC-ICP-MS
1.45 - 1.5	Siberia	Yusmastakh Formation, Billyakh Group	Bedded (carb-assoc) chert	Chakrabarti et al. (2012)	MC-ICP-MS
1.35	China	Jixian Group - Zhaozhuang	Bedded (carb-assoc) chert	Robert and Chaussidon (2006)†	SIMS
1.2	NW Greenland	NarssarssukFormation	Bedded (carb-assoc) chert	Chakrabarti et al. (2012)	MC-ICP-MS
1.2	Baffin Island, Canada	Society Cliffs Formation	Bedded (carb-assoc) chert	Chakrabarti et al. (2012)	MC-ICP-MS
1.0 - 1.1	SW Siberia	Sukhaya Tunguska Formation	Bedded (carb-assoc) chert	Chakrabarti et al. (2012)	MC-ICP-MS
0.85	Australia	Amadeus Basin, Bitter Springs Formation	Bedded (carb-assoc) chert	Robert and Chaussidon (2006)†	SIMS
0.8	Africa	Mauritanie	Bedded (carb-assoc) chert	Robert and Chaussidon (2006)†	SIMS
0.8	E. Greenland	Limestone-Dolomite Series	Bedded (carb-assoc) chert	Chakrabarti et al. (2012)	MC-ICP-MS
0.8	Svalbard, Norway	Hunnberg Formation, Nordaustlandet	Bedded (carb-assoc) chert	Chakrabarti et al. (2012)	MC-ICP-MS
0.77	Alaska	Fifteenmile Group	Bedded (carb-assoc) chert	Chakrabarti et al. (2012)	MC-ICP-MS
0.75	Svalbard, Norway	Akademikerbreen Group, Spitsbergen	Bedded (carb-assoc) chert	Chakrabarti et al. (2012)	MC-ICP-MS
0.6	China	Doushantuo Formation	Bedded (carb-assoc) chert	Robert and Chaussidon (2006)†	SIMS
0.542	Yangtze Platform, S. China	Liuchapo Formation, Yinjiang section	Bedded (carb-assoc) chert	Fan et al. (2013)	MAT 253 IRMS
0.532	Yangtze Platform, S. China	Chuanyanping Section	Bedded (carb-assoc) chert	Fan et al. (2013)	MAT 253 IRMS

N/A* = not applicable
† data not plotted in Figures 4-6, 4-7 because they only represent SIMS average values

Table 4-7. Preliminary run $\delta^{30}Si$ data including measured crystal sizes.

Point #	Mineral	Session run	Crystal Size (µm)	Crystal Size (µm)	^{28}Si	$^{28}Si_{samp/av.stnd}$	$^{30}Si/^{28}Si$	± abs	$\delta^{30}Si$	± ‰
			(long axis)	*(short axis)*	*cps x 10 ^{9}*		*drift corrected*		*samples*	
IS-02-05 (Algoma BIF, >3.7 Ga Isua Greenstone Belt; N 65° 10.350', W 049° 49.263')										
IS_02_05_@1	quartz	3.4	50	22.5	0.18	1.05	0.03265683	0.00000375	-0.64	0.18
IS_02_05_@2	quartz	3.5	50	32.5	0.18	1.04	0.03264082	0.00000240	-1.13	0.16
IS_02_05_@3	quartz	3.6	137.5	45	0.18	1.02	0.03264576	0.00000482	-0.98	0.20
IS_02_05_@4	quartz	3.7	87.5	37.5	0.18	1.02	0.03262893	0.00000318	-1.50	0.17
IS_02_05_@5	quartz	3.8	120	72.5	0.18	1.00	0.03261389	0.00000616	-1.96	0.23
IS_02_05_@6	quartz	3.9	--	--	0.00	0.00	-0.01238354		*omitted as outlier*	
IS_02_05_@7	quartz	3.12	57.5	75	0.17	0.99	0.03260866	0.00000198	-2.12	0.15
IS_02_05_@8	quartz	3.13	57.5	40	0.17	0.96	0.03263122	0.00000572	-1.43	0.22
IS_02_05_@9	quartz	3.14	72.5	45	0.18	1.00	0.03263142	0.00000267	-1.42	0.16
IS_02_05_@10	quartz	3.15	65	62.5	0.18	1.00	0.03262946	0.00000289	-1.48	0.16
IS_02_05_@11	quartz	3.16	55	40	0.18	1.00	0.03263782	0.00000272	-1.23	0.16
IS_02_05_@12	quartz	3.17	30	27.5	0.18	1.00	0.03262093	0.00000332	-1.74	0.17
IS_02_05_@13	quartz	3.20	72.5	40	0.17	0.99	0.03264293	0.00000504	-1.07	0.21
IS_02_05_@14	quartz	3.21	72.5	40	0.17	0.99	0.03263224	0.00000300	-1.40	0.17
IS_02_05_@15	quartz	3.22	225	95	0.18	1.01	0.03265713	0.00000354	-0.64	0.18
IS_02_05_@16	quartz	3.23	R	R	0.18	1.00	0.03267233	0.00000322	-0.17	0.17
IS_02_05_@17	quartz	3.24	--	--	0.17	0.96	0.03271274	0.00000334	*omitted as outlier*	
IS_02_05_@18	quartz	3.25	225	72.5	0.17	1.00	0.03263299	0.00000333	-1.37	0.17
IS_02_05_@19	quartz	3.28	R	R	0.17	0.99	0.03264345	0.00000423	-1.05	0.19
IS_02_05_@20	quartz	3.29	R	R	0.17	0.98	0.03262774	0.00000355	-1.53	0.18
IS_02_05_@21	quartz	3.30	R	R	0.17	0.97	0.03262003	0.00000498	-1.77	0.21

Table 4-7. Continued.

Point #	Mineral	Session run	Crystal Size (µm)	Crystal Size (µm)	^{28}Si	$^{28}Si_{samp/av.stnd}$	$^{30}Si/^{28}Si$	± abs	$\delta^{30}Si$	± ‰
			(long axis)	*(short axis)*	*cps x 10^9*		*drift corrected*		*samples*	
IS-02-06 (Algoma BIF, >3.7 Ga Isua Greenstone Belt; N 65° 10.353', W 049° 49.200')										
IS_02_06_@22	quartz	3.31	137.5	75	0.16	0.94	0.03258530	0.00000437	-2.83	0.19
IS_02_06_@23	quartz	3.32	132.5	130	0.17	0.96	0.03258863	0.00000577	-2.73	0.22
IS_02_06_@24	quartz	3.33	75	32.5	0.16	0.91	0.03300845	0.00000297	*omitted as outlier*	
IS_02_06_@25	quartz	3.36	62.5	77.5	0.17	0.96	0.03262307	0.00000384	-1.68	0.18
IS_02_06_@26	quartz	3.37	112.5	97.5	0.17	0.97	0.03262055	0.00000379	-1.75	0.18
IS_02_06_@27	quartz	3.38	162.5	85	0.17	0.96	0.03259679	0.00000243	-2.48	0.16
IS_02_06_@28	quartz	3.39	122.5	115	0.17	0.95	0.03259496	0.00000294	-2.54	0.17
IS_02_06_@29	quartz	3.40	122.5	115	0.17	0.95	0.03260121	0.00000323	-2.35	0.17
IS_02_06_@30	quartz	3.41	122.5	115	0.17	0.96	0.03260222	0.00000257	-2.32	0.16
IS_02_06_@31	quartz	3.44	200	150	0.16	0.94	0.03258818	0.00000474	-2.75	0.20
IS_02_06_@32	quartz	3.45	52.5	42.5	0.16	0.93	0.03257232	0.00000323	-3.23	0.17
IS_02_06_@33	quartz	3.46	127.5	100	0.16	0.92	0.03258135	0.00000553	-2.95	0.22
IS_02_06_@34	quartz	3.47	127.5	100	0.16	0.92	0.03258965	0.00000397	-2.70	0.18
IS_02_06_@35	quartz	3.48	80	37.5	0.17	0.96	0.03259637	0.00000507	-2.49	0.21
IS_02_06_@36	quartz	3.49	52.5	50	0.16	0.93	0.03256802	0.00000456	-3.36	0.20
IS_02_06_@37	quartz	3.52	75	70	0.16	0.91	0.03257200	0.00000322	-3.24	0.17
IS_02_06_@38	quartz	3.53	85	25	0.16	0.90	0.03256762	0.00000308	-3.37	0.17
IS-02-08 (Algoma BIF, >3.7 Ga Isua Greenstone Belt; N 65° 12.531', W 049° 45.504')										
IS_02_08_@39	quartz	3.54	60	45	0.17	0.98	0.03260843	0.00000372	-2.13	0.18
IS_02_08_@40	quartz	3.55	170	120	0.17	0.98	0.03261566	0.00000313	-1.90	0.17

Table 4-7. Continued.

Point #	Mineral	Session run	Crystal Size (µm)	Crystal Size (µm)	^{28}Si	$^{28}Si_{samp/av.stnd}$	$^{30}Si/^{28}Si$	± abs	$\delta^{30}Si$	± ‰
			(long axis)	*(short axis)*	*cps x 10^9*		*drift corrected*		*samples*	
IS_02_08_@41	quartz	3.56	170	120	0.17	0.97	0.03264339	0.00000262	-1.06	0.16
IS_02_08_@42	quartz	3.57	132.5	127.5	0.17	0.97	0.03262598	0.00000379	-1.59	0.18
IS_02_08_@43	quartz	3.60	132.5	127.5	0.17	0.97	0.03262962	0.00000374	-1.48	0.18
IS_02_08_@44	quartz	3.61	132.5	127.5	0.17	0.97	0.03263297	0.00000526	-1.37	0.21
IS_02_08_@45	quartz	3.62	132.5	127.5	0.17	0.97	0.03262398	0.00000454	-1.65	0.20
IS_02_08_@46	quartz	3.63	122.5	112.5	0.17	0.97	0.03264006	0.00000374	-1.16	0.18
IS_02_08_@47	quartz	3.64	87.5	40	0.17	0.97	0.03261967	0.00000351	-1.78	0.18
IS_02_08_@48	quartz	3.65	57.5	25	0.17	0.97	0.03263829	0.00000359	-1.21	0.18
IS_02_08_@49	quartz	3.68	35	17.5	0.16	0.93	0.03259348	0.00000368	-2.58	0.18
IS_02_08_@50	quartz	3.69	37.5	17.5	0.16	0.94	0.03263769	0.00000416	-1.23	0.19
IS_02_08_@51	quartz	3.70	40	30	0.17	0.96	0.03261712	0.00000494	-1.86	0.21
IS_02_08_@52	quartz	3.71	32.5	25	0.16	0.92	0.03264746	0.00000348	-0.93	0.18
IS_02_08_@53	quartz	3.72	45	27.5	0.17	0.94	0.03259799	0.00000399	-2.45	0.18
IS_02_08_@54	quartz	3.73	47.5	42.5	0.17	0.96	0.03259673	0.00000400	-2.48	0.19
IS_02_08_@55	quartz	3.74	45	27.5	0.17	0.95	0.03263920	0.00000347	-1.18	0.18
ZB 05 (Algoma BIF, ~3.0 Ga Buhwa Greenstone Belt; S 20° 34.85', E 30° 26.892660')										
ZB_05_@1	quartz	6.4	70	30	0.17	1.30	0.03254310	0.00000331	-6.22	0.20
ZB_05_@02	quartz	6.5	75	47.5	0.17	1.27	0.03257820	0.00000526	-5.15	0.24
ZB_05_@03	quartz	6.6	95	77.5	0.16	1.24	0.03257348	0.00000328	-5.30	0.20
ZB_05_@04	quartz	6.7	82.5	77.5	0.16	1.24	0.03257020	0.00000458	-5.40	0.22
ZB_05_@05	quartz	6.8	137.5	112.5	0.16	1.24	0.03257709	0.00000448	-5.19	0.22
ZB_05_@06	quartz	6.9	72.5	70	0.15	1.18	0.03258686	0.00000361	-4.89	0.21

Table 4-7. Continued.

Point #	Mineral	Session run	Crystal Size (µm)	Crystal Size (µm)	^{28}Si	$^{28}Si_{samp/av.stnd}$	$^{30}Si/^{28}Si$	± abs	$\delta^{30}Si$	± ‰
			(long axis)	*(short axis)*	*cps x 10^9*		*drift corrected*		*samples*	
ZB_05_@07	quartz	6.12	75	72.5	0.16	1.19	0.03257141	0.00000461	-5.36	0.22
ZB_05_@08	quartz	6.13	62.5	45	0.15	1.17	0.03257051	0.00000338	-5.39	0.20
ZB_05_@09	quartz	6.14	67.5	45	0.15	1.18	0.03258843	0.00000272	-4.84	0.19
ZB_05_@10	quartz	6.15	130	75	0.15	1.18	0.03259068	0.00000320	-4.77	0.20
ZB_05_@11	quartz	6.16	100	45	0.15	1.14	0.03256554	0.00000214	-5.54	0.19
ZB_05_@12	quartz	6.17	72.5	35	0.15	1.15	0.03259597	0.00000293	-4.61	0.20
ZB_05_@13	quartz	6.20	77.5	45	0.15	1.12	0.03258905	0.00000366	-4.82	0.21
ZB_05_@14	quartz	6.21	60	35	0.14	1.10	0.03258615	0.00000392	-4.91	0.21
ZB_05_@15	quartz	6.22	50	30	0.14	1.10	0.03258514	0.00000556	-4.94	0.24
ZB_05_@16	quartz	6.23	47.5	40	0.14	1.11	0.03259493	0.00000523	-4.64	0.24
ZB_05_@17	quartz	6.24	80	67.5	0.14	1.09	0.03257626	0.00000636	-5.21	0.26
ZB_05_@18	quartz	6.25	130	82.5	0.14	1.08	0.03257445	0.00000604	-5.27	0.25
ZB_05_@19	quartz	6.28	75	70	0.14	1.07	0.03258001	0.00000446	-5.10	0.22
ZB_05_@20	quartz	6.29	100	65	0.14	1.07	0.03258740	0.00000352	-4.87	0.20
ZB_05_@21	quartz	6.30	167.5	62.5	0.14	1.06	0.03255031	0.00000330	-6.00	0.20
ZB_05_@22	quartz	6.31	75	65	0.14	1.05	0.03255499	0.00000514	-5.86	0.23
ZB_05_@23	quartz	6.32	90	52.5	0.14	1.04	0.03258915	0.00000444	-4.82	0.22
ZB_05_@24	quartz	6.33	57.5	52.5	0.14	1.04	0.03257821	0.00000531	-5.15	0.24
ZB_05_@25	quartz	6.36	75	52.5	0.13	0.99	0.03256662	0.00000573	-5.50	0.25
ZB 27 (Algoma BIF, ~3.0 Ga Buhwa Greenstone Belt; S 20° 45.57', E 30° 15.29')										
ZB_27_@38	quartz	6.53	150	150	0.12	0.95	0.03260894	0.00000234	-4.21	0.19
ZB_27_@39	quartz	6.54	180	160	0.12	0.93	0.03260887	0.00000761	-4.21	0.29

Table 4-7. Continued.

Point #	Mineral	Session run	Crystal Size (µm)	Crystal Size (µm)	^{28}Si	$^{28}Si_{samp/av.stnd}$	$^{30}Si/^{28}Si$	± abs	$\delta^{30}Si$	± ‰
			(long axis)	*(short axis)*	*cps x 10^9*		*drift corrected*		*samples*	
ZB_27_@40	quartz	6.55	75	52.5	0.12	0.93	0.03260598	0.00000508	-4.30	0.23
ZB_27_@41	quartz	6.56	115	87.5	0.12	0.95	0.03262349	0.00000857	-3.77	0.31
ZB_27_@42	quartz	6.57	115	75	0.12	0.93	0.03257423	0.00000340	-5.27	0.20
ZB_27_@43	quartz	6.60	100	90	0.12	0.93	0.03259423	0.00000591	-4.66	0.25
ZB_27_@44	quartz	6.61	160	110	0.12	0.92	0.03258610	0.00000493	-4.91	0.23
ZB_27_@45	quartz	6.62	105	62.5	0.12	0.91	0.03257949	0.00000417	-5.11	0.22
ZB_27_@46	quartz	6.63	222.5	100	0.12	0.91	0.03258605	0.00000497	-4.91	0.23
ZB_27_@47	quartz	6.64	140	107.5	0.12	0.89	0.03259559	0.00000462	-4.62	0.22
ZB 169 (Superior BIF, ~3.0 Ga Buhwa Greenstone Belt; S 20° 37.08', E 30° 20.20')										
ZB_169_@48	quartz	6.65	20	16.25	0.12	0.89	0.03258949	0.00000621	-4.81	0.26
ZB_169_@49	quartz	6.68			0.12	0.88	0.03260350	0.00000243	-4.38	0.19
ZB_169_@50	quartz	6.69	20	16.25	0.11	0.87	0.03259525	0.00000520	-4.63	0.24
ZB_169_@51	quartz	6.70	17.5	17.5	0.12	0.89	0.03260906	0.00000495	-4.21	0.23
ZB_169_@52	quartz	6.71	25	16.25	0.12	0.89	0.03261108	0.00000542	-4.15	0.24
ZB_169_@53	quartz	6.72	17.5	17.5	0.11	0.87	0.03258822	0.00000409	-4.85	0.21
ZB_169_@54	quartz	6.73	17.5	17.5	0.11	0.88	0.03259873	0.00000536	-4.52	0.24
ZB_169_@55	quartz	6.76	17.5	17.5	0.11	0.87	0.03258839	0.00000734	-4.84	0.28
ZB_169_@56	quartz	6.77	17.5	17.5	0.11	0.86	0.03259529	0.00000339	-4.63	0.20
ZB_169_@57	quartz	6.78	17.5	17.5	0.11	0.85	0.03258683	0.00000579	-4.89	0.25
ZB_169_@58	quartz	6.79	17.5	17.5	0.11	0.84	0.03258325	0.00000425	-5.00	0.22
ZB_169_@59	quartz	6.80	17.5	17.5	0.11	0.83	0.03258481	0.00000653	-4.95	0.26
ZB_169_@60	quartz	6.83	20	17.5	0.11	0.83	0.03258899	0.00000532	-4.82	0.24

Table 4-7. Continued.

Point #	Mineral	Session run	Crystal Size (µm)	Crystal Size (µm)	^{28}Si	$^{28}Si_{samp/av.stnd}$	$^{30}Si/^{28}Si$	± abs	$\delta^{30}Si$	± ‰
			(long axis)	*(short axis)*	*cps x 10^9*		*drift corrected*		*samples*	
ZB_169_@61	quartz	6.84	17.5	17.5	0.11	0.83	0.03258198	0.00000746	-5.04	0.29
ZB_169_@62	quartz	6.85	17.5	17.5	0.11	0.81	0.03256445	0.00000550	-5.57	0.24
ZB_169_@63	quartz	6.86	30	15	0.11	0.82	0.03259621	0.00000679	-4.60	0.27
ZB_169_@64	quartz	6.87	27.5	17.5	0.11	0.83	0.03257442	0.00000865	-5.27	0.32
ZB 23 (Superior BIF, ~3.0 Ga Buhwa Greenstone Belt; S 20° 37.03', E 30° 21.68')										
ZB_23_@1	quartz	5.4	27.5	25	0.19	1.04	0.03259197	0.00000463	-2.99	0.22
ZB_23_@02	quartz	5.5	27.5	25	0.19	1.03	0.03259361	0.00000450	-2.94	0.22
ZB_23_@03	quartz	5.6	27.5	25	0.19	1.03	0.03259678	0.00000371	-2.84	0.21
ZB_23_@04	quartz	5.7	35	27.5	0.18	1.01	0.03263327	0.00000260	-1.72	0.19
ZB_23_@05	quartz	5.8	30	22.5	0.19	1.03	0.03261343	0.00000204	-2.33	0.18
ZB_23_@06	quartz	5.9	55	42.5	0.19	1.03	0.03261441	0.00000464	-2.30	0.22
ZB_23_@07	quartz	5.12	42.5	37.5	0.19	1.02	0.03262013	0.00000313	-2.13	0.20
ZB_23_@08	quartz	5.13	47.5	30	0.18	1.02	0.03261816	0.00000244	-2.19	0.19
ZB_23_@09	quartz	5.14	40	32.5	0.19	1.02	0.03260883	0.00000227	-2.47	0.19
ZB_23_@10	quartz	5.15	50	27.5	0.18	1.01	0.03260307	0.00000317	-2.65	0.20
ZB_23_@11	quartz	5.16	40	27.5	0.19	1.02	0.03261997	0.00000467	-2.13	0.22
ZB_23_@12	quartz	5.17	40	22.5	0.18	1.01	0.03262968	0.00000436	-1.83	0.22
ZB_23_@13	quartz	5.20	22.5	20	0.18	1.00	0.03261930	0.00000193	-2.15	0.18
ZB_23_@14	quartz	5.21	40	17.5	0.18	1.00	0.03262954	0.00000395	-1.84	0.21
ZB_23_@15	quartz	5.22	37.5	22.5	0.18	1.00	0.03263519	0.00000500	-1.67	0.23
ZB_23_@16	quartz	5.23	57.5	50	0.18	1.00	0.03263950	0.00000340	-1.53	0.20
ZB_23_@17	quartz	5.24	25	17.5	0.18	0.99	0.03262991	0.00000272	-1.83	0.19

Table 4-7. Continued.

Point #	Mineral	Session run	Crystal Size (µm)	Crystal Size (µm)	^{28}Si	$^{28}Si_{samp/av.stnd}$	$^{30}Si/^{28}Si$	± abs	$\delta^{30}Si$	± ‰
			(long axis)	*(short axis)*	*cps x 10^9*		*drift corrected*		*samples*	
ZB_23_@18	quartz	5.25	47.5	25	0.18	0.98	0.03263155	0.00000466	-1.78	0.22
ZB_23_@19	quartz	5.28	17.5	20	0.18	0.99	0.03261953	0.00000252	-2.14	0.19
ZB_23_@20	quartz	5.29	25	25	0.18	0.99	0.03262095	0.00000322	-2.10	0.20
ZB_23_@21	quartz	5.30	37.5	20	0.18	0.99	0.03260410	0.00000430	-2.62	0.22
ZB_23_@23	quartz	5.31	37.5	17.5	0.18	0.99	0.03261836	0.00000229	-2.18	0.19
ZB_23_@24	quartz	5.32	37.5	17.5	0.18	0.99	0.03262380	0.00000281	-2.01	0.19
ZB_23_@25	quartz	5.35	37.5	35	0.19	1.03	0.03263120	0.00000379	-1.79	0.21
ZB_23_@26	quartz	5.36	45	37.5	0.19	1.06	0.03262459	0.00000327	-1.99	0.20
ZB_23_@27	quartz	5.37	30	30	0.19	1.06	0.03261597	0.00000564	-2.25	0.24
ZB_23_@28	quartz	5.38	40	50	0.20	1.08	0.03262531	0.00000314	-1.97	0.20
ZB_23_@29	quartz	5.39	45	25	0.20	1.10	0.03261231	0.00000328	-2.37	0.20
ZB_23_@30	quartz	5.40	25	22.5	0.20	1.11	0.03260997	0.00000324	-2.44	0.20
ZB_23_@31	quartz	5.43	40	22.5	0.21	1.14	0.03261500	0.00000284	-2.28	0.19
ZB_23_@32	quartz	5.44	47.5	30	0.20	1.13	0.03261767	0.00000292	-2.20	0.19
ZB_23_@33	quartz	5.45	35	32.5	0.21	1.16	0.03261363	0.00000338	-2.32	0.20
ZB_23_@34	quartz	5.46	27.5	22.5	0.21	1.15	0.03261100	0.00000302	-2.41	0.20
ZB 117 (BIF*, ~3.0 Ga Buhwa Greenstone Belt; S 20° 40.74', E 30° 21.98')										
ZB_117_@66	quartz	5.88	62.5	55	0.18	0.97	0.03262788	0.00000369	-1.89	0.21
ZB_117_@67	quartz	5.91	137.5	112.5	0.17	0.93	0.03258876	0.00000427	-3.09	0.22
ZB_117_@68	quartz	5.92	120	50	0.18	1.01	0.03260996	0.00000314	-2.44	0.20
ZB_117_@69	quartz	5.93	80	52.5	0.18	1.02	0.03260096	0.00000277	-2.71	0.19
ZB_117_@70	quartz	5.94	47.5	42.5	0.18	1.00	0.03259227	0.00000260	-2.98	0.19

Table 4-7. Continued.

Point #	Mineral	Session run	Crystal Size (µm)	Crystal Size (µm)	^{28}Si	$^{28}Si_{samp/av.stnd}$	$^{30}Si/^{28}Si$	± abs	$\delta^{30}Si$	± ‰
			(long axis)	*(short axis)*	*cps x 10^9*		*drift corrected*		*samples*	
ZB_117_@71	quartz	5.95	60	47.5	0.18	0.97	0.03258762	0.00000483	-3.12	0.23
ZB_117_@72	quartz	5.96	50	40	0.17	0.94	0.03256463	0.00000494	-3.82	0.23
ZB_117_@73	quartz	5.99	115	75	0.18	0.99	0.03259901	0.00000363	-2.77	0.21
ZB_117_@74	quartz	5.100	120	97.5	0.18	0.98	0.03259302	0.00000465	-2.96	0.22
ZB_117_@75	quartz	5.101	62.5	55	0.18	0.97	0.03259809	0.00000344	-2.80	0.20
ZB_117_@76	quartz	5.102	65	40	0.17	0.96	0.03259012	0.00000445	-3.04	0.22
ZB_117_@77	quartz	5.103	100	97.5	0.15	0.84	0.03260525	0.00000267	-2.58	0.19
ZB_117_@78	quartz	5.104	115	107.5	0.17	0.96	0.03261286	0.00000287	-2.35	0.19
ZB_117_@79	quartz	5.107	62.5	45	0.17	0.96	0.03263529	0.00000230	-1.66	0.19
ZB_117_@80	quartz	5.108	72.5	57.5	0.16	0.91	0.03264287	0.00000460	-1.43	0.22
ZB_117_@81	quartz	5.109	55	45	0.17	0.92	0.03262530	0.00000362	-1.97	0.21
ZB_117_@82	quartz	5.110	82.5	70	0.17	0.92	0.03260822	0.00000255	-2.49	0.19
ZB_117_@83	quartz	5.111	97.5	80	0.17	0.93	0.03259876	0.00000321	-2.78	0.20
ZB_117_@84	quartz	5.112	80	45	0.17	0.94	0.03259922	0.00000354	-2.77	0.20
TEM CF (Algoma BIF, 2.7 Ga Abitibi Greenstone Belt; N 47° 04.173', W 079° 47.434')										
TEM_CF_A1_@1	quartz	4.4	50	25	0.13	1.00	0.03261960	0.00000690	-2.39	0.26
TEM_CF_A1_@02	quartz	4.5	70	45	0.13	1.01	0.03262973	0.00000584	-2.08	0.24
TEM_CF_A1_@03	quartz	4.6	62.5	47.5	0.13	1.04	0.03266010	0.00000473	-1.15	0.22
TEM_CF_A1_@04	quartz	4.7	55	37.5	0.13	1.03	0.03265558	0.00000369	-1.29	0.20
TEM_CF_A1_@05	quartz	4.8	55	25	0.13	1.03	0.03264138	0.00000228	-1.73	0.17
TEM_CF_A1_@06	quartz	4.9	55	25	0.13	1.04	0.03266510	0.00000489	-1.00	0.22
TEM_CF_A1_@07	quartz	4.12	52.5	40	0.13	1.03	0.03266390	0.00000668	-1.04	0.26

Table 4-7. Continued.

Point #	Mineral	Session run	Crystal Size (µm)	Crystal Size (µm)	^{28}Si	$^{28}Si_{samp/av.stnd}$	$^{30}Si/^{28}Si$	± abs	$\delta^{30}Si$	± ‰
			(long axis)	*(short axis)*	*cps x 10^9*		*drift corrected*		*samples*	
TEM_CF_A1_@08	quartz	4.13	70	47.5	0.13	1.02	0.03264452	0.00000419	-1.63	0.20
TEM_CF_A1_@09	quartz	4.14	30	32.5	0.13	1.03	0.03265882	0.00000315	-1.19	0.19
TEM_CF_A1_@10	quartz	4.15	37.5	32.5	0.13	1.03	0.03265687	0.00000228	-1.25	0.17
TEM_CF_A1_@11	quartz	4.16	75	32.5	0.13	1.03	0.03265325	0.00000510	-1.36	0.22
TEM_CF_A1_@12	quartz	4.17	45	30	0.13	1.02	0.03263826	0.00000418	-1.82	0.20
TEM_CF_A1_@13	quartz	4.20	67.5	47.5	0.13	1.02	0.03265665	0.00000501	-1.24	0.22
TEM_CF_A1_@14	quartz	4.21	87.5	72.5	0.13	1.01	0.03265180	0.00000504	-1.39	0.22
TEM_CF_A1_@15	quartz	4.22	40	30	0.13	1.01	0.03265340	0.00000311	-1.34	0.19
TEM_CF_A1_@16	quartz	4.23	62.5	45	0.13	1.02	0.03265347	0.00000392	-1.34	0.20
TEM_CF_A1_@17	quartz	4.24	42.5	27.5	0.13	1.01	0.03266297	0.00000479	-1.05	0.22
TEM_CF_A1_@18	quartz	4.25	30	25	0.13	1.00	0.03263679	0.00000509	-1.85	0.22
TEM_CF_A1_@19	quartz	4.34	40	17.5	0.13	1.00	0.03265576	0.00000566	-1.29	0.24
TEM_CF_A1_@20	quartz	4.35	62.5	47.5	0.18	1.40	0.03263039	0.00000322	-2.06	0.19
TEM_CF_A2@21	quartz	4.36	70	30	0.17	1.30	0.03266364	0.00000322	-1.04	0.19
TEM_CF_A2@22	quartz	4.37	45	32.5	0.15	1.17	0.03267346	0.00000295	-0.74	0.18
TEM_CF_A2@23	quartz	4.38	35	37.5	0.14	1.10	0.03265924	0.00000406	-1.18	0.20
TEM_CF_A2@24	quartz	4.39	37.5	35	0.14	1.08	0.03264838	0.00000528	-1.51	0.23
TEM_CF_A2@25	quartz	4.42	65	27.5	0.13	1.03	0.03264010	0.00000380	-1.76	0.20
TEM_CF_A2@26	quartz	4.43	50	35	0.13	1.02	0.03263699	0.00000493	-1.86	0.22
TEM_CF_A4__@28	quartz	4.45	45	35	0.13	1.01	0.03265807	0.00000429	-1.21	0.21
TEM_CF_A4__@29	quartz	4.46	32.5	30	0.13	1.01	0.03266769	0.00000680	-0.92	0.26
TEM_CF_A4__@30	quartz	4.47	30	20	0.13	1.01	0.03266211	0.00000290	-1.09	0.18
TEM_CF_A4__@31	quartz	4.50	45	27.5	0.13	1.01	0.03267497	0.00000574	-0.70	0.24
TEM_CF_A4__@32	quartz	4.51	30	27.5	0.13	1.01	0.03267497	0.00000355	-0.70	0.19

Table 4-7. Continued.

Point #	Mineral	Session run	Crystal Size (µm)	Crystal Size (µm)	^{28}Si	$^{28}Si_{samp/av.stnd}$	$^{30}Si/^{28}Si$	± abs	$\delta^{30}Si$	± ‰
			(long axis)	*(short axis)*	*cps x 10^9*		*drift corrected*		*samples*	
TEM_CF_A4__@33	quartz	4.52	25	22.5	0.13	0.99	0.03265387	0.00000612	-1.34	0.25
TEM_CF_A4__@34	quartz	4.53	27.5	17.5	0.13	1.00	0.03266550	0.00000439	-0.99	0.21
AB-11-12 (Silicified volcanic 2.7 Ga Abitibi Greenstone Belt; N 48° 35.268, W 079° 20.604')										
AB12_@38	quartz	4.59	25	25	0.13	0.99	0.03271651	0.00000453	0.57	0.21
AB12_@39	quartz	4.60	16.25	16.25	0.13	0.99	0.03267537	0.00000280	-0.69	0.18
AB12_@40	quartz	4.61	16.25	16.25	0.13	0.99	0.03269877	0.00000630	0.03	0.25
AB12_@41	quartz	4.62	17.5	17.5	0.12	0.97	0.03268912	0.00000413	-0.27	0.20
AB12_@42	quartz	4.63	16.25	16.25	0.12	0.97	0.03270938	0.00000726	0.35	0.27
AB12_@43	quartz	4.66	27.5	25	0.12	0.98	0.03269177	0.00000462	-0.18	0.21
AB12_@44	quartz	4.67	42.5	16.25	0.12	0.97	0.03270858	0.00000420	0.33	0.20
AB12_@45	quartz	4.68	45	17.5	0.12	0.97	0.03270406	0.00000656	0.19	0.26
AB12_@46	quartz	4.69	17.5	16.25	0.12	0.96	0.03267476	0.00000499	-0.70	0.22
AB12_@47	quartz	4.70	45	27.5	0.12	0.96	0.03269832	0.00000290	0.02	0.18
AB12_@48	quartz	4.71	17.5	15	0.12	0.95	0.03273244	0.00000478	1.06	0.22
AB12_@49	quartz	4.74	25	17.5	0.12	0.94	0.03273749	0.00000411	1.21	0.20
AB12_@50	quartz	4.75	--	--	0.05	0.36	0.03285507	0.00001185	*omitted as outlier*	
AB12_@51	quartz	4.76	--	--	0.00	0.00	0.06569811		*omitted as outlier*	
AB12_@52	quartz	4.77	--	--	0.00	0.00	0.08373950		*omitted as outlier*	

Table 4-7. Continued.

Point #	Mineral	Session run	Crystal Size (µm)	Crystal Size (µm)	^{28}Si	$^{28}Si_{samp/av.stnd}$	$^{30}Si/^{28}Si$	± abs	$\delta^{30}Si$	± ‰
			(long axis)	*(short axis)*	*cps x 10^9*		*drift corrected*		*samples*	
AB-11-11 (Silicified volcanic 2.7 Ga Abitibi Greenstone Belt; N 48° 35.268, W 079° 20.604')										
AB11_4_@51	quartz	1.71	25	25	0.17	0.97	0.03266904	0.00000417	-0.59	0.20
AB11_4_@52	quartz	1.72	22.5	15	0.17	0.98	0.03268846	0.00000282	0.00	0.17
AB11_4_@53	quartz	1.73	22.5	15	0.17	0.98	0.03268038	0.00000356	-0.25	0.19
AB11_4_@54	quartz	1.74	27.5	25	0.16	0.93	0.03269846	0.00000545	0.31	0.23
AB11_4_@55	quartz	1.77	--	--	0.16	0.93	0.03263781	0.00000497	*omitted as outlier*	
AB11_5_@56	quartz	1.78	--	--	0.16	0.90	0.03274330	0.00000368	*omitted as outlier*	

*BIF sample of unclear depositional affinity

-- outlier points
R repeat analyses
Note values are uncorrected for stnd, only used for plot 5-10 showing crystal size verus $\delta^{30}Si$

VITA

Latisha Ashley Brengman was born December 5th, 1986. She grew up in Yorkville, Illinois, spending her youth chasing butterflies and collecting rocks. Her fascination with the world and the way it works led her to pursue a Bachelor's of Arts degree at Northwestern University, where she pursued both science and music. In the Fall of 2010, Latisha entered the graduate program in the Earth and Planetary Science department at the University of Tennessee, Knoxville to pursue her passion for understanding early Earth problems. During these 5 years she worked under the direction of Professor Christopher Fedo studying Precambrian chert genesis in an effort to better understand the ancient silica cycle. Upon completion of her dissertation defense, Latisha will begin a tenure-track position at the University of Minnesota, Duluth in August, 2015.